National University of Science and Technology
POLITEHNICA Bucharest

Faculty of Industrial Engineering and Robotics

Journal of Industrial Engineering and Robotics

2026, Volume 10, Issue 4

Experimental training MODEL FOR TABLE TENNIS

VĂRZARU Gabriel-Alexandru and Scientific Coordinator S.l.dr.ing. GHEORGHIȚĂ Vlad
Faculty: Industrial Engineering and Robotics, Specialization: Applied Informatics in Industrial Engineering, Year of study: 4, e-mail: avarzaru38@gmail.com

ABSTRACT: To ensure high-performance and autonomous athletic training, this 3D-printed table tennis robot was designed and implemented as a cost-effective alternative to industrial equipment. This system simulates real-match scenarios by utilizing a precise launching head with three DC motors to independently control ball frequency, speed, and complex spin effects. By automating ball recirculation and offering programmable horizontal oscillation, it allows players to improve reflexes and technique through repetitive, customizable practice sessions. Implementing such additive manufacturing-driven hardware provides an accessible, modular training tool that bridges the gap between professional sports technology and home-based development.

KEYWORDS: table tennis robot, 3D printing, additive manufacturing, autonomous training, mechatronics

1. Introduction and Objectives

The present project aims to develop an experimental model for autonomous training in table tennis, improving sports performance, reflexes and repetition hitting technique. The system simulates real game situations by launching the balls in a controlled manner, making it a useful solution for both professional and amateur athletes. The main goal is to provide a permanently available training partner capable of executing customizable and adaptable training routines [1].

The operation of the robot is based on an automated flow that includes collecting, controlled feeding and propulsion of balls with variable speeds and effects. The control unit manages the DC motors and oscillation servo motor to change the trajectory and spin (topspin, backspin, sidespin), providing random, preset or intelligent drive modes. Operational management is fully digitized through a web interface natively hosted on the microcontroller, allowing wireless control from any smart device [2].

The structural components are manufactured by additive technologies (3D printing) on a Qidi Plus 4 equipment, using PLA and FiberFlex 30D. The design adopts an advanced geometric optimization strategy by monolithizing the components, eliminating standard structural elements [3] to reduce weight and minimize gravitational load on the fuel engine. This approach reduces prototype costs to €150-300 [1] and enables easy maintenance by allowing parts to be reprinted.

2. Functional Analysis and Technical Sizing

2.1. Need analysis and functional breakdown

In order to rigorously define the construction requirements of the project, the functional analysis tool "horned insect" (Horned Beast) was applied, a methodology that allows mapping the interactions between the system and its operating environment. By using this tool, it has been established that the robot serves the player directly (as an autonomous training partner), acts physically on table tennis balls, and has as its main purpose the optimization of reflexes and the technique of hitting through personalized repetition. Starting from this central need, the general controlled launch function has been structurally decomposed into five correlated and interdependent technical functions: kinematic ball propulsion (), effect and spin vector generation (), dynamic distribution on the ground by horizontal oscillation (), automatic recirculation and feeding), respectively global digital control of all these parameters ().

$F_1 F_2 F_3 (F_4 F_5$

In the next evaluation phase, a square ranking matrix was used to determine the weight and priority of each function in the development of the prototype. Following the binary comparison, it was shown that propulsion () and spin generation () are the critical functions of the system, representing cumulatively of the total utility of the robot (with individual weights of and, respectively,). This result directly dictated the design decision to allocate a high-performance launch head equipped with three independent DC motors and elastic friction rollers made of FiberFlex 30D, capable of ensuring pulse transmission up to 10,000 RPM. The entire functional structure thus determined was directly transposed into the technical limits of the system's operation (such as the launch rate of 30–100 balls/min and the oscillation angle of), forming the design matrix that governs the physical dimensions and the automation logic of the assembly. $F_1 F_2 60\% 33{,}30\% 26{,}70\% \pm 60°$

Table 2.1. Technical sizing and function weights

Function	Technical Feature	Unit of measurement	Limit	Weight (Pi)
F1	Launch Rate	balls/min	30 – 100	33,30%
F2	Rotation intensity	RPM	0 – 10.000	26,70%
F3	Oscillation angle	grade (°)	±60∘	13,30%
F4	Collection capacity	Number of balls	200	6,70%
F5	Operating Voltage	Volts (V)	12 – 24	20,00%

2.2. Automation logic of the assembly

Parameter control (F5) is fully digitized by native web server hosting on the flash memory of the ESP32 microcontroller. The robot generates a Wi-Fi access point, allowing the user to configure sessions directly from the browser of any smart device (phone or laptop) via real-time HTTP/WebSocket commands [2]. The logical flow executed by the system following the commands received from the remote is summarized in the organizational flowchart below.

Fig. 1. Organizational flowchart of the logical flow and operation of the assembly

3. System Design and Architecture

3.1. Electronic architecture and electrical connections

To ensure automated parameter control, the system integrates a centralized electronic architecture around the ESP32-S3 microcontroller. The general power supply is provided by a power supply (24V) and the safe distribution of the power lines and common ground (GND) is achieved via WAGO connectors.

The ESP32-S3 board [2] transmits PWM-type control signals to four dedicated driver modules. Three of these independently control the launch head's DC motors, allowing for fine variation of propulsion speed and the generation of spin vectors. The fourth driver controls the propeller drive motor for calibrating the feed frequency. The servo motor responsible for the left-right oscillation motion is connected directly to a power bus and a dedicated GPIO digital pin.

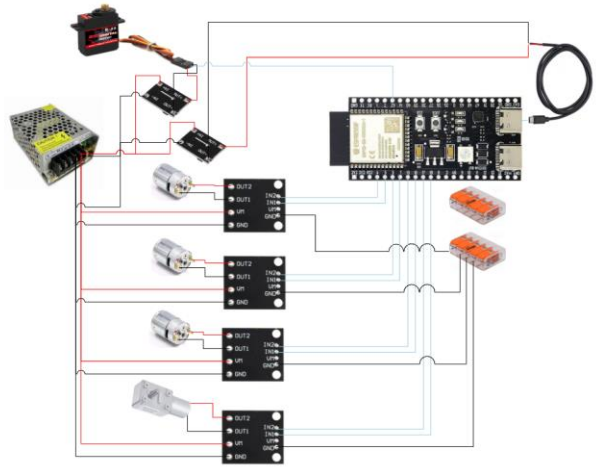

Fig. 3.1. Electrical connection diagram and hardware architecture of the system

3.2. Mechanical structure, materials and printing parameters (BOM)

The mechanical design was carried out modularly in the CAD environment, following a Design for Additive Manufacturing strategy by consolidating the structural components into a unitary and compact structure [3]. This solution eliminates intermediate joints and mechanical clearances between subassemblies, providing an integrated design that considerably shortens the guide path and streamlines the feed flow. Thus, the vertical ball stack is minimized, decreasing the gravitational pressure exerted on the adductor roller, which effectively compensates for the reduced torque of the feed motor [1], [3], as can be seen in Figure 2. The direct integration of motor housings and guide channels into a single printable part not only optimizes the additive manufacturing process by reducing the necessary support material, but also guarantees perfect coaxiality of the launch system throughout the training cycles.

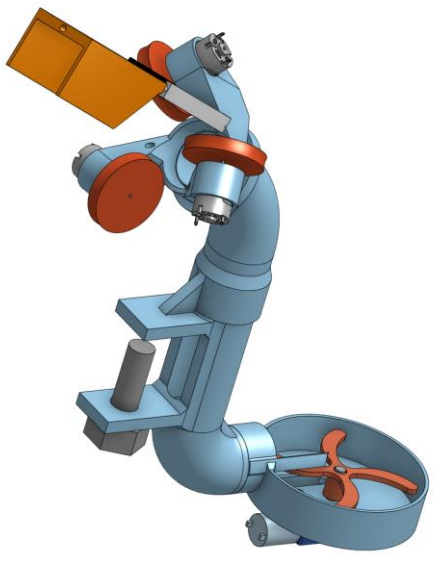

Fig. 2. CAD model

All non-standard parts were manufactured using FDM technology using a Qidi Plus 4 3D printer, printed at a layer height of 0.2 mm with 15% infill.

Table 3.1. List of Materials and Main Components (BOM)

Subassembly / Landmark	Included Components (Functional Role)	Manufacturing Method / Source	Material
Unitary Block	Feeder bowl (feeding case), L-guide, table clamping bracket	3D Printing (Monolithic Design)	PLA

Food Active Elements	Inner propeller (ball agitator), DC motor with reducer	3D Printing / Standard Purchase	PLA
Launch Head	Launching Guide Pipe, Motor Support	3D printing	PLA
Propulsion Mechanism	3x DC Motors, 3x Friction Rollers (Spin Generation)	Acquisition / 3D Printing	PLA-FiberFlex 30D
Control System	ESP32-S3 Board, Source, 4x PWM Drivers	Acquisition (COTS standard)	-

From a kinematic point of view, the system works on the basis of the direct interaction between fixed and moving components:

a. Feeding and Guiding: The PLA propeller rotates axially on the bottom of the bowl, pushing the balls to the channel at 90° in a controlled manner [1]. The interior geometry forces the ball to move from the horizontal plane to the vertical plane.

$$M_t = F_f \cdot r_{\text{mediu}} \cdot S_f = \mu \cdot m \cdot g \cdot r_{\text{mediu}} \cdot S_f \quad (1)$$

$$M_t = 0.4 \cdot 0.5 \cdot 9.81 \cdot 0.02 \cdot 1.5 = 0.059 \text{ Nm}$$

b. Oscillation Mechanism: The launch head is swivel-mounted on the vertical neck of the main structure. An external servo motor transmits the rotational movement directly to the head, changing the angle of attack over a ±60° interval to distribute the balls at different points on the table.

c. Propulsion and Spin Generation: Since the basic components make a common body, the coaxial alignment of the lower path is structurally guaranteed [3]. The upper flange of the pipe takes up the vibrations of the three DC motors excellently. As the ball leaves the tube, it is symmetrically caught by the three flexible rollers of the FiberFlex 30D [5][6]. The low hardness (30D) of this elastomer allows for a deformable contact surface, and the high coefficient of friction guarantees the transmission of kinetic impulse at speeds of up to 10,000 RPM, precisely applying topspin, backspin or sidespin effects without slipping [5].

$$v_t = \omega \cdot R = \left(\frac{2\pi \cdot n}{60}\right) \cdot R \quad (2)$$

3.3. Control and Configuration Software Interface

The operational management and calibration of the work parameters are carried out through a graphical control panel interface, based on web technologies. The server hosting this app runs natively on the microcontroller's flash memory, allowing monitoring and configuration from any smart device (phone, laptop, tablet) connected to the robot-generated Wi-Fi hotspot. The interface is modularly structured, providing the user with the following general functionalities:

a. Configuration of kinematic parameters and effect vectors: Allows linear adjustment of the propulsion speed, launch frequency (time interval between balls) and individual speed of the friction wheels. The module includes shortcuts for selecting the type of spin printed on the ball: topspin, backspin, sidespin, or flat [5].

b. Interactive matrix for the distribution of shots: A central panel that graphically simulates the surface of the playing table and allows visual mapping of the desired impact coordinates. These coordinates are automatically transposed by the system into angular commands transmitted to the oscillation servo motor.

c. Working Mode Selection and Profile Management (Presets): Provides the possibility to switch between the main modes of operation (fixed point launch, preset sequential pattern or completely random distribution) [1]. It also allows personalized training schemes to be saved in memory and quickly loaded, optimizing individual training according to the user's level.

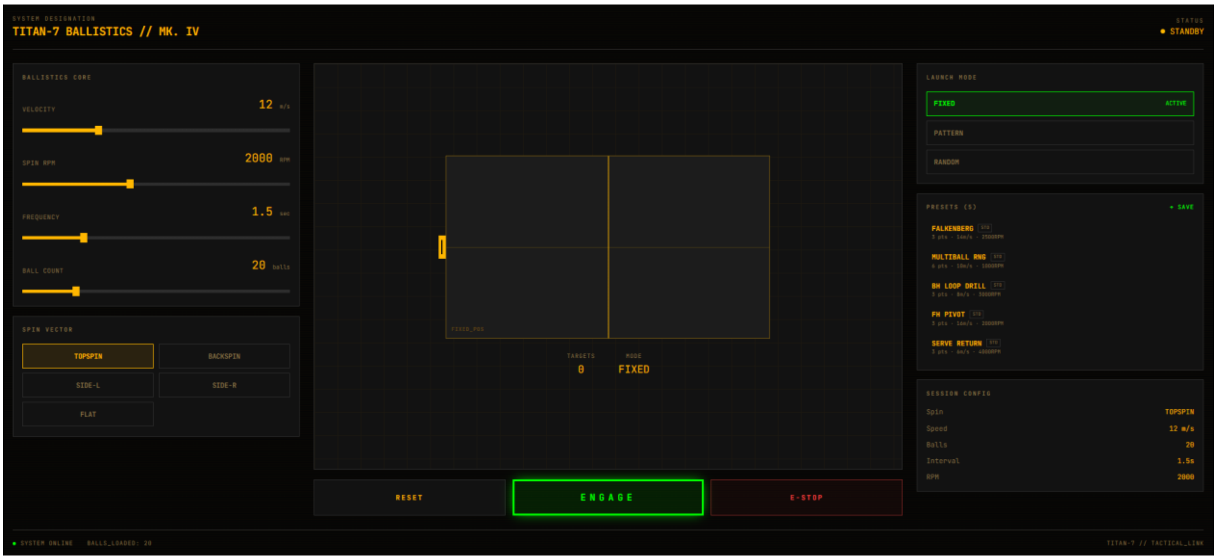

Fig. 3.2. Software control panel and web interface

4. Economic Evaluation and Cost Analysis

The main competitive advantage of the proposed experimental model is the drastic reduction of implementation and maintenance costs in relation to the functional performance offered [1]. Geometrically reinforcing components into a 3D-printed unitary structure not only increased mechanical rigidity, but significantly optimized production costs by eliminating intermediate standard parts altogether. From a financial point of view, the project demonstrates the feasibility of a professional-level system made exclusively with accessible resources.

Table 4.1. Cost and Maintenance Comparison: Commercial Robot vs. Experimental Project

Technical and economic characteristics	Top Trading Robot	Integrated Experimental Model (Project)
Estimated cost of acquisition/production	1.500 – 2.500 EUR	150 – 300 EUR
Main Materials Used	Aluminium, injected plastic parts	Rigid polymers (PLA), flexible elastomers (FiberFlex 30D), standard electronic components
Complexity and maintenance costs	High (requires proprietary spare parts)	Reduced (possibility of direct local re-printing of components)
Sustainability and flexibility	Rigid hardware configurations, closed software applications	Open architecture, universal, adaptable and scalable web interface

Unlike industrial equipment where the wear and tear of a single mechanical part leads to system downtime and high repair costs, the use of additive manufacturing allows the user to immediately reproduce degraded parts at a negligible material cost. Since the main components make a common body, the risk of unscrewing or loosening of the joints due to vibration is negligible, reducing post-implementation costs. Thus, the economic analysis confirms an extended efficiency over the entire life cycle of the product, ensuring the rapid return on investment and the democratization of access to advanced individual training technologies.

5. Conclusions and Development Directions

The realization of this experimental model demonstrates that the use of additive manufacturing technologies allows to obtain a high-performance training system at a fraction of the cost of industrial equipment [1]. The main objective was successfully achieved, resulting in a modular device capable of simulating real playing conditions by precisely controlling the frequency, speed and rotation effect of the balls [5]. Fitting components into a unitary structure has proven that intelligent geometric optimization can compensate for hardware limitations [3], eliminating mechanical play, reducing the load on the power motor, and radically simplifying physical assembly.

The flexibility of the design and the strategic use of specific materials have confirmed that the barrier between an industrial product and a self-made one has become extremely thin. The hybrid approach, the use of PLA for rigid parts and FiberFlex 30D filament to achieve high-grip deformable rollers [6] ensure a consistent ball trajectory and high reliability at high revs. In addition, complete digitalization through native web server hosting on the ESP32-S3 module provides a modern and flexible solution [2], eliminating dependence on proprietary applications and enabling instant wireless control from any smart device.

As future development directions, it is proposed to integrate artificial intelligence algorithms and computer vision sensors for real-time analysis of the player's position, allowing dynamic adaptation of the angle of attack. Another software optimization is aimed at implementing a performance history and creating a visual macro editor in the web interface for programming complex game schemes. Mechanically, the system can be extended by integrating a perimeter collection net that directs the balls back into the one-piece bowl, thus ensuring a completely closed circuit and unlimited autonomy during training sessions.

6. Bibliography

[1]. Wang Y. and Zhang X. (2021), *Design and Kinematic Analysis of a Low-Cost Table Tennis Robot Launcher with Spin Control*, https://www.mdpi.com/2076-3417/11/14/6410 , MDPI Applied Sciences.

[2]. Silva P. J. S. and Junior A. A. (2021), *Low-Cost WiFi Controlled Robot Using Embedded ESP32 Web Server*, https://www.researchgate.net/publication/351756545 , IEEE Latin America Transactions.

[3]. Yang S. and Zhao Y. F. (2015), *Additive manufacturing-enabled part consolidation: a review and framework*, https://www.researchgate.net/publication/276854191, Springer IJAMT.

[4]. Ingrassia T. and Nigrelli V. (2020), *A Systematic Framework Based on Functional Analysis and FAST Diagramming for Additive Manufacturing* Design, https://www.researchgate.net/publication/337135894, Computer-Aided Design and Applications.

[5]. Matsushima M. and Kudoh S. (2018), *Control Strategy for Table Tennis Robot to Generate Various Spin Vectors Using a Three-Wheel Mechanism*, https://www.researchgate.net/publication/322631520 , IEEE Transactions on Robotics.

[6]. Torres J., Cotelo J., and Karl J. (2021), *Mechanical Properties of PLA and TPU Parts Manufactured by Fused Deposition Modeling*, https://www.mdpi.com/2073-4360/13/15/2525, MDPI Polymers

7. Notations

BOM - Bill of Materials
CAD - Computer-Aided Design
COTS - Commercial Off-The-Shelf (Standard Components Available on the Market)

DC - Direct Current
DfAM - Design for Additive Manufacturing
F1 – F5 - Technical functions of the system (Propulsion, Spin, Oscillation, Recirculation, Control)
FAST - Function Analysis System Technique
FDM - Fused Deposition Modeling
Fn - Index number of a technical function GND - Ground (Common electric mass of the circuit)
GPIO - General Purpose Input/Output (Microcontroller Digital Input/Output Pins)
HTTP - Hypertext Transfer Protocol P_i - The mathematical weight of a technical function within the ranking matrix
PLA - Polylactic Acid (Polylactic Acid – rigid polymer used in 3D printing)
PWM - Pulse Width Modulation
RPM - Rotations Per Minute UI /
GUI - User Interface / Graphical User Interface
WAGO - Fast Lever Mechanical Connectors for Electrical Junctions
v_t - tangential velocity at the periphery of the roller (m/s)
ω – angular speed of the spindle (rads/s)
n - rated speed of the propulsion motor (RPM)
R - friction wheel radius of FiberFlex 30D (m)

DESIGN AND CONSTRUCTION OF A SYSTEM FOR DETERMINING THE WEIGHT OF STEEL COILS USING IMAGE PROCESSING

NAIDEN Matyas-Ionathan and **SAVU Tom (scientific supervisor)**

Faculty of Industrial Engineering and Robotics, Study Program: Applied Informatics in Industrial Engineering
Year of Study: IV, e-mail: naidenmatyas@gmail.com

ABSTRACT: The main theme of this project is to think of and implement ways of solving the problem of steel coil weighing. There are some solutions for this problem out there, which include weighing the coils with a dedicated scale for coils, but this solution is too expensive. This project focuses on resolving this problem with the help of image processing, a cheaper and reliable solution. This project consists of a Python dedicated app that detects both diameters of the steel coil. The steel coils in question have a standard measurement for the inner diameter, which helps the app calibrate the measurements from pixels to millimeters. After the detection, the app calculates the volume of the steel coil, after which the app calculates the weight of the steel coil. Lastly the app sends the data to an ERP (Enterprise Resource Planning) system where the consumption reporting is stored.

1. Introduction

The purpose of this project is to develop a system capable of determining the weight of steel coils through image processing, while integrating the acquired data into an Enterprise Resource Planning (ERP) system for data management. The project also includes a web interface that enables users to monitor both the operating status of the system and the current information associated with each steel coil.

The project is based on an image processing system. The steel coil is placed on an uncoiler positioned directly in front of a camera, while a software application developed in the Python programming language [1] detects both the inner and outer diameters of the coil.

The application uses the known dimensions of steel coils to convert pixel measurements into millimeters and to calculate the cylindrical annular volume of the coil. Based on the calculated volume and the density of steel, the application determines the weight of the steel coil.

To ensure the correct implementation and storage of data within the ERP system, a graphical user interface was developed using a Python library. Through this interface, the user is required to enter the article code of the weighed coil, the work center where the weighing operation is performed, and then execute the application by pressing a button. The required information is entered efficiently by scanning QR codes using dedicated barcode scanners.

The system also includes a hardware component responsible for ensuring both the proper operation of the image processing process and the accurate determination of the coil's weight. The system verifies whether any obstacles are present between the camera and the uncoiler that could interfere with image detection. It also checks whether the operating environment provides sufficient illumination. If the ambient light is inadequate, an integrated lighting source is automatically activated. These implementations provide optimal conditions for image acquisition and processing, accurate weight calculation, and prevent the user from running the application if these conditions are not met.

The application communicates with the ERP system through an Application Programming Interface (API), transmitting both the user-provided data (article code and work center) and the detected and calculated values (outer diameter, thickness, and weight) of the steel coils.

The project also includes a web interface developed using the Next.js framework [2]. This interface displays information regarding the overall weighing system, including system uptime, the number of detections performed over a selected period, the most frequently encountered user errors and their occurrence count, as well as other information related to the operating conditions of the system.

In addition, the web interface provides a dedicated page for displaying the current data of steel coils together with the image captured during the most recent diameter detection process. This information is retrieved from the ERP system through API services.

2. Current status of the project

At present, the project is in an advanced stage of development, with both the software and hardware components being largely completed.

On the software side, the Python application (shown in Figure 1.1) has been developed using several libraries available in the Python programming language. Some of the main libraries used are the following:

- OpenCV [3] is a library dedicated to image processing in Python. The application uses it for video acquisition, image preprocessing before diameter detection through various built-in functions (such as converting RGB images into binary images, enhancing image contrast, edge detection, etc.), and for detecting the coil diameters using the HoughCircles function provided by the library.
- Tkinter [4], together with its extensions Tkinter TTK [5] and Tkinter MessageBox [6], are libraries intended for developing graphical user interfaces in Python. The project uses these libraries to create an interface through which the user interacts with the application. The Python application contains a window composed of two frames, two input fields, one button, and several feedback messages that assist the user during interaction. All these interface elements were developed using the Tkinter libraries.

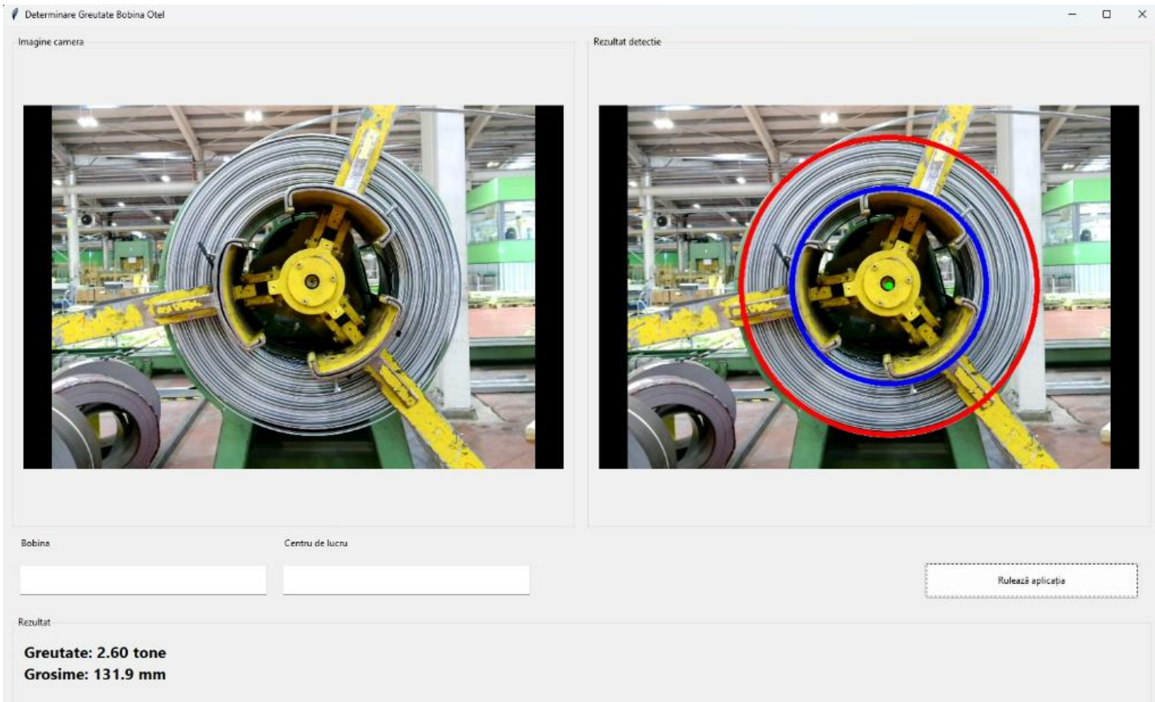

Fig. 1.1. Python application interface after running the steel coil weight determination application

Within the ERP system, dedicated tables were developed for steel coil consumption reporting. A form based on the newly created table was also developed to facilitate the reporting process. Using the SQL programming language [7], several field triggers were implemented to improve the usability and efficiency of the reporting form. After exposing the form through the ERP system's API modules, it was integrated into the Python application, thus enabling the transmission and storage of both the user-entered data and the values calculated by the application.

The calculation of the steel coil weight is based on two essential equations:

- The equation for determining the cylindrical annular volume of the steel coil:

$$V = \frac{\pi}{4} \cdot (D_e^2 - D_i^2) \cdot l \ \ [\mathrm{m}^3] \quad (1)$$

where: π is the mathematical constant pi, D_e is the outer diameter of the coil $[mm]$, D_i is the inner diameter of the coil $[mm]$ and l is the coil width $[mm]$.

- The equation for determining the weight of the steel coil:

$$m = \rho \cdot V \ \ [\mathrm{kg}] \quad (2)$$

where: ρ is the density of steel $[kg/m^3]$, V is the calculated volume $[m^3]$.

Regarding the hardware component of the project, potential situations that could cause the system to operate incorrectly were analyzed, and measures were implemented to prevent such errors. The main issues identified were the presence of obstacles between the camera and the steel coil, as well as insufficient ambient lighting. To address these situations, specific hardware requirements were established so that the system could operate under optimal conditions. The hardware components were selected according to these specifications, and an enclosure assembly was designed using the OnShape platform [8], as shown in Figure 1.2.

For data acquisition and processing from the sensors used in the system, the project employs an Arduino microcontroller. An electrical schematic was designed for the following components: an ultrasonic sensor for measuring the distance between the system and the steel coil, a photoresistor sensor for measuring ambient light intensity, an LCD display for presenting confirmation and error messages, a relay used to control the illumination LED. Furthermore, a Printed Circuit Board (PCB) was designed to integrate all these components into a single hardware system.

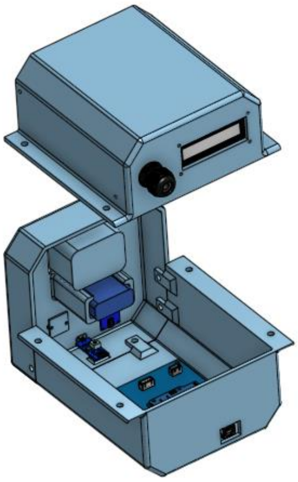

Fig. 1.2. Assembly of the steel coil weighing system enclosure

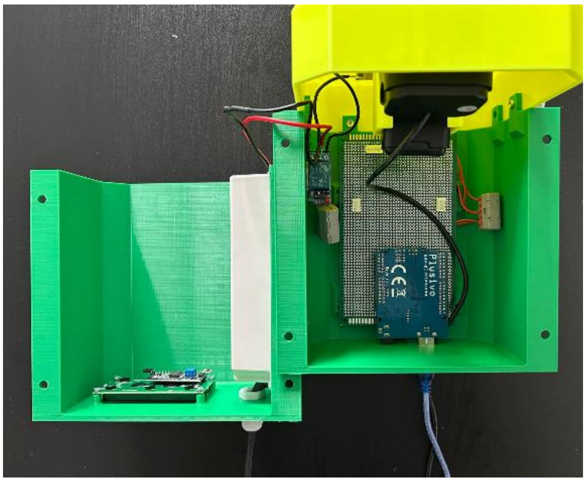

Fig. 1.3. Assembly of the components inside the 3D-printed enclosure

The 3D printing parameters for the designed enclosure were established, after which the enclosure was manufactured. During the following stage, all hardware components were installed inside the enclosure (shown in Figure 1.3), and the complete system was assembled and tested to verify its proper operation.

The remaining stages required to complete this project consist of integrating a Wi-Fi module into the system for real-time data transmission and developing a web application. The web interface will display information about the entire weighing system, including system uptime, the number of detections performed over a given period, the most frequently encountered user errors together with their occurrence count, and other details regarding the operating conditions of the system. In addition, the web interface will include a dedicated page for displaying the current data of steel coils, together with the image corresponding to the most recent coil diameter detection. This information will be retrieved from the ERP system through API services.

3. Conclusions

This bachelor's thesis aims to develop and integrate a steel coil weighing system that does not require expensive equipment. Instead, it provides an accessible and cost-effective solution by combining hardware and software components to achieve accurate weight determination.
The integration of the Python application with the ERP system eliminates potential errors that users could make when manually entering data into the system. Furthermore, the implementation of QR codes and dedicated scanners minimizes data entry errors while significantly improving the efficiency of the entire process.
The hardware component of the project is responsible not only for image acquisition but also for collecting information regarding the operating conditions of the system through the use of sensors and control components. Meanwhile, the web application enables users to monitor the system's operational status and verify possible detection errors made by the software application by displaying the current data of a steel coil retrieved from the ERP system.
Future development of the system includes the implementation of Wi-Fi modules, allowing sensor data to be transmitted more efficiently and in real time. In the long term, the system can be further enhanced through full automation by automatically identifying the article code and work center using image processing techniques, as well as by integrating additional hardware components capable of determining the operational status of the uncoiler (start-up, shutdown, and operating time). Such automation would completely eliminate the possibility of user-induced errors during the data collection and reporting process.

4. References

[1]. Python, https://docs.python.org/3/

[2]. NextJS, https://nextjs.org/docs

[3]. OpenCV, https://docs.opencv.org/3.4/d6/d00/tutorial_py_root.html

[4]. Tkinter, https://docs.python.org/3/library/tkinter.html

[5]. Tkinter TTK, https://docs.python.org/3/library/tkinter.ttk.html

[6]. Tkinter MessageBox, https://docs.python.org/3/library/tkinter.messagebox.html

[7]. SQL, https://www.w3schools.com/sql/

[8]. OnShape, https://cad.onshape.com/help/Content/Document/documents.htm

RESEARCH ON THE DEVELOPMENT OF AN AUTONOMOUS SYSTEM FOR SHOE BOX MANIPULATION IN RETAIL STORES

BACIOIU Șerban Petrișor, **SAVU Tom** (Scientific Advisor)
Faculty of Industrial Engineering and Robotics, Applied Informatics in Industrial Engineering, Year IV, e-mail: serban.bacioiu@stud.fiir.upb.ro

ABSTRACT: *This paper presents the research and development of a low-cost autonomous robotic system designed for shoe box retrieval in retail stores. The proposed system replaces the traditional role of a human store assistant: the customer scans a product barcode and selects a size, after which the robot consults a stock database, navigates autonomously to the warehouse, and retrieves the requested box. The mechanical structure consists of a quadruped-inspired mobile platform built from 20×20 mm aluminium profiles, a vertical linear guide (HGR20, 1000 mm stroke) with a ball screw actuator (SFU1605, pitch 5 mm) driven by a NEMA17 stepper motor, and a vacuum-based gripper with four Festo suction cups (Ø40 mm) actuated by a 12 V, 300 mm linear actuator (1000 N). Visual shelf localisation and barcode identification are performed in real time using LabVIEW and a Full HD USB webcam. Low-level motion control is managed by an ESP32-S3 microcontroller interfaced with an A4988 stepper driver, two relay modules, and incremental encoder feedback. The total hardware cost of the system is approximately 1590 RON, demonstrating the economic viability of the proposed solution.*

KEYWORDS: *autonomous robot, retail automation, image processing, LabVIEW, vacuum gripper.*

1. Introduction

The growing demand for operational efficiency in the retail sector has driven an accelerated expansion of robotic automation solutions, both in distribution centres and in physical retail spaces. Footwear stores represent a particular case in which serving customers involves repeated staff trips to the stockroom to retrieve boxes with the requested models and sizes. This process is time-consuming, prone to human error, and inefficient in terms of staffing costs.

Automating the shoe box retrieval flow can significantly reduce customer waiting times, eliminate picking errors, and optimise the store's operating costs. In addition, a robotic system capable of operating autonomously during business hours allows human staff to focus on higher-value customer advisory activities.

This paper proposes the research and design of a low-cost autonomous robotic system intended for retrieving and transporting shoe boxes from a retail stockroom. The proposed architecture integrates a quadruped-type mobile platform built from structural aluminium profiles, a lifting mechanism with a linear guide and ball screw, a vacuum gripper with industrial suction cups, and an image processing system implemented in LabVIEW for the visual identification of products on the shelves.

The system's operational flow begins with the customer scanning the barcode of the shoe model and entering the desired size at the robot's interface. The system queries the stock database and, if the product is available, initiates the autonomous travel sequence to the stockroom. Once the correct shelf has been located through QR code detection, the lifting mechanism travels vertically along the product column and identifies the target box by scanning barcodes. The vacuum gripper picks up the box and transports it to the customer.

The paper is structured as follows: Section 2 presents the current state of the art in retail logistics automation systems; Section 3 describes the overall architecture of the proposed system; Section 4 details the robot's mechanical structure; Section 5 presents the electronic control system; Section 6 describes the LabVIEW image processing algorithm; and Section 7 summarises the conclusions and future research directions.

2. State of the Art

Retail logistics automation has evolved considerably over the last decade, driven mainly by the requirements of e-commerce. Amazon Robotics systems [1], deployed in Amazon's distribution centres, use autonomous mobile robots (AMR) that travel beneath mobile shelving units and carry them to picking stations, eliminating staff travel through the warehouse. However, these systems are designed exclusively for large-scale warehouses and require dedicated infrastructure with prohibitive costs for independent retailers.

Ocado Group [2] has implemented, in its automated order fulfilment centres, a network of robots that move on a three-dimensional grid, retrieving product totes and ensuring optimised storage density. Processing speed exceeds several hundred orders per hour, but the solution requires the construction of a dedicated grid infrastructure, incompatible with a conventional retail store.

In the context of physical retail, Lowe's LoweBot robot [3] was designed to assist customers in identifying and locating products in-store, without performing physical manipulation operations. The Simbe Robotics Tally system [4] autonomously scans shelves to detect stock gaps and pricing errors, but it likewise does not perform picking operations. None of the current commercial solutions addresses the complete pick-and-deliver flow at an affordable cost for a small retail store.

Table 1 presents a comparative analysis of the main existing solutions relative to the system proposed in this paper.

Table 1. Functional comparison between existing automation solutions and the proposed system

Criterion	Amazon Robotics	Ocado	LoweBot	Tally	Proposed system
Physical picking	Yes	Yes	No	No	Yes
Autonomous navigation	Yes	Yes	Yes	Yes	Yes
Barcode scanning	No	Partial	No	Yes	Yes
Visual QR localisation	No	No	Partial	No	Yes
HW cost < 2000 RON	No	No	No	No	Yes
Applicable to small retail	No	No	Partial	Partial	Yes

3. System Architecture

The overall architecture of the proposed robotic system is organised into three interdependent functional levels: the mechanical level (the mobile platform and the manipulation mechanisms), the electronic level (the ESP32-S3 microcontroller and the control peripherals), and the software level (the stock database and the LabVIEW image processing). The interaction between the three levels is shown schematically in Fig. 1.

At the mechanical level, the mobile platform enables the robot's movement along the stockroom aisle, the lifting mechanism with linear guide and ball screw provides vertical access to all shelf levels, and the vacuum gripping mechanism performs the gripping and retrieval of the shoe box.

At the electronic level, the ESP32-S3 microcontroller centralises all actuation commands (stepper motor, linear actuator relay, vacuum pump relay) and sensor readings (incremental encoder [8], limit-switch microswitches). Communication with the software level is carried out via the UART serial port or via WiFi, depending on the working configuration.

At the software level, the LabVIEW application runs on a laptop connected to the camera via USB and performs real-time processing of the video stream for locating QR codes and barcodes. The stock database is queried through the microcontroller's WiFi interface and stores information about the location of each product in the stockroom (shelf column, shelf level, available quantity).

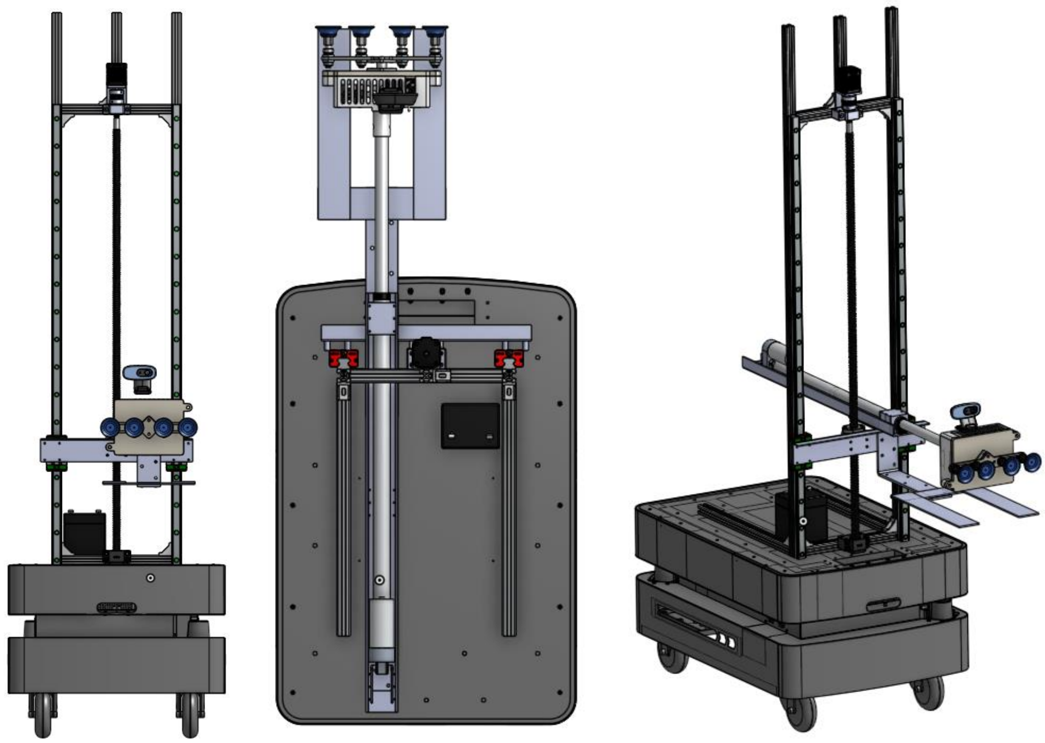

Fig. 1 3D model of the robot created in OnShape

4. Mechanical Structure

4.1. Mobile Platform

The robot's mobile platform is designed on the principle of a rigid portal frame, inspired by quadruped-type robot architecture, adapted for movement on flat surfaces inside a store. The load-bearing structure is made of 20×20 mm structural aluminium profiles (ITEM-type, slot 6), 1000 mm long, assembled using 20×20×25 mm corner brackets and M5 T-nuts in slot 6. This constructive choice ensures a favourable stiffness-to-mass ratio and allows easy reconfiguration of the frame during the prototyping stage, without specialised machining.

The reinforcement of the main joints of the actuator support is achieved using perforated galvanised-steel corner brackets (240×160×50×5 mm), mounted in the structure's main load planes. Aluminium flat bars (50×3×1000 mm) are used as support elements for the boxes carried by the robot. The platform's mechanical assembly is designed to support the combined weight of the lifting mechanism (~3 kg), the gripper (~1.2 kg), and the items on the transport fork.

The locomotion actuators of the mobile platform are not the detailed subject of this paper, which focuses instead on the box-handling mechanisms and the associated control system. The locomotion system is to be integrated in later stages of the research, in accordance with the conceptually defined quadruped-type architecture.

4.2. Lifting Mechanism

The lifting mechanism's role is to translate the gripping assembly along the vertical (Z) axis to allow access to shoe boxes located at different heights on the stockroom shelves. It consists of an HGR20-type linear guide [11] with a 1000 mm rail length, along which the HGH20CA carriages travel, and an SFU1605 ball screw (Ø16 mm diameter, 5 mm pitch) with BK12/BF12 supports. The mechanical assembly is fully supplied with a DSG16H-type coupling, which provides the flexible connection between the stepper motor shaft and the end of the ball screw.

The NEMA17 stepper motor (model 42HD8011-01 [12], 59 mm length) drives the ball screw and has a step angle of 1.8°/step (200 steps/full revolution), a current of 1.5 A/phase, a phase resistance of 2.2 Ω, and a holding torque of 650 mN·m. The A4988 driver [7], configured in 1/16 microstepping mode, generates 3200 microsteps/revolution, yielding a linear positioning resolution according to the relation:

$$\Delta x = P \cdot \alpha / (360° \cdot N) = 5 \cdot 1.8 / (360 \cdot 16) \approx 0.00156 \text{ mm/step} \qquad (1)$$

where $P = 5$ mm is the ball screw pitch, $\alpha = 1.8°$ is the motor's step angle, and $N = 16$ is the microstepping factor. The theoretical resolution of approximately 1.56 µm/step provides vertical positioning with a precision far exceeding the mechanical tolerance required for centring the gripper on the target box (estimated at ±2 mm).

The XUIPIK microswitches (SPDT, 2A/125V, long lever) mounted at the guide's travel limits provide mechanical protection against exceeding the maximum stroke, generating an immediate motor-stop signal via the ESP32-S3.

4.3. Vacuum Gripping Mechanism

The gripping mechanism consists of a Vevor 12V linear actuator [9] with a 300 mm stroke (508 mm overall length), a maximum force of 1000 N, an extension speed above 14 mm/s (0.55"/s), and a 25% duty cycle, with IP54 protection and a noise level ≤50 dB. The linear actuator performs the extension/retraction motion of the gripper relative to the shelf (Y axis), allowing the box to be approached and gripped, and subsequently retracted onto the platform's fork.

The elements in contact with the box surface are four Festo ESG-40-SF-HD-QS industrial vacuum suction cups [5], Ø40 mm in diameter, connected in parallel to the vacuum pump through a QSQ-G1/8-6 multi-way manifold. The configuration with four suction cups arranged symmetrically on the gripper plate ensures uniform distribution of the suction force, compensating for any unevenness of the box's cardboard surface and preventing it from slipping or tipping during transport.

The vacuum pump used is an oil-free diaphragm mini-pump, powered at 12 VDC (9–14V range), with a suction flow rate of 5 L/min, a vacuum level of 65 kPa, and a maximum pressure of 120 kPa, with a rated current consumption of 500 mA and a power of 6 W. The complete gripping sequence takes place in three stages: (1) extension of the linear actuator toward the visually identified box; (2) activation of the vacuum pump and application of suction to the box surface through the four suction cups; (3) retraction of the actuator with the box attached and its placement on the mobile platform's fork, followed by deactivation of the pump.

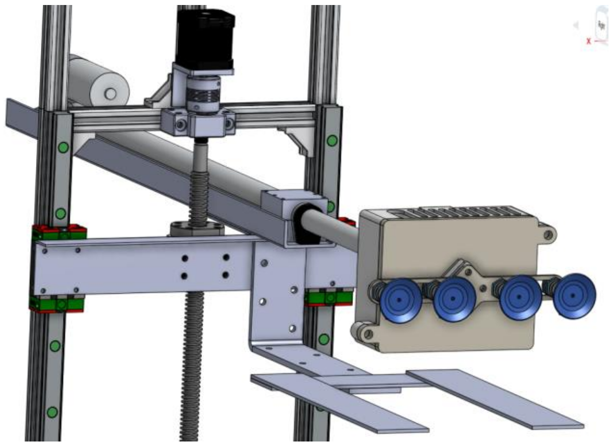

Fig. 2 Lifting and gripping mechanism: HGR20 linear guide, SFU1605 ball screw, NEMA17 motor, Vevor linear actuator, and Festo ESG-40 suction cups

5. Electronic Control System

5.1. ESP32-S3 Microcontroller

The system's electronic control is centralised in the ESP32-S3 DevKit microcontroller [6] (38 pins), powered at 5V via USB, with internal logic at 3.3V. The ESP32-S3 integrates a dual-core Xtensa LX7 processor running at up to 240 MHz, 512 KB SRAM, 384 KB ROM, WiFi 802.11 b/g/n connectivity, and Bluetooth Low Energy 5.0, as well as a generous number of configurable GPIO ports. These resources make it suitable for centralising the commands of all actuators and the sensor readings of the proposed robotic system.

The ESP32-S3 GPIO ports are used as follows: two digital pulse-type outputs (STEP and DIR) for the stepper motor's A4988 driver, two digital outputs for controlling the relay modules (linear actuator and vacuum pump), two digital inputs for reading the limit-switch microswitches, and two encoder inputs (the A and B signals of the incremental encoder [8]). WiFi communication enables querying the stock database and transmitting the commands received from the LabVIEW application on the laptop.

5.2. Stepper Motor Actuation

The A4988 Pro Reprap driver accepts 3–5.5V logic signals directly compatible with the ESP32-S3 and provides an adjustable current of up to 2A per phase, sufficient for the NEMA17 42HD8011-01 motor (1.5 A/phase nominal). The phase current is set by adjusting the reference voltage on the driver's potentiometer to the value $V_{ref} = I_{max} \cdot 8 \cdot R_{sense}$, where $R_{sense} = 0.1\ \Omega$, giving $V_{ref} \approx 0.3$ V for 1.5 A. Activation of the 1/16 microstepping mode is done by connecting the driver's MS1, MS2, and MS3 pins to the ESP32-S3's HIGH logic level. The A4988 driver has thermal and overcurrent protection, automatically stopping actuation when the maximum junction temperature is exceeded.

5.3. Power Supply and Actuator Control

The main power supply for all of the system's power components (linear actuator, vacuum pump, stepper motor) is provided by a 12V lead-acid battery, chosen for its favourable capacity-to-cost ratio and its ability to deliver high peak currents (required for the linear actuator, with a maximum current < 5A). The 5A fuse fitted on the battery's positive circuit protects the system against overcurrents caused by accidental short circuits or mechanical jams.

The direction of actuation of the linear actuator (extension/retraction) is controlled by a 2-channel optocoupler relay module (5VDC, 10A/contact, HIGH/LOW trigger selectable via jumper, 250VAC/30VDC contacts), driven by two GPIO ports of the ESP32-S3. Reversal of the actuator's direction of travel is achieved by switching the polarity of the voltage applied to the actuator's internal DC motor, achieved electronically through the configuration of the two relays. The vacuum pump is controlled separately by a single-channel optocoupler relay module (5VDC, 10A), ensuring galvanic isolation from the microcontroller's 3.3V control circuit.

Table 2 summarises the main components of the electronic and mechanical system, along with the relevant technical specifications and unit cost.

Table 2. Main system components and technical specifications

Component	Model / Type	Key specification	Cost (RON)
Microcontroller	ESP32-S3 DevKit 38-pin	Dual-core 240 MHz, WiFi+BLE	42,12
Stepper motor	NEMA17, 42HD8011-01, 59 mm	650 mN·m, 1.5 A/phase, 200 steps/rev	94,00
Motor driver	A4988 Pro Reprap	Microstepping 1/16, max 2 A	12,00
Linear actuator	Vevor 12V, 300 mm stroke	1000 N, >14 mm/s, IP54	163,00
Vacuum pump	12V DC, diaphragm, oil-free	5 L/min, 65 kPa, 500 mA, 6 W	170,00
Suction cups (×4)	Festo ESG-40-SF-HD-QS, Ø40 mm	Vacuum 65 kPa, QS fitting	–
Linear guide	HGR20 1000 mm + SFU1605	Pitch 5 mm, Ø16 mm, BK/BF12 support	470,00
Video camera	Axroad Mall Full HD, USB 2.0	1080p, 130° angle, 360° rotation	55,00
Microswitches (×2)	XUIPIK 2A/125V, long lever	SPDT, limit switch	6,80
2-channel relay	Optocoupler, 5VDC, 10A	HIGH/LOW selectable, 250VAC	14,00
1-channel relay	Optocoupler, 5VDC, 10A	Vacuum pump, HIGH/LOW selectable	9,08
Al. profiles (×3)	20×20 mm, channel 6, 1000 mm	~1729 g/m, channel 8 ITEM type	336,00
Al. corner brackets (×3 set)	20×20×25 mm	Portal frame reinforcement	219,00
TOTAL			**≈ 1590 RON**

6. Image Processing in LabVIEW

The video camera (1080p, 130° field of view, USB 2.0 interface, 360° rotation, plug-and-play) is rigidly mounted on the gripping mechanism's structure, with its field of view oriented forward toward the stockroom shelves. It moves together with the lifting mechanism along the vertical axis, allowing progressive scanning of the entire product column. The software application runs on a laptop connected to the camera via USB and to the ESP32-S3 microcontroller via serial communication (UART) or WiFi.

The image processing algorithm implemented in the LabVIEW Vision Module [10] operates in two sequential stages. The first stage consists of locating the shelf column corresponding to the requested product, through detection of the QR code displayed at the base of each column. The robot travels along the stockroom aisle and continuously captures images at a rate of approximately 10 frames/second, using the IMAQ functions from the LabVIEW Vision library. As soon as the QR code corresponding to the target column is detected and decoded, the mobile platform stops and the microcontroller receives confirmation of the correct location.

The second stage consists of vertically scanning the shelf column to identify the box bearing the requested product's barcode. The lifting mechanism translates the camera along the Z axis in controlled steps, stopping at every ~50 mm interval to analyse the current video frame. LabVIEW uses dedicated 1D barcode decoding functions (EAN-13 or Code 128 format), comparing the read code with the one transmitted from the database. Once the target box is identified, the LabVIEW script calculates the geometric centre of the bounding rectangle of the box detected in the image and determines the positioning errors relative to the centre of the video frame according to the relations:

$$ex = xc - W/2 \qquad (2)$$

$$ey = yc - H/2 \qquad (3)$$

where xc and yc are the coordinates of the geometric centre of the detected box (in pixels), and W = 1920 px and H = 1080 px are the image's width and height, respectively. The errors ex and ey are transmitted as position-correction commands to the ESP32-S3: the vertical-axis error ey is corrected by actuating the linear guide's stepper motor (a number of microsteps proportional to the error value), while the horizontal-axis error ex is corrected by laterally moving the mobile platform.

The correction process iterates until both errors fall within the preset tolerance threshold of ±5 pixels (corresponding to a linear error of approximately ±0.5 mm at the typical working distance of 300 mm from the shelf), at which point the system considers the gripper to be correctly centred on the target box and initiates the gripping sequence. The choice of LabVIEW as the implementation environment was motivated by the availability of optimised IMAQ Vision libraries, the graphical programming environment that simplifies development, and the native integration with data-acquisition and serial-port control interfaces.

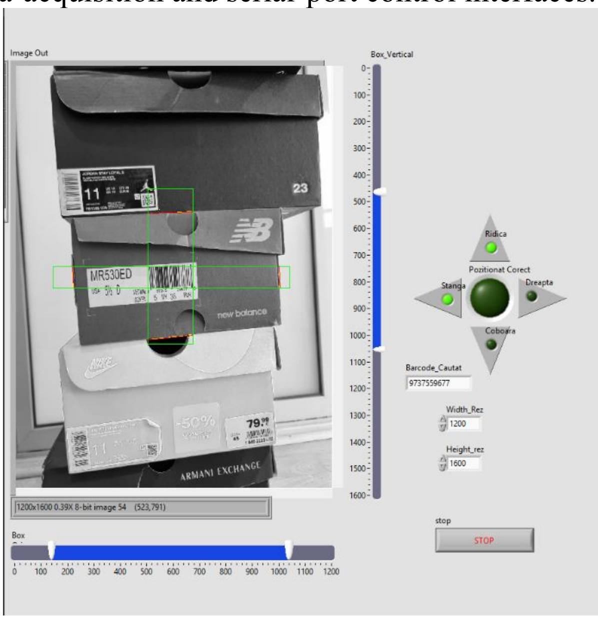

Fig. 3 LabVIEW interface of the shoe box position detection system

7. Conclusions

This paper has presented the research and design of a low-cost autonomous robotic system intended for retrieving shoe boxes in small retail stores. The main contributions consist of: (1) defining the complete system architecture, integrating a mobile platform made of structural aluminium profiles, a lifting mechanism with an HGR20 linear guide (1000 mm stroke) and an SFU1605 ball screw (5 mm pitch), a vacuum gripper with four Festo Ø40 mm industrial suction cups, and a LabVIEW image processing system; (2) the selection and justification of the electronic and mechanical components through comparative multi-criteria analysis, documented in the accompanying parts tables; (3) the definition of the visual localisation algorithm based on QR detection and barcode scanning, with two-axis position correction through centroid error calculation.

From a cost perspective, the designed system demonstrates that a functional automation solution for the pick-and-deliver flow in a retail store can be achieved with a hardware budget of approximately 1590 RON, without dedicated infrastructure or fixed floor-guidance systems. The theoretical vertical-axis positioning resolution of ~1.56 µm/step, obtained through the NEMA17 motor – A4988 driver combination in 1/16 microstepping – SFU1605 screw, far exceeds the precision required for centring the gripper on a shoe box.

The project's current limitations relate to autonomous navigation, which requires prior mapping of the stockroom, and the absence of a dynamic obstacle detection system.
The current project uses only line following for moving through the stockroom, which can make it impossible to avoid obstacles along the path. The performance of the image processing algorithm depends on the stockroom's lighting conditions, an aspect that will be addressed in later stages by adding a calibrated LED lighting ring mounted together with the camera.

Future research directions target: building a physical prototype and experimentally validating the complete picking sequence; integrating a SLAM (Simultaneous Localization and Mapping) algorithm for autonomous navigation without a prior map; adding a 2D LIDAR sensor for obstacle detection and avoidance; developing a touchscreen tablet user interface; and extending the gripping system to handle a wider range of box sizes and shapes.

References

[1]. Amazon Robotics (2024), Robotic fulfillment and logistics solutions, Amazon.com, Inc., available at: https://www.amazonrobotics.com, accessed: May 2025.
[2]. Ocado Group (2024), Automated warehouse technology – The Ocado Smart Platform, available at: https://www.ocadogroup.com/technology, accessed: May 2025.
[3]. Lowe's Companies, Inc. (2017), LoweBot autonomous retail service robot, available at: https://newsroom.lowes.com/news-releases/lowes-introduces-lowebot, accessed: May 2025.
[4]. Simbe Robotics (2024), Tally – Autonomous shelf analytics robot, available at: https://www.simberobotics.com/platform/tally, accessed: May 2025.
[5]. Festo SE & Co. KG (2023), ESG-40-SF-HD-QS Suction Cup – Product Datasheet, available at: https://www.festo.com/ro/ro/a/189175, accessed: May 2025.
[6]. Espressif Systems (2024), ESP32-S3 Series Datasheet v1.4, Espressif Systems (Shanghai) Co., Ltd., available at: https://www.espressif.com/documentation/esp32-s3, accessed: May 2025.
[7]. Allegro MicroSystems (2014), A4988 DMOS Microstepping Driver with Translator and Overcurrent Protection – Datasheet, Allegro MicroSystems LLC, available at: https://www.allegromicro.com/en/products/motor-drivers/brush-less-dc-motor-drivers/a4988, accessed: May 2025.
[8]. Autonics Co., Ltd. (2022), E40S6 Series Incremental Rotary Encoder – Datasheet,

available at: https://www.autonics.com, accessed: May 2025.
[9]. Vevor (2024), Linear Actuator 12V 20 inch 1000N – Technical Specifications, available at: https://eur.vevor.com/linear-actuators-c_11633, accessed: May 2025.
[10]. National Instruments (2023), NI Vision Module for LabVIEW – User Manual, National Instruments Corp., Austin, TX, USA.
[11]. HIWIN Technologies Corp. (2022), Linear Guideway HGR20 Series – Technical Information, available at: https://www.hiwin.com, accessed: May 2025.
[12]. Drot.ro (2025), NEMA17 stepper motor – 59 mm, 42HD8011-01, available at: https://www.drot.ro/platforma-arduino/48395-motor-pas-cu-pas-nema17-59-mm-42hd8011-01.html, accessed: May 2025.

RESEARCH ON THE DEVELOPMENT OF AN EXPERIMENTAL MODEL FOR DISEASE DETECTION IN VEGETABLE PLANTS

Gabriela-Denisa FILIMON and Lecturer PhD Eng. Vlad GHEORGHIȚĂ

Faculty: Industrial Engineering and Robotics, Specialization: Applied Informatics in Industrial Engineering, Year of study: 4, e-mail: gabifilimon20@gmail.com

Abstract: Plant diseases represent a major threat to global food security, causing annual losses estimated at 220 billion dollars worldwide. Existing mobile-based diagnostic solutions show reduced reliability in real field conditions due to uncontrolled lighting and variable image acquisition distances. This paper presents the design and development of an experimental system for automated disease detection in vegetable plants, integrating a controlled hardware acquisition station with an artificial intelligence algorithm based on YOLOv8. The hardware system includes an ESP32 microcontroller, an ultrasonic distance sensor, a light intensity sensor, and an automatic LED illumination ring, all coordinated through the MQTT protocol. The detection model was trained on a dedicated dataset and validated through performance metrics. Results demonstrate the system's capability to identify plant diseases under standardized conditions, reducing the laboratory-to-field performance gap.

KEY WORDS: YOLOv8, detection, control, capture, plants

1. Introduction

Plant diseases represent one of the main causes of agricultural losses, with recent estimates indicating annual losses of approximately 220 billion dollars worldwide [1]. In vegetable crops, late detection can compromise the entire production within a short period of time.
Existing software solutions based on mobile applications present limitations under real conditions. Their performance drops from 95% in the laboratory to 70-85% in the field, due to lighting variations and uncontrolled distance between the camera and the leaf [2].
This paper presents an integrated experimental model that combines a hardware station with a controlled environment and a YOLOv8 algorithm, reducing the influence of external factors on diagnostic accuracy.

2. Current State of the Art

The current market offers a variety of solutions for plant disease detection, differentiated by the technology used and the field of applicability.
One of the most widely used diagnostic platforms is Plantix [3]. The platform, with its application interface illustrated in Figure 1, operates as a virtual consultant accessible through a mobile device. The system identifies hundreds of pathogens based on images captured by the user, but its performance depends on image quality and lighting conditions.

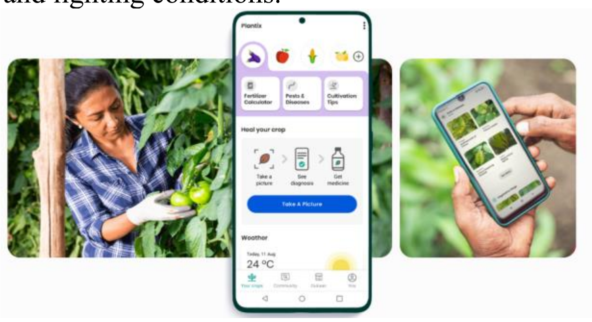

Fig. 1. User Interface of the Plantix Application [3]

Agrio [4] represents a more advanced approach, integrating artificial intelligence with parcel-level surveillance. It offers broader coverage, but high costs and the lack of adaptation to controlled environments such as greenhouses represent significant limitations.
In the academic environment, the FarmAid platform [5], illustrated in Figure 2, proposes a modular

architecture with an integrated camera and sensors, designed for disease detection in greenhouses. The platform's performance is superior to mobile applications, but the high technical complexity and cost limit its accessibility.

Fig. 2. The FarmAid Platform [5]

Compared to the presented solutions, the experimental model proposed in this paper aims to combine a controlled acquisition environment with a high-performance detection algorithm, at a reduced cost and with accessible technical complexity.

3. System General Architecture

The disease detection system for vegetable plants is structured into several interdependent subsystems: the mechanical subsystem provides physical support in a closed enclosure that limits the influence of external light; the measurement subsystem extracts data from the analyzed environment; the control subsystem, based on the ESP32-C6 microcontroller; the actuation subsystem ensures uniform capture conditions and system status indication; the software subsystem consisting of the YOLOv8 model, the Python application and the database; the processing and analysis subsystem represented by the laptop; the communication subsystem, which transmits data through the MQTT protocol; and the power supply subsystem. Figure 3 presents the IDEF0 diagram of the system.

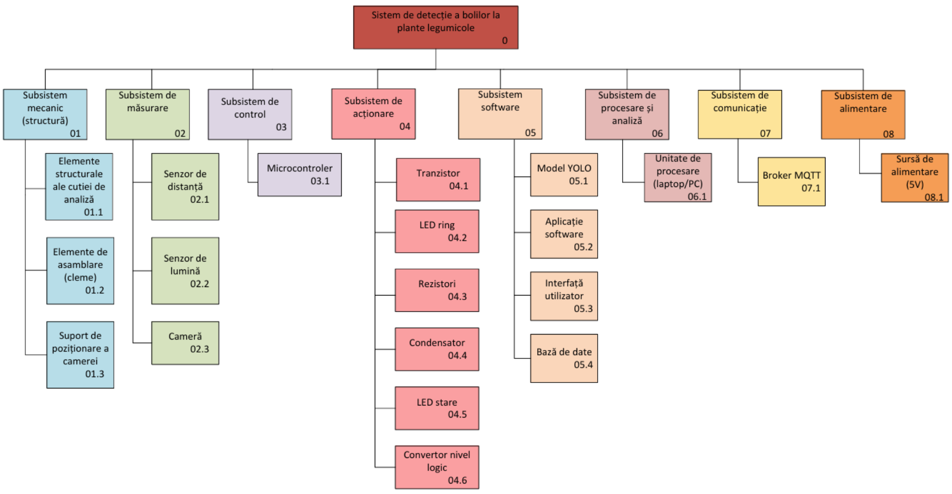

Fig. 3. The IDEF0 diagram of the system

To identify and rank the system functions, the FAST method (Function Analysis System Technique) was applied, with the diagram illustrated in Figure 4. The main function is image processing (F3), followed by diagnosis generation (F4) and leaf image capture (F1). The illumination assurance and external influence limitation functions support the acquisition process and contribute to obtaining consistent results.

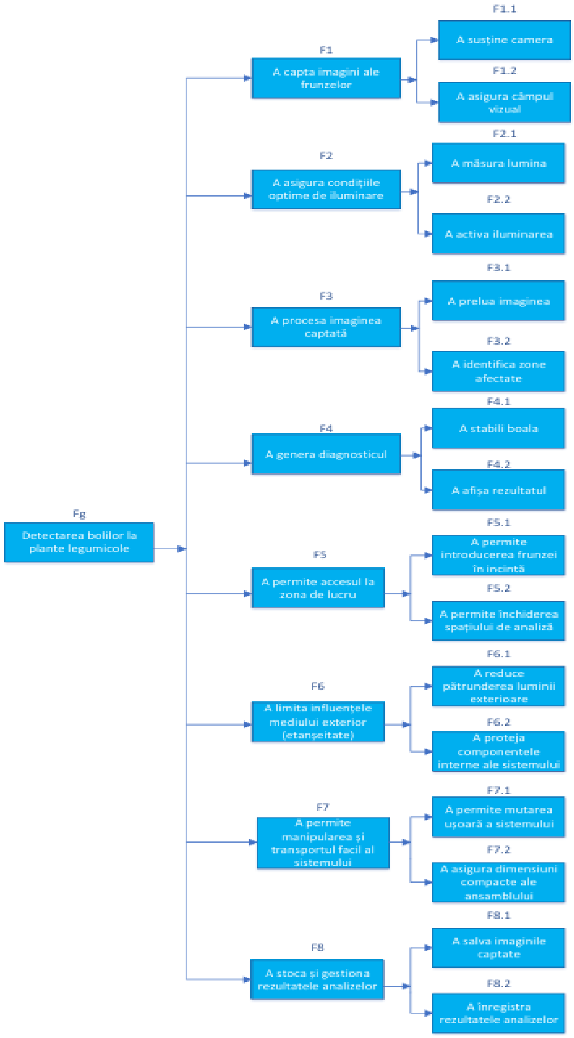

Fig. 4. The FAST diagram

The mechanical structure was designed in CATIA V5 and manufactured by FDM 3D printing using PLA filament. The assembly takes the form of a closed box, consisting of a base, lateral walls, upper wall, front wall, and a protective enclosure for the electronic components. The front wall acts as a sliding door guided by channels integrated in the lateral walls. The camera module, HC-SR04 and BH1750 sensors, the LED ring, and the RGB status LED are mounted on the upper wall. Figure 5 presents the 3D model of the assembly.

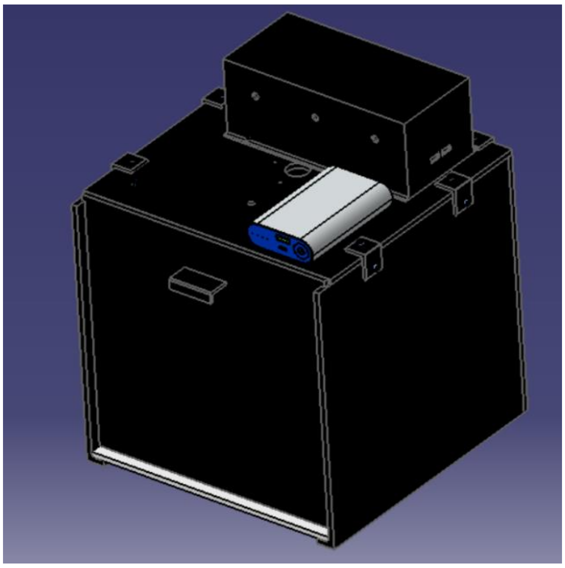

Fig. 5. The 3D model of the assembly

The system operates based on a logical sequence of operations, starting with initialization and ending with obtaining the result. The user starts the system, and the presence of the leaf is verified using the HC-SR04 sensor, whose reading is published to the MQTT broker and retrieved by the application. If no leaf is detected, the system remains in standby mode. After the leaf is detected, the BH1750 sensor measures the light intensity and, if it is below the set threshold, the microcontroller activates the LED ring through the MOSFET transistor. The user initiates the scan, and the camera captures the leaf image. This is processed by the YOLOv8 algorithm, and the results are displayed in the interface, saved in the SQLite database, and published to the MQTT broker. During the process, the RGB LED indicates the system status: blue for standby, red for scan in progress, and green for completed analysis.

4. Hardware Components

The electronic components were selected based on the functional specifications of the system and are presented in Table 1.

Table 1. Main components of the system

Component	Role	Technical Characteristics
ESP32-C6	Coordinates sensors and communication	RISC-V 32-bit, 160 MHz, WiFi 6, Bluetooth 5, 22 GPIO pins
Camera module OV3660	Leaf image capture	1920x1080 px, 64° angle, manual focus
LED ring	Uniform illumination of the analysis area	10W, 5V, 112 mm outer diameter
HC-SR04 sensor	Leaf presence detection	Range 2-450 cm, angle <15°, Trigger/Echo interface
BH1750 sensor	Light intensity measurement	0-65535 lux, 1 lux resolution, I2C interface
MOSFET IRLZ44N	Illumination system control	N-channel, logic level, Vds 55V, Id 47A
Electrolytic Capacitor	Power supply stabilization	1000 µF, 10V, radial mounting
10 kΩ resistor	Biasing (pull-down) in the control circuit	Metal film, 1/4W, ±1% tolerance
220 Ω resistor	Current limiting	Metal film, 2W, ±1% tolerance
RGB LED	System status indication	5 mm, 4 pins, common cathode
Logic level converter	HC-SR04 (5V) to ESP32	Bidirectional, 4 channels,

	(3.3V) compatibility	5V/3.3V
Power supply (Powerbank)	System power supply	5000 mAh, 5V USB output

The electrical diagram of the system is presented in Figure 6. It illustrates the connections between the microcontroller, sensors, the MOSFET-controlled LED ring, the RGB LED, and the logic level converter.

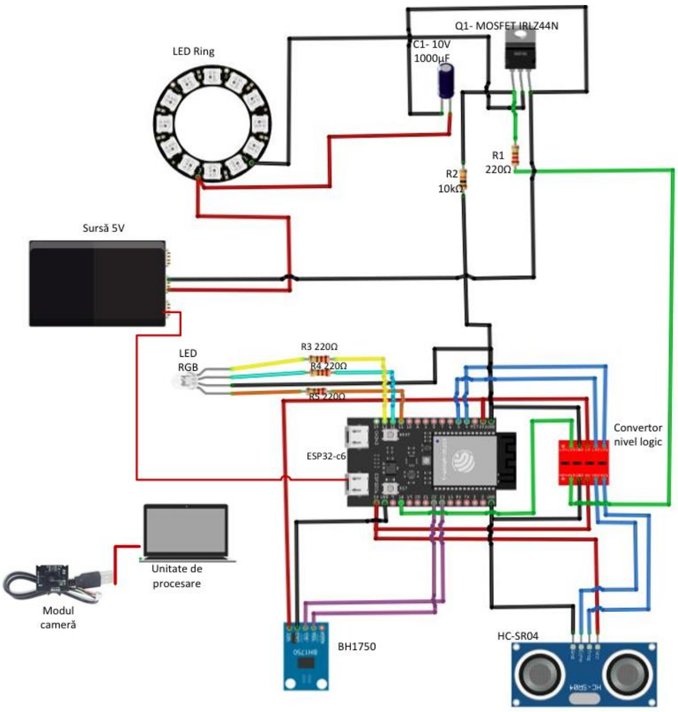

Fig. 6. The electrical diagram of the system

5. YOLOv8 Model Training

Model training was performed in Google Colab, using the YOLOv8n architecture, a variant optimized for low computational resources and short inference time. Four distinct models were trained, one for each crop: cucumbers [6], tomatoes [7], peppers [8], and eggplants [9], using datasets retrieved from the Roboflow platform. Table 2 presents the image distribution in each dataset, and Table 3 presents the training parameters.

Table 2. The image distribution in each dataset

Plant	Total images	Training	Validation	Testing
Cucumbers	1368	1194	130	44
Tomatoes	9055	6462	1721	872
Peppers	1681	1177	336	168
Eggplants	600	420	120	60

Table 3. The training parameters

Parameter	Value
Architecture	YOLOv8n
Epochs	50
Image size	640 x 640 px
Batch size	16

The performance of each model was evaluated through validation metrics generated by YOLOv8, summarized in Table 4.

Table 4. Performance metrics per model

Model	mAP50	Maximum F1	Maximum detection rate
Cucumbers	0.830	0.84	0.94
Tomatoes	0.558	0.56	0.81
Peppers	0.852	0.83	0.92
Eggplants	0.995	0.99	1.00

The comparative performance of the four models is presented in Figure 7 through the mAP50, maximum F1, and maximum detection rate metrics. It can be observed that the eggplant model achieves the highest performance, with a mAP50 of 0.995, due to the high quality of the dataset and the visually distinct symptoms between classes. The model with the lowest performance is the one for tomatoes, explained by the large number of classes (10) and the visual similarity between them. The cucumber and pepper models achieve satisfactory results.

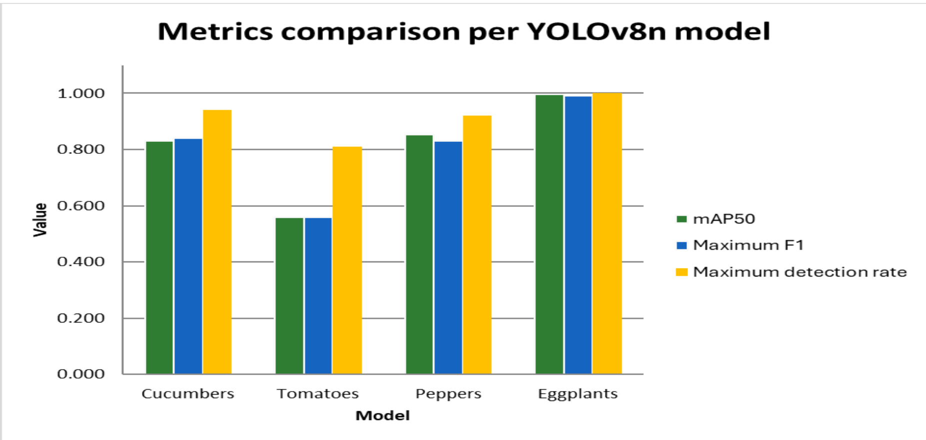

Fig. 7. Metrics comparison per YOLOv8n model

Figures 8-10 present examples of detections performed on images from the test set.

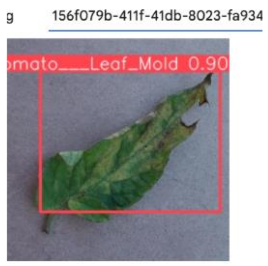

Fig. 8. Detection - tomatoes

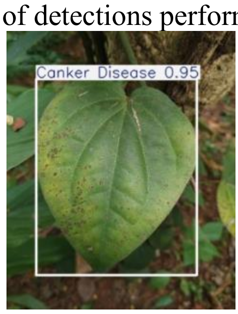

Fig. 9. Detection – peppers

Fig. 10. Detection - eggplants

6. Software Implementation

The software application was developed in Python, with a client-server architecture, where the web browser communicates with a Flask server through HTTP requests, and the server coordinates YOLOv8 inference, MQTT communication, and result storage. The four trained models are loaded once at server startup to eliminate latency at each scan.

Figure 11 presents the application architecture.

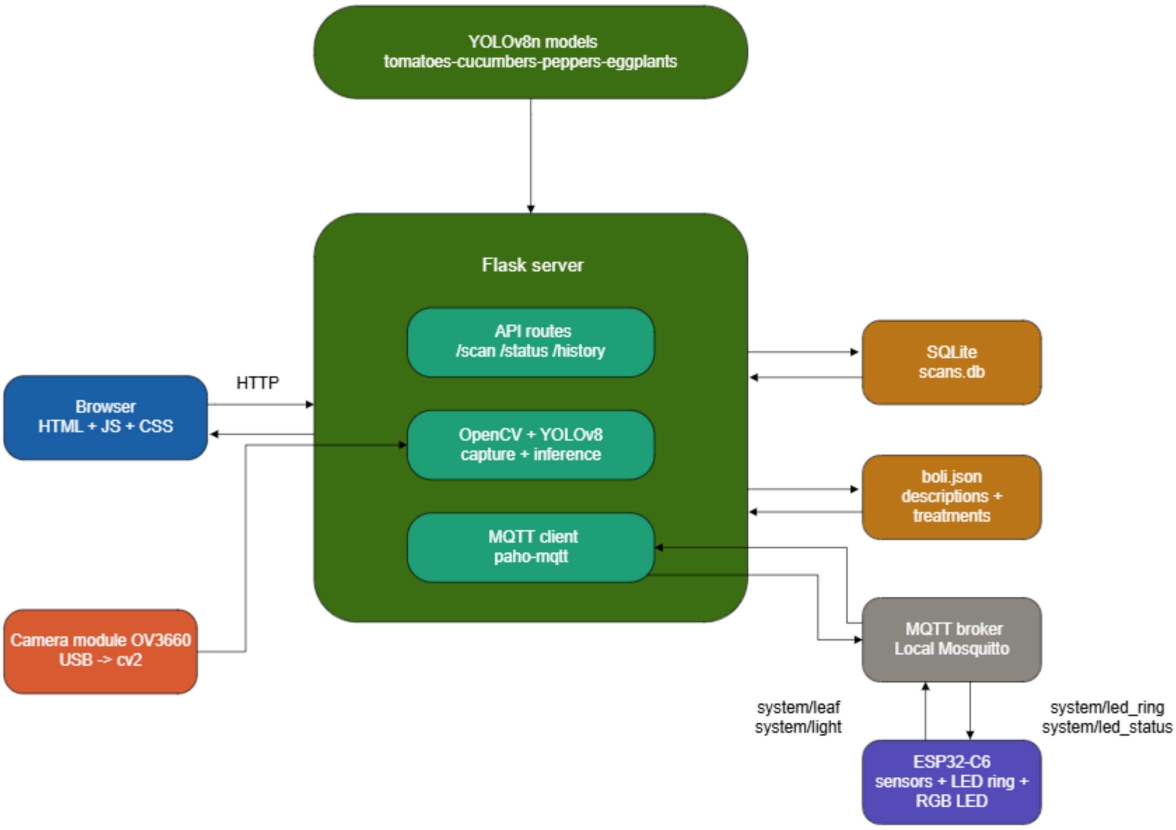

Fig. 11. The architecture of the software application

The web interface, illustrated in Figure 12, is organized into four areas: the navigation bar with a dropdown for plant selection and the “Start system” and “Start scan” buttons; the status panel with automatically updated indicators for leaf presence, illumination level and time of last scan; the visualization area with a live video stream and the last processed capture; and the history table with the last 20 scans.

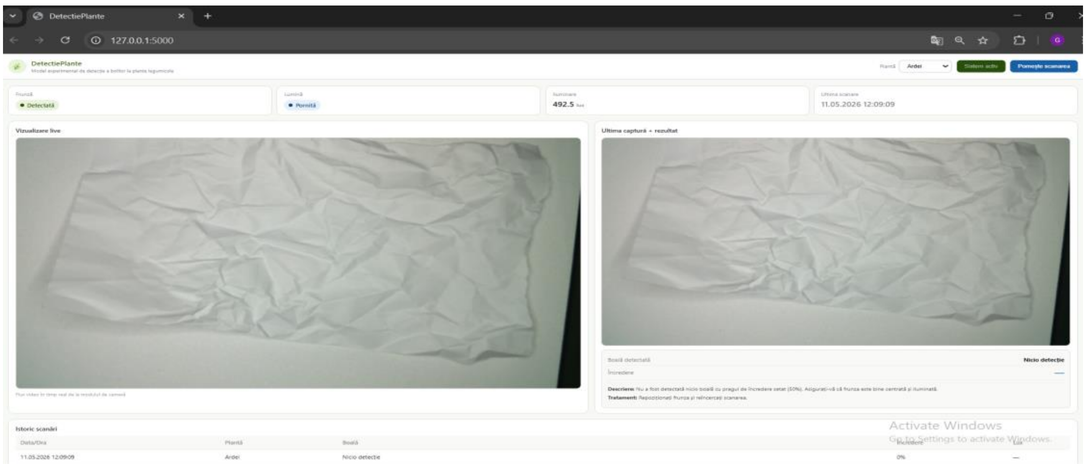

Fig. 12. Web Interface during a functionality test session

Communication between the application and hardware is achieved through the MQTT protocol, using the Mosquito broker running locally. Four topics are defined through which the ESP32 publishes leaf presence and illumination level in lux, while the application controls the RGB LED status and the LED ring. The illumination threshold was set experimentally at 500 lux to ensure stable activation of the LED ring during scanning. Scan results are automatically stored in the SQLite database, regardless of whether a disease was detected or not, including the plant type, identified disease, confidence score, date and time, and the path to the captured image.

7. Conclusions

This paper presents an integrated experimental system for disease detection in vegetable plants, combining a controlled-environment hardware station with YOLOv8n algorithms. Illumination control and leaf presence detection ensure uniform acquisition conditions, reducing the influence of external factors. Compared to existing mobile solutions, the system provides an accessible environment, representing a viable alternative for greenhouse use. Future developments aim to extend the number of crops, improve datasets, and integrate cloud connectivity.

8. References

[1]. Shafay, M., et al., "Recent advances in plant disease detection: challenges and opportunities," Plant Methods, 2025.

[2]. Ramcharan, A., et al., "Assessing a mobile-based deep learning model for plant disease surveillance," Frontiers in Plant Science, 2017.

[3]. PEAT GmbH, "Plantix - Your interactive plant doctor", 2024, Link , [Accessed 11-05-2026].

[4]. Saillog, „Agrio - Precision plant protection", 2024, Link, [Accessed 11-05-2026].

[5]. Arif S., et al., FarmAid: Plant Disease Detection Robot, Hackster.io, 2018, Link, [Accessed 11-05-2026].

[6]. Thesis DNQTN, „Cucumber Detection Disease Dataset", Roboflow Universe, 2023, Link, [Accessed 11-05-2026].

[7]. Gauri Dalvi, „Tomato Disease Dataset", Roboflow Universe, 2023, Link, [Accessed 11-05-2026].

[8]. "Pepper Leaf Dataset," Roboflow Universe, 2024, Link , [Accessed 11-05-2026].

[9]. Rafsan Hasan Pronoy, „Eggplant Disease Detection Dataset", Roboflow Universe, 2023, Link, [Accessed 11-05-2026].

Person identification and distance estimation using thermal imaging and LiDAR

Student: BULDUR Claudiu Coordonator:SAVU Tom
University:Inginerie Industriala si Robotica, Specializarea:Informatica Aplicata in Inginerie Industriala, Year of study:4, e-mail:buldurclaus123@gmail.com

Abstract:The purpose of this scientific work stems from the critical need of emergency response teams to identify victims in the aftermath of disasters. A YOLO neural model was trained and deployed using a thermal camera, which captures real-time imagery and identifies helpless individuals by analyzing their thermal signatures, framing them within bounding boxes.
To enhance localization precision, a sensor fusion was implemented between the thermal camera and a LiDAR sensor, thereby transmitting real-time distances to the victims by creating a spatial map. The system is specifically designed for emergency situations with reduced visibility, such as nighttime operations or dense fog.

Keywords: Sensor Fusion, Thermal Imaging, LiDAR, YOLO, Search and Rescue.

1. Introduction

The research is based on the need to reduce the number of casualties in disaster situations by minimizing the time required to search for and identify them under conditions of reduced visibility. The system is designed to be integrated into a remote-controlled vehicle, capable of locating people in danger and transmitting their coordinates in real time to intervention teams.

To identify people in danger, a YOLO neural network model was trained using a custom dataset consisting of images captured with a thermal camera. The training process was carried out using the PyTorch framework in a Python environment on a dedicated workstation. For the integration of the LiDAR sensor, data fusion was achieved through advanced geometric calculations. Finally, for maximum efficiency during the detection (inference) phase, the entire software assembly was centralized and executed on an NVIDIA Jetson Nano computing platform.

2. Current State

Navigation systems based on optical sensors in the visible spectrum (RGB cameras) exhibit a critical vulnerability to disruptive environmental factors such as dense smoke, aerosols, or a total lack of illumination. Although thermal cameras have solved the problem of detecting casualties by identifying the thermal signature and infrared radiation emitted by the human body, they have a major limitation: they only provide a flat (2D) image, without supplying information regarding the depth of objects in the field. The LiDAR sensor was chosen as the primary solution to overcome this deficiency, being specialized in spatial mapping and high-precision distance measurement.

For the system to be effective, the data provided by the two sensors must be fused into a single data stream. The challenge consisted in synchronizing them through geometric calculations, so that the distance provided by the laser is applied precisely to the objects identified by the YOLO model.

3) Vision System Development: Training the YOLO Model Using Thermal Camera Data

3.1) Technical Characteristics of the Thermal Sensor::

The Mini2 series represents a latest-generation uncooled thermal module, designed for strict SWaP (Size, Weight, and Power) requirements, offering an optimal balance between small size, minimal weight, and low power consumption

Figure 3.1

The camera module is capable of providing a video stream with an output resolution of up to 640x512 pixels, by combining the physical sensor with advanced processing performed by the "Falcon" chip. This enhances the image and eliminates visual noise, providing a high degree of clarity. The objective is for the YOLO algorithm to have sufficient pixels to distinguish object contours at long distances without errors.

Table 3.1.1: General Technical Specifications (Mini2 Series)

Parameter	Technical Details
Resolution	Up to 640 × 512 pixels
Detector Technology	VOx (Oxid de Vanadiu) cu pitch de 12 µm
Processing	Second-generation "Falcon" ISP Chip
Design	Optimized for portable systems and drones

The Germanium lens is a rare material that is completely transparent to heat (IR radiation). The low NETD value (under 40mK) provides the robot with extreme sensitivity, ensuring detection even when the temperature difference between the body and the surrounding environment is very small..

Table 3.1.2: Component Analysis and Functional Role

Component	Technical Specification	Functional Role
Lens	Germanium (Ge)	Allows the passage of thermal radiation (8~14 µm), unlike standard glass which blocks it.
Detector	VOx (Vanadium Oxide)	Microbolometer-type sensor that transforms detected heat into an electrical signal.
Pixel Pitch	12µm (Micron)	Ensures a high pixel density, providing detailed images on a small-sized sensor.
NETD	<40mK @ 25°C	High thermal sensitivity, capable of distinguishing temperature differences of just 0.04°C.

3.2) Training the YOLOv11 Model

3.2.1) Dataset Preparation and Semantic Annotation

The first step in developing the algorithm consisted in transforming the raw thermal images into structured data capable of being processed by a neural network. The process followed the workflow of the Label Studio platform:
Project configuration: An *Object Detection* type project was created, in which the 4 classes of interest were defined: Person, Car, Cat, and Pigeon.
Import and annotation: The 400 images captured with the Mini2 sensor were uploaded into the platform. Using the graphical interface, bounding boxes were manually drawn around each object identified in the infrared spectrum (Figure X).
Data export: The completion of the annotation allowed exporting the labels in native YOLO format, resulting in .txt files containing the normalized coordinates of the objects, which are essential for the training phase.

Figura3.2.1

3.2.2) YOLOv11 Model Training Workflow

Environment configuration (YAML): The dataset_custom.yaml file was defined to indicate to the algorithm the location of the images and the class correspondence.

```yaml
! dataset_custom.yaml
path: C:/Users/claud/Desktop/Proiect_Varianta 1
train: images/train
val: images/val

names:
  0: Masina
  1: Persoana
  2: Pisica
  3: Porumbel
```

Figure 3.2.2.1

Model initialization: The Python language was used to load the pre-trained yolo11n.pt model.

Choosing the "Nano" version ensures a high processing speed on the Jetson Nano platform.

```
yolo11n.pt
```

Figure 3.2.2.2

Training execution: The process was launched via the model.train() function, using the following control parameters:
imgsz=640 (Processing resolution);
epochs=10 (Number of iterations);
device='cpu' (Hardware used for training).

```python
from ultralytics import YOLO

model = YOLO("yolo11n.pt")

model.train(
    data=r"C:\Users\claud\Desktop\Proiect_Varianta 1\dataset_custom.yaml",
    imgsz=640,
    batch=4,
    epochs=10,
    device='cpu'
)
```

Figure 3.2.2.3

CPU was opted for because the YOLOv11 Nano model is very lightweight, allowing rapid training without expensive hardware resources.
During training, metrics such as precision and localization capability (mAP) were monitored, with the final results being automatically saved to be used in the real-time detection phase.

```
New https://pypi.org/project/ultralytics/8.4.14 available  Update with 'pip install -U ultralytics'
Ultralytics 8.3.240  Python-3.10.11 torch-2.8.0+cpu CPU (12th Gen Intel Core i9-12900H)
engine\trainer: agnostic_nms=False, amp=True, augment=False, auto_augment=randaugment, batch=4, bgr=0.0, box=7.5,
Overriding model.yaml nc=80 with nc=4

                   from  n    params  module                                       arguments
  0                  -1  1       464  ultralytics.nn.modules.conv.Conv             [3, 16, 3, 2]
  1                  -1  1      4672  ultralytics.nn.modules.conv.Conv             [16, 32, 3, 2]
  2                  -1  1      6640  ultralytics.nn.modules.block.C3k2            [32, 64, 1, False, 0.25]
  3                  -1  1     36992  ultralytics.nn.modules.conv.Conv             [64, 64, 3, 2]
  4                  -1  1     26080  ultralytics.nn.modules.block.C3k2            [64, 128, 1, False, 0.25]
  5                  -1  1    147712  ultralytics.nn.modules.conv.Conv             [128, 128, 3, 2]
  6                  -1  1     87040  ultralytics.nn.modules.block.C3k2            [128, 128, 1, True]
  7                  -1  1    295424  ultralytics.nn.modules.conv.Conv             [128, 256, 3, 2]
  8                  -1  1    346112  ultralytics.nn.modules.block.C3k2            [256, 256, 1, True]
  9                  -1  1    164608  ultralytics.nn.modules.block.SPPF            [256, 256, 5]
 10                  -1  1    249728  ultralytics.nn.modules.block.C2PSA           [256, 256, 1]
 11                  -1  1         0  torch.nn.modules.upsampling.Upsample         [None, 2, 'nearest']
 12             [-1, 6]  1         0  ultralytics.nn.modules.conv.Concat           [1]
 13                  -1  1    111296  ultralytics.nn.modules.block.C3k2            [384, 128, 1, False]
 14                  -1  1         0  torch.nn.modules.upsampling.Upsample         [None, 2, 'nearest']
 15             [-1, 4]  1         0  ultralytics.nn.modules.conv.Concat           [1]
 16                  -1  1     32096  ultralytics.nn.modules.block.C3k2            [256, 64, 1, False]
 17                  -1  1     36992  ultralytics.nn.modules.conv.Conv             [64, 64, 3, 2]
 18            [-1, 13]  1         0  ultralytics.nn.modules.conv.Concat           [1]
...
              Persoana          4         13      0.621      0.923      0.861      0.392
              Porumbel          1          1      0.788          1      0.995      0.597
Speed: 0.5ms preprocess, 37.6ms inference, 0.0ms loss, 4.9ms postprocess per image
Results saved to C:\Users\claud\Desktop\Proiect_Varianta 1\runs\detect\train
```

Figure 3.2.2.4

The final result is the unique recognition file best.pt, which contains the data resulting from the best training epoch.

Figure 3.2.2.5

4) Laser Telemetry System and Spatial Fusion

The YDLIDAR X4 model is a 2D laser scanner integrated into the structure for the purpose of compensating for the thermal camera's lack of depth information.

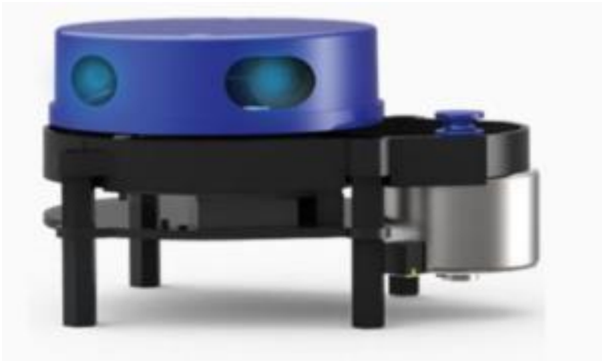

Figure 4.1

The sensor operates in three main states: idle mode, scan mode, and stop mode. Software interaction with the device is performed by sending a standardized start byte (0xA5), followed by a specific command.

Table 4.1. Executed Action

Command (Hex)	Executed Action	Response Mode
A5 60	Initializes the scan and exports the point cloud	Continuous response
A5 65	Stops the rotation and the scanning process	No response
A5 90	Requests hardware information (model, firmware version)	Single response
A5 91	Requests the operating status of the device	Single response

4.1. Transforming the Pixel into an Angle

The deviation of the center of the object detected by YOLO relative to the physical center of the camera is calculated. Using the constant of the lens's field of view, we transform this offset from pixels into a precise angle.

```
dx = x_p - cx_cam
phi_rad = math.atan(dx / F_PIXELS)
phi_deg = math.degrees(phi_rad)
```

Figure 4.1

4.2. Correlating the Angle with Laser Data (LiDAR)

The resulting angle is used as an index to search for the distance within the vector generated by the LiDAR, selecting a safety "window" of ±5 degrees. To eliminate erroneous laser reflections, the median value of the valid distances found in that zone is extracted.

```python
unghi_cautare_lidar = int((360 - phi_deg) % 360)
fereastra = [harta_lidar[a % 360] for a in range(unghi_cautare_lidar - 5, unghi_cautare_lidar + 6)]
valide = [v for v in fereastra if v > 150.0]

if valide:
    dist_L = np.median(valide)
```

Figure 4.2

4.3. Spatial Geometric Calculation (3D Fusion)

The retrieved median distance is projected onto the real axes, adding to it the physical mounting offsets between the thermal camera and the LiDAR sensor. By applying the Pythagorean theorem in 3D space, the system compensates for differences in height and depth to provide the exact distance to the people in danger.

```python
if valide:
    dist_L = np.median(valide)
    dist_x = dist_L * math.cos(phi_rad) + OFFSET_X_MM
    dist_y = dist_L * math.sin(phi_rad)
    dist_reala_3d = math.sqrt(dist_x**2 + dist_y**2 + OFFSET_Z_MM**2)
    dist_reala_m = round(dist_reala_3d / 1000.0, 2)
```

Figure 4.3

5) Hardware Architecture: Spatial Calibration and Processing Unit

To achieve precise data fusion, the geometric calibration of the system was necessary, taking into account the fixed physical distances between sensors. The mounting differences on the robot chassis were defined as constant offsets in the code. Integrating these coordinates into the 3D calculation formula ensures the compensation of perspective errors and the acquisition of the real distance relative to the people in danger.

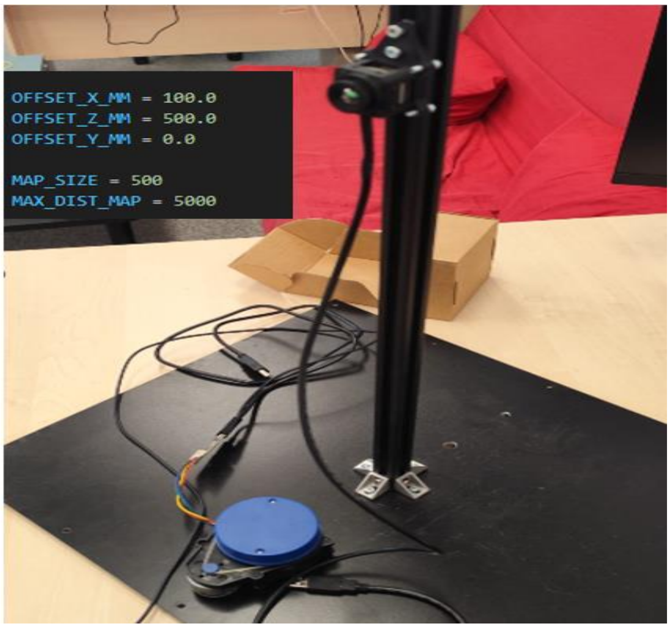

Figure 5.1

NVIDIA Jetson Nano was selected for its performance in the field of artificial intelligence at the edge computing (local processing) level. It allows fluid, parallel execution, and possesses the necessary interfaces (USB, GPIO pins, Serial ports) to ingest the video stream and telemetry data simultaneously, while providing the computing power required by a full Linux operating system.

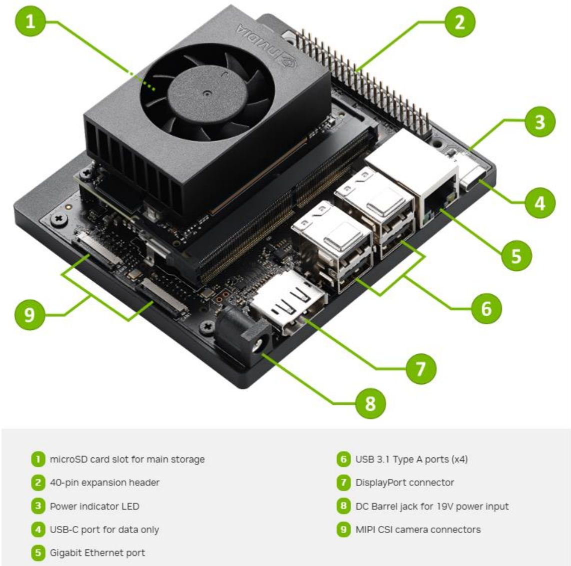

Figure 5.2

6. Conclusions

Practical tests validate the correct functioning of the sensor fusion architecture, running in real time on the NVIDIA Jetson Nano unit. As observed in Figure 6, the system successfully integrates the two data streams:

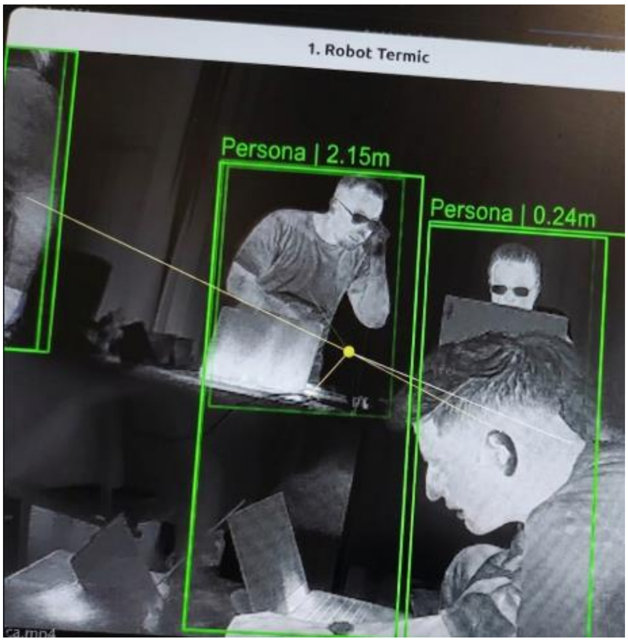

Figure 6

The model quickly identifies people in the infrared spectrum, framing them precisely with bounding boxes (labeled "Persona"). Above each detection, the exact distance is displayed (0.64m; 0.89m). This confirms the accuracy of the mathematical algorithm that visually aligns the camera pixels with the laser data and compensates for the physical distances between sensors.
The final product generated a hybrid perception system, completely autonomous and optimized for edge computing. The robot is capable of locating people under zero visibility conditions (smoke, darkness) and obtaining the spatial coordinates necessary for their rescue, confirming the achievement of all proposed technical objectives.

7) Bibliography

[1] Jiang, A., & Ahamed, T. (2025). Development of an autonomous navigation system for orchard spraying robots integrating a thermal camera and LiDAR using a deep learning algorithm under low- and no-light conditions. *Computers and Electronics in Agriculture*, 230, 109785. Link: https://www.sciencedirect.com/science/article/abs/pii/S016816992500465X
[2] NVIDIA Developer. (2024). Getting Started with Jetson Orin Nano Developer Kit. Link: https://developer.nvidia.com/embedded/learn/get-started-jetson-orin-nano-devkit#intro
[3] Shenzhen EAI Technology Co., Ltd. (2019). *YDLIDAR X4 Development Manual (V1.6)*. Technical manual.
[4] Wuxi InfiSense Technology Co., Ltd. (2023). *Mini2 Series Observation Uncooled Infrared Module Product Manual (V0.1)*. Technical manual.
[5] Code: https://pastebin.com/hpkepbtA

DESIGN AND DEVELOPMENT OF AN EXPERIMENTAL MOBILE PLATFORM WITH VARIABLE HEIGHT

RADU Jan-Alexandru (author),
Prof. Dr. Eng. SAVU Tom (scientific advisor)
Faculty: Faculty of Industrial Engineering and Robotics, Specialization: Applied Informatics in Industrial Engineering, Year of study: IV, e-mail: radujan14@yahoo.com

An experimental mobile platform with variable height for robotic applications was designed and developed. The proposed system integrates a mobile structure, a vertical lifting mechanism and a support system intended for the integration of a robotic arm. The platform aims to improve flexibility and accessibility during automated handling operations in industrial environments. The study presents the mechanical structure, the operating principle and the main stages of the design process, including the selection of the lifting mechanism and the 3D modeling of the assembly. The obtained solution represents a compact and adaptable mechatronic system suitable for educational and industrial applications.

KEYWORDS: lifting mechanism, variable height, mobile platform, mechatronic system, industrial applications.

1. Introduction

The development of robotic systems and industrial automation solutions has led to an increased use of mobile platforms in applications involving automated handling, transport, and positioning [1]. Platforms with scissor lift mechanisms are frequently used in industrial applications due to their compact structure and stability when lifting loads vertically [2].
In recent years, the development of mechatronic systems and the integration of electric linear actuators have contributed to increasing the efficiency and flexibility of mobile platforms used in industrial environments [2]. These systems allow automated operations to be carried out with high precision and increased adaptability in variable workspaces.
Scissor lift mechanisms are used in various applications due to their constructive advantages and their ability to achieve vertical displacement using a compact structure made of articulated arms [1]. The positioning of the actuator and the choice of the drive system directly influence the performance of the mechanism and the forces generated during operation [3].
Mobile platforms with variable height are used in numerous industrial applications for material handling, equipment positioning, and the execution of automated operations in variable workspaces. The integration of lifting mechanisms into mobile platforms contributes to increasing the flexibility of automated systems and adapting them to different operating conditions.
This paper presents the design and development of an experimental model of a mobile platform with variable height intended for robotic applications. The proposed system uses a vertical lifting mechanism driven by an electric linear actuator.
Recent studies on scissor lift mechanisms highlight the importance of structural analysis and mechanism stability in the design process of mobile platforms used in industrial and robotic applications [4], [5].

2. State of the Art

Mobile platforms with scissor lift mechanisms are frequently used in industrial, logistics, and maintenance applications due to their structural stability and their ability to lift vertically within a reduced construction space [4]. Companies such as JLG Industries develop electric and hydraulic lifting platforms used for equipment positioning and industrial operations [6].

Fig.1. Industrial JLG scissor lift platform [6]

In modern applications, the development of autonomous mobile robots integrated with lifting systems and automated handling mechanisms can be observed. Systems such as those developed by inVia Robotics use autonomous mobile platforms, wireless communication, and lifting mechanisms to automate logistics and industrial processes [7].

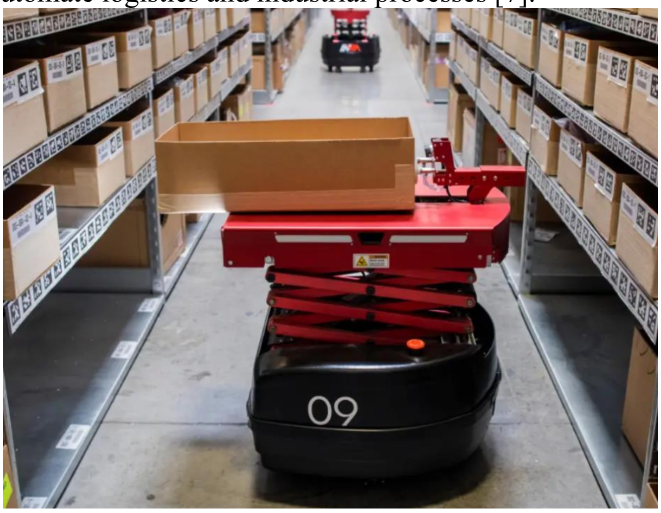

Fig.2. Autonomous mobile robot used in automated logistics applications [7]

Based on existing solutions and current trends regarding the integration of electromechanical systems and wireless communication, an experimental model of a mobile platform with variable height intended for robotic applications was developed within this paper.

3. Calculation of the Required Force

To determine the force required by the linear actuator during the lifting process, mathematical relationships specific to scissor lift mechanisms were used [1]. The actuator force calculation was performed for different positions of the mechanism, depending on the variation of the articulated arm angle during platform lifting.

The relationship used to determine the actuator force is:

$$F = \frac{n*\left(L+\frac{W}{2}\right)*\sqrt{A*(cos\theta)^2-2*B*cos\theta+C}}{B*tan\theta-A*sin\theta} \quad (1)$$

where:

(F) represents the force of the linear actuator [N];

(n) represents the number of levels of the mechanism;

(L) represents the load applied to the platform [N];

(A), (B), (C) represent the geometric parameters of the mechanism;

(θ) represents the angle of the mechanism arms relative to the horizontal.

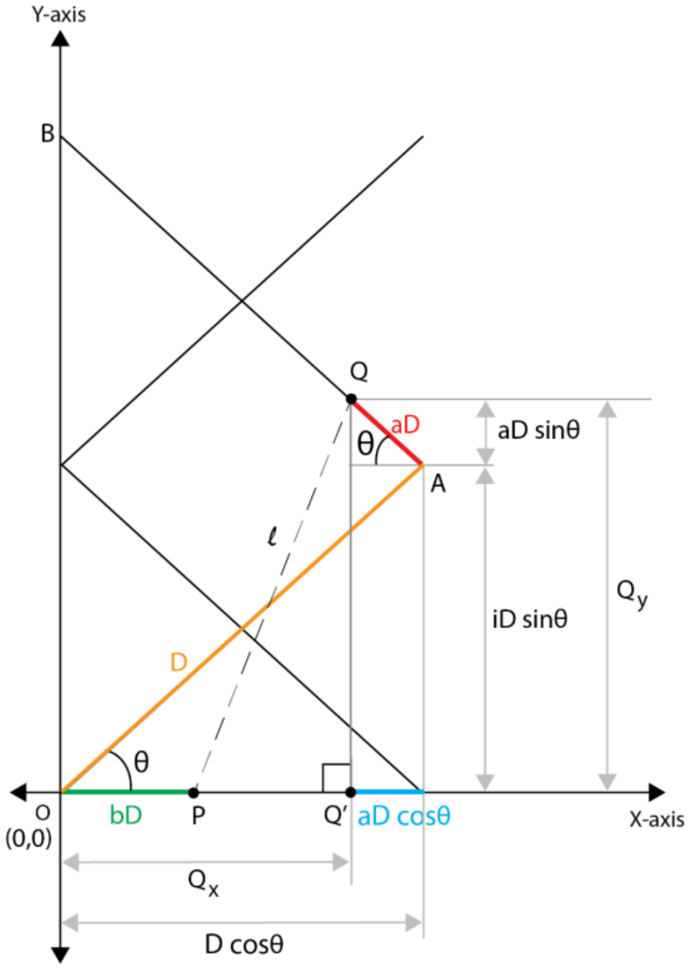

Fig.3. Geometric parameters used in the calculation of the actuator force [1]

4. Experimental Results

Table 1 shows the variation of the required linear actuator force depending on the angle of the scissor lift mechanism.

Table 1. Variation of the actuator force depending on the mechanism angle

Mechanism angle θ [°]	Actuator force F [N]
10	759.788
12	647.434
14	569.053
16	511.781

18	468.468
20	434.826
22	408.13
24	386.566
26	368.882
28	354.189
30	341.838
32	331.345
34	322.344
35	318.312

It can be observed that the force required by the actuator is higher at small mechanism angles and decreases progressively as the platform rises. This behavior is specific to scissor lift mechanisms and directly influences the selection of the linear actuator used within the system.

The values obtained from the calculations were used to verify the compatibility of the linear actuator with the requirements of the lifting mechanism. The analysis of the actuator force variation depending on the mechanism position contributes to evaluating the operation of the system and optimizing the platform lifting process.

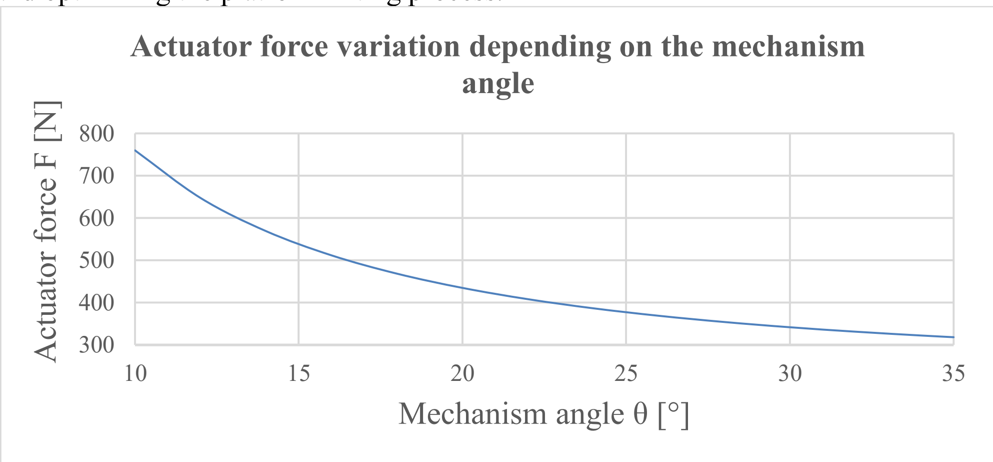

Fig. 4. Variation of the actuator force depending on the mechanism angle

The graph highlights the nonlinear variation of the actuator force depending on the position of the lifting mechanism. It can be observed that the maximum force values occur at small mechanism angles, while the increase in the angle leads to a progressive reduction in the force required by the linear actuator.

5. Structural Design

The following figures present the 3D model of the scissor lift mechanism used within the variable-height platform in different operating positions.

The developed 3D model allowed the analysis of the mechanism kinematics and the verification of compatibility between the components of the mechanical assembly in different operating positions.

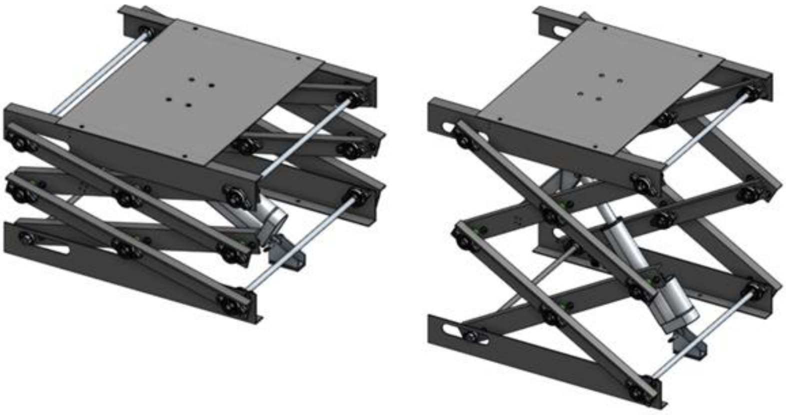

Fig. 5. 3D model of the lifting mechanism in different operating positions

The developed 3D model was used to verify the operation of the lifting mechanism and to analyze the positioning of the linear actuator within the mechanical assembly. The selected configuration allows the vertical displacement of the platform and provides the possibility of integrating the system into an autonomous mobile platform intended for robotic and industrial applications.

By creating the 3D model, it was possible to evaluate the dimensions of the mechanical assembly and verify the compatibility between the components of the lifting system. Additionally, the modeling of the mechanism allowed the analysis of the platform's vertical displacement and the visualization of the successive positions of the mechanism during operation.

Fig. 6. Housing for the integration of the electrical components of the system

The presented compartment was designed for the integration of the electrical components required for controlling the linear actuator and operating the system. The selected configuration allows the protection of the components and the organization of the electrical connections within the platform.

6. Conclusions

Within this paper, an experimental model of a mobile platform with variable height was designed and developed using a scissor lift mechanism driven by an electric linear actuator. The proposed system is intended for robotic applications, offering the possibility of integration into an autonomous mobile platform.

The 3D design of the mechanical assembly, the analysis of the actuator force variation depending on the position of the mechanism, and the assembly of the experimental model were carried out. The obtained results highlight the influence of the mechanism angle on the force required by the actuator, with the highest forces being generated at small lifting angles.

Furthermore, the hardware and software components required for controlling the linear actuator were developed and tested. The analysis and modeling of the mechanism contributed to verifying the operation of the system and selecting the constructive solution used within the project.

The results obtained within the project demonstrate the efficient operation of the lifting mechanism and the compatibility between the mechanical components and the drive system used. The developed configuration allows the platform to be adapted for different industrial applications that require vertical displacement and positioning flexibility.

7. References

[1]. Saxena, A. (2016), "Deriving a Generalized, Actuator Position-Independent Expression for the Force Output of a Scissor Lift", University of California, Berkeley.

[2]. Stawiński, Ł., Stawiński, V., Kosucki, A. and Minav, T. (2023), "Electromechanical Actuator-Based Solution for a Scissor Lift", Actuators, Vol. 12, No. 10, Article 394, MDPI.

[3]. Spackman, H. (1994), "Mathematical Analysis of Actuator Forces in a Scissor Lift", Technical Document 2643, Naval Command, Control and Ocean Surveillance Center (NCCOSC), San Diego, California.

[4]. Sabde, A.M., Jamgekar, R.S. (2016), "Design and Analysis of Hydraulic Scissor Lift by FEA", International Research Journal of Engineering and Technology (IRJET), Vol. 3, Issue 10, pp. 1277-1292.

[5]. Zhang, W., Zhang, C., Zhao, J., Du, C. (2015), "A Study on the Static Stability of Scissor Lift", The Open Mechanical Engineering Journal, Vol. 9, pp. 954-960.

[6]. JLG Industries, Scissor Lifts, https://www.jlg.com/en/equipment/scissor-lifts/micro-sized-series?tab=%22%22, accessed on 15 May 2026.

[7]. inVia Robotics, https://inviarobotics.com/our-system/invia-picker-robots/, accessed on 15 May 2026.

8. Notations

The following symbols are used within the paper:

F = the force of the linear actuator [N];

n = the number of levels of the mechanism;

L = the load applied to the platform [N];

A, B, C = the geometric parameters of the mechanism;

θ = the angle of the mechanism arms relative to the horizontal.

RESEARCH ON THE DEVELOPMENT OF AN EXPERIMENTAL ENGRAVING SYSTEM MODEL FOR SMALL-SURFACE PARTS

BILAN Alexia Iuliana, **GHIONEA Ionuț Gabriel**
Faculty: Industrial Engineering and Robotics, Specialization: Applied Informatics in Industrial Engineering, Year of study: IV, e-mail: alexiabilan02@yahoo.com

Scientific supervisor: Conf. Dr. Ing. Ionuț Gabriel GHIONEA

ABSTRACT: The current project aims to design and create a functional prototype intended for the mechanical engraving of parts with reduced surfaces. The system can process parts up to a maximum size of 120x91 mm and is a hybrid solution between a compact CNC router and the kinematic structure of a 3D printer. The device uses numerically controlled axis movements to perform precision mechanical milling and engraving operations. The project aims to develop a compact and affordable experimental system designed for engraving aluminum plates used in industrial molds, technical markings, and customization applications.

KEY WORDS: CNC, tools engraving, aluminum, precision

1. Introduction

In the context of the development of modern computer-aided manufacturing technologies, CNC systems have become essential tools for carrying out high-precision machining operations.

Mechanical engraving of small components represents an efficient method for producing permanent markings on metallic surfaces and is widely applied in the manufacture of technical labels, industrial nameplates, and customized products. Owing to the high cost of industrial equipment and the increasing demand for compact and cost-effective solutions, the development of small-scale CNC systems has become a significant area of interest in both educational and industrial fields.

The primary objective of this project is the development of a functional prototype, illustrated in Fig. 1, designed to perform engraving operations on aluminum plates with maximum dimensions of 120 × 91 mm. The paper further examines the existing constructive solutions, the mechanical and electronic components employed, as well as the operating principles of the proposed system.

The 3D model of the engraving system was designed using the CATIA V5 software [1], which is widely used in industrial companies.

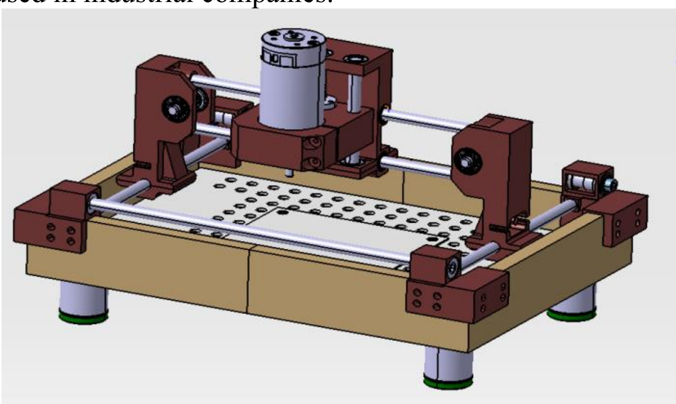

Fig.1 The 3D model of the experimental model

The main design objectives of the proposed system include ensuring structural rigidity, achieving high positioning accuracy, and reducing vibrations, while maintaining cost-effective and accessible solutions.

These objectives were achieved through the fabrication of specific components using additive manufacturing technologies (3D printing) and by increasing the rigidity of the assembly through the use of additional components, namely:

- Integration of adjustment shims for improved flatness and machining accuracy
- Securing the working area using locating pins
- Integration of support feet provided with adjustment shims in order to enhance system stability and reduce vibrations
- Clamping of the aluminum plate to be machined using fastening clamps

2. Current state

Currently, CNC router technology is focused on advanced automation, accessibility, and ease of use, while simultaneously providing solutions for improved precision (Fig. 2).

National Institute of Standards and Technology (NIST) highlights in one of its publications, “The State of Integrated CAM/CNC Control Systems: Prior Developments and the Path Towards a Smarter CNC” [2], the need for CNC systems capable of communicating and exchanging data in real time within the context of the Industry 4.0 concept, which represents the digital transformation of manufacturing through the integration of modern technologies such as the Internet of Things (IoT), artificial intelligence (AI), Big Data, and cloud computing.

The document also states that the G-code language, which has been used for CNC machine programming for more than 60 years, transmits only basic commands and does not include advanced information related to real-time analysis, automatic optimization, or intelligent adaptation of process parameters. Although effective for conventional machining operations, it remains limited in meeting the requirements of modern Industry 4.0 applications.

Therefore, NIST criticizes this limitation, as it reduces flexibility and slows down the development of intelligent CNC systems.

Fig.2 Modern CNC router

3. Designing and Development of the System

The development of this CNC mechanical engraving system aims to provide an experimental model intended for individual users and start-up companies with limited financial resources, the production cost of the system being considerably low in relation to its performance and capabilities.

Cost reduction was considered from the early design stages, particularly in the selection of manufacturing materials and fabrication technologies, with a primary focus on additive manufacturing (3D printing) [3].

a. Mobile assembly of the system

With regard to the operating principle of the system, Fig. 3 illustrates the displacement mechanism designed for the flat-end cylindrical milling cutter, based on the motion system commonly used in 3D printers. This solution was chosen due to its reliability, structural rigidity, and reduced manufacturing cost.

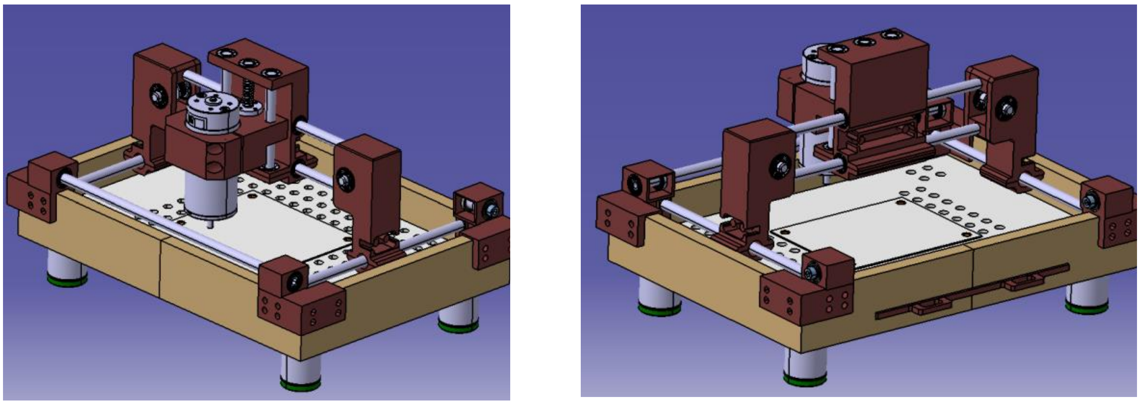

Fig.3 Mobile assembly of the system

Movement of the System Along the X and Y Axes

The spindle motion along the X and Y axes is achieved by means of Ø8 cylindrical linear guides and toothed belt transmission systems actuated by NEMA 17 stepper motors. Proper belt tension is ensured through the lateral components and the support element of the flat-end cylindrical milling cutter, which were designed with integrated tensioning mechanisms (Fig. 4).

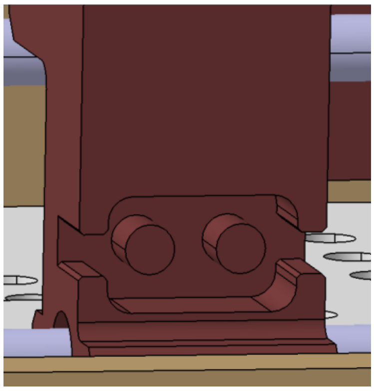

Fig.4 Belt tensioner

Movement of the System Along the Z Axis

The displacement of the engraving tool along the Z axis, presented in Fig. 5, is accomplished through the use of a screw–nut transmission mechanism actuated by a NEMA 17 stepper motor.

The spindle motor support travels along the lead screw, while the nut mounted on the support ensures precise and stable motion along the Z axis during CNC system operation. To achieve increased positioning accuracy and structural rigidity, the mechanism was additionally equipped with two lateral linear guides designed to support and stabilize the axial linear movement.

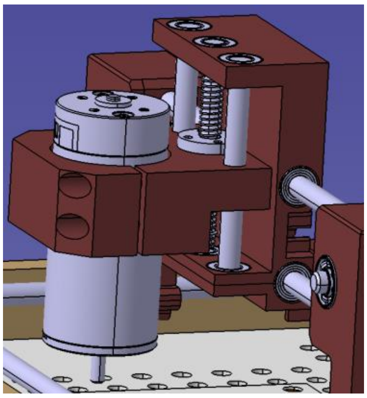

Fig.5 Z-axis motion mechanism

b. Static assembly of the system

The static assembly of the system, illustrated in Fig. 7, consists of the following components:

- Base plate
- 4 adjustment shims (intended for base plate leveling, considerably minimizing the risk of machining and positioning errors - Fig. 6)

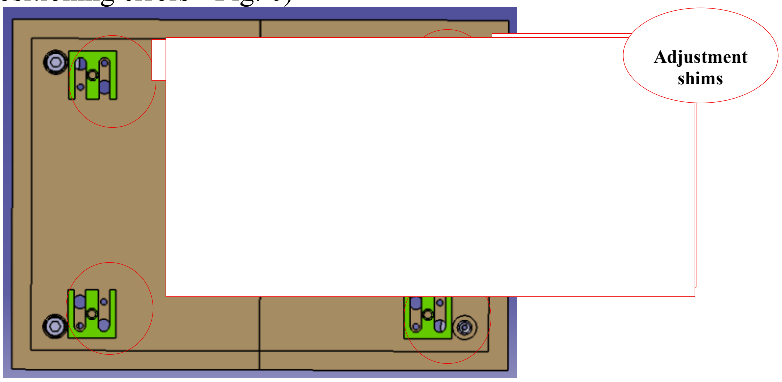

Fig.6 Representation of the Adjustment Shims

- Support feet (intended to reduce the contact between the system and the supporting surface, thereby minimizing the occurrence of vibrations)
- Aluminum plate (equipped with mounting holes for securing the workpiece during machining operations)
- Drawer (used for collecting residue from the workpiece during the engraving process)

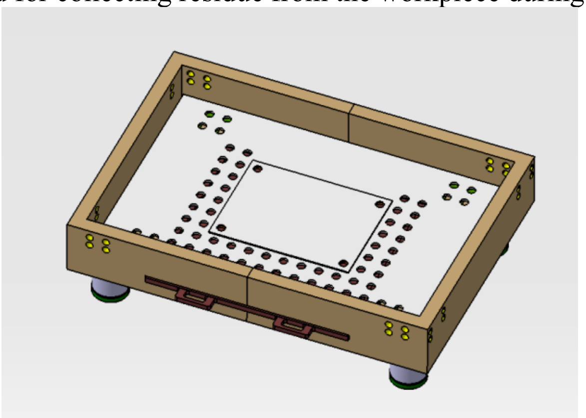

Fig. 7 Static assembly of the system

The base housing constitutes one of the key structural components of the assembly, since most of the system elements are mounted on it, thereby requiring increased structural rigidity.

To satisfy this requirement while also minimizing manufacturing costs, the housing was designed as a two-part structure manufactured using 3D printing technology. The walls of the component have a thickness of 12 mm, and the joining of the two sections is performed using locating pins for precise alignment and fixation, as shown in Fig. 8.

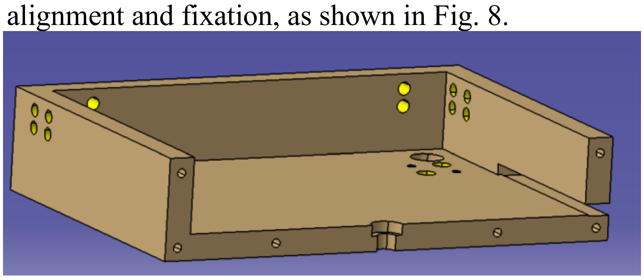

Fig.8 Reinforcement and fixation of the base plate

4. Identification and Prioritization of the Complementary Functions of the

Experimental System

To identify the functions of the analyzed system, its interactions with the surrounding environment were taken into account, the analysis being performed throughout the entire life cycle of the experimental model. The identified functions were subsequently represented in the form of a FAST diagram, according to Fig. 9.

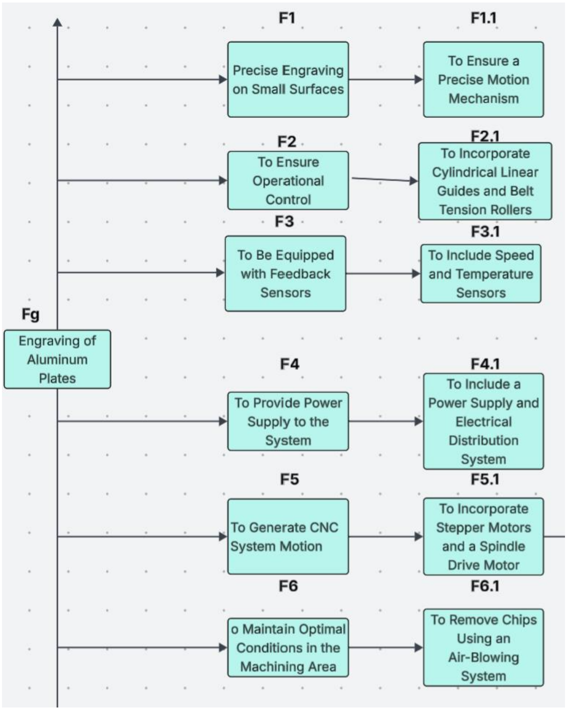

Fig.9 FAST diagram

To determine the importance level of each identified function, Table 1 presents the function prioritization matrix developed for the engraving system designed for small-sized parts.

Table 1. Function Prioritization Matrix

FUNCTIONS	F1	F2	F3	F4	F5	F6
F1	1	0	0	0	0	0
F2	1	1	0	0	1	0
F3	1	1	1	0	1	0
F4	1	1	1	1	1	0
F5	1	0	0	0	1	0
F6	1	1	1	1	1	1

Level of importance ()	6	4	3	2	5	1

As a result of the comparative analysis of the functions of the engraving system intended for small-sized components, the following hierarchy of functional importance was determined: F1 > F5 > F2 > F3 > F4 > F6.

As indicated in Table 1, Function F1, corresponding to precise engraving on small-sized surfaces, is considered the most important function of the system, since it defines the primary objective of the product. This function has a direct impact on both the quality of the machining process and the accuracy of the resulting output.

- **Essential functions**

Function F5, corresponding to the generation of motion within the CNC system, ranks second in importance, as it is essential for carrying out the engraving process. Without controlled axis movement and spindle rotation, the primary function of the system cannot be achieved.

Function F2, associated with operational control, plays a significant role in system coordination by ensuring accurate command transmission and the proper operation of the equipment.

- **Auxiliary functions**

Function F3, associated with feedback sensors, contributes to the monitoring of operating parameters such as rotational speed and temperature, thereby improving the safety and reliability of the system, without directly influencing the engraving process.

Function F4, representing the energy supply function, is essential for system operation but does not directly influence machining performance, being therefore classified as a supporting function.

- **Low-Importance Function**

Function F6, related to maintaining optimal working conditions (chip removal by air blowing), is considered the least important function, having an auxiliary role in improving operating conditions. Although it contributes to visibility and cleanliness within the working area, it is not essential for carrying out the engraving process.

5. Electrical Connection Diagram and Component Testing

To enable the operation of the assembly, several electronic components were selected, namely: a 24 V power supply unit, NEMA 17 stepper motors for axis displacement, an L298 motor driver, a DC 775 spindle motor, a CNC Shield, A4988 stepper motor drivers, a temperature sensor, a rotational speed sensor, and an Arduino UNO microcontroller board.

Based on these components, an electrical connection diagram for controlling the system was designed, as presented in Fig. 9.

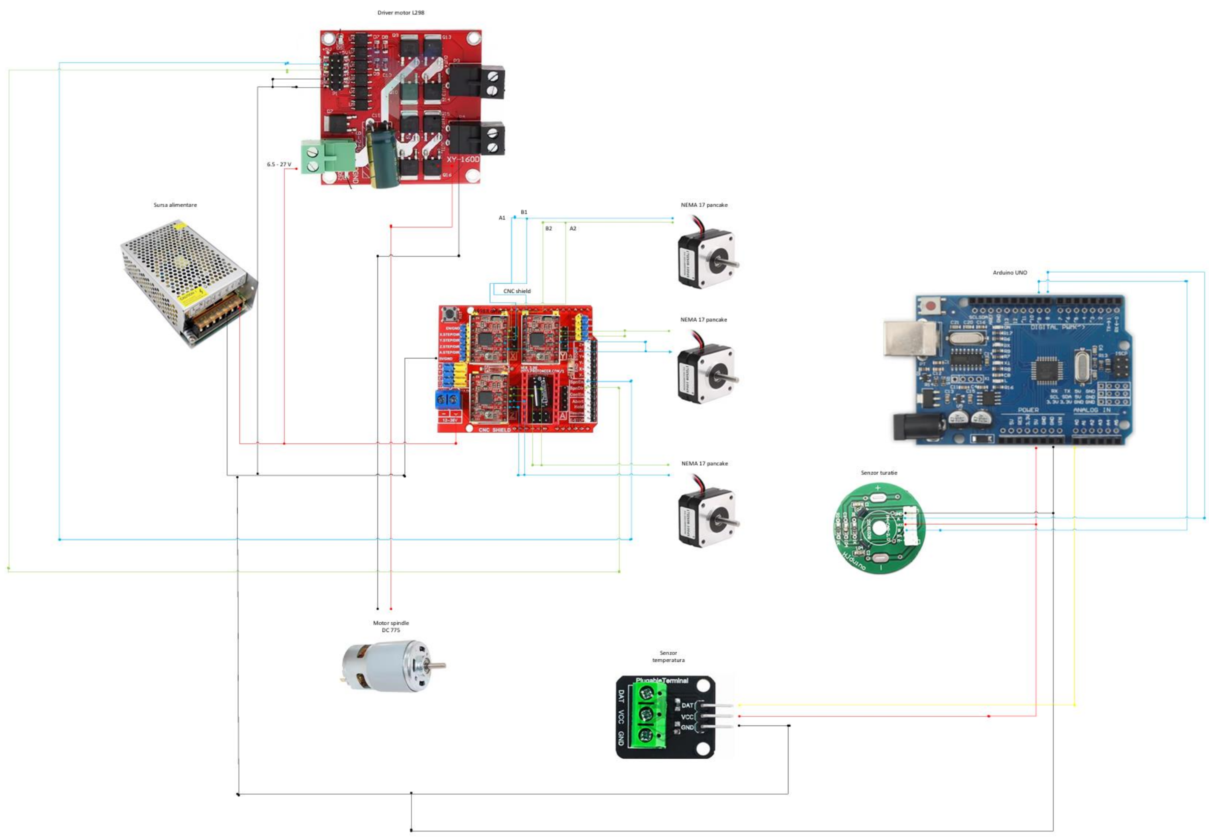

Fig.10 Electrical Connection Diagram

To ensure the correct implementation of the previously presented wiring diagram, a series of electrical connections were carried out for component testing purposes.

6. Testing code

In order to test the selected components, a dedicated software routine was developed using the Arduino IDE environment. The implemented test code was designed to validate both the communication between the Arduino board and the motor driver, and the connection between the driver and the spindle motor.

The program was structured into multiple sections to ensure efficient organization and improved code readability.

- In the first section, the PWM-supported pins were defined (Fig. 11)

```
const int ena = 3;
const int in1 = 8;
const int in2 = 9;
```

Fig.11 PWM Pin Definition

- The second section configures the pins as output signals (Fig.12)

```
pinMode(ena, OUTPUT);
pinMode(in1, OUTPUT);
pinMode(in2, OUTPUT);
```

Fig.12 Pin Configuration as Outputs

- Setting the initial direction of the motor (Fig.13)

```
digitalWrite(in1, HIGH);
digitalWrite(in2, LOW);
```

Fig.13 Initial direction of the motor

- Motor Stop Verification During Arduino Startup (Fig.14)

```
analogWrite(ena, 0);
```

Fig.14 Verification of the Initial State of the Motor

- Setting a gradual acceleration from 0 to maximum speed over a period of 10 seconds while ensuring the desired rotation direction (Fig.15)

```
void loop() {
  digitalWrite(in1, HIGH);
  digitalWrite(in2, LOW);
  for (int viteza = 0; viteza <= 255; viteza++) {
    analogWrite(ena, viteza);
    delay(39);
  }
```

Fig.15 Setting the Motor Operating Time and Rotation Direction

- Motor shutdown by setting the speed value to zero (Fig.16)

```
analogWrite(ena, 0);
```

Fig.16 Motor shutdown

- The motor enters a standby state for 5 seconds, after which the loop() function restarts and the acceleration sequence is repeated (Fig.17)

```
delay(5000);
```

Fig.17 Configuration of the delay() Function Timing

7. Conclusions

Thus, the present paper analyzed the development of an experimental engraving system intended for small-sized workpieces (aluminum plates), aiming to provide compact, accessible, and efficient solutions for both start-up companies and users interested in customization or prototyping applications.

The project is based on the integration of operating principles specific to CNC systems with a structural architecture inspired by 3D printers, aiming to achieve a balance between low cost, precision, and operational flexibility.

Important aspects regarding the future development of the prototype include:

- Increasing the structural rigidity and reducing the vibrations generated during the engraving process through the use of more rigid materials, which would naturally involve higher manufacturing costs;
- Implementation of a laser cutting function for situations in which, depending on the size of the engraved text, a portion of unengraved material remains after the engraving process;
- Automatic adjustment of the text (font) size based on the number of words or characters to be engraved;
- Implementation of a higher-performance ventilation or suction system intended to improve the cleaning of the working area.

In conclusion, the present study confirms the feasibility of developing an experimental mechanical engraving system dedicated to small-scale applications, while also demonstrating significant potential for further expansion and optimization in future development stages.

8. Bibliografie

[1]. Conf. Dr. Ing. Ionuț Gabriel GHIONEA, Computer Aided Design, UNSTPB, Year III

[2]. Roby Lynn, Moneer Helu, Mukul Sati, Tommy Tucker, Thomas Kurfess (2020), "The State of Integrated CAM/CNC Control Systems: Prior Developments and the Path Towards a Smarter CNC", 4 (issue 2), 25-42, 2572-3928

[3]. As. Dr. Ing. Vlad ENACHE, Project on Additive Manufacturing Technologies and Equipment, UNSTPB, Year IV

RESEARCH AND DEVELOPMENT OF A WEARABLE SYSTEM AND APPLICATION FOR REAL-TIME ATHLETE EFFORT MONITORING

ABAGIU Alberto Florian and TUNSOIU Nicolae (Scientific Supervisor)
Faculty of Industrial Engineering and Robotics, Applied Computer Science in Industrial Engineering, Year IV, e-mail: abagiualbertoflorian@gmail.com

ABSTRACT: This paper presents Athlete Flow, a web platform for real-time athlete moni-toring built with Next.js, React, and PostgreSQL. The application provides role-based dash-boards, squad management, performance charts, and a live training panel that streams sensor data via Server-Sent Events with sub-second latency. An in-process publish-subscribe bus decouples ingestion from delivery without external messaging infrastructure. The platform is paired with a low-cost wearable built around an ESP32-C3 attached to a Polar OH1 arm-band, integrating an accelerometer and an infrared thermometer, transmitting every 500 ms over WiFi. The architecture is modular and self-hostable, offering an accessible alternative to proprietary commercial systems.

KEYWORDS: real-time monitoring, IoT, wearable sensors, Bluetooth Low Energy, Server-Sent Events.

1. Introduction

In modern competitive sports, continuous monitoring of physiological parameters and mechanical load has become a standard component of the training process. At the professional level, commercial solutions such as Polar Team Pro [1], Catapult Vector [2], and STATSports APEX [3] provide complete packages of wearable sensors and analysis platforms; however, their per-athlete cost and requirement for a permanent subscription make them generally inaccessible to independent clubs and training groups without a dedicated budget.

This paper presents the research, design, and implementation of a custom real-time mon-itoring platform called *Athlete Flow*, whose core is a web application that allows coaches to view live physiological data, manage teams by age category, and perform retrospective analy-sis of training sessions. The platform also includes a low-cost wearable device built around an ESP32-C3, which aggregates data from a heart rate armband and complementary motion and temperature sensors.

Most clubs and training groups lack a digital system for effort monitoring; load esti-mates are subjective or inferred from visual observation by the coach. Transitioning to a full set of commercial sensors entails costs in the range of thousands of lei per athlete, while the data remains captive within the manufacturer's ecosystem, with no open export format or freely accessible programming interface.

The research objectives are: (1) integrating into a single wearable device an external heart rate source (Polar OH1, recognized for its optical accuracy relative to electrocardiography [4]), an inertial sensor (MPU-6050), and an IR temperature sensor (MLX90614); (2) transmitting the aggregated data to a self-hosted server at a rate compatible with real-time visualization (under 1 s end-to-end); (3) storing sessions in a relational database with clear role separation between coach and athlete; (4) ensuring modularity, so that the absence of a sensor at startup does not block the operation of the remaining ones.

2. Current State of the Field

The athlete monitoring market is dominated by vertical commercial solutions with inte-grated hardware and software. The *Polar Team Pro* system uses a vest with a GPS module and an optical heart rate sensor, with data accessible through a cloud platform requiring an annual subscription [1]. *Catapult Vector* (S7/S8) is the reference system in professional football, offer-ing GPS at 10 to 18 Hz, a triaxial accelerometer at 100 Hz, a magnetometer, and UWB telemetry for indoor positioning [2]. *STATSports APEX*, FIFA-certified, incorporates GPS at 18 Hz, an ac-celerometer at 600 Hz, and reports 24 metrics through its proprietary application [3]. All these systems, however, target elite clubs: the cost of a full license exceeds the budget of most teams, the ecosystems are closed (data remains in the manufacturer's cloud), and extension with addi-tional sensors—for example, non-contact body temperature—is not supported.

The academic literature confirms the potential of wearable technology in sport. The review by Seshadri et al. [5] summarizes the capability of wearable sensors to monitor the phys-iological profile of athletes, and Camomilla et al. [6] show that inertial measurement units (IMU) are mature enough for field-based performance assessment, not only in laboratory settings. For estimating distance and running cadence, algorithms based on peak detection in acceleration magnitude remain the practical reference due to their favorable trade-off between accuracy and computational cost [7], [8]. The validity of the Polar OH1 optical sensor, also used in the present work, was confirmed in the study by Muggeridge et al. [4] for intensities ranging from moderate to sprint.

For real-time data delivery to the browser, three established alternatives exist: repeated HTTP *polling* (high latency, costly), *WebSockets* [9] (full-duplex, but with a proprietary proto-col over TCP), and *Server-Sent Events* (SSE), standardized in the HTML Living Standard [10] and exposed through the EventSource API [11]. SSE provides a unidirectional server → client channel over HTTP/1.1, with automatic reconnection managed by the browser—exactly match-ing our usage profile, in which the telemetry stream flows in a single direction.

The specialized literature explicitly identifies several limitations of this generation of commercial systems—limitations that directly motivate the architectural choices of the present work. Seshadri et al. [12] show that the dominant platforms, built on a GPS plus heart rate band pairing, measure external load with reduced validity in crowded or covered spaces and do not allow fusion with additional biophysical sensors, since the stack remains closed. Dolson et al. [13], in a systematic review of 20 studies, find that continuous, non-invasive monitoring of body temperature—essential for early detection of heat stress—is absent from current commer-cial offerings, despite the maturity of infrared technology. At the governance level, Kwon [14] documents the vendor lock-in of ecosystems such as *Polar Flow* [1], in which the club effectively loses control over the biometric data of its athletes. These three directions—sensor extensibil-ity, IR body temperature, and data sovereignty—structure the technical contribution described in the following chapters.

Table 1 summarizes the functional differences between the dominant commercial solu-tions and the proposed platform.

Table 1. Functional comparison between commercial systems and Athlete Flow.

Criterion	**Polar**	**Catapult**	**STATS.**	**Athlete Flow**
GPS	Yes	10–18 Hz	18 Hz	No
Heart rate	Yes	Yes	Yes	Yes (Polar OH1)
Body temperature	No	No	No	Yes (IR)
Sensor extensibility	No	No	No	Yes (I2C)
Open data	No	No	No	Yes (self-hosted)
Cost per athlete	~3,750 lei*	>10,000 lei*	~1,375 lei**	<500 lei

*Team system, estimated price per athlete; requires additional annual subscription.

**Individual variant (Athlete Series); the Pro/Team version is priced on request.

3. Theoretical Aspects

Heart rate acquisition via BLE GATT. The *Heart Rate Service* (HRS) specification of the Bluetooth SIG [15] defines a standardized service with UUID 0x180D and a measurement characteristic 0x2A37, exposed as a notification. The first byte of the payload is a *flags* field, whose bit 0 indicates the value format (8 or 16 bits). The Polar OH1 armband implements this profile as a peripheral; the ESP32-C3 node acts as a BLE central, discovers the HRS service, subscribes to notifications, and decodes the current heart rate value. According to the Bluetooth Core Specification [16], a peripheral can maintain only a single active connection at any given time, which requires that the manufacturer's native applications (Polar Flow) be disconnected before use.

I2C sensors: IR temperature and inertial measurement unit. The MLX90614 sen-sor [17] measures the temperature of an object without contact (T_{obj}) using an infrared ther-mopile, reporting the value on the I2C bus at address 0x5A. The MPU-6050 [18] combines a three-axis accelerometer and gyroscope, accessible at 0x68. Both sensors share the same I2C bus (SDA = GPIO 8, SCL = GPIO 9 on the ESP32-C3), with arbitration ensured by their distinct addresses.

Step detection based on acceleration magnitude. The adopted approach belongs to the family of threshold-based algorithms on acceleration magnitude, described in the wearable pedometry literature [7], [8]. The algorithm uses the vector norm $a = \sqrt{a^2{}_x + a^2{}_y + az^2}$ and applies a comparator with hysteresis: a step is registered when a exceeds the upper threshold $T_h = 12.5\,\mathrm{m/s^2}$, and the state is reset only when a drops below $T_l = 0.75\,T_h$. A dead time of 250 ms prevents double triggering. Distance is estimated by multiplying the step count by a fixed stride length of 0.75 m, and instantaneous speed is derived from the interval between consecutive steps.

Real-time data transmission. For delivering the sensor stream to the browser, the plat-form uses *Server-Sent Events* (SSE) [10], a unidirectional server → client channel over HTTP/1.1, preferred over the WebSocket protocol [9] due to its simplicity and automatic reconnection man-aged by the browser. Communication between the ingestion route and the SSE routes is handled through an in-process publish-subscribe bus, which eliminates the dependency on an external queue such as Redis, providing minimal latency at zero infrastructure cost.

4. The Wearable Device

The proposed solution follows a data pipeline organized into three functional layers (Fig. 1): the wearable device as the data source, the web application as the processing and persistence core, and the browser client as the visualization interface.

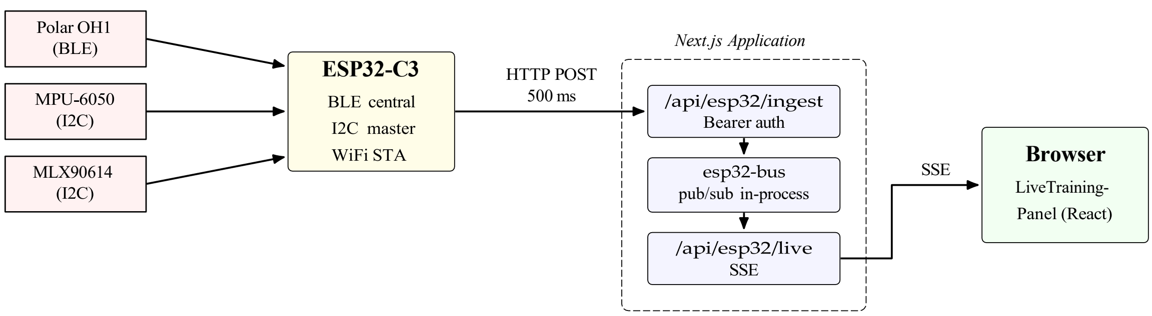

Figure 1. End-to-end architecture of the Athlete Flow platform: the pipeline from the wearable sensors, through the ESP32-C3 node and the Next.js application, to the live browser interface.

The wearable device is an assembly consisting of the Polar OH1 armband, worn on the forearm, and a 3D-printed enclosure attached to its strap, which houses the ESP32-C3 node [19] together with the MPU-6050 [18] and MLX90614 [17] sensors. The microcontroller simultane-ously fulfills three roles: BLE central for heart rate acquisition from the Polar OH1, I2C master for the inertial sensor and the IR temperature sensor, and WiFi STA for cyclic data transmis-sion. Step detection relies on a comparator with hysteresis applied to the acceleration magnitude (threshold 12.5 m/s^2, hysteresis 75 %, dead time 250 ms). Every 500 ms, the firmware aggre-gates the available readings into a JSON object and transmits it via HTTP POST with Bearer authentication. If a sensor fails to initialize at startup, the corresponding field is omitted from the payload without interrupting the transmission of the remaining data (*soft-fail* behavior). The device's role is limited to data acquisition and dispatch; all display, storage, and analysis logic resides in the web application.

5. The Web Application

The web application is the central component of the platform and is implemented in Next.js 16 with App Router, using TypeScript, React 19, Tailwind CSS 4, shadcn/ui compo-nents, and the Prisma 7 ORM over PostgreSQL 16. The choice of Next.js is motivated by the ability to define server-side API routes and React components within the same project, elimi-nating the need for a separate backend server. TypeScript provides static type checking across the entire stack, from the database schema (through the Prisma generator) to the interface com-ponents. The execution infrastructure is containerized through Docker Compose, which orches-trates three services: the Next.js server (port 3000), the PostgreSQL database (port 5432), and the Prisma Studio interface (port 5555) for direct data inspection during development. Con-tainerization allows the complete installation of the platform with a single command, without native dependencies on the host system.

Data model. The relational schema is designed around four main entities. The *User* model stores authentication data and the role (coach, athlete, or undetermined). The *Coach* model extends the user with coach-specific attributes, while *Athlete* contains the age category, group, and the configuration of the associated wearable device. The *Group* model represents a team structured by category (U15, U17, U19, Senior), owned by a coach. Training sessions are modeled through *TrainingSession* at the group level and *AthleteSessionData* at the individual level, the latter storing average and maximum heart rates, average body temperature, distance, sprint count, and alert level. The separation into two tables allows team-level aggregation with-out duplicating individual data.

Authentication and dashboards. Authentication is managed by the *better-auth* library, with role-based separation: at registration the user selects the coach or athlete role, and each API route programmatically verifies the current role. The interface adapts accordingly: the coach navigates through groups and individual records with historical charts (heart rate, load, distance, estimated VO2max) and a live training panel, while the athlete accesses only their own statistics.

Communication between the wearable device, the browser, and the database is mediated by four server-side API routes, summarized in Table 2.

Ingestion pipeline and live panel. The ingestion endpoint validates the Bearer token and republishes the reading on the in-process publish-subscribe bus, which distributes the data via SSE [11] to subscribed browsers. The live training panel is a React component with five phases (connecting, online, training, saving, completed) that displays heart rate and temperature charts in a 30 s rolling window. A watchdog mechanism automatically stops recording if the device becomes unreachable, and upon completion all accumulated readings are persisted in PostgreSQL as a training session.

Table 2. Main API routes of the application.

Method	Route	Purpose

POST	/api/esp32/ingest	Receives JSON from firmware (Bearer)
GET	/api/esp32/live	Live SSE stream per athlete
POST	/api/athlete/sessions	Saves the training session
GET	/api/athlete/devices	Device configuration per athlete

6. Conclusions

This paper presented the Athlete Flow platform, a real-time athlete monitoring system built on an open software stack. The main contribution is the development and implementa-tion of a web application that integrates an ingestion pipeline based on a Server-Sent Events connection, a relational data model with role separation that enables role-adapted dashboard visualization, and a live training panel for each athlete. The wearable device, built around an ESP32-C3 attached to the Polar OH1 armband, serves as a modular data source: the absence of a sensor at startup does not affect the operation of the remaining ones.

Current limitations include the lack of authorization on the SSE channel, the absence of a local retransmission buffer in the firmware, the fixed stride length of 0.75 m in the step detection algorithm, and the absence of a data import module for sessions stored in other ecosystems.

Future directions include per-session authentication of the live stream, importing his-torical data from commercial ecosystems (Polar Flow, Garmin Connect), automatic detection of physiological anomalies with push notifications to the coach, and a team-wide simultane-ous visualization panel. On the hardware side, automatic stride length calibration and a local retransmission buffer would increase reliability under intermittent connectivity.

References

[1] Polar Electro Oy, *Polar team pro: Team monitoring system*, Accessed: May 2026, 2024. [Online]. Available: https://www.polar.com/en/business/team-pro.

[2] Catapult Sports, *Vector athlete monitoring devices (S7/S8)*, Accessed: May 2026, 2024. [Online]. Available: https://www.catapult.com/solutions/athlete-monitoring.

[3] STATSports Group, *APEX athlete series: GPS performance tracker*, Accessed: May 2026, 2024. [Online]. Available: https://statsports.com/us/apex-athlete-series.

[4] D. J. Muggeridge et al., “Measurement of heart rate using the Polar OH1 and Fitbit Charge 3 wearable devices in healthy adults during light, moderate, vigorous, and sprint-based exercise: Validation study,” *JMIR mHealth and uHealth*, vol. 9, no. 3, e25313, 2021. DOI: 10.2196/25313.

[5] D. R. Seshadri et al., “Wearable sensors for monitoring the physiological and biochemical profile of the athlete,” *npj Digital Medicine*, vol. 2, no. 1, p. 72, 2019. DOI: 10.1038/ s41746-019-0150-9.

[6] V. Camomilla, E. Bergamini, S. Fantozzi, and G. Vannozzi, “Trends supporting the in-field use of wearable inertial sensors for sport performance evaluation: A systematic re-view,” *Sensors*, vol. 18, no. 3, p. 873, 2018. DOI:

10.3390/s18030873.

[7] K. Tumkur and S. Subbiah, "Modeling human walking for step detection and stride de-termination by 3-axis accelerometer readings in pedometer," in *2012 Fourth International Conference on Computational Intelligence, Modelling and Simulation*, IEEE, 2012, pp. 199–204. DOI: 10.1109/CIMSim.2012.42.

[8] A. Brajdic and R. Harle, "Walk detection and step counting on unconstrained smart-phones," in *Proceedings of the 2013 ACM International Joint Conference on Pervasive and Ubiquitous Computing (UbiComp '13)*, ACM, 2013, pp. 225–234. DOI: 10.1145/ 2493432.2493449.

[9] I. Fette and A. Melnikov, *The WebSocket protocol*, IETF RFC 6455, 2011. DOI: 10 . 17487/RFC6455. [Online]. Available: https://www.rfc-editor.org/rfc/rfc6455.

[10] WHATWG, *HTML living standard — server-sent events*, Accessed: May 2026, 2025. [Online]. Available: https://html.spec.whatwg.org/multipage/server-sent-events.html.

[11] Mozilla Developer Network, *Using server-sent events — Web APIs*, Accessed: May 2026, 2025. [Online]. Available: https://developer.mozilla.org/en-US/docs/Web/ API/Server-sent_events/Using_server-sent_events.

[12] D. R. Seshadri et al., "Wearable sensors for monitoring the internal and external workload of the athlete," *npj Digital Medicine*, vol. 2, no. 1, p. 71, 2019. DOI: 10.1038/s41746-019-0149-2. [Online]. Available: https://www.nature.com/articles/s41746-019-0149-2.

[13] C. M. Dolson et al., "Wearable sensor technology to predict core body temperature: A systematic review," *Sensors*, vol. 22, no. 19, p. 7639, 2022. DOI: 10.3390/s22197639. [Online]. Available: https://www.mdpi.com/1424-8220/22/19/7639.

[14] J.-W. Kwon, "Athlete data sovereignty: Addressing the legal and policy gaps in sports technology," *Frontiers in Sports and Active Living*, vol. 7, p. 1 742 484, 2025. DOI: 10. 3389 / fspor . 2025 . 1742484. [Online]. Available: https : / / www . frontiersin . org/journals/sports-and-active-living/articles/10.3389/fspor.2025. 1742484/full.

[15] Bluetooth SIG, "Heart rate service specification, version 1.0," Bluetooth Special Interest Group, Tech. Rep., 2011, Accessed: May 2026. [Online]. Available: https://www . bluetooth.com/specifications/specs/heart-rate-service-1-0/.

[16] Bluetooth SIG, "Bluetooth core specification, version 5.3," Bluetooth Special Interest Group, Tech. Rep., 2021, Accessed: May 2026. [Online]. Available: https://www . bluetooth.com/specifications/specs/core-specification-5-3/.

[17] Melexis NV, "MLX90614 family: Single and dual zone infrared thermometer in TO-39," Melexis NV, Tech. Rep., 2019, Accessed: May 2026. [Online]. Available:

https: //www.melexis.com/en/documents/documentation/datasheets/datasheet-mlx90614.

[18] InvenSense, "MPU-6000/MPU-6050 six-axis (gyro + accelerometer) MEMS Motion-Tracking devices, rev. 3.4," InvenSense Inc. (TDK), Tech. Rep., 2013, Accessed: May 2026. [Online]. Available: https://invensense.tdk.com/wp-content/uploads/ 2015/02/MPU-6000-Datasheet1.pdf.

[19] Espressif Systems, "ESP32-C3 series datasheet," Espressif Systems, Tech. Rep., 2024, Accessed: May 2026. [Online]. Available: https://www.espressif.com/sites/ default/files/documentation/esp32-c3_datasheet_en.pdf.

SEMANTIC NAVIGATION STACK: HYBRID REASONING, CROSS-ROBOT MEMORY AND LLM AGENTS FOR MOBILE ROBOTS

STAICU Andrei-Alexandru, ABAZA Bogdan-Felician
Faculty: Industrial Engineering and Robotics (FIIR), Specialization: Applied Computer Science in Industrial Engineering, Year of study: IV, e-mail: andrei.staicu@stud.fiir.upb.ro

ABSTRACT: This paper presents the Semantic Autonomy Stack (SAS), a six-layer architecture (L0-L5) for semantic-aware indoor mobile robot navigation, spanning hardware abstraction, Nav2-based navigation execution, semantic perception via Angular Sector Fusion, hybrid deterministic-VLM reasoning with executive contract, agentic orchestration via OpenClaw and cross-robot persistent memory. The stack is implemented on AIONIS, a 4WD differential-drive robot built from scratch around Raspberry Pi 5 and ESP32. Experimental validation on three robot instances achieves 91.7% patrol completion and 97.1% waypoint success over 12 multi-waypoint patrols orchestrated via natural language, with 80% of decisions resolved deterministically without VLM invocation, on consumer-grade edge hardware without GPU.

KEYWORDS: semantic autonomy stack, hybrid VLM reasoning, agentic orchestration, ROS2/Nav2 Route Server, edge computing.

1. Introduction

Autonomous indoor mobile robots have reached maturity through the adoption of ROS 2 and the Nav2 stack [1], which provide reliable localization, global planning, and local control. Navigation remains, however, predominantly geometric: the robot moves toward metric coordinates without understanding the semantic meaning of the environment and without interpreting natural-language instructions. Components such as the Nav2 Route Server enable routing over topological graphs, paving the way for semantic information injection at the route level, yet they do not natively provide semantic perception or reasoning mechanisms. In environments such as university corridors, manufacturing workshops, or logistics spaces shared with human operators, this limitation becomes critical when the robot must respond to requests formulated at the intent level rather than the position level.

This paper proposes the Semantic Autonomy Stack (SAS), a unified stack with six functional layers (L0–L5) that extends classical geometric navigation all the way to agentic orchestration through natural language. Figure 1 illustrates the layered architecture: from the mobile platform (L0) and navigation execution via Nav2 (L1), through semantic perception with camera–LiDAR fusion (L2) and hybrid deterministic–VLM reasoning with an executive contract (L3), to the agentic mission interface via OpenClaw (L4) and operational intelligence with five-level persistent semantic memory (L5). Unlike existing approaches that treat perception, reasoning and orchestration as isolated modules, SAS integrates them into a layered architecture where each layer consumes the services of the one below and exposes a standardized interface to the one above. All six layers run entirely on consumer-grade Raspberry Pi 5 hardware, without a dedicated GPU. The stack has been experimentally validated on three instances of the AIONIS platform in a real corridor of the FIIR faculty.

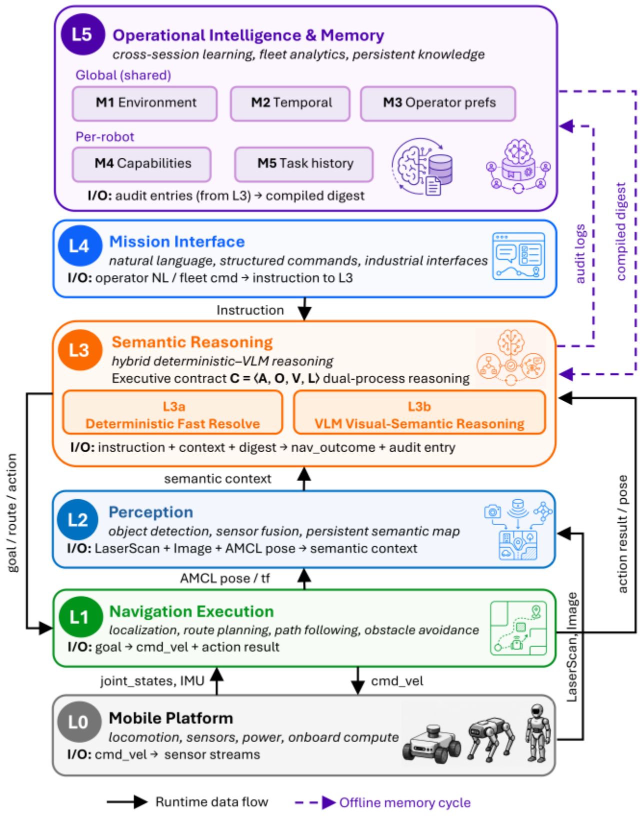

Fig. 1 Semantic Autonomy Stack (SAS) architecture: layers L0–L5 [8].

The contributions are structured as instantiations of the stack: the AIONIS hardware platform (Section 3) implements L0–L1; the lightweight semantic-aware navigation published in MDPI Sensors [6] covers L2–L3a by integrating Angular Sector Fusion with the Nav2 Route Server for context-aware routing (Section 4); and Section 5 presents the end-to-end experimental validation of layers L3–L5, including multi-waypoint orchestration across multi-robot platforms, achieving 91.7% patrol completion and 97.1% waypoint success. Section 2 reviews the state of the art, and Section 6 summarizes the conclusions.

2. State of the Art

The ROS 2/Nav2 stack is the de facto foundation for autonomous indoor mobile robot navigation [1], providing localization (AMCL), predictive control (MPPI), and global planning (SmacPlanner), but operating on binary occupancy maps without semantic understanding. Recent works extend perception through semantic maps that fuse YOLO detections with LiDAR measurements [2], yet typically stop at map annotation without integrating semantic information over topological graphs toward the planner. Our published article [6] addresses precisely this integration, connecting ASF perception to the Nav2 Route Server for context-aware routing on edge hardware. On the reasoning side, Vision-Language models have been integrated into navigation for natural-language instruction interpretation [3], including in outdoor scenarios with long-term causal planning [5]. Current systems, however, suffer from latencies of 2–9 seconds on consumer hardware and from inter-session amnesia. Dual-process approaches propose separating fast reasoning from deliberative reasoning [4], but published implementations rely on reinforcement-learning-trained classifiers, requiring labeled data and periodic updates. On the orchestration side, LLM-ROS frameworks such as ROSClaw [7] introduce model-agnostic executive layers, but validations focus on single instructions. Real patrol missions involve multiple waypoints, operational awareness, and error recovery, all capabilities validated experimentally in this work through Protocol D on multi-waypoint patrols coordinated via natural language with persistent cross-robot memory [8].

3. The AIONIS Platform (SAIM Xplorer C): Layers L0–L1

The AIONIS platform is a 4WD differential-drive mobile robot designed and built entirely by the author as part of student research activities. The mechanical chassis is constructed from goBILDA components, with four wheels driven by DC motors equipped with quadrature encoders. Three instances of the platform have been built within the FIIR faculty robotics team: two earlier configurations (Xplorer-A and Xplorer-B) use RoboClaw 2×15A drivers with 223 rpm encoders, while the most recent iteration (Xplorer-C), built from scratch by the lead author, uses two L298N modules coordinated by an ESP32 microcontroller via UART packet serial, with 178 rpm Hall encoders. The existence of multiple platforms with intentional hardware differences serves to validate the robustness of the cross-robot software. Power is supplied from a 12 V Li-ion battery pack with an integrated BMS, and the RPi5 receives 5 V via USB Power Delivery.

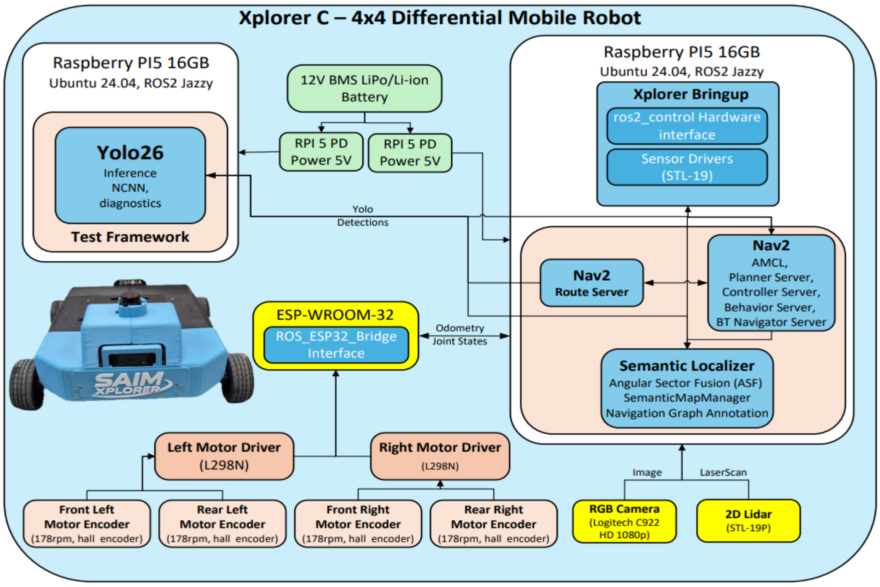

Fig. 2. Hardware architecture of the AIONIS platform (Xplorer C): the dual-RPi5 configuration with ESP32 for motor control and the sensor suite (C920 camera, STL-19P LiDAR).

The compute system is distributed across two architectural configurations. The two platforms built earlier within the FIIR faculty robotics teams (Xplorer-A and Xplorer-B) use a single-board configuration with a single 16 GB Raspberry Pi 5 running the Nav2 stack, YOLO26n perception, and the semantic pipeline simultaneously at approximately 85% CPU utilization; the experiments from [6] were validated on these platforms. The Xplorer-C platform, built from scratch by the lead author, adopts a dual-board configuration: a second RPi5 connected via direct Ethernet is dedicated to YOLO26n inference through NCNN [9], reducing the navigation processor load to approximately 48% and serving as the primary platform for Protocol D. The sensor suite is identical across all platforms: a Logitech C920 camera at 640×480 and a 2D STL-19P LiDAR at 360° and 10 Hz. At the software level, layer L0 integrates a custom ROS 2–ESP32 bridge [11], derived from ros_arduino_bridge [10] and adapted for the packet serial protocol, as well as a ros2_control hardware interface with diff_drive_controller [12] for differential kinematics abstraction, configured via a dedicated bringup package for each variant. Layer L1 is based on Nav2 and the Nav2 Route Server, fully parameterized: AMCL for localization, SmacPlannerHybrid for global planning, MPPI for local control, and Route Server for routing over the semantic topological graph. The entire configuration is launched via a single launch file that automatically parameterizes the differences between platforms, allowing the same software stack to run on any Xplorer variant without code modifications.

4. Semantic Perception and Routing: Layer L2

The first component of layer L2, published in MDPI Sensors [6], is Angular Sector Fusion (ASF), a deterministic geometric method that fuses YOLO26n detections with 2D LiDAR measurements by projecting the bounding box onto an angular sector and estimating distance using the 25th percentile. Sensor parameters are extracted at runtime from ROS 2 topics and the URDF, ensuring cross-platform portability. The full pipeline (Fig. 3) covers seven stages from detection to persistence in the adaptive GeoJSON semantic map, with an overhead below 1 ms per detection and 2–5% CPU at 3 Hz.

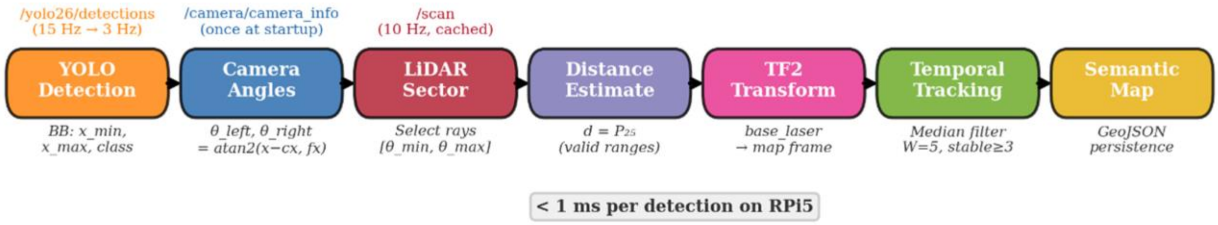

Fig. 3. Angular Sector Fusion (ASF) pipeline: the seven processing stages with overhead below 1 ms per detection on RPi5 [6].

The second component is the GeoJSON semantic map which is integrated into the Nav2 Route Server by automatically annotating topological graph edges with proximity-weighted penalties. Adaptive routing uses two scoring plugins (DistanceScorer and PenaltyScorer, weight 5:1) and a reactive replanning mechanism that recomputes the route every 2 seconds when penalties exceed the threshold of 2.0. The layer L2 implementation is structured into two software packages developed by the authors: yolo26_node for YOLO26n inference via NCNN and detection publishing, and semantic_localizer for the ASF pipeline, GeoJSON map persistence, and graph annotation, available open-source [13]. Validation was incremental: a 7-node graph with two alternative routes (Fig. 4a) confirmed rerouting upon obstacle detection (Fig. 4b); the graph extended to 24 nodes on FIIR floor 2 (Fig. 4c) validated the complete semantic map (Fig. 4d). Quantitative results are reported in [6].

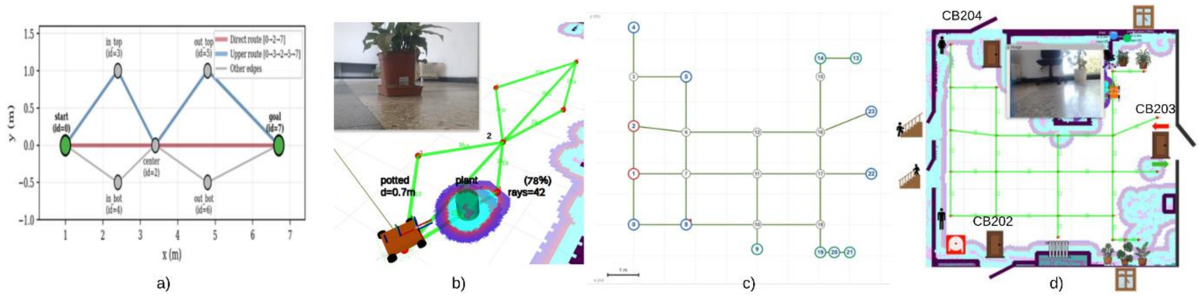

Fig. 4. Incremental validation: (a) 7-node topology [6]; (b) ASF detection in RViz (plant, d=0.7 m) [6]; (c) extended 24-node topology [8]; (d) complete semantic map in Rviz [8].

5. Hybrid Semantic Reasoning: Layer L3

Natural-language instructions range from explicit requests such as "go to lab CB204" to open-ended formulations such as "take me somewhere I can sit and relax." A fully deterministic approach cannot cover this spectrum, and systematic VLM invocation introduces a 2.6× overhead compared to the deterministic path (45.9 s vs. 121.0 s per waypoint, as measured in Protocol D). Layer L3 resolves this trade-off through a dual-process pipeline (Fig. 5): a fast deterministic path (L3a) and a deliberative path (L3b), activated sequentially.

The L3a path processes the instruction through a cascade of seven deterministic steps, each with a distinct matching criterion: M3 preference (Jaccard similarity above 0.6), explicit node identifier, node name match, object identifier match, semantic attribute scoring, unique class match, and combined proximity with class. The first step that yields an unambiguous resolution immediately returns the target node with no additional latency (below 0.1 ms). In Protocol D, 80% of the 35 waypoints were resolved via L3a, consistent with 88% in prior sessions A–C. When no step in the cascade produces a resolution, the pipeline escalates to L3b: an image is acquired from the camera via an HTTP bridge, a structured prompt is constructed that includes the graph, visible points of interest, and memory context, and the VLM model (Qwen 3.5:4b served via Ollama with num_ctx 16384 on the external workstation) returns the selected target node. L3b latency ranges from 2 to 9 seconds. Both paths converge at the executive contract (validate_action), which filters each decision through four categories: Approve enables execution, Override applies a deterministic correction to a suboptimal decision, Veto blocks actions that violate safety constraints, and Log records the decision in the audit trail. After validation, the action is dispatched to Nav2 (ComputeRoute and FollowPath), followed by a visual confirmation at the point of interest. The entire layer L3 is implemented in vlm_navigator_node, a model-agnostic ROS 2 node: the VLM interface is abstracted through a configurable HTTP endpoint, allowing Qwen 3.5:4b to be replaced by any other Ollama-compatible model without code modifications. The source code, including the L3a cascade, the L3b pipeline, and the executive contract, is available open-source [14].

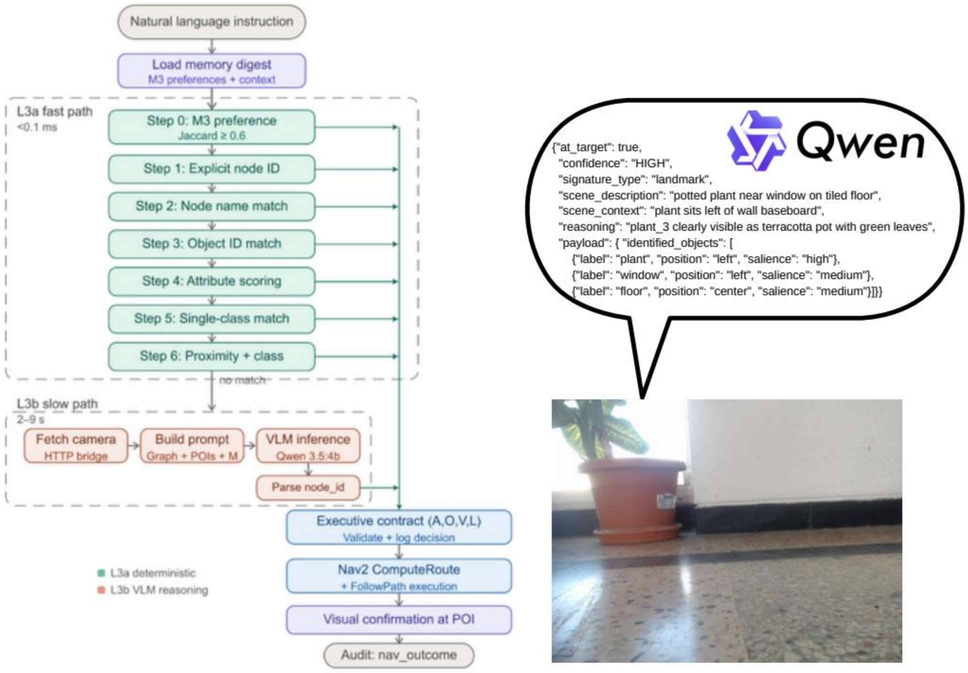

Fig. 5. L3 hybrid reasoning pipeline: the seven-step deterministic L3a cascade, fallback to the L3b VLM, and convergence at the executive contract ⟨A, O, V, L⟩ [8].

6. Agentic Interface, Operational Memory, and End-to-End Validation: Layers L4–L5

Layer L4 exposes the SAS stack through an agentic interface based on OpenClaw, an LLM agent (minimax-m2.7 served via Ollama) configured via SOUL.md. Three interaction modalities were implemented (Fig. 6c–e): a direct localhost interface, integration through the Claude App via MCP Server, and a Telegram interface, all enabling operation exclusively through natural language, with no ROS 2 knowledge required. The patrol_executor module parses the instruction, recognizes multi-stop connectors, and produces a structured PatrolPlan verifiable before execution. The orchestration loop executes for each waypoint: L3a/L3b resolution, validation via the executive contract, Nav2 navigation, final alignment, and visual confirmation; failure at a single waypoint does not abort the patrol.

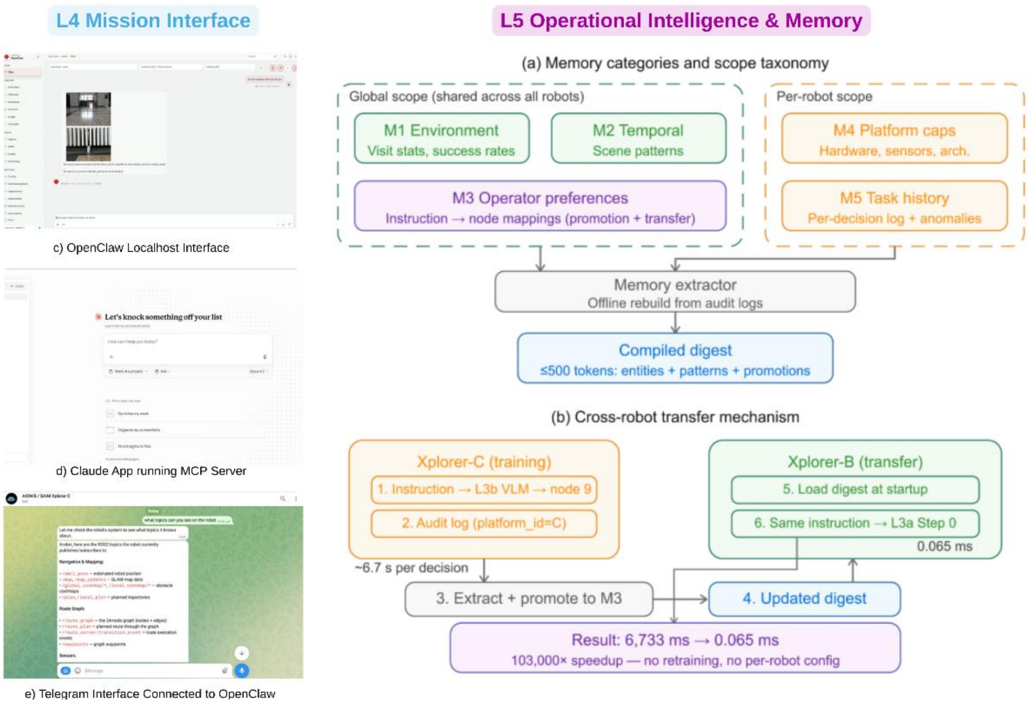

Fig. 6. Layers L4–L5 [8]: (a) M1–M5 memory taxonomy with global/per-robot partitioning; (b) cross-robot transfer with 103,000× speedup; (c) OpenClaw localhost interface; (d) Claude App with MCP Server; (e) Telegram interface connected to OpenClaw.

Layer L5 maintains five levels of persistent semantic memory, partitioned between a global scope and a per-robot scope (Fig. 6a). At the global level, M1 stores visit statistics and success rates, M2 captures temporal scene patterns, and M3 persists operator preferences as instruction-to-node mappings, promoted from prior VLM decisions. At the per-robot level, M4 describes platform-specific capabilities, and M5 retains the complete decision and anomaly log. An offline memory extractor reconstructs from audit logs a compressed summary of at most 500 tokens, loaded at startup. The cross-robot transfer mechanism (Fig. 6b) allows a preference learned via VLM on Xplorer-C (6733 ms) to be promoted into M3 and resolved deterministically on Xplorer-B through step 0 of the L3a cascade in 0.065 ms, a speedup factor of 103,000× without retraining. End-to-end validation through Protocol D demonstrated results across three dimensions: D1, 12 patrols with 35 waypoints, 97.1% waypoint success and 91.7% patrol completion (Fig. 7a), with 80% L3a resolution (Fig. 7b) and a 2.6× VLM overhead (Fig. 7c–d); D2, diagnostic accuracy of 94% with emergent autonomous detection of connection loss; D3, analytics accuracy of 88%. Table 1 summarizes the results, including zero operator interventions.

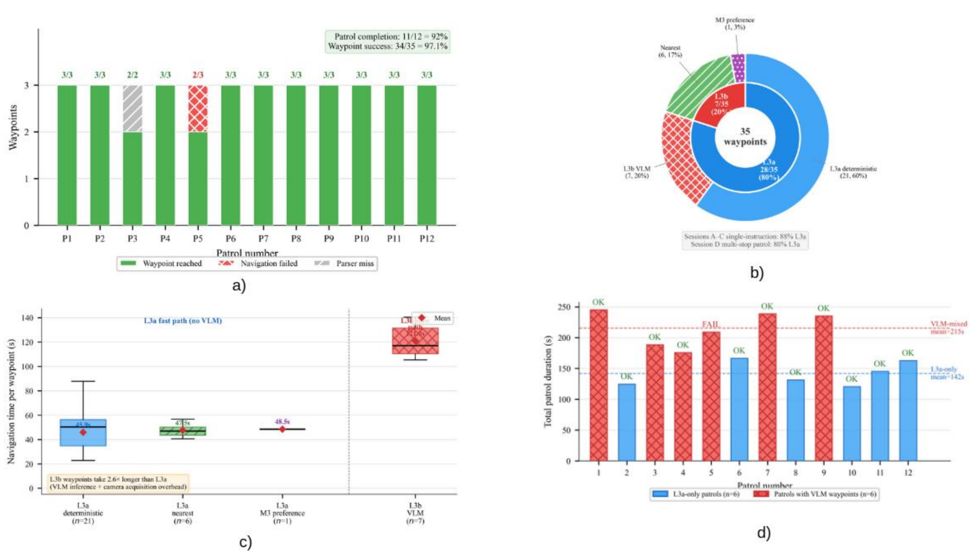

Fig. 7. Protocol D results: (a) waypoint success per patrol; (b) distribution of resolution methods; (c) time per waypoint by method; (d) total patrol duration.

End-to-end validation was carried out through Protocol D, structured across four experimental dimensions and two query dimensions. D1 (Patrol completion): 12 patrols with 35 waypoints, 97.1% waypoint success and 91.7% patrol completion (Fig. 7a). The sole patrol failure was caused by a destination absent from the graph, and the sole waypoint lost at parsing resulted from the unhandled connector "and finish at". D2 (Method distribution): the method distribution (Fig. 7b) confirms 80% L3a resolution without VLM, consistent with 88% on single instructions in sessions A–C. D3 (Navigation time): the per-method time comparison (Fig. 7c) shows a 2.6× overhead for the VLM path (121.0 s vs. 45.9 s per waypoint). D6 (Patrol duration): at the full-patrol level (Fig. 7d), the mean duration is 142 s for purely L3a patrols versus 215 s for those with at least one VLM waypoint. Diagnostic accuracy (D2-query) was 94% across 8 status queries, with emergent autonomous detection of connection loss, and analytics accuracy (D3-query) was 88% across 8 queries on audit logs. Table 1 summarizes the results, including zero operator interventions. The complete experimental dataset, raw logs, and evaluation scripts for Protocol D are publicly available [15].

Table 1. Summary of Protocol D Results

Metric	Value	Note
Completed patrols	11/12 (91.7%)	CI 95% [0.615, 0.998]
Waypoint success	34/35 (97.1%)	CI 95% [0.851, 0.999]
L3a resolution (without VLM)	28/35 (80%)	Consistent with 88% in A–C
Mean patrol duration	178.7 ± 43.1 s	12 patrols
Diagnostic accuracy	7/8 (94%)	+1 partial
Analytics accuracy	6/8 (88%)	+2 partial
Autonomous crash detection	Yes	Patrols 13–15, unplanned
Operator interventions	0	All interactions autonomous

7. Conclusions

This paper has presented a complete semantic autonomy stack for indoor mobile robots, developed along three complementary axes: the AIONIS hardware platform built entirely from scratch, lightweight semantic navigation based on Angular Sector Fusion and the Nav2 Route Server, and the Protocol D agentic interface for multi-waypoint orchestration through natural language. Protocol D demonstrated the end-to-end operability of the semantic stack under realistic multi-stop mission conditions, achieving a 91.7% patrol completion rate and a 97.1% waypoint success rate with zero operator interventions across the 12 executed patrols. The fact that 80% of multi-stop decisions were resolved deterministically is consistent with the 88% previously reported on single instructions, confirming the robustness of hybrid reasoning in more complex execution contexts.

A valuable secondary result is the autonomous detection of context-server unavailability during stress testing, which demonstrated that the OpenClaw agent possesses sufficient operational awareness to refuse unsafe actions without human supervision. Immediate research directions include robust parsing of natural-language instructions for atypical connectors ("and finish at"), scaling to patrols with five or more waypoints, cross-robot coordination on the same patrol via shared memory, validation of the framework on embedded GPU hardware such as the NVIDIA Jetson Orin to eliminate the dependency on the external workstation, and extension of the evaluation to navigation graphs covering multiple faculty floors.

8. References

[1]. Macenski, S., Foote, T., Gerkey, B., Lalancette, C. and Woodall, W. (2022), "Robot Operating System 2: Design, Architecture, and Uses in the Wild", Science Robotics, vol. 7, eabm6074.

[2]. Alqobali, R., Alnasser, R., Rashidi, A., Alshmrani, M. and Alhmiedat, T. (2024), "A Real-Time Semantic Map Production System for Indoor Robot Navigation", Sensors, vol. 24, no. 20, p. 6691.

[3]. Alqobali, R., Alshmrani, M., Alnasser, R., Rashidi, A., Alhmiedat, T. and Alia, O.M.D. (2024), "A Survey on Robot Semantic Navigation Systems for Indoor Environments", Applied Sciences, vol. 14, no. 1, p. 89.

[4]. Lee, J., Shin, H. și Ko, J. (2026), "A Dual-Process Architecture for Real-Time VLM-Based Indoor Navigation", arXiv:2601.21506.

[5]. Duan, H. et al. (2026), "CausalNav: A Long-term Embodied Navigation System for Autonomous Mobile Robots in Dynamic Outdoor Scenarios", IEEE Robotics and Automation Letters.

[6]. Abaza, B.F., Staicu, A.-A. and Doicin, C.V. (2026), "Lightweight Semantic-Aware Route Planning on Edge Hardware for Indoor Mobile Robots", Sensors, vol. 26, no. 7, p. 2232.

[7]. Cardenas, J. et al. (2026), "ROSClaw: OpenClaw ROS 2 Framework for Agentic Robot Control", arXiv:2603.26997.

[8]. Abaza, B.F., Staicu, A.-A. and Doicin, C.V. (2026), "A Semantic Autonomy Framework for VLM-Integrated Indoor Mobile Robots: Hybrid Deterministic Reasoning and Cross-Robot Adaptive Memory", arXiv:2605.02525.

[9]. Tencent (2024), "NCNN: A High-Performance Neural Network Inference Framework Optimized for the Mobile Platform", https://github.com/Tencent/ncnn.

[10]. Newans, J. (2024), "ros_arduino_bridge: ROS 2 Arduino Bridge", https://github.com/joshnewans/ros_arduino_bridge.

[11]. Abaza, B.F. (2026), "ROS_ESP32_Bridge: Customized ROS 2-ESP32 Communication Bridge", https://github.com/bogdan-abaza/ROS_ESP32_Bridge.

[12]. ROS 2 Control Contributors (2026), "diff_drive_controller", https://control.ros.org/jazzy/doc/ros2_controllers/diff_drive_controller/doc/userdoc.html.

[13]. Abaza, B.F. and Staicu, A.-A. (2026), "nav2-semantic-route-server: Semantic-Aware Route Planning for Nav2", https://github.com/bogdan-abaza/nav2-semantic-route-server.

[14]. Abaza, B.F. and Staicu, A.-A. (2026), "nav2-sas-vlm-memory: Hybrid VLM Reasoning and Semantic Memory for Nav2", https://github.com/bogdan-abaza/nav2-sas-vlm-memory.

[15]. Staicu, A.-A. (2026), "SCSS2026-ProtocolD: Experimental Dataset and Evaluation Scripts for Protocol D", https://github.com/AlexYellow01/SCSS2026-ProtocolD.

Autonomous Differential Mobile Robot with AprilTag-Based Multi-Dock Architecture in ROS 2 for Intralogistics

DUMITRESCU Andy, ABAZA Bogdan-Felician
Faculty: Industrial Engineering and Robotics, Specialization: Applied Computer Science in Industrial Engineering, Year of study: IV, e-mail: andy.dumitrescu@stud.fiir.upb.ro

ABSTRACT: This paper presents the design, integration, and experimental validation of a four-wheel differential-drive autonomous mobile robot built on the ROS 2 Jazzy framework with Nav2 for indoor intralogistics applications. The platform uses a Raspberry Pi 4 communicating via USB-Serial with an ESP32 microcontroller running a 30 Hz PID velocity loop for four DC gear-motors. An LD19 2D LiDAR enables SLAM-based mapping and autonomous navigation, while a USB camera provides AprilTag-based visual fiducial detection for a scalable multi-dock architecture using opennav_docking. The chassis and enclosure are custom-designed in SolidWorks and manufactured via FDM 3D printing in PLA. Experimental results demonstrate reliable autonomous docking and multi-waypoint navigation in a mapped indoor environment.
KEYWORDS: autonomous mobile robot, ROS 2, autonomous docking, AprilTag, Nav2

1. Introduction

Autonomous mobile robots (AMRs) are increasingly deployed in industrial intralogistics for material transport and flexible manufacturing. Unlike automated guided vehicles (AGVs), AMRs use onboard perception and planning to navigate dynamically [1]. ROS 2 and Nav2 have become the standard middleware and navigation framework for such systems [2], while the recent opennav_docking package [4] provides a generalized docking solution. However, practical implementations documenting full multi-station docking integration with external AprilTag detection remain scarce.

This paper presents a custom-built differential-drive AMR for indoor intralogistics. The contributions are: (1) end-to-end integration of a functional AMR from commercial components within ROS 2 Jazzy / Nav2, (2) a scalable multi-dock architecture with automatic dock identification switching via ROS 2 parameter configuration, enabling extension to arbitrary docking stations without manual reconfiguration, and (3) experimental validation across five dock stations configured for intralogistics material flow.

2. State of the Art

ROS 2 Jazzy provides a mature middleware for distributed robotic applications [1], while Nav2 offers a modular navigation architecture with behavior tree coordination, path planning, and costmap-based obstacle avoidance [2]. The TurtleBot series [3] and the Honeybee platform from Open Navigation [4] serve as reference implementations, though detailed documentation of the integration challenges encountered when combining custom hardware with Nav2 remains limited.

The AprilTag library enables robust 6-DOF pose estimation of planar fiducial markers from monocular cameras [5]. The opennav_docking framework provides a plugin-based docking server supporting both charging and non-charging dock types with a dock database for managing multiple stations [6]. For embedded motor control, microcontroller bridges implement closed-loop PID velocity regulation communicating with the main computer via serial protocols [7][8]. The slam_toolbox package provides optimized 2D pose-graph SLAM for occupancy grid mapping [9].

3. System Architecture

3.1 Hardware Architecture

The platform uses a two-tier computing architecture. A Raspberry Pi 4 (8 GB RAM, Ubuntu 24.04, ROS 2 Jazzy) handles perception, localization, navigation, and mission management. An ESP32 WROOM-32 microcontroller serves as a serial bridge for real-time PID motor control at 30 Hz, communicating over USB-Serial at 115200 baud [8]. Four JGB37-520 DC gear-motors (12V, 56:1 ratio, quadrature encoders, ~2400 ticks/rev) are driven by two L298N dual H-bridge modules in a skid-steer differential configuration. The wheels measure 75 mm in diameter with 410 mm separation.

Perception consists of an LD19 2D LiDAR for SLAM and obstacle detection, and a USB camera (640x480, MJPEG, 10 fps) for AprilTag fiducial detection, calibrated with the ROS 2 camera_calibration package [13][10]. Power is supplied by a 3S Li-Ion battery (12V, 15000 mAh) with a step-down converter for the 5V computing units.

3.2 Software Architecture

The software stack runs on ROS 2 Jazzy with two main packages: a bringup package containing the URDF/Xacro robot description, ros2_control parameters, and sensor launch files, and a navigation package with the Nav2 configuration, behavior tree XMLs, and docking server parameters.

The ros2_control framework [7] manages hardware abstraction through a custom plugin that communicates with the ESP32 over serial. The diff_drive_controller computes wheel velocities from TwistStamped commands and publishes odometry, while the joint_state_broadcaster feeds the robot state publisher for TF tree computation. The URDF describes the full kinematic chain: base_link, chassis, four wheel joints, the LiDAR mount (base_laser, 180 mm forward), and the camera mount (camera_link with optical frame convention).

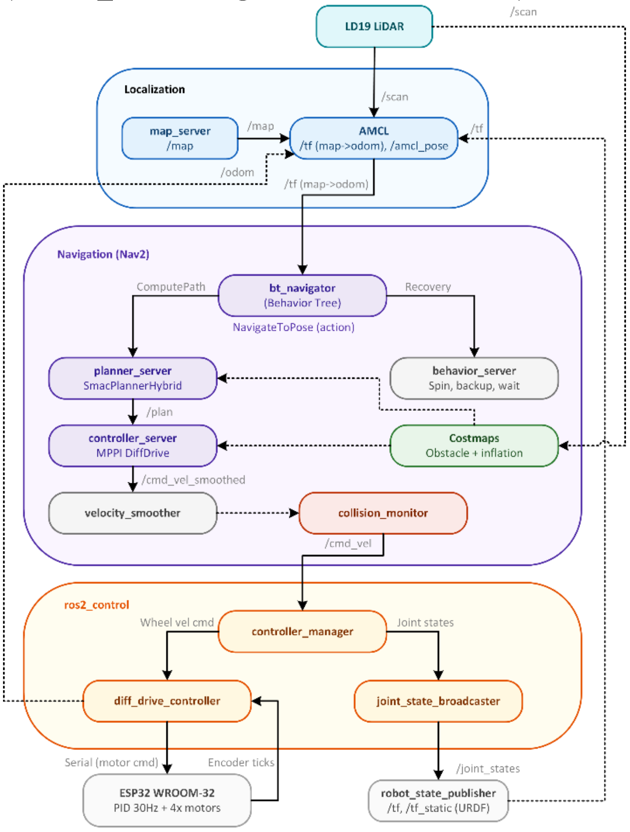

Fig. 1. ROS 2 software architecture: navigation stack, nodes, topics, and hardware interface.

4. Navigation and Docking System

4.1 SLAM and Autonomous Navigation

SLAM is performed using slam_toolbox [9], which builds an occupancy grid map from LD19 LiDAR scans during teleoperated exploration. For autonomous navigation, Nav2 [2] loads the pre-built map via map_server and uses AMCL particle filtering for localization [15]. The behavior tree navigator coordinates [16] path planning, local control with costmap-based obstacle avoidance, and recovery behaviors. Multi-waypoint missions are executed through both the RViz2 interface and the nav2_simple_commander Python API.

The planner uses SmacPlannerHybrid with Reeds-Shepp motion model for kinematically feasible paths considering the robot footprint (460 x 440 mm). The local controller uses MPPI (Model Predictive Path Integral) [14] with a DiffDrive motion model, evaluating 500 trajectory samples per cycle. A velocity smoother and collision monitor provide final command filtering, with the collision monitor reducing velocity proportionally to maintain at least 1.5 seconds to collision.

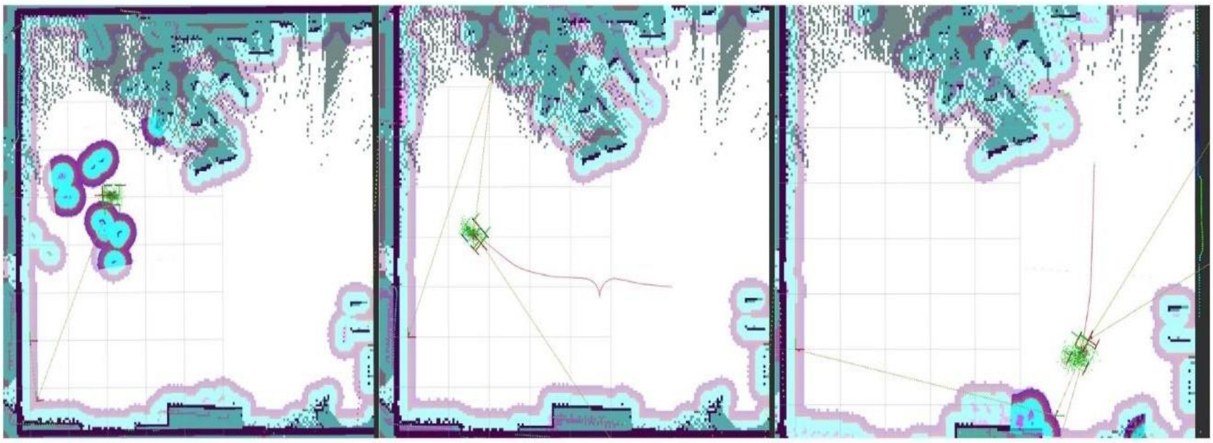

Fig. 2. SLAM-generated map of the test environment with a planned navigation path

4.2 Multi-Dock Architecture

The docking system builds on opennav_docking [4][6], using AprilTag markers (tag36h11, 150 mm) at each station detected by apriltag_ros, which publishes 6-DOF pose transforms on the TF tree [5][12]. The system currently operates with five dock stations: one home/parking position (tag ID 1, SimpleNonChargingDock) and four intralogistics stations serving as material input and output points (tag IDs 2 through 5).

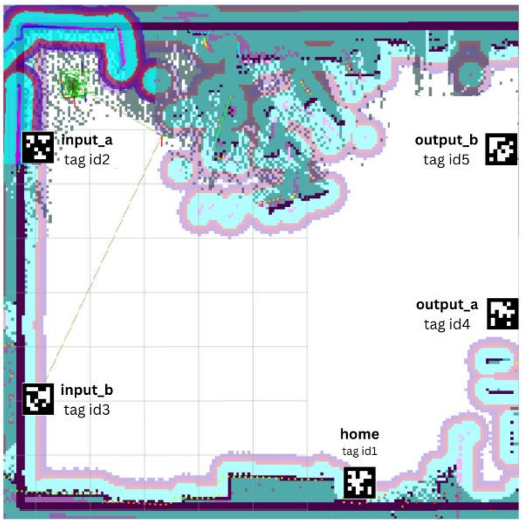

Fig. 3. Physical layout of the five AprilTag dock stations in the test environment

The primary contribution in this domain is the dock pose publisher node, which solves the problem of coordinating external pose detection with the docking server across multiple stations. Before each docking action, the mission executor sets the dock_tag_id parameter on the publisher via the ROS 2 SetParameters service, selecting the corresponding AprilTag TF frame from a configuration mapping. The publisher then tracks only the specified tag and publishes its filtered 2D pose on /detected_dock_pose. This mechanism operates transparently regardless of which station is targeted, and adding a new dock requires only three configuration additions: one entry in the tag mapping, one entry in the dock database YAML, and one plugin declaration in the Nav2 parameters.

The docking_server applies exponential smoothing to the external detection pose before driving the robot via a graceful motion controller. A staging pose in front of each dock ensures perpendicular approach. The external_detection_translation_x parameter defines the stopping distance relative to the tag. Staleness checks and position jump detection ensure robust operation under intermittent tag visibility.

Each dock station is defined with an optional approach point in the dock database, specifying a favorable pre-staging waypoint (x, y, yaw) from which the robot approaches the dock along a short trajectory. The mission executor navigates to this point via the NavigateToPose action before initiating the docking sequence, reducing path planner artifacts on long-distance approaches.

The dock database is maintained in a dedicated YAML file, decoupled from navigation parameters. The architecture supports a higher-level mission dispatcher that coordinates navigation and docking sequences for material transport between input and output stations.

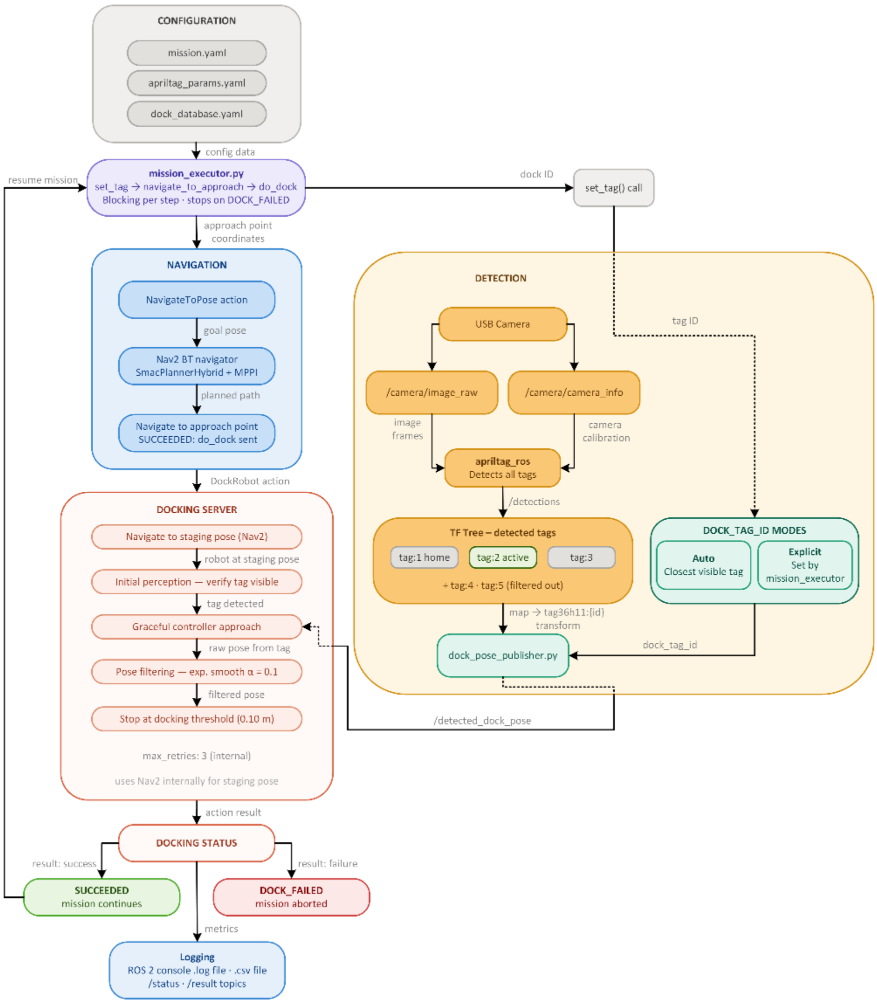

Fig. 4. Multi-dock architecture

Table 1 summarizes the key docking controller parameters determined through iterative tuning. The filter coefficient (filter_coef) controls exponential smoothing of the detected tag pose, balancing responsiveness against measurement noise from the USB camera. The staging offset and external detection translation together define the approach geometry: the robot first navigates to a staging pose 0.80 m in front of the dock, then the docking controller drives toward the tag until reaching 0.35 m from its surface. The graceful controller gains (k_phi, k_delta) govern angular and lateral correction during the final approach phase, with values tuned below the Nav2 defaults (3.0, 2.0) to accommodate the lower detection rate of the USB camera compared to depth sensors.

Table 1. Docking system configuration parameters

Parameter	Value	Description
filter_coef	0.1	Exponential smoothing for pose filtering
docking_threshold	0.10 m	Distance to consider docking complete
staging_x_offset	-0.80 m	Staging pose offset in front of dock
external_detection_translation_x	-0.35 m	Stopping distance from AprilTag
external_detection_timeout	30.0 s	Timeout for external pose detection
v_linear_max	0.10 m/s	Max linear velocity during approach

v_angular_max	0.85 rad/s	Max angular velocity during approach
k_phi	2.2	Graceful controller angular gain
k_delta	1.0	Graceful controller distance gain
controller_frequency	30.0 Hz	Docking controller loop rate
AprilTag family	tag36h11	Visual fiducial marker family
Tag size	0.150 m	Physical printed tag dimension
Camera resolution	640 x 480 px	Resolution matching calibration
Camera format	MJPEG (mjpeg2rgb)	Pixel format for reduced bandwidth

5. Experimental Results

5.1 Embedded Motor Control Validation

The ESP32 firmware implements independent PID velocity control for each motor at 30 Hz using a four-term controller with proportional (Kp = 140), integral (Ki = 100), derivative (Kd = 20), and output offset (Ko = 20) gains. Full quadrature decoding of the JGB37-520 encoders provides approximately 2400 ticks per revolution, a 4x improvement over single-channel reading that required complete PID retuning due to the increased resolution. Per-motor calibration factors compensate for mechanical and electrical variations between motor units and are persisted in EEPROM, allowing the controller to maintain balanced wheel velocities without runtime recalibration. The experimentally determined factors (C1 = 0.99, C2 = 1.00, C3 = 0.84, C4 = 0.82) reveal significant manufacturing variability of up to 18% between motors of the same model, underscoring the necessity of individual calibration in multi-motor differential platforms. The resulting controller achieves stable velocity tracking without oscillation across the full operating speed range, with the calibration factors ensuring that commanded linear and angular velocities translate to symmetric wheel behavior at the differential drive level.

5.2 Navigation Performance

The SLAM-generated map (Fig. 5) was validated against physical measurements of the test environment (an open indoor layout). The robot performed multi-waypoint navigation missions using both the RViz2 waypoint follower and programmatic sequences via nav2_simple_commander. Nav2 was configured with AMCL localization and costmap parameters tuned for the environment. Recovery behaviors (spin, backup) were triggered occasionally and resolved without operator intervention.

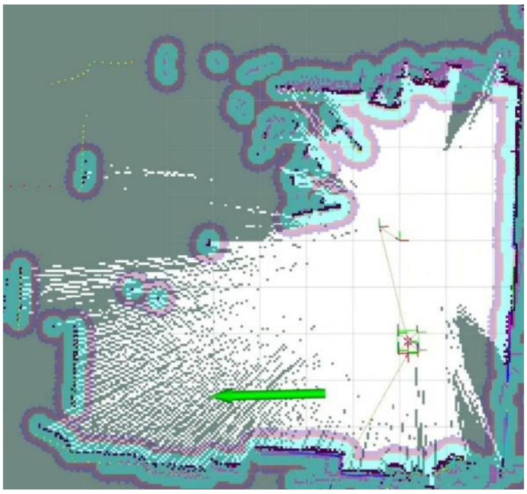

Fig. 5. SLAM mapping during teleoperated exploration: occupancy grid construction with LiDAR scan data, costmap inflation layers, and planned navigation path visible in RViz2

AMCL localization used a DifferentialMotionModel with 3500 maximum particles and a likelihood field laser model. The costmap inflation radius was set to 0.39 m (exceeding the circumscribed robot radius of 0.32 m) with a cost scaling factor of 8.0, providing a gradient that balances obstacle avoidance with passage traversability. The system operated reliably on a Raspberry Pi 4 with typical CPU utilization around 50% across four cores when all navigation, perception, and docking nodes were active simultaneously.

5.3 Docking Performance

The experimental campaign comprised 54 docking trials across 5 stations [11], yielding an overall success rate of 85.2% (Wilson 95% CI: 73.4-92.3%). Per-station rates ranged from 73% (output_b) to 100% (home), with undocking perfectly reliable at 14/14. Position repeatability was the system's strongest result: intra-station standard deviations remained below 0.05 m and angular repeatability averaged 4.4 degrees, confirming consistent controller convergence regardless of approach trajectory. The median position offset of 0.617 m represents a systematic, mechanically compensable distance between base_link and the tag frame, not contact inaccuracy.

Failure analysis identified navigation to the staging pose (FAILED_TO_STAGE, error 903) as the dominant failure mode (4 of 8 failures), confirming that the Nav2 path planner, not the docking controller, is the primary reliability bottleneck. Tag detection failures (error 904) occurred exclusively at output_b, indicating a station-specific environment issue. Multi-dock missions (4 sequential docks per run) completed in 3 of 5 valid attempts, with all mid-mission failures attributable to the same individual station weaknesses. No correlation was found between docking duration and position error ($r = -0.031$, $p = 0.839$), confirming that recovery maneuvers do not degrade final accuracy. The approach-point mechanism was further validated through alternative starting position trials, which showed equal or better success rates than home-start trials for every station (Fisher's exact, $p > 0.14$).

The docking duration showed high variance across stations, with median times ranging from 37 s (output_b) to 120 s (home). The primary contributor to extended docking times was the navigation phase to the staging pose, where the SmacPlannerHybrid path planner occasionally generated Reeds-Shepp curves requiring forward-reverse maneuvers near the goal. This behavior was mitigated through planner parameter tuning (analytic_expansion_ratio reduced to 0.5, reverse_penalty increased to 3.0) and the introduction of approach points, predefined waypoints in favorable positions from which the robot approaches each dock along a short, predictable trajectory. Full experimental data including per-trial logs and analysis scripts are available in the companion repository [11].

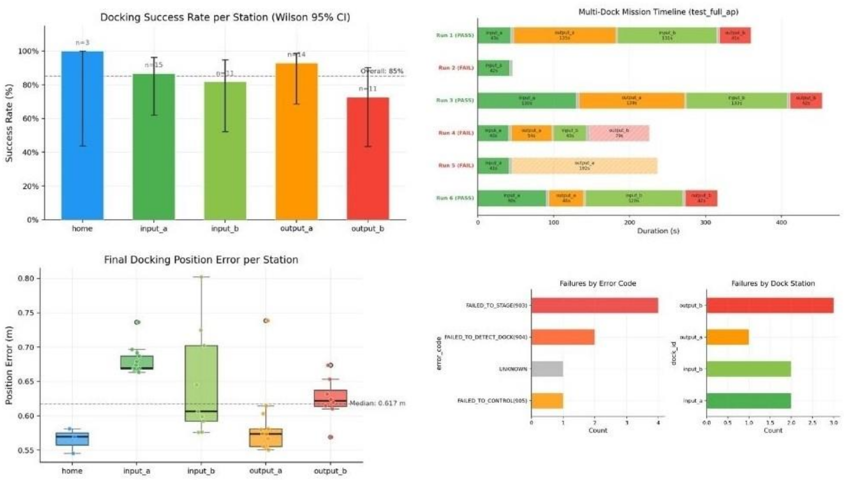

Fig. 6. Multi-station docking performance: success rates, position accuracy, mission execution and failure analysis across 54 trials.

6. Conclusions

This paper presented a low-cost autonomous mobile robot for indoor intralogistics, integrating custom hardware, embedded PID motor control, ROS 2 Jazzy navigation with Nav2, and AprilTag-based autonomous docking into a single functional platform. The primary contribution is the multi-dock architecture built on opennav_docking, where a dock pose publisher receives the target station identifier via ROS 2 parameter configuration from the mission executor and switches the tracked AprilTag frame accordingly. The system currently operates with five dock stations and scales to additional stations through three configuration entries per dock.

Practical integration challenges addressed include bandwidth optimization of the wireless DDS link through camera pixel format selection, and consistent camera calibration management for accurate fiducial pose estimation. Future work includes a mission dispatcher for automated material transport coordination between input and output stations, battery monitoring integration via ROS 2 BatteryState for autonomous power management, and scaling the system to more complex multi-station layouts with optimized routing strategies.

7. Bibliography

[1]. Macenski, S., Foote, T., Gerkey, B., Lalancette, C. and Woodall, W. (2022), "Robot Operating System 2: Design, Architecture, and Uses in the Wild", Science Robotics, vol. 7, no. 66, eabm6074.

[2]. Macenski, S., Martin, F., White, R. and Clavero, J.G. (2020), "The Marathon 2: A Navigation System", Proceedings of the 2020 IEEE/RSJ International Conference on Intelligent Robots and Systems (IROS), Las Vegas, NV, USA, pp. 2718-2725.

[3]. ROBOTIS (2023), TurtleBot3 e-Manual, https://emanual.robotis.com/docs/en/platform/turtlebot3/overview/.

[4]. Macenski, S. (2024), opennav_docking: Nav2 Compatible Docking Task Server, Open Navigation LLC / NVIDIA, https://github.com/open-navigation/opennav_docking.

[5]. Olson, E. (2011), "AprilTag: A Robust and Flexible Visual Fiducial System", Proceedings of the IEEE International Conference on Robotics and Automation (ICRA), Shanghai, China, pp. 3400-3407.

[6]. Macenski, S. and Jambrecic, I. (2023), "Open Navigation's Nav2 Docking Framework", Proceedings of ROSCon 2023, New Orleans, LA, USA.

[7]. Bischoff, R., Huber, W., et al. (2022), ros2_control: A Generic and Simple Control Framework for ROS 2, https://control.ros.org/.

[8]. Newans, J. (2023), ros_arduino_bridge for ROS 2, GitHub repository, https://github.com/joshnewans/ros_arduino_bridge.

[9]. Macenski, S. and Jang, I. (2021), "SLAM Toolbox: SLAM for the dynamic world," Journal of Open Source Software, 6(57), 2783.

[10]. OpenCV (2024), Camera Calibration and 3D Reconstruction, https://docs.opencv.org/4.x/d9/d0c/group__calib3d.html.

[11]. Dumitrescu, A. (2025), "AprilTag-Based Docking Experimental Results Analysis", GitHub repository, https://github.com/AndyD01/AprilTag-Based-Docking-Experimental-Results-Analysis.

[12]. Wang, J. and Olson, E. (2016), "AprilTag 2: Efficient and Robust Fiducial Detection", Proceedings of the IEEE/RSJ International Conference on Intelligent Robots and Systems (IROS), Daejeon, South Korea, pp. 4193-4198.

[13]. Zhang, Z. (2000), "A Flexible New Technique for Camera Calibration", IEEE Transactions on Pattern Analysis and Machine Intelligence, vol. 22, no. 11, pp. 1330-1334.

[14]. Williams, G., Drews, P., Goldfain, B., Rehg, J.M. and Theodorou, E.A. (2016), "Aggressive Driving with Model Predictive Path Integral Control", Proceedings of the IEEE International Conference on Robotics and Automation (ICRA), Stockholm, Sweden, pp. 1433-1440.

[15]. Fox, D. (2003), "Adapting the Sample Size in Particle Filters Through KLD-Sampling", The International Journal of Robotics Research, vol. 22, no. 12, pp. 985-1003.

[16]. Colledanchise, M. and Ögren, P. (2018), "Behavior Trees in Robotics and AI: An Introduction", CRC Press.

8. Notations

The following symbols and abbreviations are used throughout this paper:

AMR = Autonomous Mobile Robot
AGV = Automated Guided Vehicle
ROS 2 = Robot Operating System 2
Nav2 = Navigation 2 (ROS 2 navigation stack)
SLAM = Simultaneous Localization and Mapping
AMCL = Adaptive Monte Carlo Localization
PID = Proportional-Integral-Derivative
FDM = Fused Deposition Modeling
PLA = Polylactic Acid (thermoplastic filament)
TF = Transform (coordinate frame transformation)
URDF = Unified Robot Description Format
BT = Behavior Tree
DOF = Degrees of Freedom
DDS = Data Distribution Service
CI = Confidence Interval
MPPI = Model Predictive Path Integral
EEPROM = Electrically Erasable Programmable Read-Only Memory
API = Application Programming Interface
USB = Universal Serial Bus
PWM = Pulse Width Modulation
YAML = YAML Ain't Markup Language

RESEARCH ON THE DESIGN AND IMPLEMENTATION OF A WEARABLE IOT SYSTEM FOR OCCUPATIONAL SAFETY IN INDUSTRIAL ENVIRONMENTS

CRISTIAN Alexandru-Andrei, TARBĂ Ioan-Cristian
Faculty of Industrial Engineering and Robotics, Specialization: Computer Applications in Industrial Engineering,
Year of study: IV, e-mail: alexandru.cristian@stud.fiir.upb.ro

ABSTRACT: The paper presents WorkSentinel, a wearable Internet of Things (IoT) prototype for occupational safety in industrial environments. The system combines a biometric belt, a belt-mounted central unit and a desktop base station. The belt estimates heart rate and oxygen saturation, while the central unit aggregates biometric data with gas, fall, battery and location information. Data are transmitted through a fixed LoRa uplink packet and interpreted in WorkSentinel Monitor. The paper focuses on architecture, integration, alert logic and functional validation.

KEYWORDS: occupational safety, wearable IoT, biometric monitoring, gas detection, LoRa.

1. Introduction

Occupational safety in industrial environments requires the monitoring of risk factors that are difficult to observe rapidly through conventional methods [1]. A worker may be exposed to toxic gases, high physical effort, a fall event or leaving the supervised area. Thus, wearable IoT systems can complement personal protective equipment by periodically transmitting relevant data to a supervision point [2].

Existing commercial solutions, such as Blackline Safety G7 [3], MSA Altair io 4 and ISmarch J3-LORA, show the growing interest in connected devices for industrial safety. The proposed project follows an experimental implementation, built modularly and documented at hardware, firmware and software level. The emphasis is placed on the complete data chain, from biometric measurement to alert visualization in the application.

2. Overall System Architecture

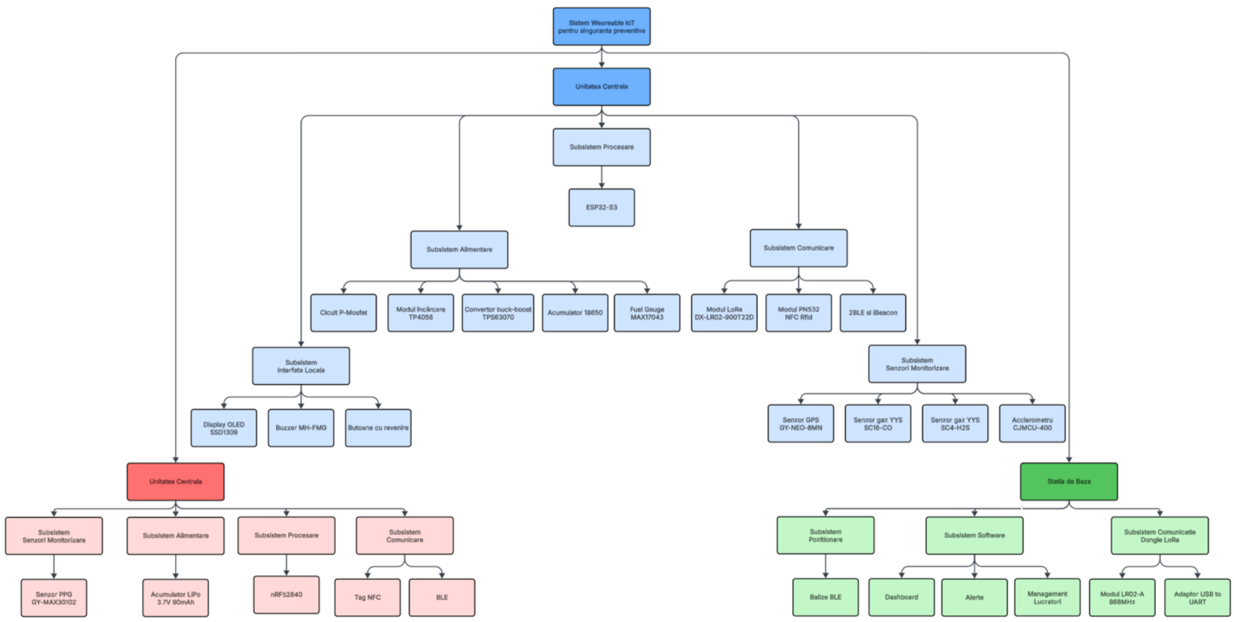

Figure 2.1. Subsystems diagram

The system architecture is organized into three components, presented in Figure 2.1: the Cardiovascular Monitoring Belt, the Central Unit and the Base Station. This separation allows the PPG sensor to be positioned stably on the body, while the Central Unit remains accessible for the SOS button, display, buzzer, gas sensors and LoRa antenna. The Base Station converts the radio packets into information for the supervisor.

From a functional point of view, the Cardiovascular Monitoring Belt transmits biometric data through Bluetooth Low Energy (BLE), the Central Unit combines these data with local measurements and transmits the resulting packet through LoRa, while the desktop application validates and displays the worker status. This flow allows each subsystem to be treated as an independent module.

The pairing process is designed for rapid field use. The worker NFC tag identifies the person entering the shift, while the belt tag provides the BLE address for direct connection. For localization, the system uses the Neo-M8N module outdoors and DX-CP28 BLE beacons indoors. Therefore, the location_mode field indicates how the localization payload must be interpreted.

3. Cardiovascular Monitoring Belt

The Cardiovascular Monitoring Belt uses the Seeed XIAO nRF52840 Sense module and the GY-MAX30102 sensor for PPG signal acquisition [4]. The electrical schematic in Figure 3.1 shows the integration of the microcontroller, the optical sensor, the local button, the status LED and the LiPo battery supply. The separate node allows placement on the wrist or on the biceps, where optical contact can be maintained more steadily.

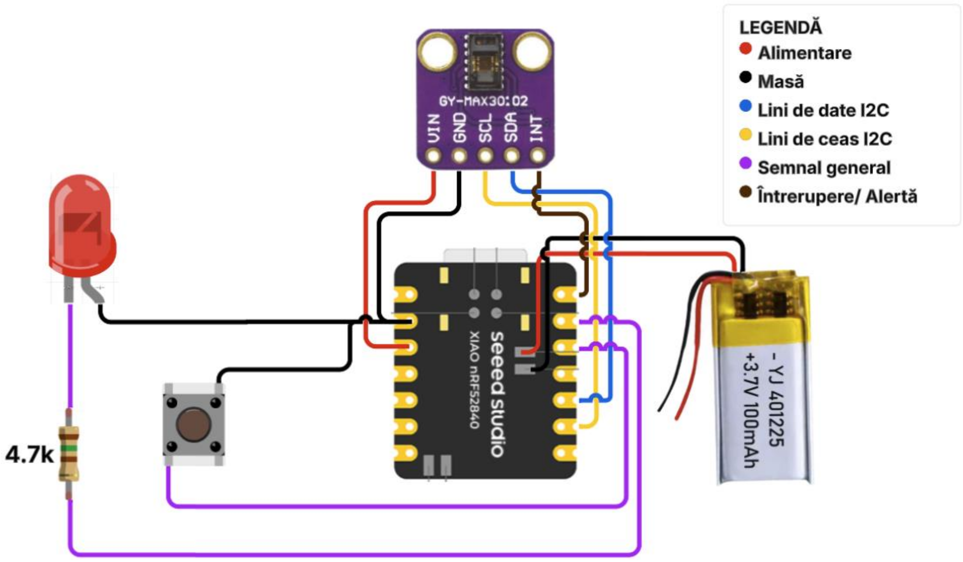

Figure 3.1. Electrical schematic of the Cardiovascular Monitoring Belt

In firmware, the belt transmits processed values to the Central Unit, not raw PPG samples. The BLE packet contains the heart rate, the oxygen saturation and the belt_flags field, with transmission performed periodically, once every second. The belt_flags field indicates the validity of skin contact, the BPM value and the SpO_2 value, so that the Central Unit can separate valid values from unstable readings.

The configuration of the GY-MAX30102 sensor was selected as a compromise between measurement stability and power consumption [4]. The sampling rate is 100 Hz, the red and infrared LEDs are active, and contact is validated through thresholds with hysteresis. Thus, the values transmitted through BLE are accepted results after the minimum measurement conditions have been verified.

PPG signal processing is performed through the Adaptive Motion Kalman algorithm, introduced to reduce fluctuations and artifacts generated by arm movement [5]. The algorithm uses the optical signal from the GY-MAX30102 and the inertial data provided by the LSM6DS3TR-C. The PPG signal is separated into direct and alternating components, while the motion reference is used to estimate the artifact.

To verify the filtering algorithms, a comparison application was developed for controlled sessions. The obtained values were compared against the Amazfit Helio Strap, used as a practical reference. Following the tests, AdaptiveMotionKalman provided the best compromise between estimation stability and tracking of heart rate variations. Figure 3.2 presents the 10-minute comparison between the reference and the result of adaptive filtering.

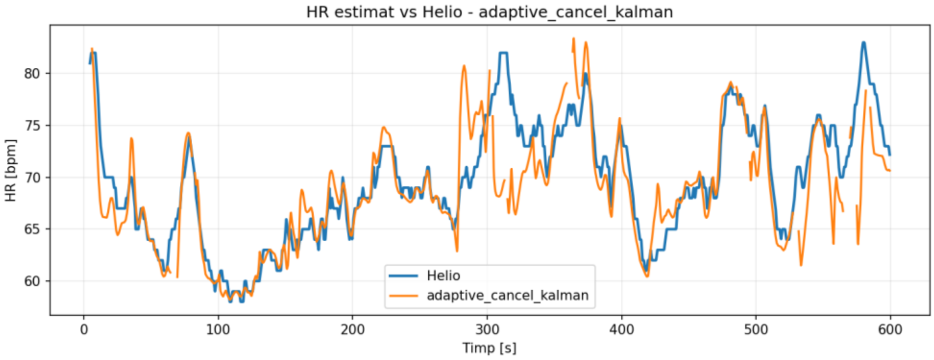

Figure 3.2. Comparison chart for the 10-minute recording

After artifact reduction, the heart rate is estimated through spectral analysis over temporal windows and introduced into a scalar Kalman filter. The Kalman gain is adapted according to signal quality and motion level, so that stable measurements influence the BPM value more strongly. In the current configuration, the system cannot guarantee stable estimates during medium to intense movement, because the optical contact changes significantly. Therefore, value interpretation is controlled through belt_flags.

4. Central Unit

The Central Unit is the field data acquisition and transmission node. It uses the ESP32-S3-WROOM-1 N16R8 for peripheral control, the CJMCU-400 module for motion detection, the YYS SC16-CO and YYS SC4-H_2S sensors for gas monitoring, the Neo-M8N module for outdoor localization and the DX-LR02-900T22D module for LoRa communication. The schematic of the monitoring subsystem is presented in Figure 4.1.

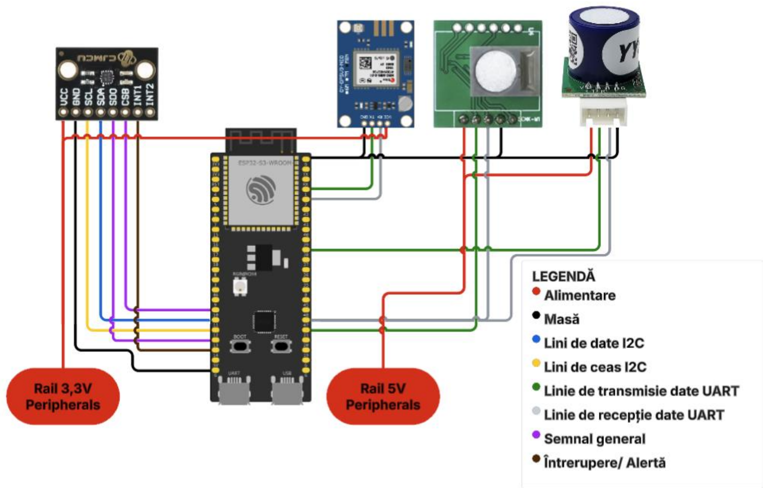

Figure 4.1. Electrical schematic of the monitoring subsystem

Module integration required the power supply to be separated into two branches, one at 5 V and one at 3.3 V. The gas sensors are supplied from the 5 V branch, controlled through a high-side P-MOSFET switch, while the other peripherals are supplied from the 3.3 V branch, controlled in a similar way. This solution reduces consumption in deep sleep mode. The electrical schematic of the power supply is shown in Figure 4.2.

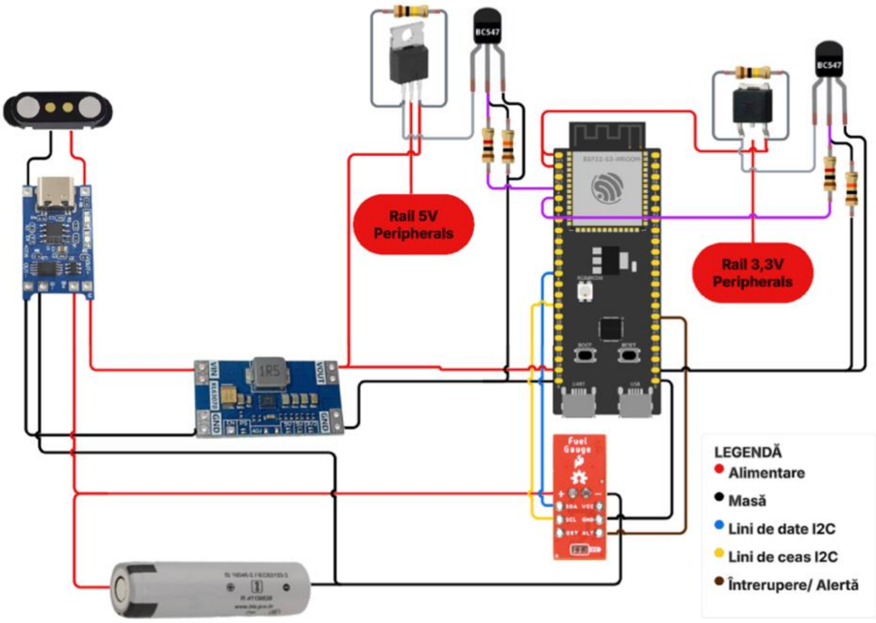

Figure 4.2. Electrical schematic of the power supply subsystem

From a logical point of view, the Central Unit firmware activates alerts only based on data considered valid. The thresholds used in the implementation are 20 ppm for CO, 5 ppm for H_2S, the 50 BPM to 140 BPM interval for heart rate and 90 % as the lower limit for SpO_2. The motion state is transmitted through the fall_state field, which differentiates between stationary state, normal motion and impact.

For the gas sensors, the alert logic takes into account the stabilization time of the electrochemical elements [6],[7]. The firmware defines separate reading windows for CO and H_2S and disables alert interpretation until the end of the warm-up period. This stage is necessary because the values read immediately after power-up may reflect internal stabilization, not the actual concentration in the environment.

For fall detection, the CJMCU-400 module, based on the BMA400 chip, is read through SPI at 100 Hz [8]. The acceleration values on the three axes are expressed in mg and are used to calculate the magnitude of the acceleration vector:

$M = \sqrt{(a_x{}^2 + a_Y{}^2 + a_z{}^2)}$ (4.1)

At rest, this magnitude is around 1000 mg, corresponding to gravitational acceleration. For this reason, the algorithm analyzes the deviation from this reference value:

$\Delta M = M - 1000 \vee$ (4.2)

The fall_state field differentiates three situations: stationary state, normal motion and impact. The stationary state corresponds to small deviation values, normal motion to moderate deviations, while impact is identified when the deviation exceeds 2500 mg and then returns below the stationary threshold of 150 mg. The impact is latched because the acceleration peak may last less than the normal LoRa transmission interval. In the final implementation, the impact first triggers a local alert, and the absence of confirmation within 30 s activates the FALL_DETECTED flag.

5. LoRa Protocol and the WorkSentinel Monitor Application

Communication between the Central Unit and the Base Station is performed using the DX-LR02 module [9]. The system uses a fixed binary packet, because this solution reduces the transmission size and enables deterministic interpretation at reception. Table 5.1 presents the structure of the LoRa uplink packet transmitted by the Central Unit.

Table 5.1. LoRa uplink packet structure

Byte	Field	Type	Description
0-1	central_unit_code	uint16_t	Unit code
2-5	worker_code	char[4]	Worker code

6-7	sequence_id	uint16_t	Sequence number
8	battery_percent	uint8_t	CU battery level
9	heart_rate_bpm	uint8_t	BPM from BLE
10	spo2_percent	uint8_t	SpO_2 from BLE
11	belt_flags	uint8_t	Belt validity
12	fall_state	uint8_t	Fall state
13-16	co_ppm, h2s_ppm	uint16_t	CO and H_2S
17-25	location_mode, location_payload	uint8_t	Localization
26-27	flags	uint16_t	System flags

Table 5.2. Structure of the flags field

Bit	Name	Hex mask	Description
0	PAIRING_MODE	0x0001	The unit is in pairing mode
1	FALL_DETECTED	0x0002	A fall has been detected
2	CO_ALERT	0x0004	The CO value exceeded the defined threshold
3	H2S_ALERT	0x0008	The H_2S value exceeded the defined threshold
4	SOS_PRESSED	0x0010	The SOS button has been pressed
5	HR_ALERT	0x0020	Heart rate exceeded the alert threshold
6	SPO2_ALERT	0x0040	Oxygen saturation dropped below the defined threshold
7	LOW_BATTERY	0x0080	The battery dropped below the minimum threshold

In the desktop application, LoRa packets are received through the dongle connected to the PC and passed through an interpretation pipeline. Figure 5.1 shows the reception and validation flow: serial bytes, delimitation, parsing, validation and application update. The same 28-byte structure is implemented in the firmware and in the parser, reducing the risk of different interpretations. The central_unit_code, worker_code, sequence_id and flags fields allow successive packets to be correlated with the same worker.

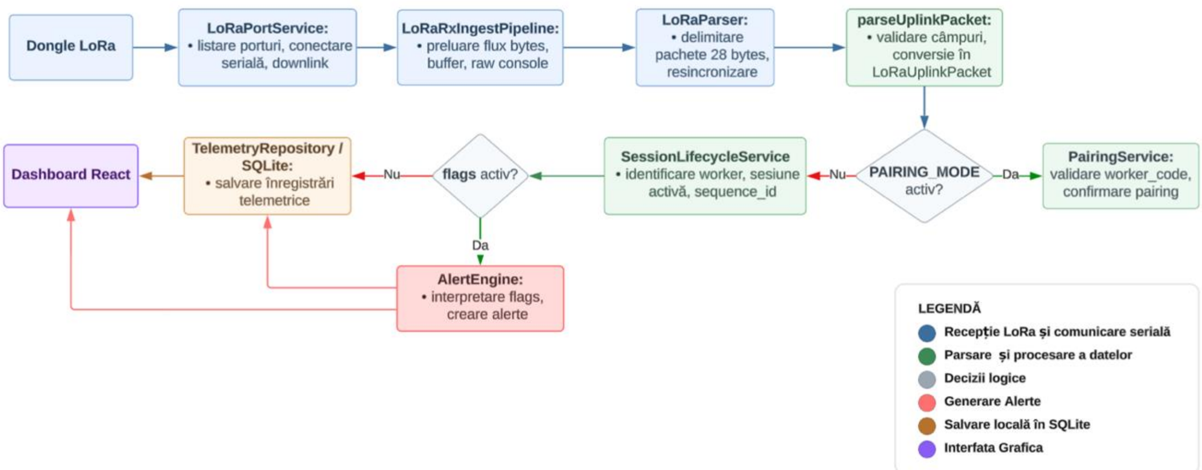

Figure 5.1. Reception and interpretation pipeline for LoRa packets

The application interface, presented in Figure 5.2, displays worker status as cards containing battery level, biometric values, gas measurements, position and identification data. Separately, the application includes a list for alerts that occur during the shift. This structure highlights critical events and links the state of each worker to the shift session, not to an isolated packet.

The separation between location_mode, GPS coordinates and indoor data allows the dashboard to display the position regardless of the data source. For outdoor mode, scaled coordinates are transmitted, while for indoor mode the major and minor iBeacon identifiers of the dominant beacon are sent together with RSSI. Association with the configured zone is performed in the application, keeping the radio packet compact.

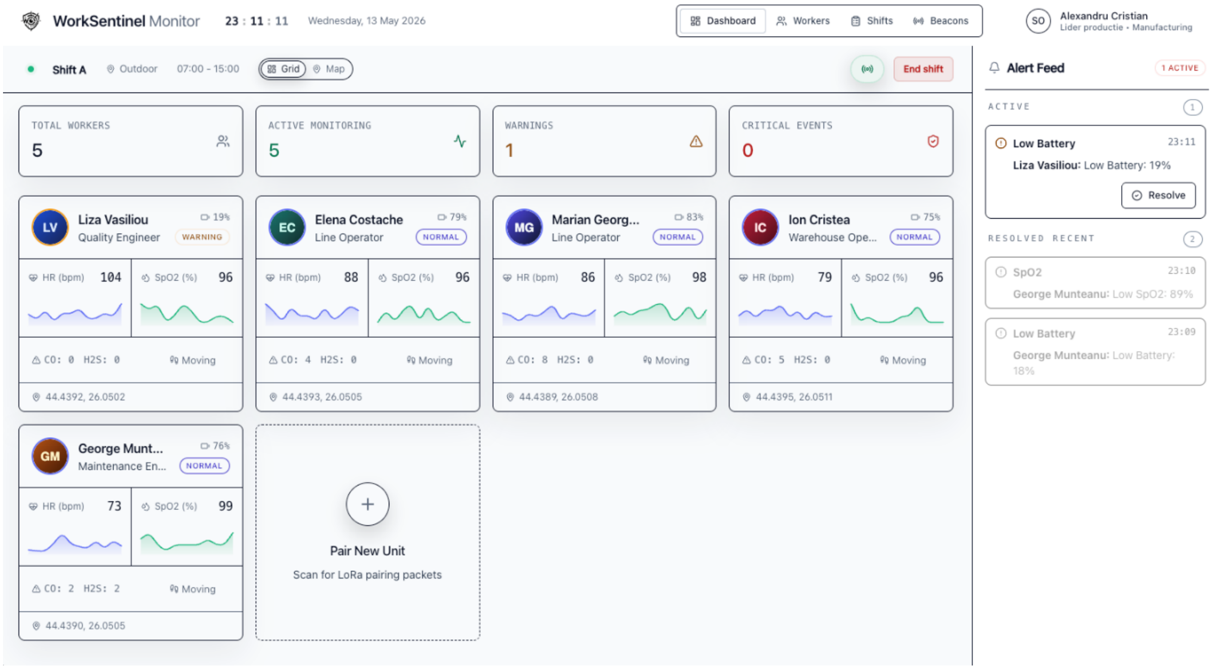

Figure 5.2. Application dashboard in Grid mode

6. Prototype Implementation and Testing

The prototype was implemented by mounting and wiring the modules inside the enclosures of the two wearable devices of the system. For the Cardiovascular Monitoring Belt, integration focused on positioning the GY-MAX30102 sensor and the Seeed XIAO nRF52840 Sense module in a compact assembly intended to be worn on the body, as shown in Figure 6.1.

Figure 6.1. Assembled Cardiovascular Monitoring Belt

For the Central Unit, presented in Figure 6.2, the components were organized inside the enclosure so that all of them could operate within the required parameters, while the connection wires could be routed without excessive tension.

Figure 6.2. Assembled Central Unit

Testing was performed in stages, starting with the power supply, then continuing with the sensors, communications and desktop application. Table 6.1 presents the main checks performed for each subsystem.

Table 6.1. Individual testing stages

Testing stage	Verified subsystem	Test objective	Verification method
Electrical testing	Power supply, rails and MOSFET switches	Voltage and continuity verification	Multimeter and Serial Monitor
Local interface testing	SSD1309, buzzer, buttons and LED	Display and signaling verification	Display and Serial Monitor
Sensor testing	Gases, accelerometer, GPS, PPG	Verification of read data	Display and Serial Monitor
Communication testing	BLE, NFC, LoRa	Data exchange verification	Display and Serial Monitor
Integrated testing	Complete system	End-to-end flow verification	Application

Final testing checked whether the same information correctly reaches the Central Unit screen, the LoRa packet and the application. Thus, an SOS alert, a gas value above the threshold or a fall event were not verified only as sensor signals, but as events that pass through the entire system. For important alerts, the same state must appear in the alert logic, in the flags field and in the application interface. In addition to individual tests, complete scenarios were defined, from worker identification and belt pairing to LoRa transmission and alert display in the dashboard.

Table 6.2. End-to-end verification scenarios

Verified function	Test action	Expected result
Worker identification	Reading the personal NFC tag	The Central Unit stores the worker identifier
Belt pairing	Reading the belt NFC tag and initiating BLE	The Central Unit receives the biometric data from the belt
Periodic transmission	Normal system operation	The packet is transmitted through LoRa and displayed in the application
Manual alert	Pressing the SOS button	The event is marked in the packet and displayed in the application
Environmental alert	Value above threshold for CO or H_2S	The packet includes the gas alert state
Biometric or motion alert	Abnormal BPM/SpO_2 value or impact	The packet includes the corresponding alert state

7. Conclusions

The paper presents the implementation of a wearable IoT system prototype for monitoring worker safety in industrial environments. The solution integrates a Cardiovascular Monitoring Belt, a belt-mounted Central Unit and a desktop application. Biometric data, gas measurements, motion state, positioning and alerts are combined into a common packet, transmitted through LoRa to the Base Station.

The prototype demonstrates that a modular solution built from accessible components can cover important functions: biometric monitoring, gas detection, fall signaling, localization and alert transmission. In its current form, the system remains experimental, and the main limitations are related to sensor calibration in real industrial conditions, heart rate stability during motion and testing with multiple workers.

8. References

[1] “ISO 45001:2018 - Occupational health and safety management systems - Requirements with guidance for use”, International Organization for Standardization, Geneva, 2018.

[2] “Wearables for Industrial Work Safety: A Survey”, E. Svertoka, S. Saafi, A. Rusu-Casandra, R. Burget, I. Marghescu, J. Hosek, A. Ometov, Sensors, vol. 21, no. 11, art. 3844, MDPI, 2021. [Online]. Available: https://www.mdpi.com/1424-8220/21/11/3844 [Accessed March 15, 2025].

[3] “G7 Connected Safety - Product Documentation”, Blackline Safety, 2024. [Online]. Available:

https://www.blacklinesafety.com/products/g7-series [Accessed March 15, 2025].

[4] "MAX30102 High-Sensitivity Pulse Oximeter and Heart-Rate Sensor for Wearable Health", Maxim Integrated, datasheet. [Online]. Available: https://www.analog.com/media/en/technical-documentation/data-sheets/max30102.pdf [Accessed March 15, 2025].

[5] "Wearable Photoplethysmography for Cardiovascular Monitoring", P. H. Charlton, P. A. Kyriacou, J. Mant, V. Marozas, P. Chowienczyk, J. Alastruey, Proceedings of the IEEE, vol. 110, no. 3, pp. 355-381, 2022. [Online]. Available: https://ieeexplore.ieee.org/document/9733047 [Accessed March 15, 2025].

[6] "SC16-CO Datasheet", YYS, datasheet. [Online]. Available: https://www.scribd.com/document/747547909/Carbon-Mono-Oxide-Sensor-SC16-CO [Accessed March 15, 2025].

[7] "SC4-H2S Datasheet", YYS, datasheet. [Online]. Available: https://jumpshare.com/share/BwZYcvKiVPlGso9tDnz1 [Accessed March 15, 2025].

[8] "BMA400 Triaxial Acceleration Sensor", Bosch Sensortec, datasheet. [Online]. Available: https://www.bosch-sensortec.com/media/boschsensortec/downloads/datasheets/bst-bma400-ds000.pdf [Accessed March 15, 2025].

[9] "DX-LR02-900T22D Module Specification", Shenzhen DX-SMART Technology Co., datasheet. [Online]. Available: https://manuals.plus/asin/B0DKXM392Q [Accessed March 15, 2025].

Research regarding the implementation of an experimental model for automated tennis ball collection

NEGOIȚĂ Alina-Andreea and Lecturer PhD Eng **TARBĂ Ioan Cristian (Scientific Supervisor)**

Faculty of Industrial Engineering and Robotics, Specialization: Applied Computer Science in Industrial Engineering, Study Year: IV, e-mail: negoitaalina436@gmail.com

ABSTRACT: This paper presents the development of an autonomous robotic system designed for tennis ball collection, aimed at optimizing training efficiency by minimizing downtime. The system integrates artificial intelligence algorithms with autonomous navigation to effectively identify and collect targets. The hardware architecture was meticulously engineered to ensure high operational reliability. The design of the cylindrical collection mechanism is based on precise volumetric calculations to guarantee the required storage capacity. The resulting model offers a compact and high-performance solution for optimizing sports club resources, providing a cost-effective alternative to existing commercial systems.

KEYWORDS: robot, autonomous, collection, navigation

1. Introduction

1. Tennis is globally regarded as one of the most demanding and respected sports, placing high requirements on players in terms of both skill and physical condition. However, a brief analysis of training sessions reveals an inefficiency in the time spent on court. Approximately 20–30% of training time is used for collecting tennis balls [1].

The optimal solution is the development of a collection system capable of autonomous movement. Equipped with a camera module and an optimal path-planning algorithm, this system streamlines the tennis ball collection process. From a mechanical architecture standpoint, it incorporates a dedicated ball-capturing mechanism.

2. Current State of the Art

Currently, the sports equipment market offers both manual and fully automated solutions. Traditional approaches involve mechanical devices such as rolling baskets that require human effort. On the other hand, the autonomous systems market includes several alternatives. These automated systems feature artificial intelligence, efficient navigation, and high collection capacity. Representative systems include Tennibot (Fig. 1), Ballpicker Connected Line (Fig. 2), and Seekerbot (Fig. 3).

Fig. 1 Tennibot

Fig. 2 Ballpicker

Fig. 3 Seekerbot

However, as shown in the analysis presented in Figure 4, the main drawback of these systems is their relatively high cost, making them inaccessible for many clubs or amateur players.

BALL COLLECTION MECHANISM ANALYSIS

CHARACTERISTICS	TENNIBOT	BALLPICKER CONNECTED LINE	SEEKERBOT	NEEWER TB05S
AUTONOMOUS NAVIGATION	Using artificial intelligence	Controlled with SMS or app	Controlled with app	Manually
EFFICIENCY NAVIGATION	Using artificial intelligence	Technology GPS RTK	Using artificial intelligence and sensors	Non autonomous
COLLECTION CAPACITY	Up to 140 balls	Up to 300 golf balls	Up to 50 balls	35 balls
BALL DETECTION TECHNOLOGY	Using artificial intelligence	-	Using artificial intelligence	-
BATTERY LIFE	Up to 5 hours	Continuous navigation	Up to 90 min	-
PRICE	$2245	€25.475	$1,499	€74,99

Fig. 4 Competitor Analysis

3. General System Architecture

The autonomous tennis ball collection system encompasses a series of critical functions for the entire process. These functions are presented in the system FAST diagram (Fig. 5).

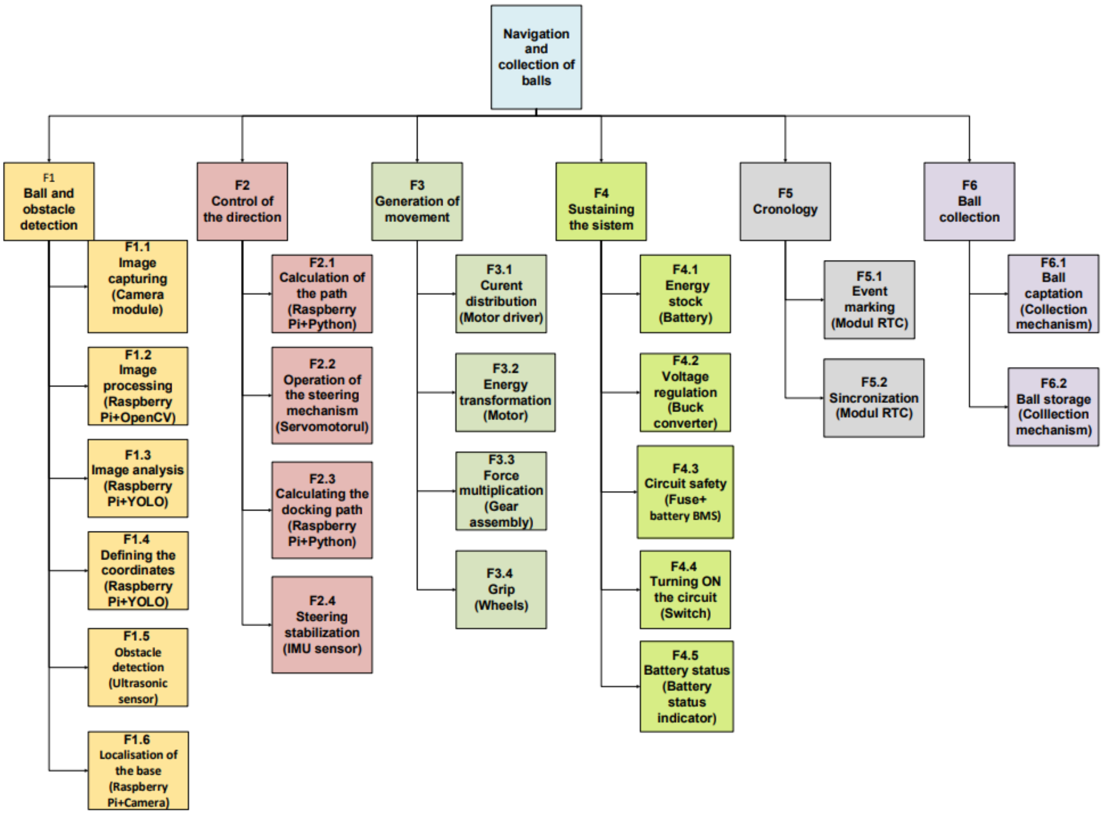

Fig. 5 System FAST Diagram

The FAST diagram indicates a complex and robust architecture designed to fulfill the primary objective of autonomous navigation and collection. The decision-making layer of the robot is supported by the mechanical system. By combining these functions, efficient operation in terms of time and resources is ensured, resulting in an intelligent and autonomous system.

The logical architecture of the system is divided into 3 components:

1. **1.** The sensory component is responsible for data collection via two hardware components: the video camera and the ultrasonic sensor. Each of these has a well-defined role. The camera, together with the YOLOv8n model, identifies tennis balls and their spatial coordinates, while the ultrasonic sensor alerts the system to potential obstacles in the environment.
2. **2.** The intelligent component is responsible for decision-making. It manages the robot's operating modes (scanning, patrolling, collecting, etc.) and optimally plans the collection process.
3. **3.** The execution component translates these logical decisions by managing the PWM signals for both the drive motor and the steering mechanism, while converting coordinates into steering angles and travel durations.
4. Design of the Tennis Ball Collection Mechanism

The collection mechanism has a cylindrical shape, comprising two main subassemblies: the rotating subassembly and the support subassembly. Its design focuses on efficient ball pickup, ball retention, and rapid discharge of the mechanism.

The main body consists of 3 essential components:

- Wheels: These represent the direct interface with the ground. With an outer diameter of 160 mm, they feature ribs covered in elastomeric material for optimal grip. Each wheel has 12 central bores for wire assembly and 3 L-shaped profiles for bayonet connection with the cap.
- Retention caps: Their role is to keep the balls inside the collector. The assembly between the cap and the wheel is achieved through a bayonet-type mechanism using the 3 pins on the outer diameter of the cap.
- Central shaft: Coordinating the movement of the two wheels and providing rigidity to the assembly, it serves as a torque transmission element via a key-type profile.

The architecture of the main body of the mechanism is illustrated in Figure 6.

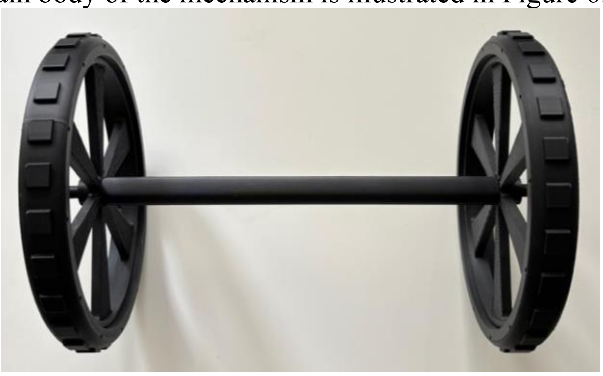

Fig. 6 Main Body

The support and fastening system (Fig. 7) contains the following main components:

- Lateral arms: With a square cross-section of 15×15 mm, these are assembled with the main body via two bearings. The two arms feature a detachable locking pin, required for the discharge process.
- Fastening components: These are inserted onto the two arms and secure the assembly to the chassis.

Fig. 7 Fastening System

Kinematic and collection elements:

- Bearings: The rotary motion is supported by a pair of 6000Z bearings. Durability calculations indicate that their properties are outstanding for this application. An intermediate bushing with a keyway is required for torque transmission.
- Collection wires: The foundation of the capture mechanism is elastic deformation. Elastomeric wires are used, which deform elastically upon contact with the ball and return to their original shape after the ball enters the collector. Given the wheel circumference of approximately 47 cm relative to the ball diameter of 6.5 cm, 12 equally spaced elastic wires were determined to be optimal.

The collection mechanism in its final assembled version is presented in Figure 8.

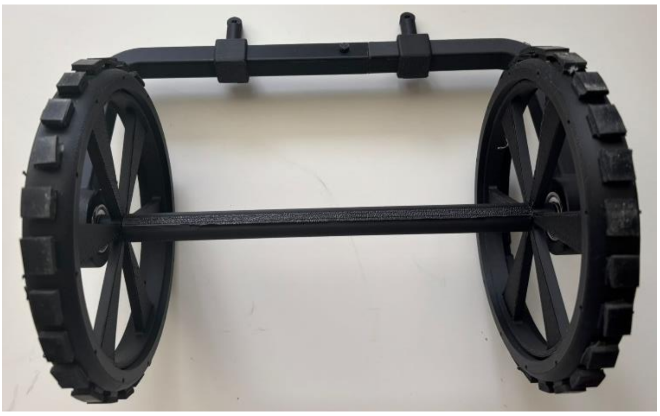

Fig. 8 Collection Mechanism

5. Software Implementation

The operating system is Raspberry Pi OS (Linux), with Python 3 as the primary programming language. The YOLOv8s model is used for tennis ball recognition.

The main algorithms of the software system are:

- 3D detection and localization: the YOLOv8s model detects the tennis ball and its 3D position.
- Collection order: the Nearest Neighbour algorithm determines the robot's path.
- Ball collection: performed by computing the robot's trajectory based on ball coordinates in 3 stages: turning using the gyroscope, driving straight once aligned with the ball, and an extra 3 seconds to ensure collection.
- Patrolling: the court is divided into a grid with 1.2 m spacing, which the robot sequentially patrols.
- Stuck detection: performed using the gyroscope.
- Obstacle avoidance: using the ultrasonic sensor, the robot steers or reverses until the obstacle is cleared.

The critical system parameters were calibrated experimentally, yielding the following values:

- FOCAL_LENGTH_PX=134 (camera focal length calibration used for distance calculation);
- REAL_SPEED_M_S=0.158 (actual robot speed at 70% motor duty cycle);
- TURN_FACTOR=0.8 (gyroscope turn correction factor);
- COLLECTOR_GROUP_M=0.20 (maximum lateral distance between two balls to be collected together).

Software architecture results:

- Ball detection range: 0.3–2 meters;
- Lateral ball detection by widening the detection angle using a servomotor;
- Court navigation;
- Automatic obstacle avoidance.

System limitations:

- Imprecise positioning on court;
- MPU6050 disturbed by motor electromagnetic noise;
- Dependence on ambient lighting for ball detection.

Optimization of the YOLO detection process was achieved by training on the COCO dataset. Initially, the “sports_ball” class was used, which covers all ball types — a general class that generated errors. The “Tennis Ball Detection Computer Vision Model” dataset was subsequently used, containing 4,329 images under various environmental, lighting, and positional conditions.
The advantages of the custom model include improved detection accuracy under various lighting conditions and elimination of confusion with other ball types.

6. Formulas Used

The following formulas were used for sizing the collection mechanism:

2. $$Vc = \pi \times R^2 \times H (cm^3) \quad (1)$$

Where:
R=7,5cm,
H=20cm.
Thus, the cylinder volume is: Vc=3534cm^3
Considering the spherical shape of the balls, their space occupancy ratio in a random arrangement is approximately 60% [2]. Therefore, the following formula is used for the usable cylinder volume:

3. $$Vu = 60\% \times Vc (cm^3) \quad (2)$$

The usable cylinder volume has a total value of: $Vu = 2120cm^3$
Using the average tennis ball diameter of 6.7 cm and equation 3, the average volume of a tennis ball is obtained.

4. $$Vm = \frac{4 \times \pi \times r^3}{3} (cm^3) \quad (3)$$

5.

From the last equation, the tennis ball volume is $Vm = 157cm^3$
The desired capacity is 10 balls, so their total volume is $Vt = 1570cm^3$. The total volume of the balls is less than the usable volume of the collector:

$$Vt \leq Vu \quad (4)$$

7. Conclusions

The development of an autonomous robotic system for tennis ball collection highlighted various processes for selecting components with specifications suited to the application, as well as careful mechanical, electrical, and logical design. The result is a system capable of ball recognition and optimal path planning through the implementation of artificial intelligence algorithms and mathematical computation logic. Through a carefully selected mechanical and electrical architecture, the robotic system navigates the tennis court independently and efficiently. The development and manufacture of the collection mechanism positioned at the front of the robot enables precise tennis ball collection.

8. References

[1]. *** Tennibot (2024), "Tennis Ball Collector – AI Powered Tennis Ball Retriever", available at: https://www.tennibot.com/tennis/ball-collector/ [accessed 5 May 2025].

[2]. *** BallPicker Connected (2020), product image, available at: https://www.robotdagiardino.ch/itheephy/2020/11/BallPicker-Connected-Line-600x600.jpg [accessed 5 May 2025].

[3]. *** Potent Tennis (2024), "SeekerBot 2.0", available at: https://potenttennis.com/products/seekerbot [accessed 5 May 2025].

[4]. Dullien, F. A. L. (1992), Porous Media: Fluid Transport and Pore Structure (2nd ed.), Academic Press, ISBN 978-0-12-223651-8.

Design and PRELIMINARY VALIDATION OF AN AMR-BASED Environmental MAPPING KIT FOR PHARMA WAREHOUSES

CIOCONEA Adina-Mariana[1], MIU Ana-Maria[1], WIDIASTUTI Elok[2] and **ABAZA Bogdan-Felician**

[1]Faculty: Industrial Engineering and Robotics, Specialization: Computer Applications in Industrial Engineering, Year of study: I , e-mail: cioconea.adina@gmail.com
[2]Faculty: Industrial Engineering and Robotics, Specialization: Industrial Design and Innovative Products, Year of study: I

Summary: Pharmaceutical QA relies on rigorous monitoring to ensure product efficacy. However, traditional static mapping is ill-suited for high-bay warehouses, requiring a vast number of sensors that demand costly, individual NIST-traceable calibration. These fixed systems create spatial blind spots, often missing vertical thermal stratification and transient "hot spots" caused by airflow imbalances. Additionally, manual installation at height introduces significant HSE risks and labor costs. This research proposes an AMR-mounted mapping kit to provide dynamic 3D environmental profiles. This mobile platform streamlines GDP-compliant validation by replacing fragmented sensor networks with a single, preliminary autonomous monitoring platform that eliminates data gaps and manual labor.

KEYWORDS: Pharmaceutical warehouse, GDP compliance, AMR, Environmental monitoring, Thermal mapping.

1. Introduction

Pharmaceutical warehouse management plays a critical role in maintaining quality, safety, and effectiveness of medicines through the supply chain process. Pharmaceutical products are highly sensitive to environmental conditions, especially temperature and humidity, therefore it requires a storage system that complies with Good Storage Practice (GSP) and Good Distribution Practice (GDP). The World Health Organization (WHO) asserts that storage conditions such as temperature and humidity should be monitored, managed, and recorded regularly to control pharmaceutical products' quality [11].

Uncontrolled temperatures in pharmaceutical warehouses can lead to a decline in drug stability, degradation of active ingredients, and a reduction in the therapeutic efficacy of pharmaceutical products. Additionally, inadequate environmental conditions such as poor ventilation, high humidity, excessive light exposure, and suboptimal monitoring systems, can increase the risk of product damage, contamination, and operational losses due to expired or unfit-for-distribution medications [12]. The WHO also states that temperature is the most critical environmental parameter affecting the quality of pharmaceutical products during storage and distribution [8].

The objectives of this paper are:

- To identify the limitations of conventional thermal mapping methods in high-bay pharmaceutical warehouses;
- To design and select an Autonomous Mobile Robot (AMR)-based system capable of performing 3D thermal mapping;
- To experimentally validate critical subsystems, including AprilTag-based localization and on-device thermal inference at the edge;
- To demonstrate the feasibility of the proposed architecture for compliance with GDP requirements.

2. State of the Art

Pharmaceutical warehouse validation is an important step for maintaining the storage of pharmaceutical products in the environment for healthcare products to preserve quality, safety, and therapeutic properties in all stages of storing and distributing them. The European Union GDP Guidelines (2013/C 343/01) and WHO Technical Report Series stipulate that pharmaceutical storage facilities should employ an environmental control system that maintains the temperature, humidity, airflow, and room pressure within validated limits [4].

In conventional practice, the process of validation of pharmaceutical warehouses is carried out mainly by applying static data loggers positioned at different points in the temperature mapping period. The goal is to determine the temperature distribution of the storage area to be used to identify hot spots and cold spots or areas that could potentially have temperature excursions. WHO Supplement 8 on Temperature Mapping of Storage Areas also advises including sensors at different horizontal and vertical positions, such as high-tier storage racks, to locate temperature differences caused by air stratification [13].

With the advancement of digital technology, the installation of automated monitoring systems in pharmaceutical warehouses is shown to enhance traceability, increase the speed of recognizing temperature excursions, and assist GDP regulation and 21 CFR Part 11 electronic data integrity, as prescribed by GDP regulations and 21 CFR Part 11 [4], [14]. Furthermore, recent studies highlight that industry 4.0 technologies, including AI- and IoT-based monitoring systems, are continuously adopted in the pharmaceutical sectors [15].

Moreover, AMRs have become increasingly important due to their autonomous navigation capabilities and minimized reliance on fixed infrastructure [10]. Recent research indicates that by incorporating environmental sensors, LiDAR and SLAM algorithms into autonomous robots, the indoor environmental mapping can be enhanced in terms of accuracy and efficiency [1]. It enables visualization of temperature and humidity distributions in the form of heat maps that enable the analysis of the environmental conditions of the warehouse. This strategy is more relevant in contemporary pharmaceutical warehouses, which usually have higher-tier storage racks because the temperature distribution can greatly vary in these storage regions [5].

3. Needs Analysis and Problem Definition

In the storage of pharmaceuticals and vaccines, controlling environmental conditions is mandatory for pharmaceutical products to be of good quality, stable and therapeutic effects to be obtained. Temperature and humidity for a pharmaceutical product should be carefully monitored and controlled throughout the whole storage and distribution cycle, and variations in these parameters can result in pharmaceutical products' degradation or treatment drug effect loss [4], [12].

On such a situation, consumers are interested in having an able system to continuously monitor the storage of pharmaceutical products particularly for temperature and humidity to control the critical storage conditions at 15°C-25°C using good accuracy. In pharmaceutical supply chain temperature management [14], it is highlighted that temperature excursions play a significant role in the deterioration of pharmaceutical products and the enhancement of operational losses.

WHO temperature mapping guidelines recommend monitoring at multiple spatial levels in high-bay pharmaceutical warehouses to identify vertical thermal stratification and critical hot and cold areas. As a result, monitoring systems should be designed to multi-level data acquisition, including lower, intermediate, and upper storage racks within spanning heights approximately 8-12 m [13]. Research of vertical temperature concentration in warehouses shows that data at different temperature categories in warehouses can affect the uniform use of storage conditions for delicate goods, as there is a difference in temperature between the storage space [2]. In the same line, temperature mapping in pharmaceutical warehouses studies that sensors at multiple points and heights detect critical zones [7]. For early detection of changes in environmental factors, the monitoring system should periodically measure and permit us to check for additional key parameters such as the differential pressure.

In this context, the users should be provided with accessible and interpretable information through intuitive visualization tools, e.g., heat maps, and graphic representations of the distribution of environmental parameters. Moreover, the system should promote the real-time signal when the permitted limit is exceeded not only but also to periodically test the calibration and the verification process of the warning system to secure accurate and reliable monitoring [6].

4. System Functional Analysis

A Function Analysis System Technique (FAST) diagram shown in Fig. 1. was generated to map the relationships among system functions. Both methods were employed as the foundation for concept development, ensuring that the proposed design solution effectively fulfills user needs in a systematic manner.

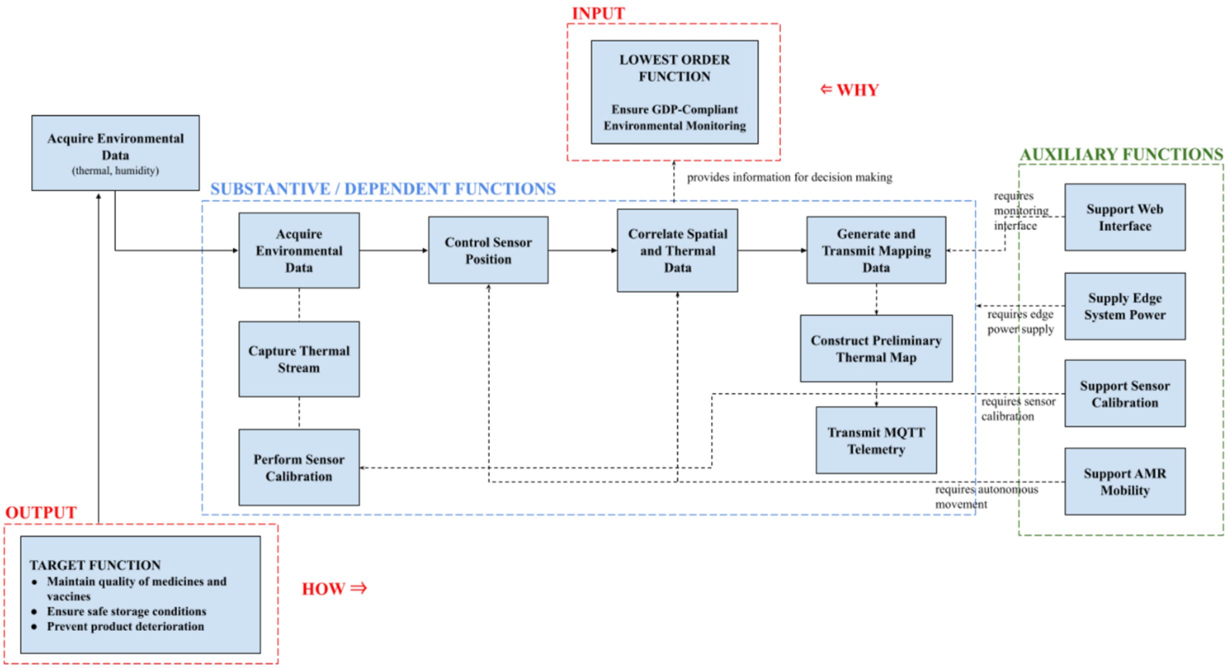

Fig. 1. Function Analysis System Technique (FAST) diagram

The user requirements obtained from the needs analysis process in chapter 3 were transformed into specific design parameters. These requirements were represented using a Detail Characterization in Table 1. to identify detailed product characteristics.

Table 1. Detail Characterization

Function Level	Function Description	Function Category
F0	Ensure GDP-Compliant Environmental Monitoring	High Order
F1	Perform Mobile Environmental Data	Primary Basic
F1.1	Acquiring Environmental Data	Secondary
F1.2	Control Sensor Position	Secondary
F1.3	Correlate Spatial and Thermal Data	Secondary
F1.4	Generate and Transmit Mapping Data	Secondary
F1.1.1	Capture Thermal Streams	Supporting
F1.1.2	Perform Sensor Calibration	Supporting

5. Concept Generation and Selection

This experimental CPS prototype explores an automated 3D thermal mapping alternative to static warehouse monitoring. Preliminary features include vision-based navigation, Z-axis thermal scanning, hotspot detection, and audit reporting.

5.1. Concept Generation and Selection Matrix

To balance navigation performance, manufacturing cost, and operational energy consumption, five architectural concepts were evaluated and comparatively analyzed, as presented in Table 2:

- C1: Vision-Tag & Thermography (Edge SBC). Uses a Single Board Computer (SBC - e.g., Raspberry Pi 4 with 4GB RAM) to manage an RGB camera (AprilTags navigation) and a radiometric thermal matrix. Energy consumption: Efficient (10-15W). Provides high battery autonomy.
- C2: RFID Scanning & Smart Labels. The robot uses a UHF RFID scanner to read smart labels (with integrated temperature sensors) attached to each pallet. Operational cost: Very high from a logistics perspective. Although the robot consumes little energy, each pallet requires a disposable smart label, generating very high long-term costs.
- C3: 2D LiDAR + Thermography. Uses a planar laser for localization (2D SLAM). Sensor costs are moderate. Correlating temperature with the Z-axis requires additional computational complexity to associate the 2D map with vertically acquired thermal measurements.
- C4: 3D LiDAR + Thermography. Uses 3D point-cloud mapping onto which thermal data is directly superimposed. Although extremely precise, the 3D LiDAR sensor has a prohibitive cost, while data fusion requires massive computational power on the Edge unit (dedicated GPU processors), resulting in extremely high operational energy consumption.
- C5: 3D Stereo Cameras + Thermography. Depth cameras are cheaper than 3D LiDAR; however, they require significant onboard processing power for stereo image computation. Additionally, in pharmaceutical warehouses they present a major risk of errors caused by reflections generated by metallic pallet foils.

Table 2 provides a qualitative breakdown to serve as an initial screening for the five proposed designs (C1-C5). It highlights the specific pros and cons of each technology, weighing them against core financial boundaries-such as CAPEX and OPEX-as well as technical demands, including data correlation and Edge computing capabilities.

Table 2. Qualitative Technological Concept Selection Matrix

Evaluation Criterion	C1: AprilTags	C2: RFID Labels	C3: 2D LiDAR	C4: 3D LiDAR	C5: 3D Stereo
Manufacturing Cost (CAPEX)	Medium (~1050 RON)	Low (~800 RON)	High (~3500 RON)	Very High (>20k)	High (~4500 RON)
Operational Sustainability (OPEX)	Efficient (Low Power)	Prohibitive (Consumables)	Medium	Poor (High Power)	Poor
Edge Computing Feasibility	High (SBC Ready)	Maximum	Medium	Low (Requires GPU)	Low
3D Data Correlation Reliability	High (Algorithmic)	Direct (Tag-based)	Complex	Maximum	High
Final Decision	SELECTED	Rejected	Rejected	Rejected	Rejected

Since qualitative reviews can sometimes introduce bias, the final selection was grounded in a mathematical framework. By applying the Analytic Hierarchy Process (AHP), Table 3 assigns specific mathematical weights to each evaluation criterion via pairwise comparisons (maintaining a Consistency Ratio of CR = 1.6%). This rigorous approach allows us to calculate a definitive global score and rank the concepts completely objectively.

Table 3. Quantitative Selection Matrix based on AHP Methodology

Evaluation Criterion	Weight	C1	C2	C3	C4	C5
Manufacturing Cost (CAPEX)	0.390	0.85	0.90	0.45	0.05	0.35
Operational Sustainability (OPEX)	0.390	0.95	0.15	0.55	0.20	0.40
Edge Computing Feasibility	0.152	0.75	0.95	0.60	0.15	0.30
3D Data Correlation Reliability	0.068	0.80	0.90	0.50	0.95	0.85
GLOBAL SCORE	1.000	0.87	0.59	0.53	0.19	0.36
RANKING	-	1st	2nd	3rd	5th	4th

5.2. CPS Architecture and Design: Hardware and Software Components

Concept 1 implements an Industry 4.0 cyber-physical architecture. The Physical Layer features a Single Board Computer (e.g., Raspberry Pi 4), an RGB camera, and I2C thermal/humidity sensors. The Cyber Layer runs on Linux, utilizing OpenCV for AprilTags recognition and an MQTT client for SQL and Web communication.

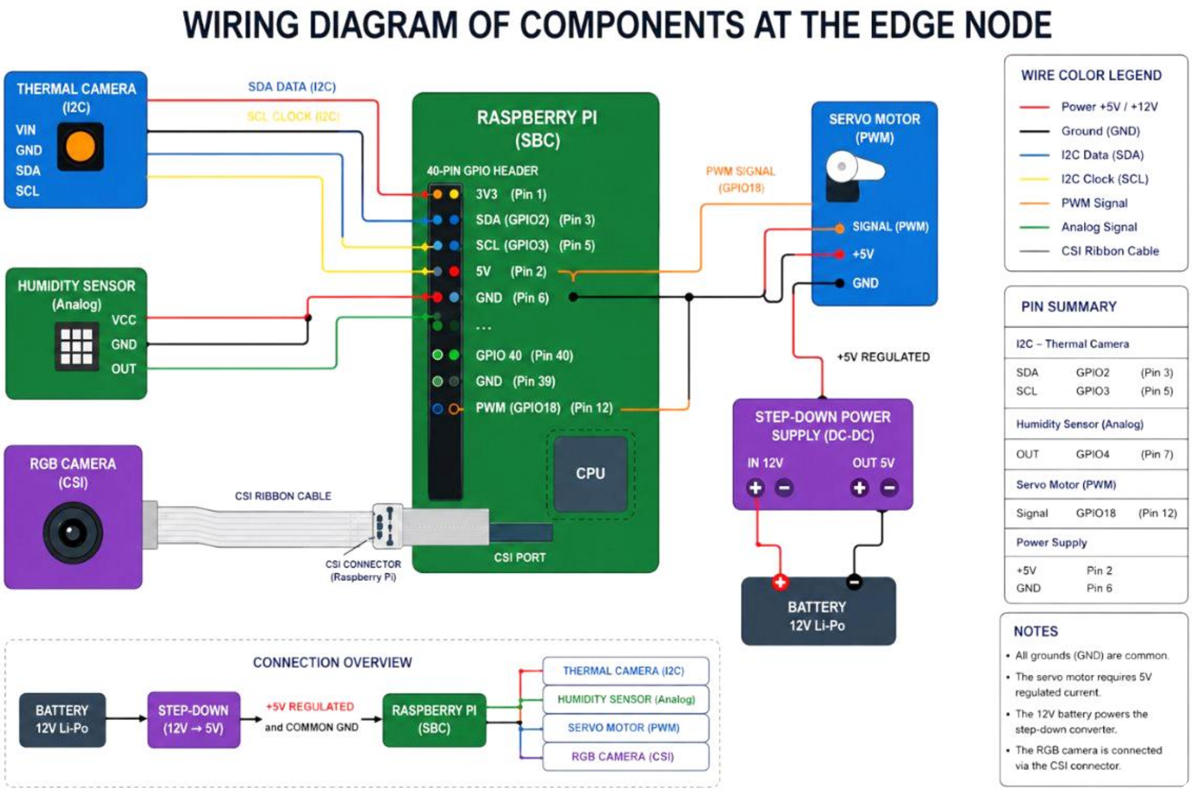

Fig. 2. Electrical wiring diagram of the components connected to the Edge Node.

5.3. Data Flows, Interface, and Core Technical Functions

The information flow is bidirectional and structured around five core technical operations within the Edge architecture:

- Localization: OpenCV AprilTag recognition for X-Y coordinates.
- Thermal Acquisition: I2C radiometric environmental scanning.
- XYZ-Temp Correlation: Fusing visual X-Y data with Z-axis elevation and thermal readings.
- Map Generation: Structuring correlated data into JSON payloads.

- Data Transmission: MQTT communication for Cloud telemetry.

The data exchange with Cloud/Network applications includes:

- Input Data (towards the CPS): List of target coordinates (X,Y), temperature alert thresholds, and remote calibration commands.
- Output Data (towards the Cloud): Live telemetry (X,Y,Z,T,H), battery status, and JSON packets for thermal map rendering. Data transmission is performed through MQTT.

5.4. Clients, Applications, and Roles in Industry 4.0

The CPS design complies with the six Industry 4.0 (I4.0) design principles: interoperability (MQTT), virtualization (Thermal Map), decentralization (Edge Computing), real-time capability, service orientation, and modularity (I2C bus).

Interaction with this CPS is defined through web applications with role-based access rights for different clients:

- QA Quality Auditor (Main Role): Accesses historical SQL reports and the Thermal Map for validating pharmaceutical batches according to GDP regulations [4], [3].
- Warehouse Manager (Client): Monitors fleet status (active AMR location) and warehouse thermal occupancy through a Web Dashboard.
- Maintenance Technician: Monitors hardware parameters such as sensor errors, battery status, and MQTT connection quality.

6. Experimental Validation of Subsystems

The current stage of research focuses on the preliminary experimental validation of key subsystems rather than a fully integrated commercial solution. This "early proof-of-concept" phase is designed to verify the feasibility of using a mobile, CPS-inspired architecture to meet the rigorous demands of GDP thermal mapping.

6.1. Real-time Thermal Inference

To address GDP requirements for automated hotspot alerting, the YOLO26n model was selected for its balance of speed and accuracy on Edge devices. It serves to identify thermal anomalies and risk zones automatically. The thermal experiment was conducted using the NVIDIA Jetson Orin Nano as the primary Edge Computing node and InfiRay Mini2 640 Thermal Camera. This experiment was conducted in a closed room, static testing under controlled lighting and temperature (25°C). Metrics: Inference latency (ms) and throughput (FPS).

The thermal sensing subsystem utilizes a 640×512 uncooled vanadium oxide detector (12μm pixel pitch) featuring a sensitivity of ≤40mK @ 25°C within the 8-14μm spectral band. Inference is accelerated via NVIDIA TensorRT 10.3.0, optimized for FP16 precision.

The physical configuration of the thermal sensing subsystem is depicted in Fig.3. This overview highlights the edge computing hardware and the thermal imaging apparatus in their static testing environment, culminating in a sample frame of the real-time inference output that confirms the successful deployment of the TensorRT-accelerated model.

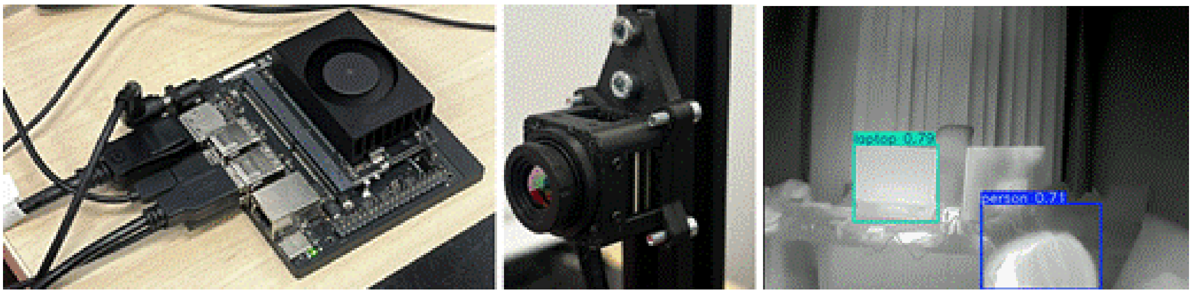

Fig. 3. Experimental setup: (left) NVIDIA Jetson Orin Nano edge node;
(center) Thermal camera; (right) Real-time YOLO26n inference on the thermal stream.

To quantify these performance disparities, Table 4 details the specific inference latency (ms) and throughput (FPS) metrics recorded for both deployment frameworks. We compared the baseline PyTorch implementation against a hardware-optimized TensorRT engine. The results indicate that FP16 precision on the Orin Nano is a better path for real-time AMR operation.

Table 4. Performance comparison PyTorch vs TensorRN

Model	Backend	Precision	Inference Latency	End-to-End FPS
YOLO26n	PyTorch	FP32	~ 170 ms	5 FPS
YOLO26n	TensorRT	FP16	~ 13.4 ms	27 FPS

Temperature values are obtained by converting the camera's radiometric signal using a manufacturer-provided calibration curve based on the principles of thermal radiation. The Stefan-Boltzmann law, adapted for micro bolometric sensors, states that the total power radiated per unit area is proportional to the fourth power of absolute temperature:

$$j \quad = \varepsilon \sigma T^4 \tag{1}$$

Where: j is radiant exitance $\left(W \cdot \{m\}^{\{-2\}}\right)$, ε is emissivity, σ is the Stefan-Boltzmann constant $\left(5.67 \times 10^{-8}, \frac{W}{cdotm^{-2}} \cdot K^{\{-4\}}\right)$, and T is temperature (K)

In the current POC, the USB UVC interface provides an 8-bit stream. Future integration via UART will allow for raw 14-bit data extraction, where temperature T is calculated per pixel:

$$T = \frac{DN - B}{R} \tag{2}$$

(Where DN is the Digital Number, B is Bias, and R is Responsivity).

6.2. Visual Localization and Pose Estimation

For a mobile mapping kit to replace static sensors, every thermal reading must be mapped to a precise 3D coordinate. We utilized AprilTags (tag16h5 family), of size 126 mm to provide absolute positioning relative to warehouse shelving and to determine the maximum angular displacement (Roll and Pitch) at which stable pose estimation is maintained for "on-the-spot" thermal measurements.

Experimental Conditions:

- Camera: Myria MY8077 (tested at 640x480 resolution to prioritize low latency).
- Test Range: 0.5-4.0 m for distance, 1 and 2 m for detection on various orientations.
- Environment: Room with under illumination ~300 lux.

Visual localization is executed via Python using the pupil_apriltags, cv2, NumPy, and math libraries to perform 6-DOF (degrees of freedom) pose estimation and absolute 3D positioning (X, Y, Z) relative to warehouse shelving. The distance d to a tag is calculated via the Euclidean norm of the translation vector $t\rightarrow$:

$$d = \sqrt{t_x^2 + t_y^2 + t_z^2} \tag{3}$$

Orientation (Roll, Pitch, Yaw) was derived from the rotation matrix R using the following Euler conversion:

$$sy = \sqrt{R_{0,0}^2 + R_{1,0}^2} \tag{4}$$

$$\theta_y = atan2(-R_{2,0}, sy) \tag{5}$$

The system successfully identified multiple tags simultaneously, providing distance and orientation overlays with stability.

To illustrate the practical application of this localization method, Fig.4 provides a sample frame from the camera feed, highlighting the 6-DOF pose estimation wireframes and the system's operational frame rate.

Fig. 4. AprilTag detection showing the 3D wireframe and the "FPS: 39" indicator.

Key Performance Observations:

- Spatial Accuracy: The system demonstrated sub-centimeter precision at close range (< 1 m), with the spatial error margin remaining within ±2% at a 3-meter distance.
- Processing Throughput: Real-time performance was sustained at 39 FPS by leveraging multi-threading (4 threads) and a quad_decimate parameter of 2.0.
- Detection Robustness: The implementation of a stringent confidence filter (threshold > 35) effectively mitigated all false positive or "ghost" detections.
- Effective Field of View (FOV): The operational FOV was measured at 70° at a 1-meter distance, observing a slight reduction to 66° at 2 meters.

Future Integration Considerations:

- Active Illumination: The integration of an onboard light source is required to maintain detection reliability in low-contrast operational zones.
- Marker Orientation: Fiducial tags must be optimally tilted to ensure favorable incidence angles relative to elevated camera trajectories.

7. Conclusions, Current State and Future Work

This development demonstrates that a prototype architecture for an AMR-based monitoring platform is technically feasible at the subsystem level.

The original contributions of this work include:

- Structured methodology: A multi-criteria selection process for the technological solution (Concepts C1-C5).
- Precision positioning: The application of April Tags for absolute positioning with sub-centimeter stability in industrial environments.
- Optimized Edge Architecture: A low-cost Edge Computing setup (NVIDIA Jetson Orin Nano + TensorRT) specifically optimized for real-time GDP validation tasks.
- Mobile Mapping Framework: Demonstration of a mobile thermal mapping kit as a viable, high-fidelity alternative to traditional static sensors.

Future Works include:

- Implementing UART connections for raw 14-bit data extraction for processing the region temperature.
- Correlating RGB and thermal images for precise physical point temperature collection.
- Designing the rotational positioning system for autonomous camera orientation.

The current study is limited to preliminary subsystem validation and does not yet include full AMR integration, autonomous navigation validation, long-duration warehouse deployment, or complete 3D thermal map reconstruction.

8. Bibliography

[1] C. Fu, V. Gonzalez, and R. Lovreglio, "Automated construction indoor monitoring using autonomous mobile robots," Automation in Construction, vol. 119, 2020.

[2] C. Porras-Amores, F. R. Mazarrón, and I. Cañas, "Study of the Vertical Distribution of Air Temperature in Warehouses," Energies, vol. 7, no. 3, pp. 1193-1214, 2014.

[3] E. A. Lee, "Cyber Physical Systems: Design Challenges," in Proc. 11th IEEE Int. Symp. Object-Oriented Real-Time Distributed Computing (ISORC), Orlando, FL, USA, 2008.

[4] European Commission, "Guidelines of 5 November 2013 on Good Distribution Practice of medicinal products for human use," Official Journal of the European Union, Nov. 2013.

[5] "Five Key HVAC Design Guidelines for Pharmaceutical Facilities." [Online]. Available: https://accurateairinc.com/five-key-hvac-design-guidelines-for-pharmaceutical-facilities/. [Accessed: Apr. 26, 2026].

[6] H. V. Gangadharappa et al., "Temperature Mapping Study on Cold Room," International Journal of Pharmaceutical Sciences Review and Research, vol. 44, no. 1, pp. 265-274, 2017.

[7] I. Tabašević, D. D. Milanović, V. Spasojević Brkić, and M. Misita, "Temperature Mapping in Pharmaceutical Warehouse - Framework for Pharmacy 4.0," in Proc. X Int. Conf. Industrial Engineering and Environmental Protection, Zrenjanin, Serbia, 2020.

[8] N. Kumar and P. K. Jha, "Temperature excursion management: A novel approach of quality system in pharmaceutical industry," Saudi Pharmaceutical Journal, vol. 25, pp. 1079-1086, 2016.

[9] R. Bogue, "Mobile robots in warehouses: Developments and trends," Industrial Robot: The International Journal of Robotics Research and Application, vol. 49, no. 1, pp. 1-6, 2022.

[10] R. Keith and H. M. La, "Review of Autonomous Mobile Robots for the Warehouse Environment," arXiv preprint arXiv:2406.08333, 2024.

[11] World Health Organization, Good Storage and Distribution Practices for Medical Products, WHO Technical Report Series No. 1025, Annex 7, Geneva, Switzerland, 2020.

[12] World Health Organization, Model Guidance for the Storage and Transport of Time- and Temperature-Sensitive Pharmaceutical Products, WHO Technical Report Series No. 961, 2011.

[13] World Health Organization, "Supplement 8: Temperature Mapping of Storage Areas," WHO Technical Report Series No. 961, Annex 9, Geneva, Switzerland, 2011.

[14] X. Wang, "An Analysis of Temperature Control Management in the Pharmaceutical Supply Chain," Advances in Economics Management and Political Sciences, vol. 133, pp. 49-54, 2025.

[15] Y. Ale et al., "IoT in Revolutionizing the Pharmaceutical Sector: Applications and Challenges," Biomedical and Pharmacology Journal, vol. 18, Special Issue, 2025

Modular Ergonomic Desk: Design, Analysis, and Optimization

NĂSTASE Marian-Sebastian, CIOBĂNESCU Codruț-Decebal, GIURGI Darius-Mihai, DUMITRESCU Andrei

Faculty: Industrial Engineering and Robotics, Program: Industrial Design and Innovative Products, master's degree second year, e-mail: nastase_sebastian@yahoo.com

ABSTRACT: The aim of this research is to design a modular ergonomic desk that combines ergonomics, aesthetics, and structural efficiency. The study examines the key dimensions, proportions, forms, and tolerances, alongside safety, comfort, and usability considerations. Various design concepts were developed to capture desirable visual attributes while avoiding undesirable ones, with the final concept selected using decision matrices. Materials and surface treatments were specified, evaluating their advantages and disadvantages. Structural analyses were performed to verify the desk's mechanical performance. These results demonstrate that the proposed design offers a practical, user-centered solution that addresses both ergonomic requirements and market needs.

KEY WORDS: Modular desk, ergonomics, Industrial Design

1. Introduction

Considering the need to develop an ergonomic, functional product adapted to current user requirements, the detailed design stage plays an essential role in transforming the concept into a feasible technical solution. In the case of the modular ergonomic desk, this stage aims to define the product's constructive, dimensional, and aesthetic characteristics. The paper seeks to establish optimal proportions and dimensions, evaluate ergonomic and safety conditions, and develop a coherent design adapted to the targeted market segment. In addition, the materials and the main load acting on the product are analyzed in order to ensure functionality and user comfort.

2. Status of the product related topics

Now, in the present, the furniture design for offices is strongly influenced by the need to adapt to a sedentary lifestyle and to meet users ergonomic requirements. Current studies highlight the importance of maintaining proper posture and alternating working positions, which has led to the development of height-adjustable desks. At the same time, there is a growing trend toward customizable solutions that allow the workspace to be arranged according to individual needs [1].

From a constructive point of view, most existing products are built with simple shapes and standardized dimensions to ensure compatibility and production efficiency. The materials most used are wood, metal or composites, due to their optimal balance between strength, cost, and durability. However, many existing solutions have limitations regarding configuration flexibility and the integration of multiple functions, highlighting the need for the development of innovative, adaptable, and ergonomic products. Considering these aspects, the development of a fully customizable modular desk adapted to the diverse needs of users is proposed [2].

3. Proportions, Shapes, Dimensions, and Tolerances

The product proportions were established by considering ergonomic principles and referencing the standard dimensions of office furniture, to ensure user comfort during use. The height of the desktop, as well as the overall dimensions, were determined to allow a correct body posture and an efficient use of the workspace.

The adopted shapes are predominantly simple and geometric, based on straight lines and clearly defined volumes, which facilitates both the integration of the modules and the manufacturing process. The modular concept requires formal coherence between components, each element being designed to integrate harmoniously into the overall assembly.

The product dimensions were defined to enable flexible desktop configuration through the use of standardized modules. These can be added or removed depending on the user's requirements, thus contributing to the adaptability of the system.

Regarding tolerances, functional clearances were provided between the modules and the main structure to facilitate rapid assembly and disassembly. Their values were selected in accordance with the manufacturing methods used and the need to ensure stable joints without compromising the rigidity of the assembly. Table 1 presents the proportions of the modular desk.

Table 1. Dimensional Proportions of the Modular Desk

Length: 1550 mm	Number and module types: 2
Width: 825 mm	Number of standard modules: 18
Height: 750 mm	Number of heavy-load modules: 6
Thickness of the table: 25 mm	Number of designed modules: 10
Maximum height: 1350 mm	Module dimensions: 250x200 și 250x150

4. Evaluation of Ergonomic Conditions

User safety was a fundamental criterion in the design of the modular desk. From an electrical standpoint, the use of a 12V supply voltage significantly reduces the risk of electric shock, with the system being classified as a low-voltage installation. The connections are insulated and integrated into the structure of the desktop, while the presence of overload and moisture protection fuses ensure automatic shutdown of the power supply in hazardous situations. From a mechanical perspective, the lifting system is stable and controlled, and the rounded edges with secure joints help prevent injuries.

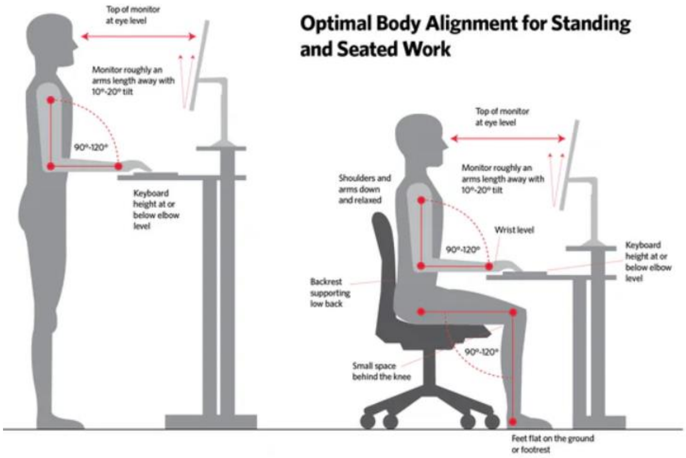

Fig. 1. Ergonomic Conditions of the Modular Desk[3]

The product sizing was based on standard anthropometric data (ISO 9241, EN 527) in order to ensure correct posture both in sitting and standing positions. The desktop height allows maintaining an approximate 90° angle at elbow level, ranging between 65-75 cm for the seated position and 95-115 cm for the standing position. The electric adjustment system facilitates the transition between positions, contributing to the reduction of sedentary behavior and muscular discomfort [4].

The product is adapted to the user's physical limits by eliminating mechanical effort, as height adjustment is performed electrically. The modular configuration allows easy handling of components, which are secured using tight fit pins and removed with the aid of a dedicated tool, thereby reducing effort and operational complexity.

Product use is intuitive, requiring no operating manual. The modules can only be assembled in a single correct configuration, while the electrical connection system prevents polarity reversal through the position of the contacts, eliminating the risk of incorrect use.

User comfort is ensured through height adjustability and the modular configuration of the desktop, which allows the workspace to be adapted to individual needs. This flexibility contributes to efficient task organization and the creation of an ergonomic and adaptable working environment.

Compatibility between control elements and indicators is achieved through a simple interface consisting of three buttons and a display. The controls are ergonomically positioned, while visual and functional feedback enables fast and clear interaction.

5. Designing Product Aesthetics

In the design phase of the modular desk, the establishment of desired and undesired visual attributes represents an essential element in defining the product identity, these being determined according to the targeted market segment. The undesired attributes are directly associated with the desired ones, forming complementary pairs, as presented in Table 2. At the same time, they are prioritized according to their area of influence on the different components and functionalities of the product. This organization enables an efficient approach to the design process by focusing on the relevant attributes to each analyzed area [5].

Table 2. Desired and undesired attributes

Area of influence	Desired attributes	Undesired attributes
Functionality and reliability (very high importance; essential attributes to ensure a pleasant user experience)	Stable	But not heavy
	Reliable	But not rigid
	Compact	But not overly dense
	Efficient	But not cluttered
Visual perception (high importance; design influences buyer perception)	Attractive	But not kitsch
	Elegant	But not exaggerated
	Refined	But not opulent
	Premium	But not extravagant
Aesthetic trend (these attributes reflect the conveyed artistic values)	Minimalist	But not monotonous
	Contemporary	But not fashionable
Intuitiveness and user experience (attributes influencing the efficiency of product use)	Intuitive	But not obvious
	Logical	But not restrictive
	Easy to use	But not obvious
Tactile interaction (high importance; these attributes enhance the sensation at touch)	Smooth	But not glossy
	Uniform	But not without texture
	Fine	But not slippery
Innovation and adaptability (these attributes reflect the level of progress and uniqueness of the product)	Innovative	But not eccentric
	Revolutionary	But not unnecessarily complex

For the design phase of the modular desk, three distinct concepts were proposed, which are to be evaluated based on criteria such as balance, proportion, harmony, compactness, complexity, elegance, and originality.
Concept 1 features a clear geometric form and a robust structure, combining stability with minimalism. The modularity and the discreet integration of electrical components ensure a clean and intuitive design.
Concept 2 stands out through the clear segmentation of the desktop surface and the use of color to emphasize customization, offering an attractive, flexible, and expressive appearance while maintaining visual balance.
Concept 3 adopts a unified visual language that is minimalist and elegant, with discreet modularity and a neutral color palette. It highlights material quality and creates a premium, calm, and refined design.

Table 3. Concept Evaluation

Comparison Criteria	Importance	Concept 1 		Concept 2 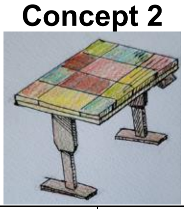		Concept 3 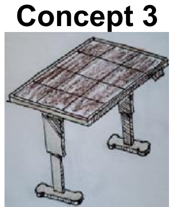	
Balance	15	5	75	4	60	4	60
Proportion	13	5	65	5	65	5	65
Harmony	10	5	50	3	30	4	40
Compactness	12	4	48	4	48	4	48
Complexity	10	5	50	5	50	4	40
Elegance	10	4	40	3	30	2	20

Originality	10	4	40	4	40	4	40
Accessibility	8	4	32	4	32	4	32
Adaptability	12	5	60	5	60	5	60
TOTAL	100	-	460	-	415	-	405

After the evaluation, Concept 1 achieved the highest score and will be further developed. It combines modularity, ergonomics, and a minimalist design, offering an intuitive and adaptable solution. The neutral color scheme with subtle accents highlights the product's technological and premium character.

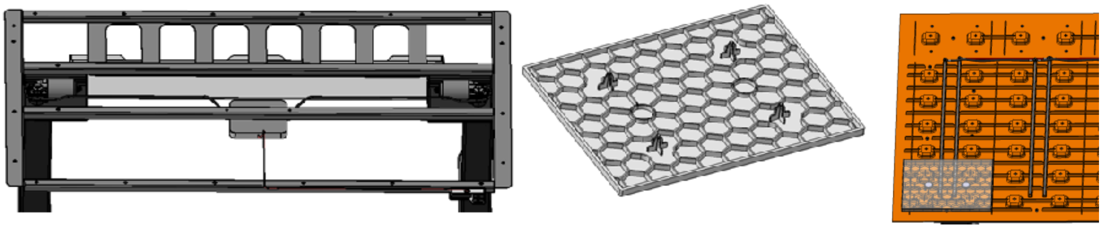

Fig. 2. Metal Frame, module, and base plate

The table of the modular desk consists of a main component and interchangeable modules, fixed using pins and screws to ensure a quick and secure configuration. The entire assembly is supported by a robust metal structure, providing stability and enabling easy integration of the modules. Vertical adjustment is achieved through a telescopic mechanism supplied by Ketterer, mounted on the metal frame. This combination of a modular desktop, adjustable legs, and a solid structure allows ergonomic adaptation of the workspace and full flexibility of configurations [6].

The modular desk includes a variety of ergonomically designed modules intended for quick access and comfortable use: monitor/laptop stand, office accessories, headphone holder, USB charging devices, an adjustable drawing module, and an integrated lamp. Each module is easily attached to the main desktop, allowing rapid addition, removal, or reconfiguration depending on the user's activities. The modular design optimizes the workspace and facilitates organization for both professional, recreational, and creative tasks. All modules comply with ergonomic principles and contribute to a functional and aesthetic overall system.

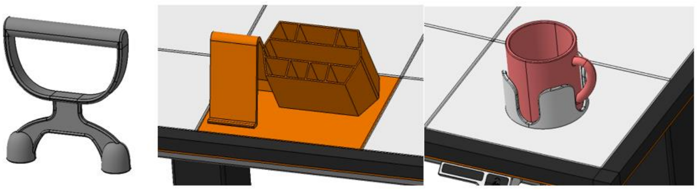

Fig. 3. Module overview

6. Material selection and surface treatments

The materials used for the modular desk are selected based on technical, ergonomic, and aesthetic requirements, considering strength, weight, electrical properties, and cost. Durability and user comfort are prioritized, while standardized elements such as screws, connectors, rivets, and nuts are purchased from specialized suppliers.

Table 4. Material selection

Component	Proposed material	Characteristics	Treatments	Advantages	Disadvantages
Module	ABS	Aesthetic quality and surface finish	-	Lightweight; impact resistant; easily colorable; easy to injection	Sensitive to high temperatures; not UV resistant without treatment;
Table		Reduces weight			
Frame					

Component	Proposed material	Characteristics	Treatments	Advantages	Disadvantages
Corner connectors				mold; low cost	moderate resistance to organic solvents
Transverse stiffening element	Steel	Density ~7.85 g/cm³; high tensile and compressive strength; produced by hot or cold rolling; easy to weld and machine.	Zinc coating, painting, galvanizing, quenching and tempering	High mechanical strength; low cost; widely available	High weight; susceptible to corrosion
Lateral stiffening element					
Leg connection element					
Cable management system	Steel/ Stainless steel	Flat rolled sheet; variable thicknesses; good weldability and formability.	Zinc coating, painting	Easy to process; good strength; corrosion protection possible	-
Central unit mounting plate					
Leg housing					
Telescopic housing fastening elements					
Mechanism housing fastening element	POM (Delrin)	High wear and fatigue resistance; dimensional stability; produced by extrusion or injection molding.		Lightweight; impact-resistant; easily colorable; suitable for injection-molded parts; low cost	Sensitive to high temperatures; not UV-resistant without treatment; moderate resistance to organic solvents
Desk leg foot	Steel/ Stainless steel	High tensile and compressive strength; produced by hot or cold rolling; easy to weld and machine.	Zinc coating, painting, galvanizing, quenching and tempering	High mechanical strength; low cost; widely available	High weight; susceptible to corrosion
Ground contact element	ABS	Aesthetic quality and surface finish Injection-molded plastics	-	Lightweight; impact-resistant; easily colorable; suitable for injection-molded parts; low cost	Sensitive to high temperatures; not UV-resistant without treatment; moderate resistance to organic solvents
Plastic elements attached to the desk foot					
Electrical rail	Copper	Very high electrical conductivity;	-	Very high electrical conductivity;	Higher cost

Component	Proposed material	Characteristics	Treatments	Advantages	Disadvantages
		density ~8.96 g/cm³; malleable and ductile; produced by casting and rolling.		low energy losses; ductile and malleable; easy to process	
Magnetic metal elements for modules	Steel	High magnetic permeability; produced by casting and rolling.	-	Strong magnetic attraction; low cost; easy to process	Heavier than other materials

7. Description and calculation of the main product loads. Analytical verification

The main load analyzed in the case of the modular desk is the bending of the table, generated by the loads applied during use, such as work equipment (laptop, screen, etc.). This load is critical because it directly influences structural strength, stability, and user comfort. To evaluate the mechanical behavior, a static analysis using the finite element method was performed, considering a uniformly distributed load equivalent to a mass of 100 kg, representing an unfavorable but realistic operating condition.

The analysis was carried out using ANSYS software, starting from the simplification of the 3D geometry of the desktop to allow efficient discretization. The rest of the structure was considered rigid. The material used for the desktop is ABS, with mechanical properties obtained from MatWeb databases. For the accurate modeling of the contacts between the modules and the base plate, the fixing pins were replaced with equivalent springs, determined through a static analysis that evaluated the displacement of the pins when a force of 1 N acted upon them. Based on the resulting displacement, spring stiffness was determined. The model was discretized using a mixed mesh (Tri3 and Quad4 elements), ensuring an optimal compromise between accuracy and geometric flexibility.

The simulation conditions were defined by fixing the edge of the plate to restrict its displacement. In addition, displacement-type boundary conditions were imposed to limit the degrees of freedom of the modules relative to the frame, blocking movements along the X and Y directions. For the base plate, displacement along the Z direction was restricted in the contact areas with the metal structure. The load was applied in the form of uniformly distributed pressure over the desktop surface, corresponding to a total mass of 100 kg.

To evaluate the structural behavior, three loading cases were analyzed: the stress of a 100 kg mass uniformly distributed over the entire table surface, the stress of a 20 kg mass on a single upper module, and the stress of the same mass distributed over a group of six modules. These scenarios allowed the analysis of both the global and local structural loads.

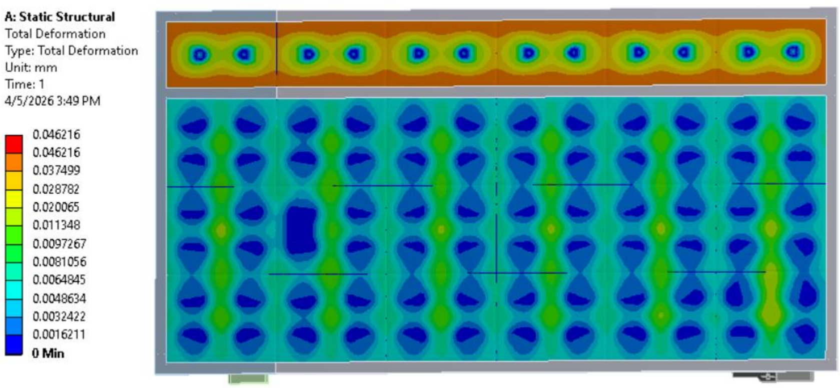

Fig. 4. Total deformation of the table under a 100 kg load

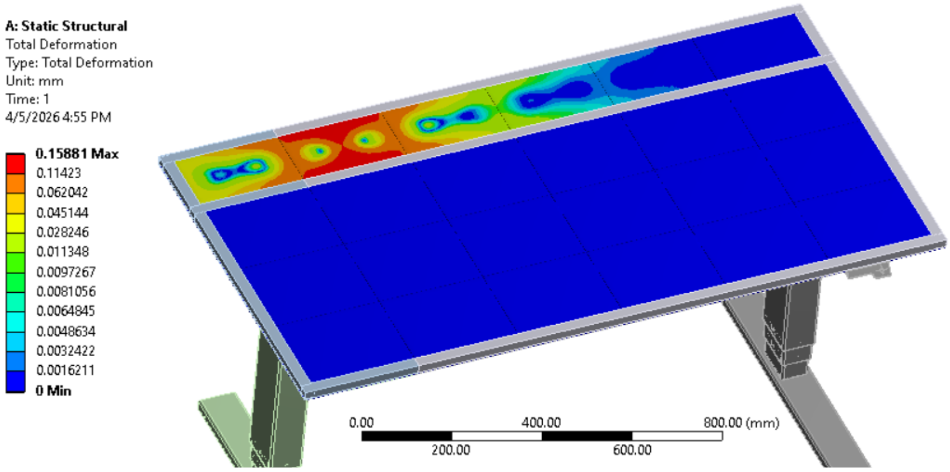

Fig. 5. Total deformation of the table under a 20 kg load applied to a single module

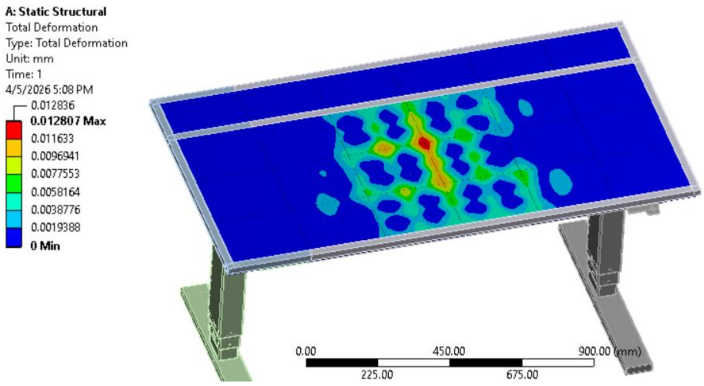

Fig. 6. Total deformation of the table under a 20 kg load applied to six modules

8. Conclusions

The proportions, shapes, dimensions, and tolerances were established for a modular ergonomic desk designed to meet ergonomic, functional, and aesthetic requirements. The development process included ergonomic analysis, concept generation, and the selection of a final solution based on criteria such as balance, harmony, compactness, elegance, originality, and adaptability. The final concept integrates a minimalist design with a modular structure, enabling flexible workspace configuration and improved user comfort through interchangeable components.

Materials and manufacturing solutions were selected according to structural, electrical, and aesthetic requirements, ensuring a balance between durability, manufacturability, and cost. A finite element analysis performed in Ansys confirmed the structural rigidity and stability of the desk under different loading scenarios, with results remaining within acceptable limits. Overall, the proposed modular desk provides an ergonomic, adaptable, and efficient solution for modern working environments.

9. References

[1]. Arnold, A.E.; Coffeng, J.K. et al. (2016), "The relationship between job satisfaction and productivity-related costs: A longitudinal analysis.", J. Occup. Environ. Med., 58, 874–879.

[2]. Tew, G.A., et al. (2015), „Systematic review: height-adjustable workstations to reduce sedentary behaviour in office-based workers." Occupational Medicine, vol. 65, no. 5, pp. 357–366.

[3] CALIFORNIA STATE UNIVERSITY, EAST BAY. Ergonomics: General Information [online]. Available at: https://www.csueastbay.edu/riskmanagement/ergonomics/general-information.html [Accessed: 8 April 2026].

[4]. Shikdar, A. A., Al-Kindi, M. A. (2007), Office Ergonomics: Deficiencies in Computer Workstation Design, International Journal of Occupational Safety and Ergonomics, Vol. 13, No. 2, pp. 215–223, DOI: 10.1080/10803548.2007.11076722.

[5]. Dumitrescu, A. (2007), Experiment for Testing the Concept of Product Personality, Scientific Bulletin of Politehnica University of Bucharest, Series D, Vol. 69, No. 3, pp. 55-62, ISSN 1454-2358

[6]. Pheasant, S., Haslegrave, C. (2006), Bodyspace: Anthropometry, Ergonomics and the Design of Work, CRC Press, Boca Raton, ISBN 978-0-415-28520-9

Mobile Emission Filtration System for Electrical Discharge Machining

BĂRĂSCU Maria-Alexandra, **CHIFELEA Alina-Ștefania**, **GRIGORE Irina**, **SIMION Dragoș-Andrei** and **GHICULESCU Liviu-Daniel**
Faculty of Industrial Engineering and Robotics, National University of Science and Technology Politehnica Bucharest (UNSTPB), specialization: Nanostructure Engineering and Unconventional Processes , 1st Year,
e-mail: irina.grigore2411@gmail.com

ABSTRACT: Electrical discharge machining (EDM) uses mineral oils as a dielectric fluid, whose thermal decomposition generates harmful emissions in the form of vapors and aerosols. This paper details the CAD design of a mobile three-stage extraction and filtration system aimed at reducing the impact of these pollutants on the work environment and operator health. The sealed equipment integrates a metallic demister for oil coalescence and recovery, followed by HEPA and activated carbon filters to capture submicron particles and volatile compounds. The modular structure and optimized airflow ensure safe and efficient operation.

KEYWORDS: electrical discharge machining (EDM), industrial emissions, filtration systems, environmental protection

1. Introduction

Electrical discharge machining (EDM) technology is essential in the machine building industry for manufacturing high-precision parts. [1], [12] The process uses mineral oils as a dielectric fluid, but the high local temperatures generated lead to their vaporization and thermal decomposition. [8], [11] The result is the formation of emissions in the form of vapors and aerosols that affect operator health and air quality, requiring the use of dedicated filtration systems to comply with occupational safety standards. [9], [10]

The main objective of this paper is the design of a mobile filtration system capable of efficiently capturing and neutralizing these emissions directly at the source. We aim to develop a modular and robust system, dimensioned to successively capture smoke, fine particles, and volatile gaseous compounds, while simultaneously ensuring high maneuverability in the workspace.

2. State of the Art

The analysis of the current state of the art regarding the filtration of emissions generated by electrical discharge machining highlights a growing concern for occupational health and industrial environmental protection. [9], [11] In the context of technological evolution, filtration systems have transitioned from rudimentary general ventilation solutions to highly efficient local extraction units. [1], [16] The main challenge remains the diversity of emitted pollutants, which includes both micrometric-sized solid metallic particles and aerosols resulting from the vaporization of the dielectric fluid, thus requiring multi-stage filtration systems. [3], [14], [15]

Following these technological solutions, specialized literature and recent patent documentation highlight a clear direction oriented towards the direct capture and treatment of vapors and aerosols generated by dielectric vaporization.

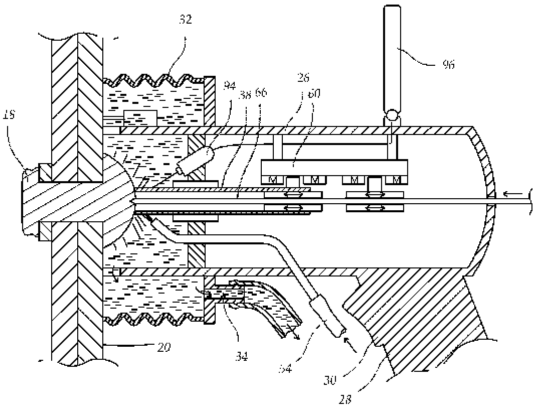

Fig. 1. The Hand-held device [5]

Patent US20100096365A1 – „Hand-held electro-discharge device" [5] describes a portable electrical discharge device used for removing metallic fasteners. The documentation emphasizes that the EDM process generates vapors, aerosols, and micro-particles resulting from the extremely high temperatures produced by electrical discharges. The proposed solution includes an integrated system for capturing and exhausting emissions directly from the electrode area, aiming to reduce workplace contamination and protect the operator.

Patent CN102009236B – „Spindle hood for electric discharge forming machine" [2] presents a hood-type structure for electrical discharge machines, designed to capture and exhaust the smoke generated during electrical discharges. The structural solution utilizes smoke guiding channels and purification elements to reduce aerosols and fine particles resulting from the vaporization of the dielectric fluid and the machined material. The system contributes to operator protection and the reduction of workplace contamination.

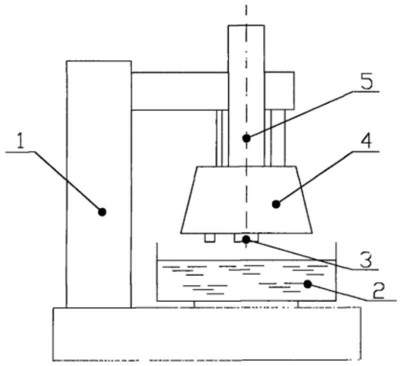

Fig. 2. Diagram of the EDM machine with the device installed [2]

3. Strategic marketing

Dividing the product market into market segments is based on the particularities in the level of demands regarding the quality and structure of the offer, the assertion and manifestation of demand from buyers, the frequency and average size of the purchase, etc. In any type of enterprise, the role of marketing is to contribute to a better understanding of its audience in order to adapt it to the external environment and achieve maximum efficiency. [4]

3.1. Identification of market opportunities

a. Customer needs portfolio

Three needs will be identified, numbered N1, N2, N3:

- N1: The need to ensure the occupational health of operators. The EDM process generates harmful vapors and aerosols from the thermal decomposition of mineral oils, which must be eliminated to prevent respiratory ailments. [9], [10]
- N2: The need to comply with industrial environmental protection standards. Air quality in production workshops must fall within legal limits, requiring dedicated filtration systems. [11]
- N3: The need to optimize workspace and production flexibility. There is a demand for mobile and versatile systems that can serve various EDM machines without structural modifications. [2], [5]

b. Opportunities / Products

„*Competition today is more than ever based on product development capabilities.*" [4]

The products that fully or partially satisfy these needs are represented by Mobile Emission Filtration Systems (IMF-EDM). These are specialized equipment designed to provide efficient local capture, using a three-stage filtration system (demister, HEPA, and activated carbon) to neutralize pollutants directly at the source. [6], [7] The market opportunities for the proposed system are represented by the increased demand for a safe working environment and the need to comply with occupational health standards in the machine building industry. [15]

c. Target customers for product distribution

Selecting customers involves identifying actual and potential clients who could benefit from the mobile filtration system.

The use of the equipment is addressed to the following types of customers:

1. Enterprises in the machine building industry, especially SMEs utilizing electrical discharge machining technologies for high-precision parts;
2. Research and educational institutions (Universities):
   - students - occasional use in laboratories;
   - professors/researchers - use for experimental purposes;
   - laboratories specialized in unconventional processes - frequent use.

3.2. Formulating the mission for the development of the selected product

Table 1 presents the customer selection matrix.

Table 1. Customer selection matrix

Customer Category	Lead Users	Average Users	Occasional Users	Centers
Category 1 (Industry/SMEs)	8	3	2	
Category 2 (Research laboratories)	2	5	2	1
Category 3 (Education/Students)	1	2	6	

* A rank-type scoring system was used for the Customer selection matrix, with a grading scale from 1 to 10.

Table 2 represents the guide for conducting the customer needs identification interview for the mobile filtration system (IMF-EDM) product.

Table 2. Guide for conducting the customer needs identification interview for the IMF-EDM product

Client: Address: Phone: Willing to collaborate? Yes / No	Interviewers: Date: Current uses: User's occupation:	
Question	Client Statement	Interpreted Need
1. Do you consider local filtration to be an efficient solution for improving air quality?	a) Yes; b) No	Solution effectiveness
2. Do you use liquid dielectric electrical discharge machines in your activity?	a) Yes; b) No	Process relevance
3. How often do you use EDM machines in a week?	a) Daily; b) Several times; c) Occasionally; d) Rarely	Exposure frequency
4. What are the main reasons you would use a filtration system?	a) Operator health; b) Environmental standards; c) Workshop cleanliness; d) Odor reduction; e) Others	Needs prioritization
5. Are you satisfied with the currently existing general ventilation systems?	a) Yes, entirely; b) Yes, mostly; c) Not really; d) No	Current satisfaction level
6. Do you think a mobile system can help you maintain industrial hygiene standards?	1 2 3 4 5 (Likert Scale)	Importance of mobility
7. What are the main selection criteria?	a) Filtration efficiency; b) Noise level; c) Mobility; d) Cost; e) Reliability; f) Others	Purchasing criteria
8. Are you willing to pay a higher price for a system with real-time air quality monitoring?	a) Yes; b) No	Investment readiness
9. Do you believe that reducing emissions at the source contributes to increasing process precision by eliminating sediments?	a) Yes; b) No	Technical impact

4. Establishing the specifications

In order to design a mobile emission filtration system generated in the electrical discharge machining (EDM) process, it is necessary to define a coherent set of technical and functional specifications, adapted both to the process requirements and the manufacturing possibilities in a university laboratory environment. In this case, the specifications must ensure a balance between performance, structural simplicity, and low costs.

The electrical discharge machining process involves the use of electrical discharges in the presence of a dielectric fluid, which leads to the appearance of emissions in the form of aerosols, vapors, and fine particles resulting from the decomposition of the liquid and the erosion of the machined material. [3], [14] These pollutants necessitate the design of a system capable of ensuring their efficient capture and filtration directly from the work area, thus reducing the impact on the environment and on the operators. [11]

From a functional point of view, the proposed system must be mobile, compact, and easy to integrate in the proximity of the EDM machine. Mobility is ensured by mounting it on a frame equipped with wheels, which allows rapid repositioning according to needs. The dimensions of the system must be kept within a reduced range, on the order of one meter in height and approximately half a meter for the base, so as not to affect the ergonomics of the workspace.

An essential parameter in sizing the system is the suctioned air flow rate, which is established in the range of 500–1000 m^3/h. Choosing this range allows the use of commercial centrifugal fans, which can generate the necessary pressure to overcome the losses in the filtration system without involving high costs or complex industrial equipment. In correlation with the air flow rate, the flow velocity in the ducts must be maintained in an optimal range to avoid particle deposition and excessive pressure losses, using standard diameter ducts of approximately 100-150 mm.

The capture of emissions is carried out locally, as close as possible to the active zone of the EDM process, by means of an extraction hood or a positionable flexible arm. Placing this system at a distance of approximately 20-40 cm from the source allows reducing the dispersion of pollutants into the ambient environment and increases the overall efficiency of the installation.

From the point of view of filtration, the adopted solution consists of a staged system that allows the progressive retention of different types of particles and compounds. The first stage is represented by a Demister filter, designed to capture large particles and protect the subsequent filtration elements. The second stage consists of a fine filter, HEPA type or equivalent, capable of retaining the small-sized particles and aerosols generated in the process. [15] Finally, to eliminate the volatile compounds originating from the dielectric, an activated carbon filter is used, which is an accessible and frequently used solution in similar applications. [6], [7]

The fan represents the active element of the system, being responsible for air circulation through the entire installation. Choosing a centrifugal fan with a power between 200 and 500 W allows ensuring an adequate flow rate and sufficient pressure for the efficient operation of the system, while maintaining an acceptable noise level for the laboratory environment.

Table 3. Requirements-Metrics Matrix

Requirements		Req. imp.	Metrics/ characteristics										
			Air flow	Filtration efficiency	Noise level	Consumed power	Dimensions	Mass	Mobility	Sealing	Filtration type	Maintenance	Safety
			1	2	3	4	5	6	7	8	9	10	11
1.	IMF-EDM captures emissions directly from the work area	5	●	●			●		●	●	●		●
2.	IMF-EDM reduces smoke and aerosols resulting from EDM	5	●	●						●	●		●

3.	IMF-EDM can be moved between multiple machines	4					●	●	●				
4.	IMF-EDM does not produce excessive noise	3			●								
5.	IMF-EDM has low energy consumption	4	●			●							
6.	IMF-EDM allows rapid replacement of filters	4					●				●	●	
7.	IMF-EDM protects the operator	5	●	●						●	●		●
8.	IMF-EDM has a compact construction	3					●	●	●				
9.	IMF-EDM can be built with commercial components	4	●	●	●	●	●				●	●	
10.	IMF-EDM operates stably during the process	4	●	●	●	●				●	●		●

Table 4. Target Specifications

No.	Characteristic size	Type	Rel. Imp.	Units	Limit Val.	Target Val.
1.	Suctioned air flow rate	GTB	5	m^3/h	>500	800
2.	Particle/aerosol filtration efficiency	GTB	5	%	>90	95
3.	Filtration fineness	STB	5	µm	<1	0,3
4.	Consumed power	STB	4	W	<500	300
5.	Noise level	STB	3	dB	<70	60
6.	Suction duct diameter	GTB	3	mm	>100	125
7.	Capture distance from source	STB	4	cm	<40	25
8.	Total system mass	STB	3	kg	<50	35
9.	Overall dimensions	STB	3	mm	<700×700×1500	500×500×1200
10.	Number of filtration stages	GTB	5	-	≥3	3
11.	Filter replacement time	STB	4	min	<20	10
12.	Mobility	GTB	4	Yes/No	Da	Da
13.	Sealed housing	GTB	5	Yes/No	Da	Da
14.	Electrical supply	-	3	V	230	230

The structural construction of the system must be robust, but easy to manufacture, using materials such as steel or aluminum for the frame and sheet metal or plexiglass for the housing. This solution allows the protection of internal components and facilitates access for maintenance and filter replacement.

The evaluation of the system's performance can be carried out by analyzing the filtration efficiency, the reduction of particle concentration in the air, the pressure losses, and the energy consumption. Even in the absence of complex equipment, these determinations can be made through simple experimental methods, using air quality sensors or comparative observations before and after filtration. [13], [17]

5. Conceptual Design

5.1. Definition of system functions

The general function of the mobile emission filtration system for electrical discharge machines (IMF-EDM) is to capture, filter, and exhaust the contaminated air resulting from the electrical discharge machining process, reducing the concentration of harmful particles and metallic vapors to permissible values for the operator and the surrounding environment. [11]

Table 5. System functions

No.	Function Type	Function Description
1.	General function	Elimination of emissions (smoke, fine particles, vapors) generated in the EDM process.
2.	Component function	Multiple 3-stage filtration (demister, HEPA filter, activated carbon filter)
3.	Main functions	a. Filtration of contaminated air from the work area b. Transport of air through the system c. Filtration of solid particles and vapors

		d. Exhaust of clean air into the environment
4.	Critical functions	a. Fine particle filtration efficiency b. Air flow rate c. System sealing d. Operator safety

5.2. Constructive solutions

Based on the performed analysis, the following constructive solutions were identified:

Table 6. Constructive solutions

No.	Constructive Solution	Implementation
1.	Mobile system	Mounting the system on wheels for easy movement between machines
2.	Staged filtration system	Pre-filter, HEPA filter + activated carbon filter
3.	Extraction fan	Ensures the necessary contaminated air flow rate
4.	Flexible capture ducts	Allows positioning near the emission source
5.	Monitoring system	Sensors for particles and air flow
6.	Sealed housing	Reduces losses and increases efficiency
7.	Easy maintenance	Quick access to filters for replacemen

5.3. System block diagram

The block diagram of the filtration system is as follows:

This structure allows the separation of filtration stages and the optimization of each component.

Table 7. Main requirements identified for the IMF-EDM system

User requirement	Importance
Emission elimination	Very high
Mobility	Very high
Low cost	High
Easy maintenance	High
Low noise level	Medium
Operational safety	Very high

5.4. Selection of constructive solution

The selection of the constructive solution for the IMF-EDM system was made based on the analysis of existing patents, user needs, expert consultations, and the established technical specifications.

The analysis of EDM patents highlighted the need for local capture of emissions, the use of multi-stage filtration, and the creation of a compact and sealed construction. [2], [5] These solutions were integrated into the IMF-EDM system concept.

Following the interviews conducted in the marketing chapter, the main requirements were identified: high filtration efficiency, mobility, low noise, and easy maintenance. Thus, a mobile system with three-stage filtration and a centrifugal fan was chosen. [15], [16]

The analysis of requirements and specifications showed that the chosen solution meets the conditions regarding air flow rate, filtration efficiency, mobility, and operator safety, being considered the optimal solution for the IMF-EDM system. [1], [4]

5.5. Conceptual model of the system

At the conceptual level, the mobile emission filtration system resulting from the electrical discharge machining process is composed of the following main elements, represented schematically in figure 3.

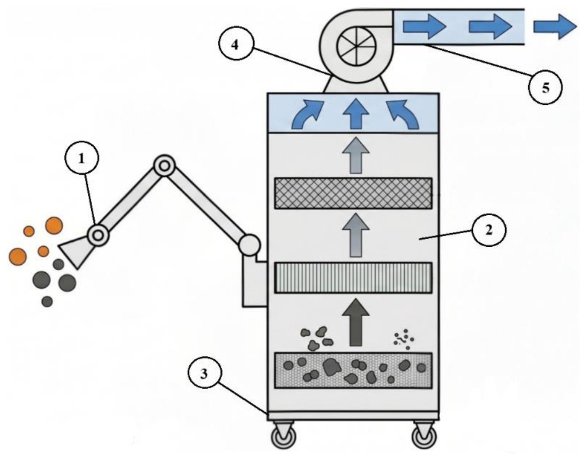

1. Capture system (flexible arm with hood);
2. Filtration unit (multi-staged);
3. Mobile housing;
4. Suction fan;
5. Air exhaust system;
6. Control panel

Fig. 3. Conceptual level EDM emission filtration system

6. Detailed Design

Figure 4 presents the 3D assembly of the mobile filtration system. The capture and purification process of the contaminated air resulting from electrical discharge machining is also described here.

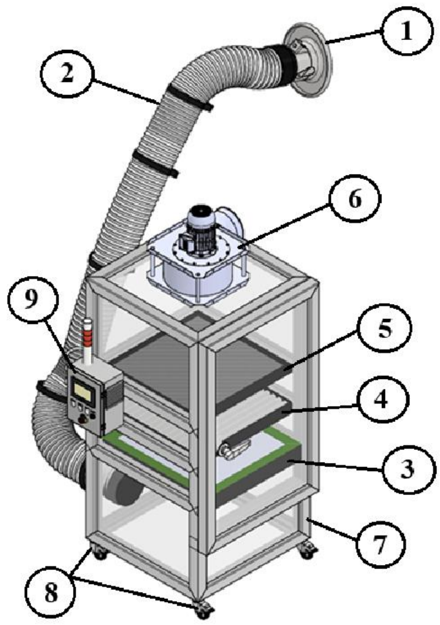

Fig. 4. Mobile emission filtration system assembly

Process description:
The air loaded with dielectric vapors, aerosols, and fine metallic particles is captured directly from the source through the extraction hood (1), being transported through the articulated arm (2). Due to the vacuum created by the centrifugal fan (6) mounted at the top, the airflow is drawn into the sealed enclosure. The first purification stage takes place at the demister (3), which retains large-sized solid particles. The pre-filtered air continues its upward trajectory, passing through the HEPA filter (4), where fine aerosols and oil micro-particles are blocked. The final filtration stage occurs when the flow passes through the activated carbon filter (5), which has the role of absorbing volatile organic compounds and neutralizing the specific burning odors. The entire system is supported by an aluminum frame (7), mobile due to the wheels (8), and the operation and monitoring of the filtration efficiency are centralized using the control panel (9). The clean air, free of toxic compounds, is exhausted back into the workshop environment through the fan's outlet (6).

7. Conclusions

The project validates the necessity and feasibility of a modern technical solution for capturing emissions generated in the electrical discharge machining (EDM) process. The designed equipment directly addresses the risks associated with operator exposure to toxic vapors and aerosols resulting from the thermal decomposition of dielectric liquids.

By integrating a successive three-stage dry filtration system, the installation ensures optimal retention of pollutants, returning clean air to the workshop premises.

8. References

[1]. Abbas, N. M., Solomon, D. G. and Bahari, M. F. (2007), „A review on current research trends in electrical discharge machining", International Journal of Machine Tools and Manufacture, vol. 47, no. 7, pp. 1214-1228.

[2]. Chen, J., Ling, Z., Lu, G., Zhang, Y. and Chen, G. (2012), „Spindle hood for electric discharge forming machine", China Patent no. CN 102009236 B.

[3]. Dvornik, D. et al. (2022), „Particle generation mechanisms in EDM", Metals, vol. 12.

[4]. Ghiculescu, L.D. and Ionescu, N., 2025, Creativity and Intellectual Property, Moodle Platform, Bucharest. Available at: https://curs.upb.ro/2025/my/courses.php Accessed: 15.05.2026

[5]. Gold, K. S., Rudgley, M., Gibbons, M., Legge, J. T. and Gerlach, R. K. (2010), „Hand-held electro-discharge device", US Patent no. US 2010/0096365 A1

[6]. Katz, S. and MacRae, D. (1948), „Filtration of Aerosols by Granular Charcoal", Journal of Physical and Colloid Chemistry, vol. 51, pp. 695–597.

[7]. Kovach, J. L. (1978), „Aerosol and Particulate Removal by Activated Carbon", in Carbon Adsorption Handbook, Ann Arbor Science, pp. 359–369.

[8]. Kumar, A. et al. (2024), „Reduction of air contaminant gases emitted from EDM", Atmosphere.

[9]. Leppert, T. (2018), „A review on ecological and health impacts of electro discharge machining (EDM)", AIP Conference Proceedings.

[10]. Mathew, J. et al. (2010), „Evaluation of occupational exposure to aerosol emitted from EDM", International Journal of Environment and Health.

[11]. Tönshoff, H. K., Egger, R. and Klocke, F. (1996), „Environmental and Safety Aspects of Electrophysical and Electrochemical Processes", CIRP Annals, vol. 45, no. 2.

[12]. Sharma, S. K. et al. (2019), „Principle of EDM process", Micromachines Review.

[13]. Viner, A. S. et al. (1992), „Ozone generation in DC-energized electrostatic precipitators", IEEE Transactions on Industry Applications, vol. 28, no. 3.

[14]. Voigt, O. and Peuker, U. A. (2022), „Suitability of Eroded Particles from EDM", Metals Journal, vol. 12.

[15]. Wang, F. et al. (2022), „Advances in particulate matter filtration technologies", Green Energy & Environment.

[16]. Wu, X. et al. (2024), „Sustainable and high-efficiency green electrical discharge machining", Journal of Cleaner Production.

[17]. Yamamoto, T. et al. (2001), „Electric air cleaner composed of nonthermal plasma reactor and electrostatic precipitator", IEEE Transactions on Industry Applications, vol. 37, no. 5.

DETAILED DESIGN, PROTOTYPING, AND CERTIFICATION FOR THE MODULAR ERGONOMIC DESK

BORCAN Geanina Adina, NAE Adriana, NICOLAE Mihaiță Florin, PÎRVULESCU Sorin Cristian
Faculty of Industrial Engineering and Robotics, Master's Program in Industrial Design and Innovative Products,
Year of Study:II, e-mail: borcanadina22@gmail.com

Supervisor: Prof. dr. ing. **Andrei Dumitrescu**

ABSTRACT: This chapter presents the detailed development of a modular ergonomic desk with adjustable support for laptop and monitor use. The product is designed to improve comfort, flexibility, and workspace ergonomics for modern users. The design process includes product architecture, ergonomic analysis, stability and safety considerations, material selection, adjustable mechanisms for height and angle regulation. The final solution focuses on modularity, intuitive use, portability, and manufacturability.
KEYWORDS: ergonomic desk; modular design; ergonomics; adjustable mechanisms; product architecture; industrial design; workspace flexibility; portability.

1. Introduction

In the context of the growing adoption of hybrid work and the frequent use of laptops and monitors, the workspace must provide ergonomics, flexibility, and comfort. Users require adaptable solutions capable of supporting proper posture and ensuring the efficient organization of daily activities.

The proposed product is a modular ergonomic desk equipped with height-adjustment mechanisms, as well as adjustable laptop and monitor supports. Its design aims to enhance comfort, stability, and flexibility in use, making it suitable for both educational and professional environments.

2. Current Situation Analysis

Ergonomic furniture has evolved significantly with the growth of hybrid work and the increasing use of digital devices. Although adjustable desks and laptop stands are widely available, many existing solutions offer limited functionality and a low degree of modularity and adaptability. Therefore, there is a need for the development of a modular ergonomic desk that combines ergonomics, stability, and flexibility in a practical and user-friendly solution.

3. Conceptual Design – Identification of Critical Functions.

Among the main functions previously identified, a list of critical functions was established (Table 1), as these determine the overall success of the product.

These critical functions correspond to the requirements considered most important by users and have a direct impact on daily use and user experience.

Table 1. Critical Product Function.

Function No.	Funcția critică a produsului
$Ø_{11}$	Laptop Surface Angle Adjustment
$Ø_{21}$	Monitor Surface Height Adjustment
$Ø_{31}$	Desktop Reconfiguration
$Ø_{41}$	Ensuring Overall Stability

4. Detailed Design

4.1. Proportions, Shapes, Dimensions and Tolerances

Based on the needs of the target users, the following product proportions and dimensions were established:

- Overall dimensions suitable for storage, transportation, and placement within users' rooms: 1200 mm length, 700 mm depth, and an adjustable height ranging from 650 mm to 1050 mm. Operator accommodation space: 965 mm length and 532 mm height.
- Monitor platform vertical travel distance: 250 mm.
- Laptop platform tilt angle: up to 30°.

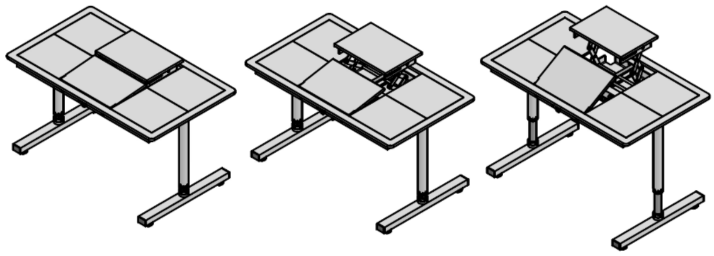

Fig. 1. Modular Desk Positions

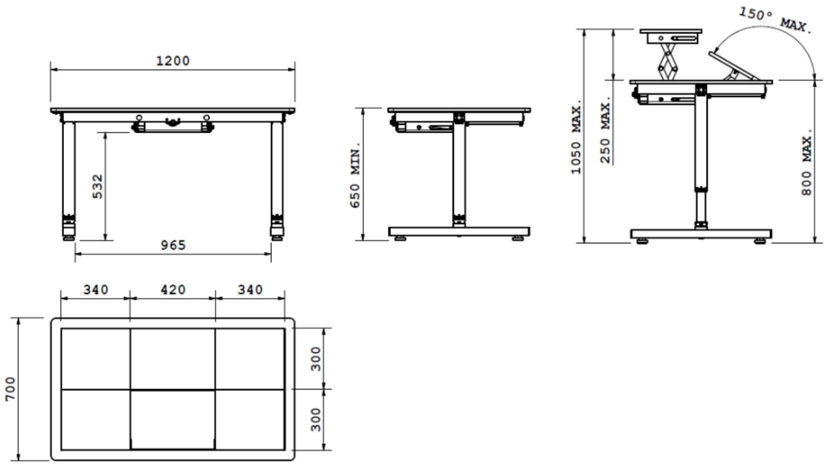

Fig. 2. Preliminary Overall Product Dimensions

4.2. Determination of Ergonomic and Anthropometric Requirements

The design of the modular ergonomic desk requires the establishment of clear conditions to ensure comfort, safety, and efficiency during use.

Product Usability and Clarity:

- The edge worktop remains fixed within the desk's metal frame.
- The passive worktop modules are interchangeable and replaceable. They are supported by the metal frame, while unintended movement is prevented through the use of locating pins.
- The active monitor platform moves vertically through a scissor-lift mechanism operated by a hand crank.
- The active laptop platform pivots, while its angle is manually adjusted using a turnbuckle mechanism to achieve the desired inclination.

The desk is designed for seated use and is dimensioned to accommodate the majority of users within the 5th to 95th percentile anthropometric range (P5–P95), ensuring ergonomic comfort and accessibility. [1, 2]

The data used during the design process include:

- Height ranges for fixed desks and height-adjustable desks, according to the EN 527-1 standard [3].
- Ergonomic recommendations for monitor positioning, ensuring that the top of the screen is at or slightly below eye level while maintaining a comfortable viewing distance, in accordance with OSHA/HSE ergonomic guidelines [4].
- Anthropometric reference data regarding eye height and elbow height, used to determine the appropriate working height.
- The comfortable manual reach zone used for the positioning of adjustment mechanisms.
- The laptop platform allows the adjustment of the tilt angle up to approximately 30°, reducing strain on the cervical area and improving user comfort during use.

Height, sitting [mm]

The distribution of the body measurements shows a Gaussian distribution. For ergonomic design, the 5th, 50th and 95th percentiles are commonly used.

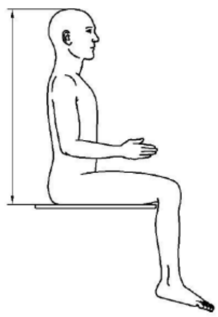

Country	Male			Female		
	P5	P50	P95	P5	P50	P95
Germany	855	910	965	810	860	910
Euro	790 (P5)		905 (P50)		985 (P95)	
Italy	820	882	946	775	835	894
Japan	856	909	964	800	850	898
Korea	869	922	974	811	858	905
Thailand	813	870	925	778	823	925
USA	856	919	985	809	861	925
China	858	908	958	809	855	901
Mexico	825	877	927	790	831	879
Malaysia	776	857	929	757	820	876

Eye Height, sitting [mm]

The distribution of the body measurements shows a Gaussian distribution. For ergonomic design, the 5th, 50th and 95th percentiles are commonly used.

Country	Male			Female		
	P5	P50	P95	P5	P50	P95
Germany	740	795	855	705	755	805
Euro	680 (P5)		790 (P50)		860 (P95)	
Italy (n.a.)						
Japan	738	789	842	687	735	780
Korea	755	805	857	701	747	792
Thailand	705	758	810			
USA	739	801	867	701	753	811
China	749	798	847	695	739	783
Mexico (n.a.)						
Malaysia	654	731	803	621	696	760

Fig 3. Anthropometric Measurements for Seated Operations [5]

4.3. Definition of Design Elements

To develop the product design, a set of desired and undesired visual attributes was established and grouped into three categories: functional–ergonomic, expressive–stable, and technological–harmonious. Based on these groups, three design concepts were developed:

• Concept 1

- Comfortable, ergonomic, user-friendly, modular, and practical.
- Colors and finishes: light grey or white desktop surface with a subtle wood texture, matte grey metal structure, and discreet accents on the control elements.

• **Concept 2**
- Comfortable, ergonomic, user-friendly, modular, and practical.
- Colors and finishes: warm wood-look desktop surface with a matte finish, featuring rounded edges and softer proportions.

• **Concept 3**
- Precise geometric forms, glossy black finish, and high-tech accents.
- Colors and finishes: graphite/black base, subtle industrial details on the mechanisms, and wear- and scratch-resistant surfaces.

The final concept was selected using a decision matrix (Table 4.1), in which the three proposed concepts were evaluated against a set of relevant criteria. Each criterion was assigned a weighting factor representing its importance, with the sum of all weights equal to 100. The concepts were assessed using a 1–5 rating scale, where 1 indicates poor compliance with the criterion and 5 indicates excellent compliance.

Table 2. Final Concept Decision Matrix.

Criterion	Weight	Concept 1 (score)	Concept 1	Concept 2 (score)	Concept 2	Concept 3 (score)	Concept 3
							
Balance	15	4	60	5	75	4	60
Proportion	13	4	52	5	65	4	52
Harmony	7	4	28	5	35	3	21
Functionality	15	4	60	4	60	3	45
Elegance	5	3	15	5	25	3	15
Originality	5	4	20	3	15	5	25
Accessibility	25	1	25	5	125	3	75
Adaptability	15	1	15	1	15	5	75
Total	100		275		415		368

After evaluating the results, it can be observed that Concept 2 achieved the highest score

4.4 Material and Surface Treatment Selection

The selection of materials for this product resulted from the need to balance performance, weight, and ease of manufacturing, as presented in Table 3.

Table 3. Materials and Surface Treatments Selected for the Product Components

Component Group	Selected Material	Key Properties	Surface Treatment
Lift mechanism legs and arms	Aluminum 6082-T6 [6]	High bending strength; Low density	Powder coating
Welded frame, lift mechanism base, hand crank	S235JR structural steel [7]	Easy to weld, form, and machine	Powder coating
Pins and shafts	AISI 304 stainless steel [8]	High wear resistance; Excellent corrosion resistance	–
Leadscrew, turnbuckle, threaded rods	C45 carbon steel [9]	High machining accuracy; Enhanced buckling resistance	Induction hardening (55–60 HRC); Black oxide finish
Leadscrew nut	Igus Drylin Iglidur J polymer [10]	Self-lubricating properties	–

Bearing supports	PA66 nylon [11]	High wear resistance	–
Covers	Polypropylene (PP) [11]	Cost-effective; High flexibility	–
Plain bearings	Polytetrafluoroethylene (PTFE) [12]	Low coefficient of friction	–
Radial and thrust bearings, retaining rings, bolts, washers, nuts	Standard components	Cost-effective solution	–
Worktops	Poplar plywood [13]	Lightweight; Easy to machine and finish	Sanding; PVC edge banding for straight edges; Wood filler for rounded edges; Painting
Anti-slip pads	Neoprene rubber [14]	High durability and grip	–

5. Prototype Manufacturing and Testing

5.1 Virtual Prototype Development

The Modular Ergonomic Desk prototype (BEM_10_000) was developed as a parametric three-dimensional model using Autodesk Inventor.

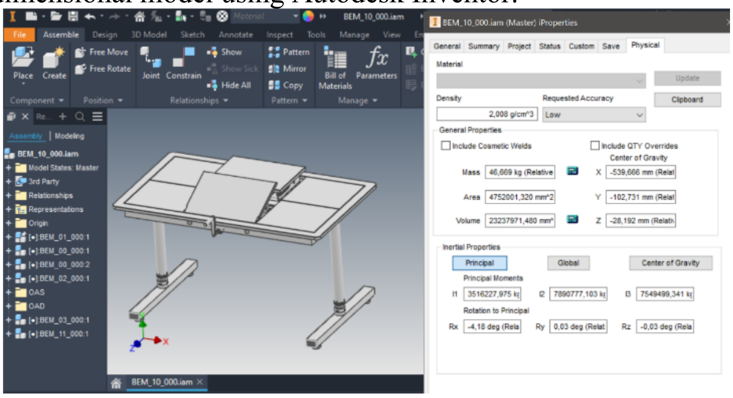

Fig. 4. Virtual Prototype of the Modular Ergonomic Desk

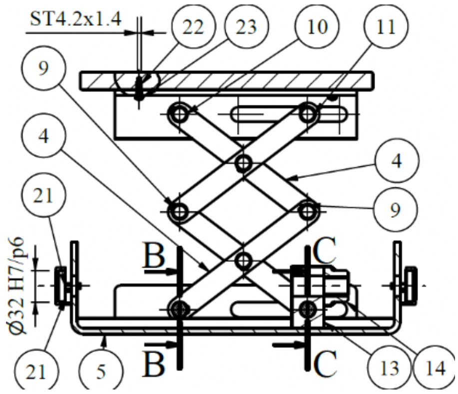

Fig. 5. Double Scissor Mechanism Detail

The critical subassembly of the product is the active monitor platform, which is raised by a manually operated double-scissor mechanism driven by a self-locking TR20×2 leadscrew. This system provides a vertical travel of 250 mm while ensuring stability under load. The mechanism is manufactured from 6082-T6 aluminum, S235JR structural steel, and stainless-steel shafts with precise fits. The tilt angle of the laptop platform can be adjusted between 0° and 30° through a turnbuckle-based fine-adjustment system. [15].

5.2. Prototype Testing Program

The prototype testing program was structured into five categories (Table 4), comprising a total of 29 individual tests. The testing plan was developed in accordance with the requirements of the European standards EN 527-1:2011 (office work tables – dimensions), EN 527-2:2016+A1:2019 (safety, strength, and durability requirements), and EN 1730:2012 (test methods for tables) [16].

Table 4. Overview of the Prototype Testing Program

Category	No.	Key Test Requirement	Acceptance Criterion
Functionality (T_F)	6	250 mm monitor platform travel; 0–30° laptop platform tilt angle	Smooth operation without jamming; crank torque ≤ 4 N·m at a 10 kg load
Strength (T_R)	6	1000 N static load applied to the main worktop (EN 1730, Cl. 6.3)	Deflection ≤ 5 mm; residual deflection ≤ 1 mm
Durability	5	5,000 scissor mechanism cycles;	Torque increase ≤ 30%; no cracks

(T_D)		10,000 vertical load cycles	or structural damage
Ergonomics (T_E)	6	P5–P95 anthropometric accommodation; crank effort; usability testing	≥ 90% of participants report comfort; crank force ≤ 30 N
Safety (T_S)	6	Tip-over stability; leadscrew self-locking capability	No leg lift-off; vertical displacement ≤ 5 mm after 24 h

6. Product Certification and Use

Product certification is carried out based on the physical prototype through the completion of the 29 tests grouped into five categories: functionality, strength, durability, ergonomics, and safety. The tests are performed in accordance with the European standards EN 527-1:2011 (dimensions), EN 527-2:2016+A1:2019 (safety, strength, and durability requirements), and EN 1730:2012 (test methods) [17]. These standards define the minimum requirements for office desks and include assessments of stability, resistance to vertical and horizontal loads, fatigue performance, and long-term durability.

The documentation required for the certification process includes:

- Technical file – manufacturing drawings, bill of materials, and critical fits and tolerances.
- Description of the design solutions, materials, and manufacturing technologies employed.
- Test reports for all 29 tests, including measured values and verification of compliance with the acceptance criteria.
- User manual and maintenance schedule.
- Declaration of conformity with EN 527-2:2016+A1:2019 and EN 1730:2012.

Recyclability was considered from the early design stages through the selection of materials that can be easily separated and recycled, as well as through the modular product architecture, which facilitates disassembly and component replacement at the end of the product's service life.

Table 5. Recyclable Materials

Component	Material	Collection Method
Frames, legs, and scissor arms	Aluminum 6082-T6	Recyclable
Worktop supports and hand crank	S235JR steel	Recyclable
Joint shafts	AISI 304 stainless steel	Recyclable
Leadscrew and threaded rods	C45 steel	Recyclable
Leadscrew nut	Iglidur J polymer	Collected separately
Bearing supports	PA66 nylon	Recyclable
Covers	Polypropylene (PP)	Recyclable
Bearings, bolts, and washers	Standard steel	Recyclable
Worktops	Poplar plywood	Recyclable
Anti-slip feet	Neoprene rubber	Recyclable
Packaging	Cardboard	Recyclable

More than 85% of the total product mass (39.67 kg) can be recycled or recovered, supporting the principles of the circular economy within the furniture industry.

7. Conclusions

The results demonstrate that a structured design approach can successfully lead to the development of a viable and user-friendly modular ergonomic desk. The proposed solution incorporates key adjustment features, including a height range of 650–1050 mm, a 250 mm monitor travel, and a laptop tilt angle of up to 30°, while clearly separating passive and active components to enhance stability and ease of use.

Among the three design concepts evaluated, Concept 2 – Expressive and Stable was selected as the most balanced solution in terms of ergonomics, visual clarity, home integration, and manufacturability. The selected materials and proposed manufacturing and testing procedures provide a solid basis for prototype development and product validation.

8. References

[1]. CEN (European Committee for Standardization). (2011). *EN 527-1:2011, Office furniture - Work tables and desks - Part 1: Dimensions*. Brussels: CEN.
[2]. CEN (European Committee for Standardization). (2019). *EN 527-2:2016+A1:2019, Office furniture - Work tables - Part 2: Safety, strength and durability requirements*. Brussels: CEN.
[3]. CEN (European Committee for Standardization). (2012). *EN 1730:2012, Furniture - Tables - Test methods for the determination of stability, strength and durability*. Brussels: CEN.
[4]. ISO (International Organization for Standardization). (2024). *ISO 9241-5:2024, Ergonomics of human-system interaction - Part 5: Workstation layout and postural requirements*. Geneva: ISO.
[5]. Continental AG. (2024). *Ergonomics Requirement Specification for External Machine Manufacturers: Our Requirements to New Machines. Anthropometric Data* (PDF) [online]. Accesat la 15.05.2026.
[6]. Davis, J.R. (ed.), “Aluminum and Aluminum Alloys”, ASM International, Materials Park, Ohio, 1993, pp. 639-641.
[7]. CEN (European Committee for Standardization). (2019), “EN 10025-2: Hot Rolled Products of Structural Steels — Part 2: Technical Delivery Conditions for Non-Alloy Structural Steels”, Brussels. CEN.
[8]. CEN (European Committee for Standardization). (2014), “EN 10088-1: Stainless Steels — Part 1: List of Stainless Steels”, Brussels.
[9]. CEN (European Committee for Standardization). (2019), “EN 10083-2: Steels for Quenching and Tempering — Part 2: Technical Delivery Conditions for Non-Alloy Steels”, Brussels.
[10]. Igus.eu (f.a.),” drylin® injection-moulded flange lead screw nuts”[online] . Accesat la 15.05.2026
[11]. Rosato, D.V., Rosato, M.G. (2000) “Injection Molding Handbook”, 3rd edition, Kluwer Academic Publishers, Boston, pp. carrier 784–791.
[12]. Banks, R.E., Smart, B.E., Tatlow, J.C. (1994), “Organofluorine Chemistry: Principles and Commercial Applications”, Plenum Press, New York, pp. 339–341.
[13] . Bodig, J., Jayne, B.A. (1982), “Mechanics of Wood and Wood Composites”, Van Nostrand Reinhold, New York, pp. 227–234.
[14] . Mark, J.E. (ed.) (2013), “Rubber Science and Technology”, 2nd edition, Academic Press, New York, pp. 276–281.
[15]. MakeItFrom.com. (f.a.), „6082-T6 Aluminum Material Properties”, MakeItFrom.com. [online]. Accesat la 15.05.2026
[16]. CEN (European Committee for Standardization). (2012), „EN 1730:2012, Furniture - Tables - Test methods for the determination of stability, strength and durability”, Brussels: CEN.
[17]. Giavon, Andrea. (f.a.). *The safety and durability of office furniture*. CATAS, San Giovanni al Natisone (UD), Italy (articol tehnic) [online]. Accesat la 15.05.2026.

LASER CUTTING CNC MACHINE

MOROIANU Bogdan Cristian[1], POPA Cătălina Alexandra[1], GIURCĂ Gabriel[2], ILIE Alexandru[2], NEACȘU Nicoleta Bianca[2]
Research Advisor: Professor Dr. Eng. GHICULESCU Liviu-Daniel

Department: Industrial Engineering and Robotics, Specialization: INPN[1], IEMA[2], Year of study:I,
e-mail:alexandracatalina2002@gmail.com

ABSTRACT: This paper presents the design of a 5-axis CNC machine for laser cutting of non-metallic materials. The equipment uses a kinematic configuration consisting of the X, Y and Z linear axes and the rotational A and C axes, enabling the machining of complex three-dimensional parts. The mechanical structure is designed as a moving gantry system, using TEGO phenolic plywood due to its high rigidity and low cost. The developed system provides a modular, flexible, and affordable solution for prototyping, research, and small-scale production applications.

KEYWORDS: CNC, laser cutting, non-metallic materials.

1. Introduction

Modern computer-aided manufacturing technologies have evolved significantly in recent years, driven by increasingly stringent requirements for precision, flexibility, and productivity in machining processes. Among these, laser cutting technology plays a key role in the machining of non-metallic materials, offering advantages such as high precision, high processing speed, and the ability to create complex shapes without direct mechanical contact with the workpiece.

Multi-axis CNC systems expand machining capabilities by orienting the cutting head relative to the workpiece surface, and are used to produce components with complex geometries. The integration of additional rotational axes into a laser cutting system contributes to increased equipment flexibility and improved process quality.

The objective of this work is to design a 5-axis CNC machine for laser cutting of non-metallic materials, utilizing a mobile gantry structure and a modular system that integrates the A and C rotation axes. The development of this equipment aims to provide an affordable and efficient solution for prototyping, research, and small-batch production applications.

2. Strategic marketing of the product

2.1. Identifying market opportunities

a. Customer needs portfolio

Three needs have been identified, labeled N1, N2, and N3.

-N1: The need for precision and fine detail
-N2: The need to increase productivity
-N3: The need to process sensitive materials

b. Opportunities / Customers

For each identified need, the following will be established:

a) Market opportunities (the causes of the need's emergence)

- For N1: the absence of a CNC laser cutting machine for precision and fine detail
- For N2: the absence of a CNC laser cutting machine for fast production
- For N3: the absence of a CNC laser cutting machine for processing materials that are difficult to machine using classic machines

b) Customers who will be interested in these products:

- Research and education institutions:
  - students;
  - professors;
  - research laboratories.
- Enterprises that use laser cutting:

- micro-enterprises;
- small and medium-sized enterprises;
- large enterprises.

2.2. Mission formulation

The table below shows the customer selection matrix.

Table 1. Customer selection matrix

Customer Types	Students	Professors	Research Laboratories	Micro-enterprises	Small and Medium-sized Enterprises	Large Enterprises
Companies	-	-	-	1	1	1
Educational institutions	1	1	1	-	-	-

Table 2 presents the interview guide for identifying customer needs for our product, the CNC laser cutting machine.

Table 2. Interview guide for identifying customer needs for the product

Age Range: ....
Do you want to collaborate?

Yes No

Occupation: ....

No.	Question	Customer statement	Interpreted need
1	Have you used a CNC laser machine?	a)Yes b) No	
2	If yes, how often do you use it?	a)Daily b)Weekly c)Occasionally d)Very rarely e)I have not used it at all	
3	What was the CNC laser machine used for?	a)Prototyping b)Production c)Research d)Personal projects e) I have not used it at all	
4	Which parameters do you consider most important?	a)Laser power b)Cutting speed c)Positioning accuracy d)Material type e)Control software	
5	Which materials have you processed with CNC laser?	a)Wood b)Metal c)Plastic d)Composite materials e)Others	

6	Do you consider the use of a CNC laser machine to be safe?	a)Yes b)No c)I am not sure	
7	Which risks do you consider most important?	a)Burns b) Laser radiation c)Smoke/toxic gases d)Mechanical failures	
8	What improvements would you make to a CNC laser machine?	....	
9	What do you consider the main advantages of laser cutting compared with traditional methods?	a)Higher precision b)Higher speed c)Reduced material losses d)Automation	
10	Would you recommend the use of CNC laser in industry?	a)Yes b)No c)It depends on the application	

Table 3 presents the prioritization of needs and their relative importance for the CNC laser cutting machine product.

Table 3. Prioritization of needs and their relative importance

No	Need	Relative importance
1	The need to increase precision	5
2	The need to increase productivity	5
3	The need to increase safety measures	4
4	The need for variety in processable materials	3

3. Analysis of competitive products

In order to establish a performance benchmark for the CNC equipment, three products currently available on the market were analyzed: xTool D1, Ortur Laser Master 2 Pro, and AlgoLaser Delta (Figures 1, 2, 3). These machines are representative of the category of CNC laser systems designed for processing non-metallic materials. The characteristics of the analyzed competing products are presented in Table 4, [1,2,3].

Table 4. Machine specifications

Fig. 1. Algolaser DIY KIT MK2
Laser power: ~10W.
Laser type: IR (1064 nm diode).
Wavelength: 1064 nm.
Spot size: ~0.03 mm.
Materials: cardboard, plastic, leather, wood.
Cutting area: ~400×435 mm.
Cutting speed: medium.

Fig. 2. xTool D1
Laser power: 5–10 W.
Laser type: blue diode.
Wavelength: ~450 nm.
Spot size: ~0.08 mm.
Materials: wood, plastic, leather, painted metal.
Cutting area: ~300×300 mm.
Cutting speed: high.

Fig. 3. Ortur Laser Master
Laser power: 5–10W.
Laser type: blue diode.
Wavelength: ~450 nm.
Spot size: ~0.06–0.1 mm.
Materials: wood, leather, cardboard.
Cutting area: ~400×400 mm.
Cutting speed: high.

Focus: Auto / preset. Noise level: low. Safety system: housing + eye protection. Fume extraction: optional. Software: proprietary app (PC / mobile). Dimensions: small, portable. Weight: ~3 kg. Price: €300–€600.	Focus: fixed + calibration distance. Noise level: medium. Safety system: optional housing, STOP button. Fume extraction: optional. Dimensions: 600×450×110 mm. Weight: ~10–12 kg. Power supply: 24 V adapter. Price: €600–€1500.	Focus: fixed. Noise level: medium. Safety system: sensors + safety shut-off. Fume extraction: No. Dimensions: 580×550×150 mm. Weight: ~7–8 kg. Power supply: 24 V adapter. Price: €350–€650.

4. Conceptual design

4.1 Identifying critical issues

Critical issues are those factors that have a decisive impact on the product's performance and success, namely:

- overheating of the material in the cutting zone;
- the generation of smoke and gases during cutting;
- loss of precision due to vibrations in the CNC system;
- incorrect focusing of the laser beam;
- risk of eye injury caused by laser radiation;
- wear of the mechanical components of the motion system;
- insufficient heat and smoke evacuation;
- variations in cutting quality depending on the processed material [4].

4.2 Highlighting relevant natural phenomena

Table 5 highlights the main component functions and the natural phenomena associated with them [5].

Table 5. Natural phenomena applicable to component functions

No.	Component function	Applicable natural phenomena
1	Laser beam generation	Stimulated emission of radiation, population inversion, conversion of electrical energy into electromagnetic radiation
2	Laser beam guidance and focusing	Reflection and refraction of light, optical focusing, rectilinear propagation of laser radiation
3	Interaction of the beam with the material	Absorption of laser energy by material, conversion of light energy into thermal energy
4	Cutting the material	Local melting, vaporization of material, intense local heating
5	Movement of the laser head along the axes	Translational motion, conversion of rotational motion into linear motion, mechanical friction
6	Position and trajectory control	Positional feedback, numerical control, automatic motion control
7	Exhaust of smoke and debris	Forced ventilation, fluid flow, pressure differences
8	Cooling of components	Heat transfer, convection, heat dissipation
9	System power supply	Electrical energy conversion, power supply and distribution

5. Manufacturing. Testing the product prototype

5.1 Detailed design of a 5-axis CNC machine for laser cutting of non-metallic materials

Figure 4 shows the general structure of the 5-axis CNC machine designed for laser cutting of non-metallic materials (wood, MDF, acrylic, plastic, leather, foam, technical textiles, etc.). The proposed solution combines precise linear movements along the X, Y, and Z axes with the additional degrees of freedom provided by the A/C kinematic subassembly (Figure 5), enabling the creation of complex surfaces, beveled edges, and three-dimensional shapes without manual repositioning of the workpiece.

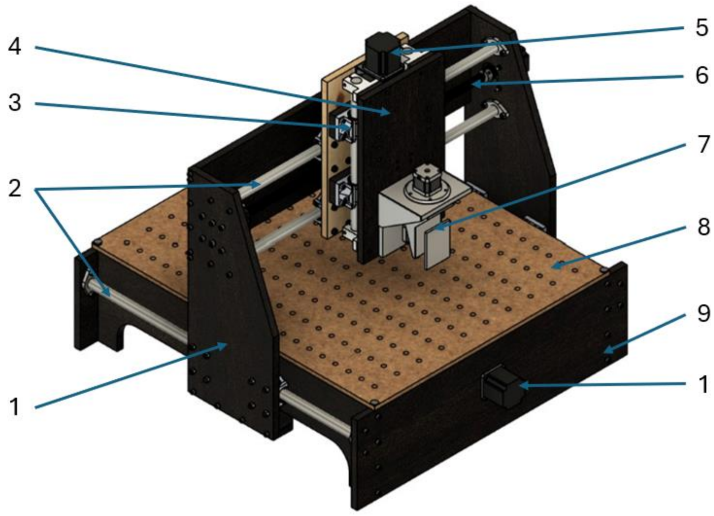

Fig. 4. Structure of the laser cutting machine

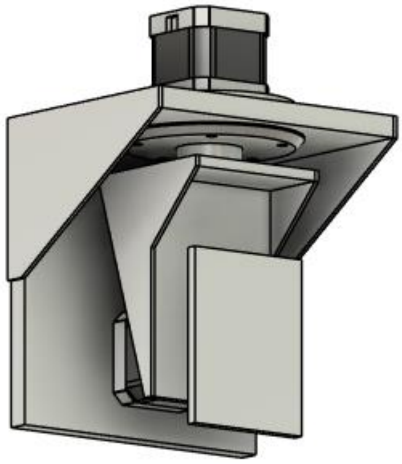

Fig. 5. A/C rotation subassembly

The machine features balanced proportions, optimized for an ideal balance between rigidity, precision, and compact size. The main dimensions provide a working volume of 350 × 400 × 150 mm (travel: X-axis 350 mm, Y-axis 400 mm, Z-axis 150 mm), making it suitable for both prototyping and small-batch production, while maintaining a compact footprint.

The CNC machine is built on a rigid gantry-type structure with a movable table, made of laminated phenolic plywood (Tego). The worktable (8) is mounted on the Y-axis structure (9) and is equipped with holes for securing workpieces and exhausting smoke generated during the cutting process.

Movement along the X, Y, and Z axes is achieved via trapezoidal screws (12) equipped with anti-backlash bushings (11), driven by NEMA23 stepper motors (10) for the X and Y axes, and NEMA17 (5) for the Z axis. Precise guidance is ensured by the guide rails (2) and linear bearings (3).

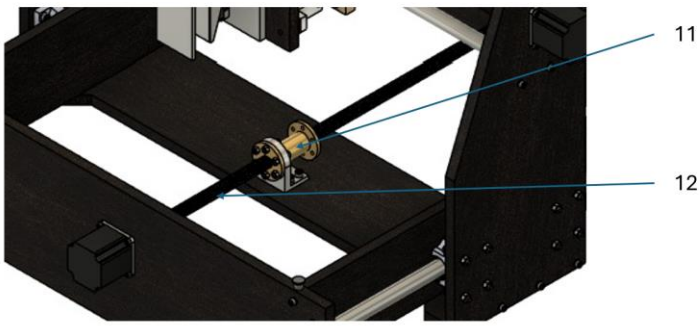

Fig. 6. Anti-backlash bushing and trapezoidal screw

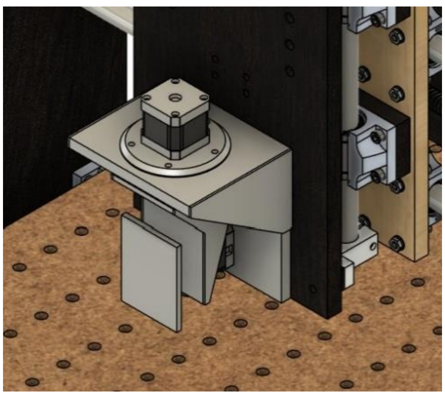

Fig. 7. Detail of the A/C rotation subassembly

The A/C rotation subassembly (7) is mounted on the front plate of the Z-axis (4), allowing the laser head to be oriented along two additional axes: tilt along the A-axis and continuous rotation along the C-axis (Figure 7). By integrating this subassembly, the equipment becomes a 5-axis simultaneous CNC system, capable of executing complex spatial trajectories and three-dimensional oriented cuts.

The equipment's command and control system is implemented using an Arduino UNO development board running GRBL firmware, with the interface provided by the Universal Gcode Sender (UGS) software. The stepper motors are controlled via TB6560 drivers, ensuring precise synchronization and high positional repeatability. The command and control components are powered by a switching power supply, while the laser diode is powered by a separate source, a measure that significantly reduces electromagnetic interference between the two subsystems.

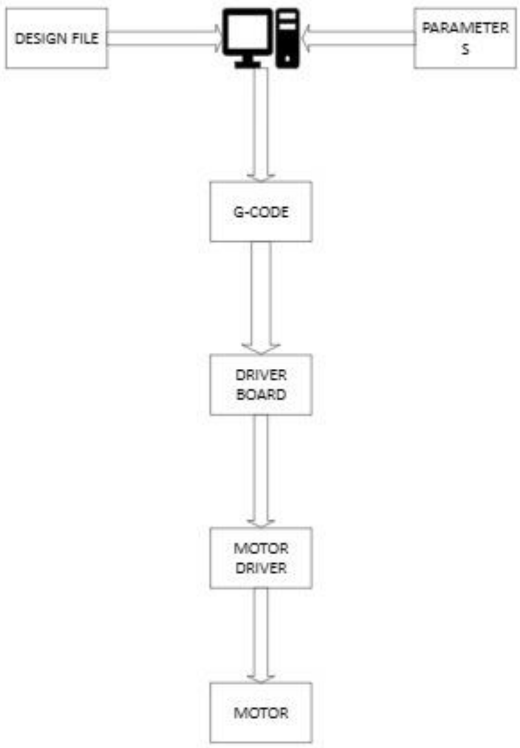

Fig. 8. Block diagram of the command and control system

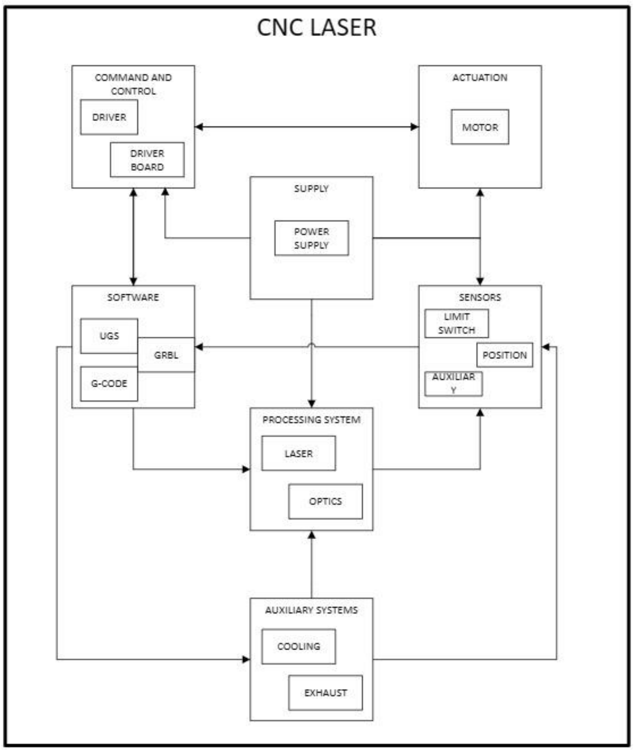

Fig. 9. Operational diagram

6. Product approval

The certification process for the 5-axis CNC laser cutting machine intended for non-metallic materials involves the following steps: defining requirements, analyzing technical documentation, verifying design compliance, conducting functional and performance tests, testing safety measures, validating the machine on representative materials, and preparing the final certification report [6, 7, 8]. After completing all stages, it is confirmed that the product meets the required technical, functional, and safety requirements and may be put into service for its intended purpose. The sequence of steps required for product approval is detailed in the diagram in Figure 10.

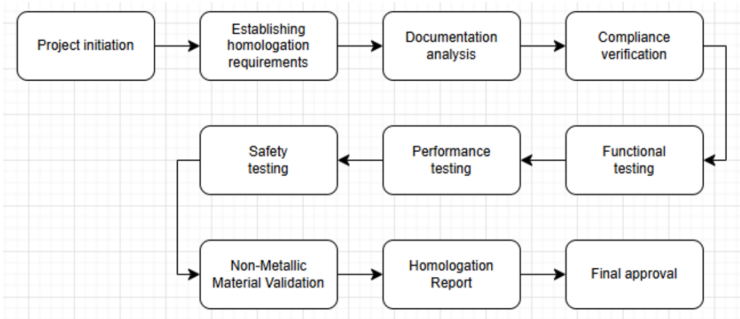

Fig. 10.Steps required for product approval

7.Machining cost calculation

We have conducted a market study to analyze the estimated prices of the specific components required for a 5-axis CNC machine. Based on this data, Table 6 presents the structural elements, the required quantities for assembly, and the associated costs for each component category, [9-18].

Table 6. Product features

Category	Specific components	Estimated quantity	Estimated price (RON)
Structure (Tego)	Phenolic plywood (Tego) 18-21mm, CNC/laser cut	1.5 - 2 m²	225 - 320
Linear Guides	Linear rails (SBR/TBR) + Linear bearings (X, Y, Z)	6 bars + 12 bearings	1240 - 1670
Drive System	Lead screws + Anti-backlash nuts	3 sets	100 - 150
Motors (X, Y, Z Axes)	2x NEMA23 (X, Y) + 1x NEMA17 (Z)	3 pcs.	450 - 600
A/C Subassembly	Gears / Rotary housing	1 set	300 - 500
Control Electronics	Arduino UNO + CNC Shield + 5x TB6560 Drivers	1 set	325 - 450
Laser System	Laser diode (10W-20W optical power)	1 pcs.	450 - 800
Power Supply	2x Switching power supplies (24V for motors, 12V for laser)	2 pcs.	120 – 200
Miscellaneous	Cables, limit switches, screws, connectors	-	300 - 500
Estimated total			3.510 – 5.190 RON

8. Conclusions

This thesis presents the design of a 5-axis CNC machine for laser cutting of non-metallic materials, utilizing a kinematic configuration comprising the X, Y, and Z axes, as well as the A and C rotational axes. The main contribution of this work lies in the development of modular and affordable equipment, based on a mobile gantry structure made of TEGO phenolic plywood, a material chosen for its favorable ratio of stiffness, weight, and manufacturing cost. The integration of additional rotational axes on the Z-axis allows for expanded machining capabilities and the production of parts with complex geometries.

The proposed solution offers high flexibility and the possibility of using the equipment in prototyping, research, and small-batch production applications. The results highlight the possibility of creating an efficient system for machining non-metallic materials, using low-cost components and design solutions.

9. Bibliography

[1]. *** ALGO LASER DIY KIT MK2, available at: https://www.banggood.com/[EU-Direct]Algolaser-DIY-KIT-MK2-Laser-Engraver-10W-12000mm-or-min-Touchscreen-Precision-Laser-Module-Expandable-Workspace-p-2023609.html, accessed on: 13.05.2026.

[2]. *** xTool D1, available at: https://support.xtool.com/search-result?q=xtool+d1, accessed on: 13.05.2026.

[3]. *** Ortur, available at: https://orturtech.com/pages/laser-specification, accessed on: 13.05.2026.

[4]. Steen, W. M., Mazumder, J. (2010), Laser Material Processing, Springer, 4th Edition, 978-1-84996-061-8.

[5]. Marinescu, N. I., et al. (2017). *Technological Processes with Beams, Oscillations, and Jets*. Printech, ISBN 978-606-521-104-9.

[6]. ***STYLECNC, available at: https://ro.stylecnc.com/user-manual/how-does-laser-cutting-machine-work.html, accessed on: 14.05.2026.

[7]. *** STYLECNC, available at: https://ro.stylecnc.com/user-manual/list-26-2.html, accessed on: 14.05.2026.

[8]. *** Zintilon, available at: https://www.zintilon.com/ro/blog/5-axis-cnc-machining/, accessed on: 14.05.2026.

[9]. *** KRN Formwork, available at: https://www.krncofraje.ro/produs/placaj-tego-plop-21mm-furnir-intreg-1220-x-2440/, accessed on: 14.05.2026.

[10]. ***CNC-KIT:https://www.cnc-kit.ro/catalog?q=SBR, accessed on: 14.05.2026.

[11]. *** RepRapMania, available at: https://www.reprapmania.ro/cumpara/surub-trapezoidal-tr8-avans-8mm-200mm-lungime, accessed on: 14.05.2026.

[12]. *** 3DParts, available at: https://piese3d.ro/set-piulite-tr82-anti-backlash, accessed on: 14.05.2026.

[13]. *** Assefair, available at: https://assefair.ro/steppere/28-motor-pas-cu-pas-nema23-3nm-4a.html, accessed on: 14.05.2026.

[14]. *** Arduino UNO Rev3, available at: https://ardushop.ro/ro/electronica/1210-arduinoR-uno-rev3-smd-7630049200074.html, accessed on: 14.05.2026.

[15]. *** Ardushop, available at: https://ardushop.ro/en/motors-and-drivers/2144-tb6560-3a-stepper-motor-driver-6427854032911.html, accessed on: 14.05.2026.

[16]. *** Bitmi, available at: https://www.bitmi.ro/placa-de-expansiune-cnc-v4-pentru-arduino-nano-12334.html, accessed on: 14.05.2026.

[17]. *** eMAG, available at: https://www.emag.ro/modul-laser-cu-focalizare-reglabila-20w-450nm-pentru-cnc-6151103136135/pd/DFM8X4YBM/, accessed on: 14.05.2026.

[18].*** A2T, available at: https://www.a2t.ro/default-category/sursa-de-alimentare-in-comutatie-24v-2-2a-51-8w-mean-well-lrs-50-24, accessed on: 14.05.2026.

MARKETING STUDY OF A MECHANICAL DEVICE FOR PARKING SPACE Security

DUMITRACHE Mădălina-Diana, BICĂ Mihai-Daniel ,DURIGO Mario-Gabriel, GRIGORE Gabriel-Adrian, SANDOVICI Maria-Smaranda și Prof. Dr. Ing. **DUMITRESCU Andrei (Conducător Științific)**

Faculty: Industrial Engineering and Robotics, Major: Industrial Design and Innovative Products, Year of Study: 1st year of Master's program, Email: dmadalinad123@gmail.com

ABSTRACT: This paper presents a marketing study and functional analysis of a mechanical device designed for parking space security. The study is based on the increasing need for parking space protection in crowded urban areas, where unauthorized occupation of private parking spaces has become a common issue. Existing parking blockers were analyzed from both functional and ergonomic perspectives, identifying several limitations related to usability, safety, and durability. Based on this analysis, an improved conceptual solution is proposed, focused on ergonomic interaction, assisted movement, and improved accessibility. The paper also discusses the possibility of integrating smart functions, such as remote control and automated operation, in order to improve user experience and product efficiency.

KEY WORDS: Parking blocker, mechanical device, applied ergonomics, accessibility, conceptual design.

1. Introduction

The increase in the number of vehicles and the rapid expansion of urban areas have led to increasingly frequent problems regarding the use and security of parking spaces. In residential and commercial areas, the unauthorized occupation of private parking spaces is a common occurrence, which has prompted the development of solutions designed to protect them.

One of the most widely used solutions is the mechanical parking blocker, a device that restricts access by unauthorized vehicles. Although these products are affordable and widely used, many existing models have ergonomic and functional limitations, such as awkward operation, exposure of the locking system to environmental factors, and a lack of control over the mechanism's movement.

The objective of this paper is to conduct a marketing study on a mechanical device for securing parking spaces and to identify opportunities for improving existing products. The study analyzes market opportunities, user needs, and competing products, with the aim of developing an improved concept based on ergonomics, safety, and ease of use.

The proposed concept retains the classic mechanism of the folding-bar lock but introduces features such as ergonomic operation, assisted lifting, and optimization of the locking system. The possibility of integrating smart features, such as remote control or automation of the mechanism, is also being explored.

2. Current state

in residential, commercial, and private areas due to the increasing number of vehicles and the decreasing availability of parking spaces [1]. In congested urban areas, the unauthorized occupation of private parking spaces is an increasingly common problem, which has led to the development of solutions designed to protect and demarcate parking spaces.

The most common solutions are mechanical barriers with a swing-down bar, typically made of galvanized steel or stainless steel—materials chosen for their resistance to wear and outdoor conditions [2]. These products work by raising a metal bar that prevents unauthorized vehicles from entering and lowering it when the user wishes to use the parking space.

The market offers both simple mechanical versions and automatic models, which differ in terms of their drive system, level of automation, and design complexity [3]. Mechanical versions are preferred due to their low cost and simple design, but they require direct user intervention. In contrast, automatic versions use electric motors, remote controls, or electronic control systems, offering a higher level of comfort and accessibility.

From an ergonomic standpoint, many existing products have significant limitations. They are operated manually, requiring the user to bend down to manipulate and unlock them, and the locking mechanisms are located close to the ground, exposing them to water, dust, low temperatures, and mechanical wear [4]. In addition, certain products do not provide effective control over the bar's movement, posing a risk of sudden or awkward movements during use.

Another issue identified with some existing products is their lack of ergonomic and aesthetic integration into the urban environment. Many of the options available on the market are designed purely from a functional standpoint, without taking into account the user experience, accessibility, or visual integration into the urban space.

In recent years, the development of smart technologies and the growing interest in automation have also influenced this field. Solutions have begun to emerge that enable remote control, sensor integration, and the automation of security mechanisms [5]. These systems aim to increase convenience and reduce direct interaction with the product, but they involve higher costs and require additional power supply, protection, and maintenance solutions.

An analysis of current trends and existing products reveals an opportunity to develop a device that retains the mechanical simplicity of traditional products while offering user-oriented ergonomic and functional improvements. Developing such a product can contribute both to increased comfort and safety during use and to adapting the product to the current demands of the modern urban environment.

3. Strategic Marketing and Identifying Opportunities

3.1. Identifying market opportunities

The shortage of parking spaces in urban areas and the unauthorized occupation of private spaces call for the development of effective security solutions [1]. The market opportunity lies in addressing users' biomechanical needs through ergonomic, durable, and easy-to-maintain products that reduce the physical effort required to operate conventional systems. The integration of smart features and the modernization of mechanical components represent major competitive advantages in a market where users prioritize safety and ease of use.

3.2. The development team's mission statement

The team's mission is to develop a mechanical device designed to secure parking spaces that optimizes the user experience through accessibility, safety, and ergonomics, overcoming the limitations of current solutions [1]. Based on a folding barrier mechanism, the concept incorporates modern human-product interaction solutions and ease of use [5]. The strategic objectives aim to reduce physical effort, enhance safety, and ensure an aesthetic design suited to the urban environment [3], resulting in a robust, durable product that can withstand outdoor conditions [2].

3.3. Analysis of Potential Customers (5W1H Method)

Potential customers were selected using the 5W1H (What, Who, Where, When, Why, How) competitive analysis method to identify user categories and how the product is used [6].

Table 3.3.1. 5W1H Analysis of the Proposed Product

Element	Analysis

What?	Mechanical device for securing parking spaces
Who?	Owners of private parking spaces, tenants, businesses, parking lot managers
Where?	Residential areas, private parking lots, commercial spaces, office buildings
When?	Daily use, especially in congested urban areas
Why?	Protecting the parking space against unauthorized use
How?	By raising and lowering a mechanical locking bar

The analysis indicates that the device is designed for urban users who need a simple, effective, and affordable solution to protect their parking spot from unauthorized use.

3.4. Analysis of Competitive Products

To identify specific needs and assess interest in the product, methods such as observing similar products and conducting a survey of potential users were employed [7]. The identified requirements aim to produce a cost-competitive product that is rigorously tailored to current market demands [4].

Table 3.3.1. Comparative Analysis of Competitive Products

Product Name	Estimated Price	Popularity (1-9)	Functional Features	Other Features	Market Segment
Simple mechanical parking lock	Low	7	Manual operation	Simple construction	Residential
Automatic parking lock with remote control	High	8	Automatic operation	Smart function	Residential / Commercial
Foldable stainless steel parking lock	Mediu	7	High durability	Compact design	Residential
Parking lock with alarm	High	6	Audible alarm	Extra security	Commercial

The analysis shows that users place the highest priority on functionality, weather resistance, and reduced physical effort during operation.

Table 3.4.2. Competitive Products-Technical Specifications

Feature	Unit of Measurement	Product 1	Product 2	Product 3
Material	-	Steel	Steel/Stainless Steel	Stainless Steel
Operation Type	-	Manual	Automatic	Manual

Locking System	-	Padlock	Electronic	Padlock
Weather Resistance	-	Medium	High	High
Ergonomics Level	-	Low	High	Medium

The analysis of competing products revealed an opportunity to develop a product that combines mechanical simplicity with ergonomic and functional improvements, without significantly increasing production costs.

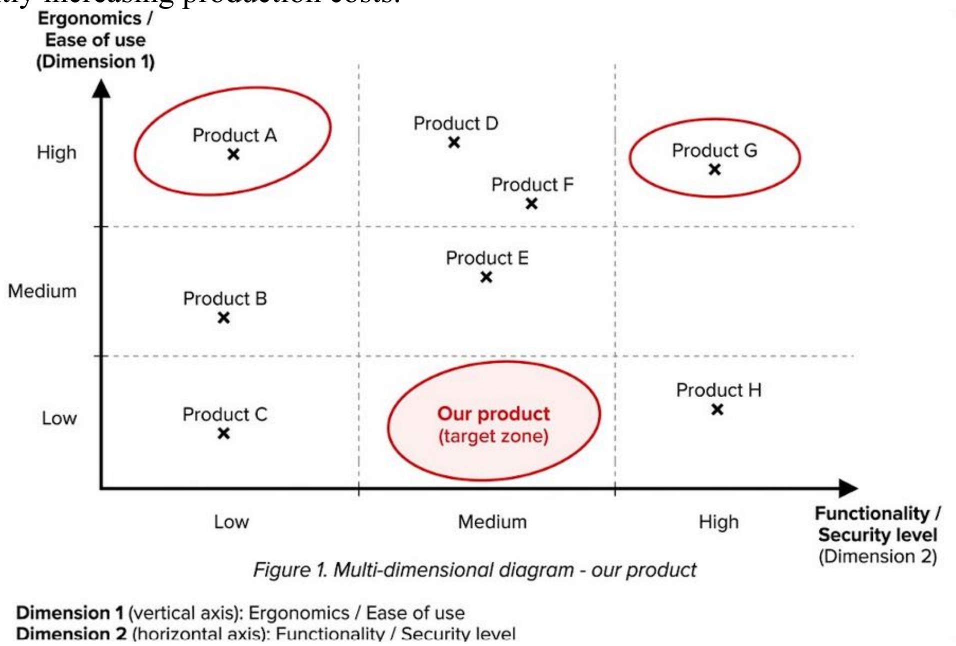

Fig. 1. Multidimensional diagram illustrating the conceptual positioning of the proposed product relative to competing products

4. Project Management and Financial Analysis

4.1. Work Breakdown Structure (WBS)

The project implementation was based on the use of the Work Breakdown Structure (WBS) method, ensuring rigorous resource planning and effective risk management throughout the entire development cycle [8], [9]. The hierarchical structure facilitated a logical workflow, beginning with market analysis and documentation—a critical stage for identifying strategic opportunities and establishing the theoretical foundation regarding ergonomics and industrial design. This was complemented by the analysis. This was supplemented by an analysis of the existing product, which critically assessed the functional shortcomings of the current standard locks.

The third phase, concept development, represented the technical core of the project, focusing on the integration of the power-assisted drive system, the redesign of the locking mechanism, and the definition of the architecture for the “smart” version. These solutions were validated during the strategic marketing phase by applying the 5W1H method and statistically analyzing user requirements gathered through a questionnaire. The project was completed with the preparation of the technical documentation, which included a summary of the results and the creation of the visual materials needed to present the final solution.

4.2. Estimated budget and profitability of the prototype

The development of the prototype involves costs related to the purchase of materials (steel, fastening systems), assisted lifting mechanisms, and safety components. The project's financial management aims to optimize production costs to ensure market competitiveness [10]. Profitability is supported by the optimal balance between the high durability of the materials and the affordable purchase cost, thereby meeting urban users' need for economic efficiency.

Table 4.2.1. Estimated Cost Breakdown

Resource	**Estimated Cost (RON)**
Metal structure	250
Locking system	80
Assisted lifting system	120
Fasteners / Fixing elements	50
Painting and finishes	70
Smart components (optional)	250
Prototype manufacturing	300
Documentation and auxiliary materials	80
Estimated Total	1200

Analysis of profitability and financial sustainability: The financial assessment confirms the device's high market potential. The initial costs of 1,200 RON include design, concept testing, and implementation, while operational costs are minimized due to mechanical simplicity, requiring only minimal maintenance.

The project's economic sustainability is ensured by:

- Diversified revenue streams: Direct sales to urban users, integration into residential complexes, or partnerships with parking lot operators.
- Competitive advantage: Low production costs combined with high demand for ergonomic solutions position the product as a superior alternative in the current market.
- Scalability: The modular architecture allows for the future development of customized smart variants, increasing the product's added value.

5. Establishing technical specifications

5.1. Requirements - Quality Characteristics Correlation Matrix

During the product development process, user requirements were translated into measurable technical specifications using the principles of the Quality Function Deployment (QFD) method [11]. The purpose of this stage is to identify the relationship between user needs and the product's functional characteristics.

The main requirements identified for the proposed product are:

- effective securing of the parking space;
- ergonomic use;
- reduction of physical effort;
- durability for outdoor use;
- safety in use.

These requirements were correlated with the product's main quality characteristics:

- strength of the metal structure;
- locking system;
- assisted lifting system;
- ergonomic design;
- corrosion resistance.

The analysis shows that the most important features for users are product safety, durability, and ergonomics.

5.2. PEST Analysis (Political, Economic, Social, Technological Context)

A PEST analysis was used to identify external factors that may influence the development and use of the product [1].

Political factors

- regulations governing the use of devices installed in urban areas;
- safety and usage standards for mechanical equipment.

Economic factors

- increasing demand for parking security solutions;
- interest in affordable and sustainable products;
- the impact of material costs on the final price.

Social factors

- increase in the number of motor vehicles;
- lack of parking spaces in urban areas;
- increased interest in comfort and ergonomics.

Technological factors

- development of smart systems;
- use of sensors and automated control;
- emergence of remote control or mobile app-based solutions.

The PEST analysis highlights the existence of a favorable context for the development of a modern device designed to secure parking spaces.

5.3. Product Usage Value (PUV)

The product's utility value represents its ability to meet users' needs through functionality, safety, and comfort [7].

The following main dimensions of the product's utility value (PUV) were identified for the proposed product:

• functional – effective securing of the parking space;

• ergonomic – simple and comfortable use;

• economic – low cost of use and maintenance;

• aesthetic – visual integration into the urban environment;

• technological – the possibility of integrating smart functions.

By combining these characteristics, the product aims to improve the user experience and adapt to current market demands.

6. Concept Development

During the conceptual development phase, two design variants of the product were analyzed. The first variant uses a fixed central base and a movable, foldable frame, featuring a simpler and more rigid construction. The second variant proposes an enclosed perimeter base, which provides additional protection for the mechanism and a more discreet visual integration into the road surface.

Both variants were developed based on the classic mechanism of existing parking barriers, but aimed to improve the user experience and optimize the interaction between the user and the product. The design process sought to maintain a simple mechanical construction that is easy to manufacture and maintain, yet adapted to current requirements regarding ergonomics and safety in use.

The proposed concept uses a movable, folding frame that rotates around a fixed axis between the raised position, used to block access, and the lowered position, which allows the vehicle to park. In the closed position, the product occupies minimal space and is designed to integrate as discreetly as possible into the roadway surface, reducing the risk of inconveniencing the user or the vehicle.

In the version with a central base, the mechanism is more visible and structurally more accessible, which facilitates installation, maintenance, and any necessary repairs to the system. At the same time, this solution provides greater rigidity to the assembly and allows for a simpler mechanical structure. The enclosed version aims to protect the mechanism from external factors, such as water, dust, or dirt buildup, and offers a more compact visual appearance that is better integrated into the urban environment.

During the concept development, aspects related to ergonomics and safety were also analyzed. Thus, solutions were proposed such as the introduction of a dedicated operating area, reducing the effort required for operation, and more efficient control of the moving frame's movement. Additionally, elements of visibility and urban integration were taken into account, such as reflective markings and compact structural forms.

The conceptual development process included the creation of preliminary sketches to highlight working positions, movement paths, and how the mechanism integrates into the product’s structure. These sketches allowed for the comparison of design variants and the identification of the advantages and limitations of each solution.

Following a preliminary analysis, the central base variant was deemed more suitable for concept development due to its structural simplicity, rigidity, and ease of implementation. Furthermore, this variant provides a more suitable foundation for potential future developments, including the integration of smart features or power-assisted drive systems.

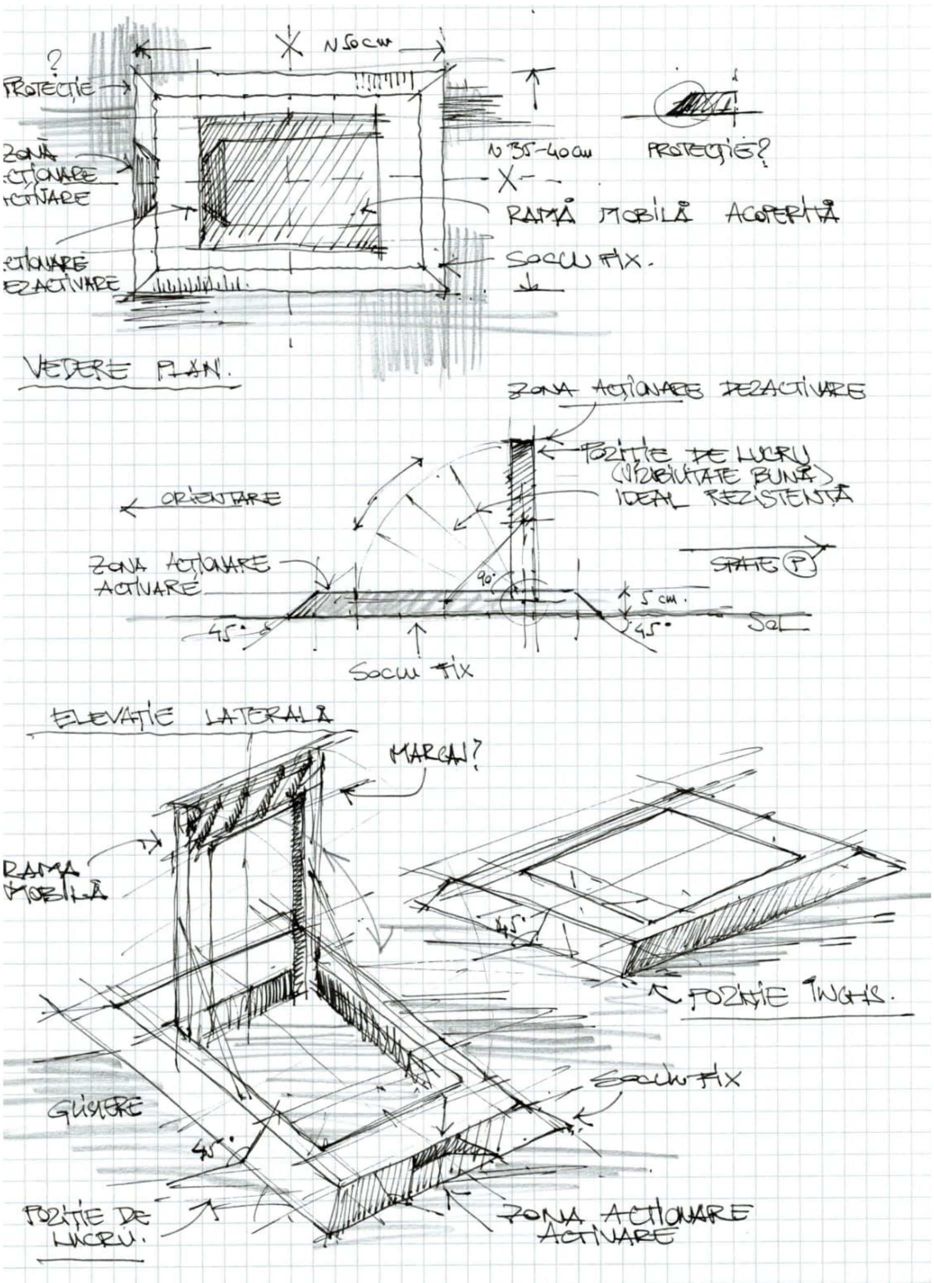

Fig. 2. Conceptual design of a parking blocker with a sealed base and a foldable movable frame

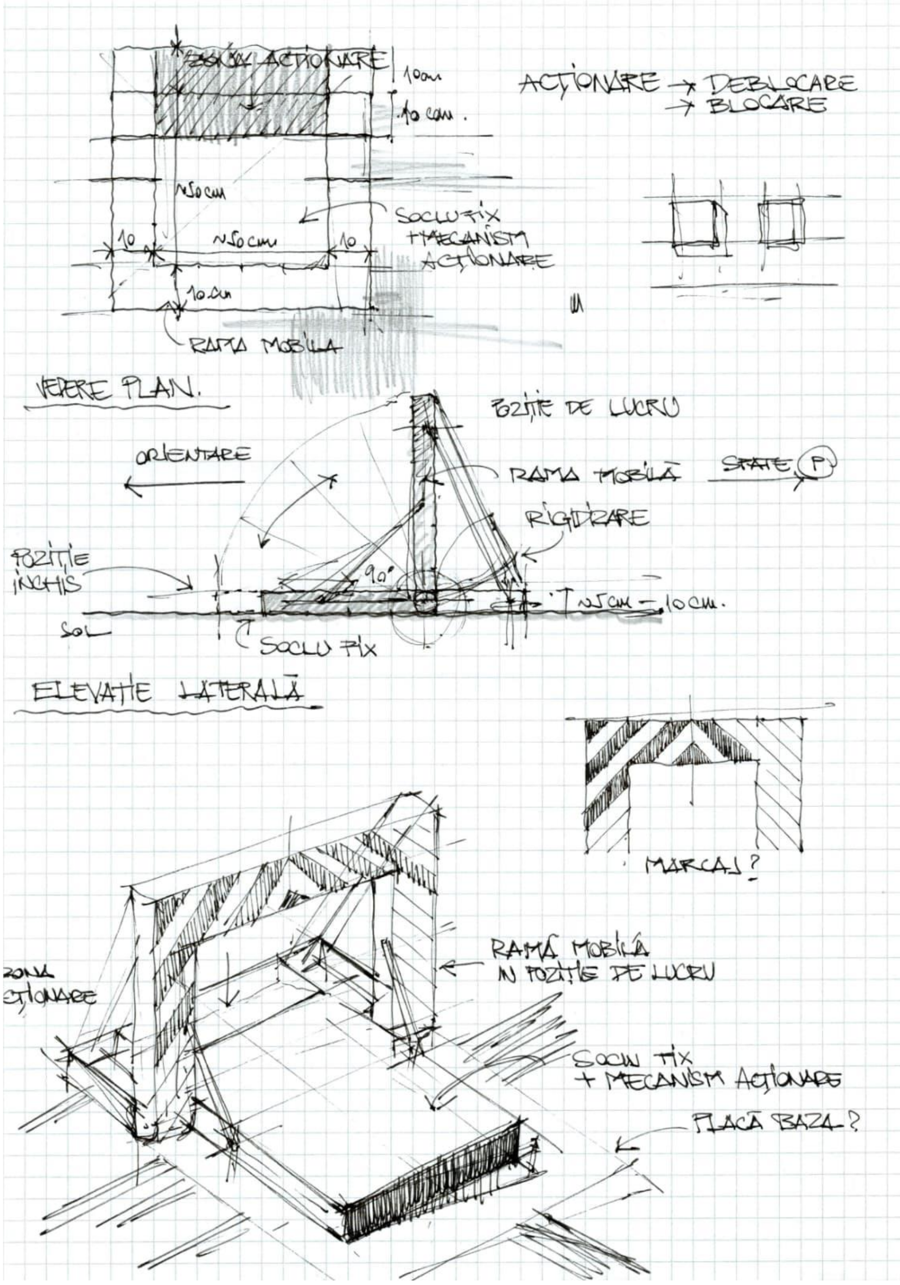

Fig. 3. Conceptual design of a parking blocker with a central base and a foldable movable frame

7. Conclusions

The objective of this study was to conduct a marketing analysis of a mechanical device designed to secure parking spaces and to identify opportunities for improving existing products. Following an analysis of the market, competing products, and user needs, it became clear that there is a demand for ergonomic, durable, and user-friendly solutions.

The study demonstrated that existing mechanical parking locks have functional and ergonomic limitations, particularly regarding operation, accessibility, and user comfort. It was also observed that many current products are primarily focused on basic functionality, without giving sufficient consideration to the user experience or aesthetic integration into the urban environment.

Based on these observations, two conceptual variants of the product were developed, based on the classic mechanism with a folding movable frame, but integrated into an improved design solution. The development process focused on reducing the effort required to use the product, protecting the mechanism from external factors, and achieving a compact and user-friendly structure.

The proposed concept aims to combine mechanical simplicity with ergonomic improvements and the possibility of integrating smart features, contributing to increased comfort, safety, and accessibility of the product. The introduction of solutions such as power-assisted operation, optimization of the locking system, and the possibility of remote control can represent a competitive advantage over existing products on the market.

Analyses conducted using methods such as QFD, PEST analysis, and evaluation of competing products have shown that the development of such a product is justified both from a functional standpoint and in light of current user requirements. Furthermore, the conceptual sketches created have allowed for the visualization of possible development directions and have contributed to defining a coherent design solution.

In conclusion, this paper highlights the potential for developing a modern mechanical device for securing parking spaces, adapted to the current urban context and focused on improving the user experience.

8. Bibliografie

[1]. Kotler, P. şi Keller, K. L. (2016), *Marketing Management*, Pearson Education, Harlow, ISBN 978-1292092621.

[2]. Ulrich, K. T. şi Eppinger, S. D. (2015), *Product Design and Development*, McGraw-Hill Education, New York, ISBN 978-0078029066.

[3]. Pahl, G., Beitz, W., Feldhusen, J. şi Grote, K. H. (2007), *Engineering Design: A Systematic Approach*, Springer, London, ISBN 978-1846283185.

[4]. Drăghici, G. (1999), *Ingineria integrată a produselor*, Editura Eurobit, Timișoara, ISBN 973-96065-7-1.

[5]. Norman, D. A. (2013), *The Design of Everyday Things*, Basic Books, New York, ISBN 978-0465050659.

[6]. Cross, N. (2008), *Engineering Design Methods: Strategies for Product Design*, John Wiley & Sons, Chichester, ISBN 978-0470519264.

[7]. Baxter, M. (1995), *Product Design: Practical Methods for the Systematic Development of New Products*, Chapman & Hall, London, ISBN 978-0412572609.

[8]. Kerzner, H. (2017), *Project Management: A Systems Approach to Planning, Scheduling, and Controlling*, Wiley, New Jersey, ISBN 978-1119165354.

[9]. Meredith, J. R. şi Mantel, S. J. (2017), *Project Management: A Managerial Approach*, Wiley, New Jersey, ISBN 978-1119369097.

[10]. Lock, D. (2020), *Project Management*, Routledge, London, ISBN 978-0367349981.

[11]. Akao, Y. (1990), *Quality Function Deployment: Integrating Customer Requirements into Product Design*, Productivity Press, Portland, ISBN 978-0915299416.

[12]. Pahl, G., Beitz, W., Feldhusen, J. şi Grote, K. H. (2007), *Engineering Design: A Systematic Approach*, Springer, London, ISBN 978-1846283185

[13]. Kano, N. (1984), “Attractive Quality and Must-Be Quality”, *Journal of the Japanese Society for Quality Control*, vol. 14, no. 2, pp. 39-48, ISSN 0386-8230.

Research on the Development of a Device for Assisting Eyeglasses Selection

CERNEA Victor, SAS Loredana-Maria, LIHOR Teodor, **TARBA Ioan-Cristian**

Faculty of Industrial Engineering and Robotics, Specialization: Computer Applications in Industrial Engineering,

Year of study: 2nd, email: cerneavictor0@gmail.com

ABSTRACT: The paper presents the advanced stage of development of the OptiMirror system, an innovative virtual eyeglass fitting device integrated into an interactive kiosk. Compared to the previous iteration, the current system introduces a complete hardware subsystem, based on Time-of-Flight sensors and ESP32 microcontroller, which provides real-time metric telemetry to the web application. Combining MediaPipe FaceMesh for the detection of 468 facial landmarks, Three.js with orthographic camera for rendering 3D models in GLB format, and a pinhole mathematical model for deterministic scaling, OptiMirror eliminates the main limitation of existing commercial systems: the absence of automatic metric accuracy. The paper details the scaling and projection algorithms, the hardware and software architecture, performance optimizations, and future research directions.

KEYWORDS: augmented reality, distance sensor, glasses, facial recognition

1. Introduction

Choosing the right pair of glasses, whether for vision correction or sun protection, requires an assessment of the aesthetic, functional and ergonomic aspects of the available models. The main challenges in choosing a pair of eyeglasses include ensuring that the frame complements the wearer's features, ensuring comfort during prolonged wear, and ensuring that the lenses provide the required level of functionality. Whether in shopping malls or airports, consumers expect solutions that balance speed of decision-making with high visual accuracy. The satisfaction they get from their shopping experience is directly related to the reliability of the fitting systems and the variety of models available through them. Virtual try-on (VTO) systems aim to meet these consumer needs by allowing them to virtually try on different eyewear models without having to try on each pair of glasses. The previous iteration of the OptiMirror system, presented at the 2025 conference, used software-only methods to analyze facial features using MediaPipe FaceMesh and rendered 3D models of goggles using Three.js with sub-100ms latency and good stability under different lighting conditions. However, as with most virtual fitting systems on the market, the system relied on statistical estimates of interpupillary distance to virtually size the goggles to the wearer's face, which increased the risk of sizing errors that the system may encounter.

The goal of this project is to develop a new iteration of the OptiMirror system that incorporates hardware elements in addition to the software elements that previously existed in the previous version of the system. The new system will use separate hardware components to measure the wearer's interpupillary distance with a high accuracy, compared to traditional methods. These measurements will allow the sizing of virtual glasses based on each wearer's face, eliminating sizing errors. In addition, there will be software enhancements to the system, such as implementing an algorithm based on the pinhole camera model to calculate the interpupillary distance, developing a full-stack local system for the privacy of the wearer's biometric data, and various software enhancements that will allow the system to run at 60 frames per second on a commercial tablet.

2. The analyzed problem and the research objectives

The problem addressed in this stage of the research is the elimination of metric errors in virtual eyewear fitting systems. The previous work demonstrated that face tracking algorithms and 3D image generation algorithms can be incorporated into a web browser, but the problem of scaling the 3D model with the user's face remains unresolved.

The main objectives of this iteration are the following: integrating hardware capable of accurately measuring the distance between the glasses and the face with an error of less than 5 mm between 200 and 1200 mm; developing a scaling algorithm that can use this measurement to correctly scale the 3D model; implementing a full-stack architecture that does not depend on the cloud to protect users' biometric data; and finally optimizing the application to be able to run at a minimum of 60 frames per second on mobile hardware, while the algorithm that fulfills the face tracking requirement and 3D visualization is being executed.

One issue that was also addressed in this iteration is hardware independence. Many commercial solutions for virtual glasses require proprietary hardware (e.g. Apple's TrueDepth sensor). OptiMirror's solution must be compatible with any webcam and any tablet that can be used with a modern web browser.

3. Existing solutions and current practices

Virtual try-on for eyewear has seen significant development in the commercial sector in recent years. Warby Parker [1] used Apple's TrueDepth sensor to map a customer's face, providing remarkable accuracy in determining the correct frame size for their glasses. However, this system relies on proprietary Apple hardware, making the products unsuitable for commercial use in public showrooms. Fitting Box Technology has created a solution that works with any webcam, using machine learning algorithms to estimate the three-dimensional position of a customer's face from a two-dimensional image. However, the lack of a measurement of the distance to the customer's face means that the size of the glasses is not accurate. Companies such as Zenni Optical and Specsavers have built try-on functionality into their websites. However, they offer a wider selection of frames, but without any face shape analysis or automated sizing capabilities.

A review of existing solutions reveals a critical gap in the industry related to the lack of metric accuracy in cross-platform solutions. All existing solutions from leading commercial virtual try-on companies either include expensive proprietary hardware or completely ignore the issue [2]. OptiMirror's approach is to include a low-cost depth sensor that can wirelessly connect to a commercial tablet to provide metric measurements without relying on other platforms.

Related literature on this topic includes the widespread adoption of MediaPipe Face Mesh, which can detect 468 facial landmarks in real time on both CPU and GPU via WebGL. There has also been a growing body of literature on combining computer vision with hardware sensors to enhance proprietary software solutions for virtual try-on applications. In addition, the field of computer vision is based on the pinhole camera model, which is used in the scaling algorithm for OptiMirror's Virtual Try-On system. Both Hartley and Zisserman provide excellent approaches to this topic in their books on computer vision theory [3]. Recent studies have also explored the use of depth-from-motion techniques to infer spatial relationships from single-camera video streams. These methods, while promising, still suffer from latency and environmental sensitivity issues. Other researchers have focused on neural radiance fields for generating photorealistic renderings of eyewear on moving faces. However, such approaches remain computationally intensive for real-time commercial applications. Collectively, this body of work underscores the ongoing trade-off between accuracy, hardware dependence, and real-time performance in virtual try-on systems.

4. Theoretical aspects and challenges

4.1. The scaling model based on hardware telemetry

The key advancement of the technology over the previous iteration is the deterministic scaling mechanism. The pinhole camera model describes how a real object is projected onto the sensor using the relationship:

$$D_{sensor} = f \cdot \frac{D_{real}}{d} \quad (1)$$

where f is the focal length of the camera, D_{real} is the actual size of the object, and d is the distance between the object and the camera. The problem is that d it is an unknown if we only use the 2D image obtained from the browser.

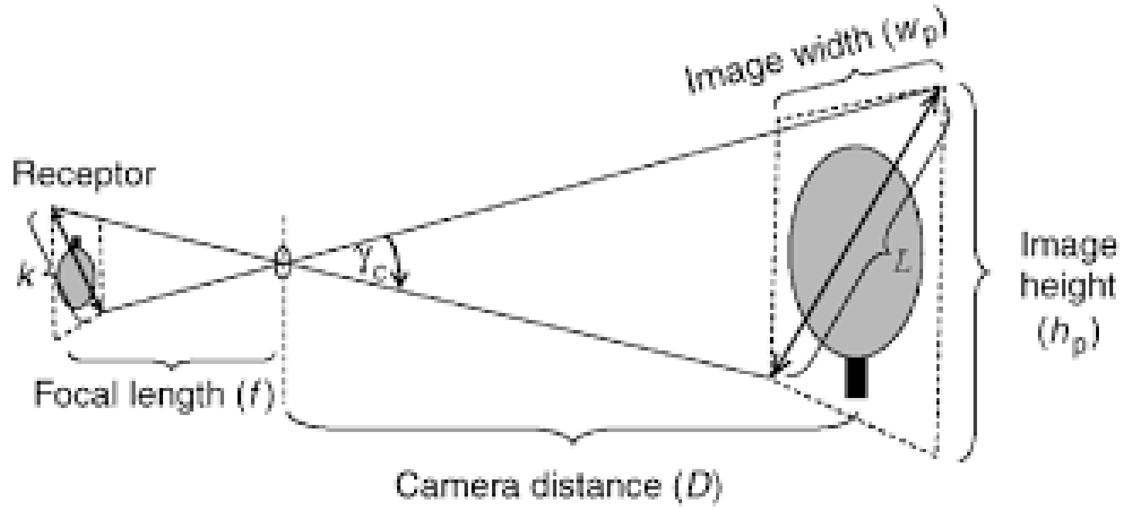

Figure 1. Pinhole camera model

OptiMirror approaches the scaling problem in a completely different way compared to the competition. Distance d is measured directly with the ToF sensor and is expressed in millimeters (d_{mm}). The introduction of this parameter allows the transformation of the optical equation into a deterministic scaling. The scaling factor p is the number of pixels that an object of 1 millimeter has at the measured distance. This parameter is defined using the following formula:

$$p = \frac{f}{(d_{mm} \cdot s)} \quad (2)$$

where f is the focal length of the system (constant in our case, 800 mm, but it can be adjusted for each system), d_{mm} is the distance measured by the sensor and s is a bias factor that can be adjusted depending on the hardware and which serves to compensate for different hardware batches.
It is important to know that a glasses model that has a frame width of 140 mm in Blender will occupy 140 p pixels on the screen at the distance measured by the sensor. Therefore, a 1:1 relationship between the physical and digital world is possible, which cannot be achieved in any software way, regardless of the quality of the artificial intelligence algorithms or predefined calibrations.

4.2. Orthographic camera and coordinate system synchronization

One architectural decision that has a profound impact on dimensional fidelity is the use of an orthographic camera within the Three.js scene, instead of the perspective camera used by default by the Three.js library. The perspective camera could introduce a second source of variation in the size of objects relative to the distance between the object and the user. The orthographic camera ensures that only two of the three dimensions (the scale of the object and the factor $p$calculated from the telemetry) influence the apparent size of the viewed objects - a unit in Three.js is equivalent to one pixel present on the screen.

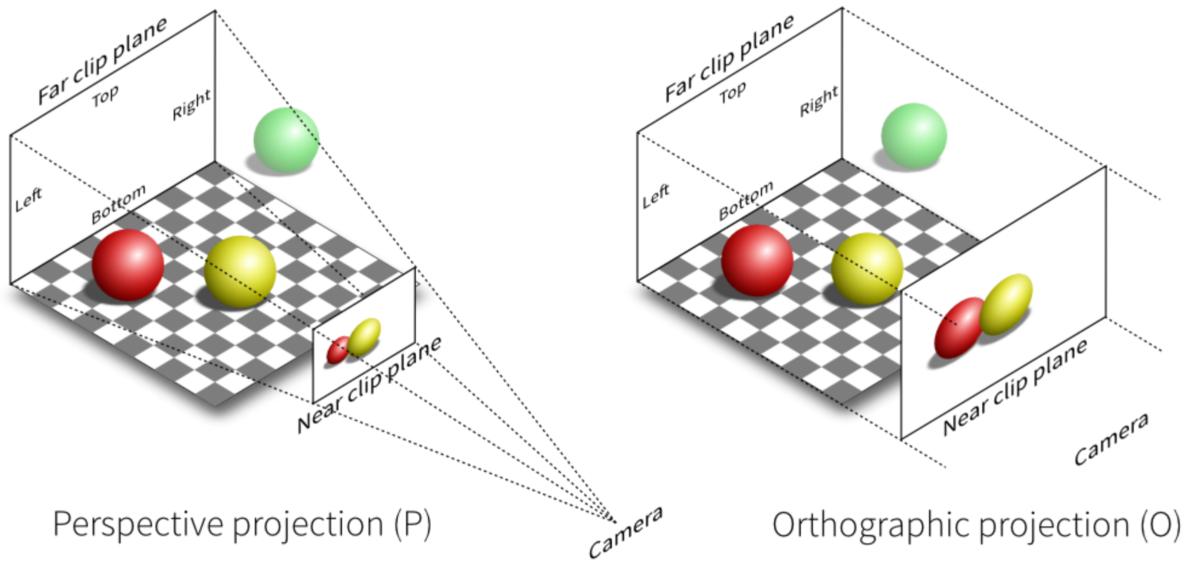

Figure 2. Perspective camera model (left) and orthographic camera model (right)

To transform MediaPipe coordinates (which are normalized and have their origin in the upper-left corner of the screen) into Three.js space (which is Cartesian and has its origin in the center of the sreen), three transformations are required. The first step is to horizontally flip the X-axis to create the illusion that the space is reflected relative to a mirror. This transformation has the form:

$$x_{mirrored} = (1 - x_{normalized}) \cdot W_{canvas} \tag{3}$$

The second step is to translate relative to the Three.js coordinate system origin and flip the Y axis. The last transformation is to scale the space by the factor p to translate the coordinates into metric units. With this transformation, the point that has the central coordinates relative to the user's face is placed at the Three.js scene origin.

4.3. Facial landmark selection and signal filtering

The MediaPipe library provides access to 468 facial landmarks, but not all of them are suitable for a system with temporal stability requirements. Landmarks describing the position of the eyes, eyelids, and lips are affected by facial expressions and blinking. In testing, the nasal region resulted in the best stability of these points. Landmark 6 describing the base of the nose is used to anchor the system, and landmarks describing the irises (159 and 386) are used to determine the angle of inclination of the head. The ToF sensor is a sensor that produces readings affected by white noise, but also by outliers. To filter these values, an exponential moving average (EMA) filter has been implemented [4]. This formula is:

$$v_{filtered}(t) = \alpha \cdot v_{raw}(t) + (1 - \alpha) \cdot v_{filtered}(t - 1) \tag{4}$$

The coefficient used for the distance value was $\alpha = 0.3$, and for the rotation angle was $\alpha = 0.4$. These values were determined in user testing sessions.

4. 4. Innovations in 3D model management

Compared to the previous iteration of the project which used generic GLB models [5], this iteration introduces two innovations in the model preparation process. The first of these is the removal of the lower portions of the frame models that are exported from Blender. Although the lower portions of the models are hidden from view when the model is rendered in a front view, they still contribute 30-40% of the triangles that make up the models. Removing these portions reduces the size of the models from 15,000-20,000 triangles to 10,000-14,000 triangles, which helps ensure higher frame rates on entry-level tablets.

The second innovation in the model preparation process is the separation of the lens frame to create two separate models within the same GLB file. Such separation allows manipulation of lens properties without affecting the model geometry. The single GLB file can contain all lens color variations: clear, smoke, colored, and metallic. By grouping these models into the same file, the need to store multiple files is eliminated.

5. System architecture

5.1. Hardware subsystem

The hardware subsystem is designed modularly and includes the following components:

- An 11-inch iPad tablet with A16 processor, 2360×1640 px Liquid Retina display and 12 MP front camera;
- An ESP32 microcontroller with Wi-Fi connectivity functionality;
- A VL53L1X Time-of-Flight (ToF) distance sensor with an accuracy of 5 mm in the range of 40 - 4000 mm and I²C interface;
- An auxiliary lighting system that has 5mm LEDs and is controlled by ESP32;
- A 14.8 V / 1550 mAh LiPo battery with voltage management;
- A mechanical frame made of 20×20 mm aluminum profiles with 3D printed fasteners.

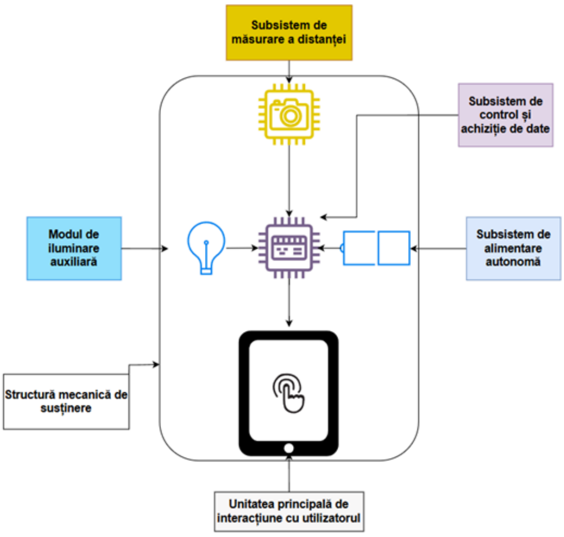

Figure 3Kiosk hardware architecture

The hardware subsystem works as follows: the ToF sensor measures the distance to the user at 50 ms intervals, the values are taken by the ESP32 which controls the lighting system depending on the user's presence in the optimal area (below 100 cm), and the distance data is transmitted to the tablet via WebSocket at a frequency of 20 Hz. On the tablet, the values are taken and entered into the scaling algorithm. WebSocket was chosen over HTTP, because this protocol offers lower latency (full-duplex TCP connection) and is compatible with Safari. This system also includes a fallback in case of errors. If the WebSocket connection is destroyed, the frontend tries to reconnect a maximum of 5 times at 2 second intervals. If the sensor communicates an out-of-range error, the distance is estimated from the apparent width of the user's face, and the system indicates this by displaying a yellow indicator.

5.2 Software architecture

The software architecture is local, full-stack and without dependencies on cloud services. Video processing and facial feature extraction happen completely in the browser sandbox, using only the local resources of the device. The backend, built with Node.js and Express, is dedicated only to commercial orders and GLB files. Biometric data does not leave the terminal device, so the system complies with GDPR and has no issues related to the transmission of facial data over the network.

The database is an instance of SQLite, which stores only the commercial metadata for a single tablet device. The database was built with this solution to keep the implementation lightweight and to avoid starting a database server daemon process on the tablet device. The database has three tables: a table for eyeglass models that stores the commercial name, GLB file, interpupillary distance (between the closest points of the two pupils, measured in Blender), stock, and an emoji for each model; a table for orders placed in the web kiosk, which assigns each order to an eyeglass model, color, contact information, and an automatic date; a table for website administration with the credentials required to access the administration panels. A JSON field is used to represent the color palette that exists for each model, which is an attribute limited to a certain number of colors for each model. Static GLB models are served via Express from a dedicated directory, accessible to the tablet via the kiosk's local network. The backend provides REST routes for inserting, retrieving, updating, and deleting glasses models (CRUD). The /api/glasses route is opened to receive GLB files and metadata using multer. When a model is deleted, the GLB file is also deleted via the fs library. The admin panel exposes optical calibration parameters, allowing for adjustment of focal length (f) and bias (s), all without requiring changes to the source code.

The frontend is built with React, React Three Fiber (with Zustand and Framer Motion). The 3D transition with Three.js runs at 60 Hz and is separated from React to avoid potential device performance issues. The rapidly changing data from the video and facial landmarks is only part of the Zustand library collection, accessed only by the *useFrame function* in Three.js. This development approach is one of the reasons why the app runs at 58-60 fps on devices with average hardware parameters.

6. Experiments and results

The tests were conducted on multiple devices (in addition to the 11-inch iPad, which is the main platform, but also on desktop laptops with Chrome and Firefox browsers) and in various lighting conditions. The results obtained indicate improved performance of the system compared to the previous version.

Metric accuracy has increased; while in the first prototype the scaling errors (relative to the actual frame dimensions) averaged 8-12% (software estimate based on statistical IPD), in the new version this value is below 2%, especially in the range from 300 to 900 mm, when the ToF sensor is active. Results obtained from tests with different people and categories of users indicate that the virtual frames "look real", instead of "like an approximation".

The system performance is better than in the previous version. Implementation of several optimizations (merging meshes with the same material, removing temples from GLB models, decoupling the Three.js loop from the React reconciler via Zustand, LRU cache for up to 5 models) allowed a frame rate of about 58-60 fps on the iPad, compared to 48-52 fps in the previous version. The system latency is below 50 ms, which is an acceptable value for simulating a mirror.

A separately evaluated aspect was the hardware subsystem simulated in the Wokwi platform (with the HC-SR04 sensor as a replacement for the VL53L1X, unavailable in the simulator): the control logic (measurement, comparison with threshold, LED activation) worked correctly, validating the functional flow before physical implementation.

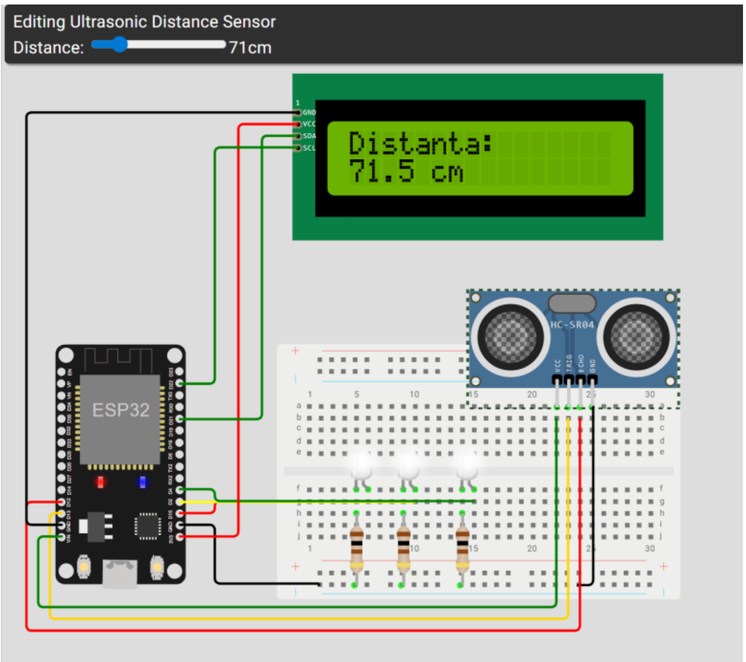

Figure 4. Simulation of the distance measurement subsystem in the Wokwi platform

Figure 5. Projection of virtual glasses on the user's face

7. Conclusions

This paper presented the significant evolution of the OptiMirror system compared to the previous iteration, by integrating a complete hardware subsystem that ensures the metric accuracy of the system inside the scaling algorithm. The contributions that were made in this iteration are the following:

- Scaling algorithm, based on ToF sensor telemetry and pinhole camera model, which reduces scaling errors to below 2%;
- Hardware architecture, which allows communication via WebSocket between ESP32 and tablet, as well as an adaptable mechanical structure;
- Use of the orthographic camera and synchronization of coordinate systems, which ensures a 1:1 ratio between the real and virtual size of the 3D model;
- Innovations in the management of GLB models, by separating the frame from the lenses and eliminating the model temples, so that each model is saved in a single file;
- The full-stack architecture works locally on client devices, so biometric data never leaves the system.

Future research for this system will be carried out in the framework of solving the 3D model occlusion problem, implementing a recommendation system based on convolutional neural networks, expanding the catalog through photogrammetric scanning of face frames, and expanding the functions that can be offered from the kiosk interface. It is possible to extend this system to other accessories and accessories

for the face and body, allowing the technology to be expanded to a wider field.
However, there are also some limitations to the system. The VL53L1X sensor tends to receive outlier readings in case of strong reflection from certain surfaces (glasses, light skin), which are filtered by EMA but which introduce an additional delay during sensor reading of approximately 100 ms. Another 120 mA of current is consumed in auxiliary lighting, which reduces the autonomy to approximately 10 hours of device operation. Future work will focus on replacing the ToF sensor with the VL53L5CX sensor, implementing a hybrid recommendation based on convolutional neural networks and extending the application to mobile platforms (Android and iOS).

7. Bibliography

[1] Warby Parker, “Warby Parker Mobile Apps,” [Interactive]. Available: https://www.warbyparker.com/app. [Accessed November 2025].

[2] B. Konarzewski and M. Reiner, "Augmented Shopping: Virtual Try-On Applications in Eyewear E-retail," 2023.

[3] AZ Richard Hartley, Multiple View Geometry in Computer Vision, 2004.

[4] SO Haykin, Adaptive Filter Theory, Haykin, 2013.

[5] The Khronos Group, "glTF - Runtime 3D Asset Delivery," May 2025. [Interactive]. Available: https://www.khronos.org/gltf/.

CONVERSION OF A CLASSIC HEATING BOILER INTO AN INTELLIGENT SYSTEM WITH WEATHER-COMPENSATED HEATING CURVE CONTROL

POPAN Cristian-Ovidiu, IVAN Victor-Ştefan and Asst. Prof. Ph.D. Eng. **MUNTEANU Iulian-Sorin (Scientific coordinator)**

Faculty: Industrial Engineering and Robotics, Specialty: Technological Systems Engineering and Management, Year of study: I - Master, e-mail: cristi.popan@gmail.com

ABSTRACT: This paper presents a low-cost solution for converting a conventional heating boiler into an intelligent system with weather-compensated heating curve control. The prototype is based on an Arduino Uno microcontroller, which processes the outdoor temperature and the user-selected heating curve slope to determine the required heating water temperature. This value is converted into an angular position and transmitted to a 270° servomotor that mechanically adjusts the boiler temperature knob. The system displays the outdoor temperature, calculated water temperature, servomotor angle and selected slope on an LCD interface. The solution demonstrates how an analog boiler can be upgraded through a simple embedded control architecture, without direct intervention in its internal electronics.

KEYWORDS: weather-compensated heating, Arduino Uno, smart heating, servomotor control, boiler retrofitting

1. Introduction

In an era where energy efficiency and reducing resource consumption are key objectives for both users and society, the optimization of heating systems has become a major area of interest.
Most conventional boilers, especially older models, operate based on an "on/off" room thermostat or by manually adjusting the temperature of the heating medium. In this operating mode, the boiler produces water at a fixed temperature, regardless of outdoor weather conditions.
The concept of a thermal compensation curve (or heating slope) changes this operating paradigm. The basic principle involves correlating the temperature of the heating medium with the outdoor temperature: as the outdoor temperature drops, the temperature of the water sent to the radiators must increase, following a predefined mathematical function. In this way, the system anticipates the building's heating requirements and continuously adjusts operating parameters to maintain an optimal balance between comfort and energy consumption.
Modern condensing boilers frequently use such climate compensation algorithms, but many conventional boilers do not come with this feature as standard.
By using an open-source platform such as Arduino Uno, the proposed solution offers the advantages of low cost, high flexibility, and the possibility of future expansion with additional features, such as consumption monitoring, wireless connectivity, or integration into a "smart home" system.
This paper aims to present both the theoretical principles underlying climate compensation and to describe the design, implementation, and testing phases of the developed module.

2. Current status of the thermal compensation curve concept

The heating curve sets the optimal water temperature in the radiators so that the indoor temperature remains constant, regardless of external weather conditions. The operating principle is simple: as the outdoor temperature drops, the temperature of the heating medium must rise to compensate for the building's additional heat loss.
Mathematically, the compensation curve can be approximated by the following equation:

$$T_{tur} = T_{int} + k \cdot (T_{ref} - T_{ext}) \tag{1}$$

where:
- - the temperature of the water sent to the radiators;
- - desired indoor temperature;
- - the measured outdoor temperature;

- - reference outdoor temperature;
- - heating slope.

The parameter determines the system's sensitivity to outdoor temperature fluctuations. The correct choice of this value depends mainly on the building's insulation and the type of heating system.

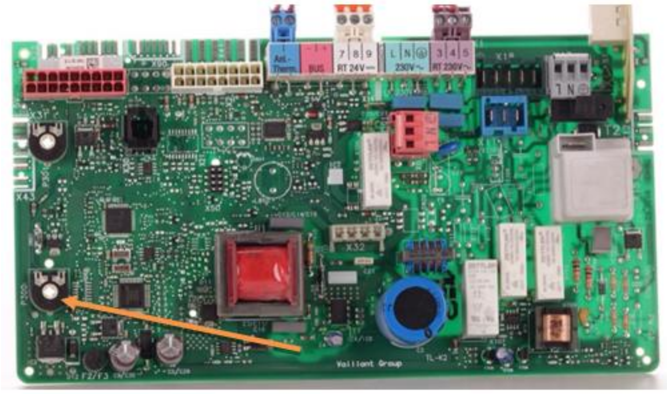

Fig.1. Boiler main board

The compensation curve also varies depending on the type of heating system used. Traditional radiators operate at high fluid temperatures, typically between 60°C and 80°C, rapidly transferring thermal energy via convection. In contrast, underfloor heating is a low-temperature system characterized by very high thermal inertia. In this case, the concrete screed acts as a thermal accumulator capable of storing significant amounts of energy.

For underfloor heating systems, the temperature of the heating medium should generally not exceed 45°C–50°C. Exceeding this limit can lead to:

- damage to the screed (cracks caused by excessive expansion);
- peeling of floor finishes (hardwood, tile);
- physical discomfort (circulatory issues in the legs).

The system based on the Arduino Uno platform allows the implementation of strict software limits for the maximum temperature. The servomotor used for the mechanical actuation of the boiler potentiometer is controlled so that it cannot exceed the safety thresholds set by the program. This approach provides an additional level of protection for the heating installation and transforms a classic boiler into a system capable of automated climate control.

3. System architecture and hardware components

The system architecture is built around the Arduino Uno platform, which coordinates data acquisition, control algorithm processing, and the mechanical actuation of the control system.

The general structure of the system consists of the following functional blocks:

• central processing unit;
• outdoor temperature sensor;
• display and control interface;
• servomotor-based mechanical drive system;
• buttons for setting the desired slope;
• power supply.

The system operates by reading the outdoor temperature and calculating the optimal temperature of the heating medium according to the *user-defined compensation curve*.

The result is converted into *an angular position of the servomotor*, which *mechanically actuates the boiler's potentiometer*.

3.1 The central unit – Arduino Uno

The main component of the system is the Arduino Uno development board, which serves as the "brain" of the entire system and performs the following key functions:

• collecting data from the temperature sensor;
• calculating the temperature of the heating water according to the compensation algorithm;
• generating PWM signals to control the servomotor;

• updating the information displayed on the screen;
• managing user commands entered via buttons.
An important advantage of using this platform is the software's flexibility. The algorithm can be easily modified or expanded to implement additional functions.

3.2 The 270° servomotor

The boiler control is operated by a 270° rotary servomotor. The choice of this type of servomotor is essential for mechanical compatibility with most rotary potentiometers used on conventional boiler control panels, as it can almost exactly replicate the mechanical travel of a temperature control potentiometer. This provides a direct mapping between the servomotor's position and the temperature selected on the boiler.
In this project, the servomotor's shaft is mechanically coupled to the boiler's potentiometer, allowing for automatic adjustment of the heat transfer fluid temperature between the available minimum and maximum values (e.g., 30°C – 80°C).
The position of the servomotor is determined by a proportional relationship between the calculated temperature and the angle of rotation:

$$\theta = k \cdot (T_{set} - T_{min}) \tag{2}$$

where:
- - the servomotor angle;
- - temperature calculated by the algorithm;
- - minimum boiler temperature;
- - temperature–angle conversion factor.

3.3 Human–Machine Interface (HMI)

A human-machine interface based on an LCD display and control buttons has been implemented for system monitoring and configuration. This interface allows the user to view operating parameters in real time and modify certain settings without connecting to a computer.
The LCD display serves to transform an internal process—invisible to the user—into a transparent and easy-to-monitor system. The information displayed includes:
• the outdoor temperature measured by the sensor;
• the calculated temperature of the heating water;
• the angular position of the servomotor;
• the heating slope value.
Two buttons were used to configure the parameters, allowing the user to adjust the compensation slope value. This solution offers a simple and intuitive method for adapting the system's behavior to the building's thermal characteristics.

3.4 Outdoor temperature sensor

The outdoor temperature sensor is the main input element of the control system. It continuously measures the outdoor temperature and transmits the data to the microcontroller.
The accuracy of this measurement is very important because the entire compensation curve depends on the outdoor temperature value. Any measurement error can lead to incorrect adjustments of the heat transfer fluid temperature and, consequently, to a decrease in energy efficiency.
To obtain accurate readings, the sensor must be installed:
• in an area protected from direct sunlight;
• away from artificial heat sources;
• protected from moisture and precipitation.

3.5 General System Operation

The system's operating process can be described in the following steps:
- ➢ The outdoor sensor measures the ambient temperature;
- ➢ The Arduino Uno reads and processes the measured value;
- ➢ The algorithm calculates the optimal temperature of the heating medium using the

compensation curve;
- The calculated temperature is converted into a rotation angle;
- The servomotor adjusts the position of the boiler's potentiometer;
- The updated parameters are shown on the LCD display.

4. Calculation and control algorithm

The system operates via a program developed for the Arduino Uno platform, written in C/C++ using the Arduino IDE. The software is designed to implement climate compensation logic, control the position of the servomotor, and facilitate user interaction through the LCD display and configuration buttons.

The program runs continuously in the main loop(), periodically performing read, calculation, and control operations. The software structure was designed so that the system operates stably, with minimal servomotor movements and the ability to quickly adjust operating parameters.

4.1 Used libraries

The following libraries were used to implement the hardware functions:

- **Servo.h** – for controlling the servo motor via PWM signals;
- **Wire.h** – for I2C communication;
- **LiquidCrystal_I2C.h** – for controlling the LCD display with an I2C interface.

4.2 System variables and parameters

The program uses several variables to store operating parameters and calculated values.

The outdoor (test) temperature is stored in the variable , and the heating slope (start) is defined by . The desired indoor temperature is set to . Safety limits for the water temperature have also been defined:

- minimum temperature: 20°C;
- maximum temperature: 75°C.

4.3 System configuration

In the *setup ()* function, all hardware components of the system are initialized: the serial port for debugging, the button input pins, the LCD display, and the display backlight.

The buttons are configured in INPUT_PULLUP mode, which allows the use of the microcontroller's internal pull-up resistors and eliminates the need for additional external resistors.

Upon system startup, an introductory message is displayed confirming the correct initialization of the module.

4.4 Adjusting parameters using the buttons

The system allows real-time modification of the simulated outdoor temperature and the heating slope via four buttons, 2 for temperature and 2 for heating slope.

The outdoor temperature can be adjusted within the range: , and the slope can vary between:

Value constraints are enforced using the *constrain ()* function, preventing the entry of invalid parameters.

To prevent accidental multiple readings of the buttons, a delay (*delay (150)*) has been introduced, which functions as a simple software debounce mechanism.

4.5 The Viessmann compensation curve algorithm

The calculation of the water temperature is based on an algorithm inspired by the compensation curves used in commercial Viessmann systems. Unlike a simple linear relationship, the algorithm used introduces a polynomial correction factor that allows for a more realistic approximation of thermal behavior.

The difference between the indoor and outdoor temperatures is calculated using the following equation:

$$\Delta T = T_{room} - T_{ext} \tag{3}$$

The compensation factor is determined using the equation:

$$F = 1.4347 + 0.021 \cdot \Delta T + 0.0002479 \cdot \Delta T^2 \tag{4}$$

The water temperature is then calculated using the formula:

$$T_{flow} = T_{room} + P \cdot \Delta T \cdot F \tag{5}$$

This method allows for a progressive and natural variation in the water temperature, similar to the behavior of modern climate-controlled heating systems.

After calculation, the temperature is limited by the software to the permissible range:

$$20^{\circ}C \leq T_{flow} \leq 75^{\circ}C \tag{6}$$

4.6 Conversion of temperature to angular position

The calculated temperature must be converted into the mechanical position of the servomotor that controls the boiler's potentiometer.

The conversion is performed using the following equation:

$$\theta = (T_{flow} - T_{min}) \cdot \frac{270}{T_{max} - T_{min}} \tag{7}$$

where:

- represents the servomotor angle;
- is the calculated temperature;
- and represent the boiler temperature limits.

The servomotor used has a maximum stroke of 270°, which allows for complete mapping of the boiler control.

4.7 Servomotor control and anti-buzzing optimization

A common issue with servomotors is the continuous application of the PWM signal, which causes vibrations and mechanical noise ("buzzing"). To eliminate this effect, an *"attach/detach"* logic has been implemented.

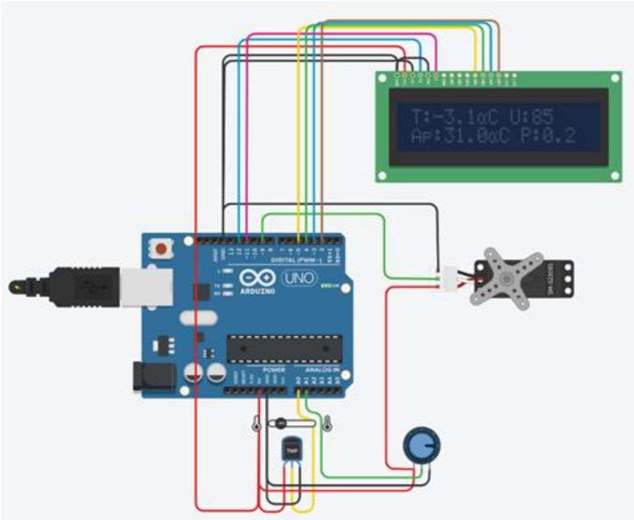

Fig. 2. System simulation in Tinkercad

The servomotor is activated only when the calculated position differs from the previous position.

4.8 Displaying parameters on the LCD screen

The LCD interface continuously displays the system's main parameters: outdoor temperature (T); servomotor angle (Ang); calculated heat transfer fluid temperature (Ap) slope value (P). Real-time display allows monitoring of system behavior and facilitates system calibration.

4.9 General operating flow

The implemented algorithm operates cyclically according to the following sequence: (a) reading button commands; (b) updating configuration parameters; (c) calculating the heat transfer fluid temperature; (d) applying safety limits; (e) calculating the servomotor angle; (f) positioning the servomotor; (g) updating the LCD display; (h) repeating the control cycle.

5. System design and construction

The system development process was carried out in two main stages: design and virtual simulation, followed by the physical implementation and testing of the prototype.

5.1 Design and virtual simulation

In the initial stage, the system was designed and tested using the Tinkercad platform (see Fig. 2). The simulation environment allowed for the rapid creation of electrical connections and verification of component functionality without the use of physical hardware.

5.2 System construction

Following the successful simulation of the system in Tinkercad, the necessary subassemblies were procured, and real-world testing ensued. A sequence of the steps followed can be seen in the images below:

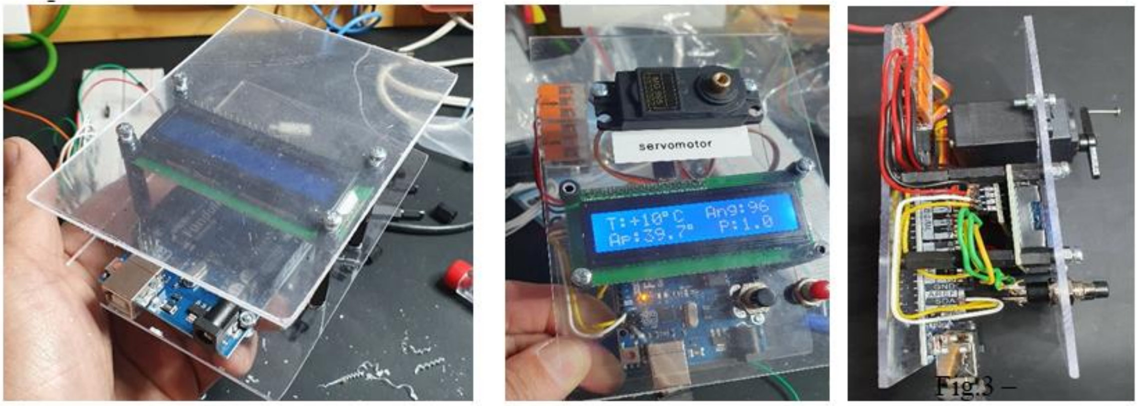

Fig.3 – LCD display assembly; Servomotor assembly; Wiring

Fig. 4. The system built on the Arduino Uno platform, which provides automated climate control

5.3. Analysis of compensation slopes

The compensation slope expresses the ratio between the temperature variation of the heating medium and the outdoor temperature variation. Its value is selected based on the type of system and the building's insulation level. For traditional radiators and poorly insulated buildings, higher slopes are required, while for underfloor heating or well-insulated buildings, lower slopes are appropriate.

Table 1 Slope values depending on the heating system and building insulation

Heating system	Building type	Slope Value (P)	T [water] at -10°C outside
Traditional radiators	Old, uninsulated house	1.5 — 2.0	70°C — 85°C
Modern radiators	Moderately insulated house	1.0 — 1.2	55°C — 65°C
Underfloor heating	Standard insulation	0.5 — 0.8	35°C — 42°C
Underfloor heating	Passive house	0.2 — 0.4	28°C — 32°C

For an underfloor heating system, a slope of 0.6 can generally result in a water temperature of approximately 28°C at +10°C outside and approximately 40°C at -10°C outside. By adjusting the slope using the buttons, the user can calibrate the system's behavior based on the building's actual thermal response. The simultaneous display of the slope, calculated temperature, and actuator angle allows verification of how the algorithm converts outdoor conditions into a mechanical command for the boiler.

6. Conclusions

This paper presented the development of a functional prototype for converting a conventional heating system into a smart system with climate compensation curve control.

The proposed solution modernizes a boiler with analog control through a functional *retrofitting* method, without direct intervention on the internal electronics; the temperature of the water is controlled by mechanically actuating the boiler's knob with a servomotor controlled by an Arduino Uno.

The original contribution of this work lies in the integration of a simple and scalable hardware-software architecture, consisting of an Arduino Uno microcontroller, an LCD interface, configuration buttons, a climate compensation algorithm, and a 270° rotation servomotor.

From a software perspective, the innovative contribution consisted of implementing the calculation of the heating medium temperature based on the outdoor temperature and the selected slope, limiting the temperature to safe ranges, converting the calculated temperature into an angular position, and introducing anti-chatter logic to reduce the load on the servomotor.

The prototype highlighted the specific relationship within a mechatronic system between the input parameter, control algorithm, human-machine interface, and actuator. By adapting the temperature of the heat transfer fluid to outdoor conditions, the solution can help increase thermal comfort, reduce sudden operating cycles, and limit thermal stress on the system. Its non-invasive nature, low cost, and simplicity of implementation allow the concept to be adapted to various heating systems.

Future developments may include the integration of a real outdoor temperature sensor, measurement of supply and return temperatures, wireless connectivity, energy consumption monitoring, and experimental calibration of the compensation curve on a real system under variable seasonal conditions.

From this perspective, the prototype can serve as an educational and practical platform for studying HVAC automation and the modernization of traditional heating systems.

7. Bibliography

[1]. Arduino, Arduino Uno Rev3 – Official Documentation, accessed in 2026.

[2]. Arduino, Arduino IDE – Language Reference and Libraries Documentation, accesat 2026.

[3]. Viessmann, Heating Curve and Weather Compensation Principles, accessed in 2026.

[4]. Autodesk Tinkercad, Tinkercad Circuits Simulation Environment, accessed in 2026.

[5]. Technical documentation for the 270° PWM servo motors and I2C LCD displays used in the project, accessed in 2026.

[6]. Arduino and HVAC technical resources on servo motor control and heating system automation, accessed in 2026.

[7]. Bolton, W., Mechatronics: Electronic Control Systems in Mechanical and Electrical Engineering, Pearson Education, 2009.

DEVELOPMENT AND IMPLEMENTATION OF A ROBOTIC SYSTEM FOR DENTAL IMPLANTOLOGY PROCEDURES: FROM CONCEPT TO CLINICAL APPLICATIONS

SĂTEANU Claudiu-Constantin, **GIGIU** Octavian-Niculae and Assoc. Prof. Ph.D. Eng. **UNGUREANU Liviu-Marian**

Faculty: Industrial Engineering and Robotics, Specialization: Modeling and Simulation of Mobile Mechanical Systems, Year of Study: II, e-mail: claudiu.sateanu@stud.fiir.upb.ro

The paper analyzes the evolution of dental implantology and highlights the limitations of conventional methods and computer-assisted systems, such as the rigidity of static guides, the influence of human error, and the lack of real-time adaptability. In this context, a robotic system aimed at improving the precision and safety of implantology procedures is proposed. The research focuses on the integration of medical imaging into robotic coordinates, the development of control algorithms, and the CAD modeling of the mechanical assembly. The hardware and software architecture, data flow, and coordinate transformations required for the operation of the system are presented. The implementation includes data processing, communication with the robot, and the complete integration of all components. The results obtained confirm the advantages of dynamic and robotic systems compared to conventional techniques.

KEYWORDS: implantology, robotics

1. Introduction

The development of digital systems, medical imaging and robotics has led to the emergence of new methods of assisting the doctor in the process of planning and positioning of dental implants. In this context, it is proposed to develop and implement a computer-assisted robotic system for precise positioning of dental implants. The main objectives pursued are the integration of medical images into robotic coordinates, the development of control algorithms and coordinate transformation, CAD modeling of the mechanical assembly and the creation of a hardware and software architecture capable of allowing precise control of the robot in the medical application.

To achieve these objectives, stages of documentation and analysis of existing systems, mechanical design and CAD modeling, software development for data processing and robotic control, as well as the integration of hardware and software components into a functional system were carried out. In the final stage, experimental tests were performed to evaluate the accuracy and repeatability of the proposed system, the results obtained highlighting the potential of using medical robotics in the field of dental implantology.

2. Current state

Dental implantology represents one of the most important development directions of modern dentistry, due to the need to obtain the most precise, minimally invasive and predictable interventions. The evolution of digital technologies has led to the emergence of surgical planning and guidance systems, which aim to increase the precision of implants and reduce patient recovery after classical interventions. Currently, the integration of robotics and artificial intelligence in the medical field opens new perspectives for the automation and optimization of implantology procedures.

Conventional methods of dental implantology are mainly based on the experience of the doctor and the use of static surgical guides. These guides are made based on images obtained by computed tomography (CT) and allow the orientation of surgical instruments according to a plan. Although these solutions offer higher precision compared to manual interventions, they have important limitations. These include the rigidity of the guide, the impossibility of adapting in real time to changes occurring during the intervention, and the influence of errors generated by patient positioning or mechanical tolerances of the guide. In recent years, dynamic surgical navigation systems have begun to be used to overcome the limitations of static guides.

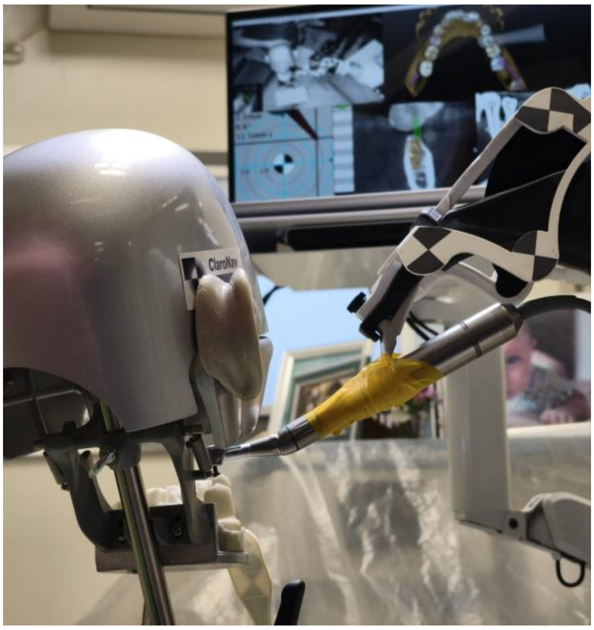

Fig. 1. Integration of the robotic system with the medical planning and control interface

Although dynamic systems increase the flexibility and precision of the intervention, they still depend on the operator's experience and require very precise manual coordination. In parallel, the development of efficient methods for calibrating and transforming coordinates between imaging systems and robotic space is being pursued. Despite all the progress made, there are still numerous technical and technological challenges. These include real-time data synchronization, communication latencies, the accuracy of coordinate transformations and the safety of human-robot operator interaction.

The work aims to integrate medical images into a robotic system based on a KUKA LBR MED arm [1], develop control algorithms and create an architecture capable of allowing precise positioning of surgical instruments. This approach aims to highlight the advantages of dynamic robotic systems compared to conventional methods and contribute to the development of future robotic-assisted medical applications.

3. Architecture and design of the robotic system

The proposed robotic system for dental implantology application is designed as an integrated hardware-software platform intended for precise positioning of surgical instruments based on information obtained from medical imaging and digital planning systems. The system architecture aims to achieve a link between the virtual planning environment and the physical execution of robotic movements.

The system consists of several main components: the medical robot, the data processing system, the software modules for the interpretation of coordinates, the communication system and the auxiliary mechanical assemblies. The experimental platform is built around the KUKA LBR MED medical robot [1], chosen due to its high precision, the large number of degrees of freedom and the possibility of integration into medical applications. The robot allows the execution of controlled and repeatable movements, being suitable for applications requiring high-precision positioning.

Fig. 2. Experimental setup for validating robotic instrument positioning

The hardware system includes a computer dedicated to data processing and software algorithm execution, as well as auxiliary components for communication and control. Communication between the robot and the computer is achieved through KUKA-specific protocols, used for coordinate transfer and motion synchronization [2].

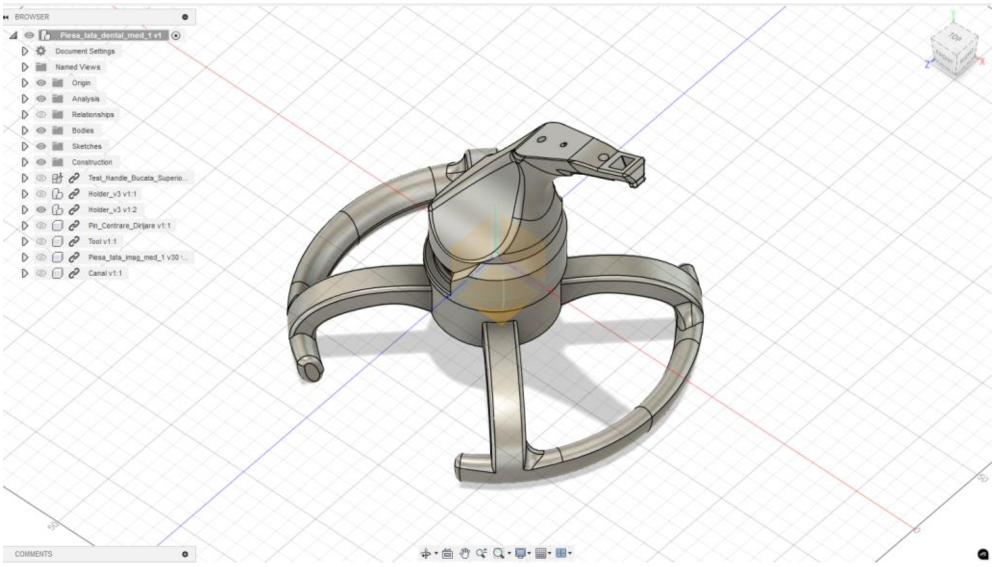

Fig. 3. Mechanical assembly designed for fixing and guiding medical components

In order to integrate the robot into the medical application, CAD modeling of the mechanical components necessary for positioning and fixing the experimental system was performed. The three-dimensional models were developed using specialized CAD software, aiming to obtain a modular structure that is easy to adapt to different experimental configurations.

4. Software development and robotics integration

Medical data processing is one of the essential steps of the developed robotic system. The data from medical imaging is interpreted and converted into coordinates that can be used to control the robot.

Modules have been developed to process information from the imaging systems and generate the positions required for the insertion of the dental implant. Data processing includes the identification of points of interest, the transformation of coordinates and the verification of the consistency of the information transmitted to the robot. These are still in full testing.

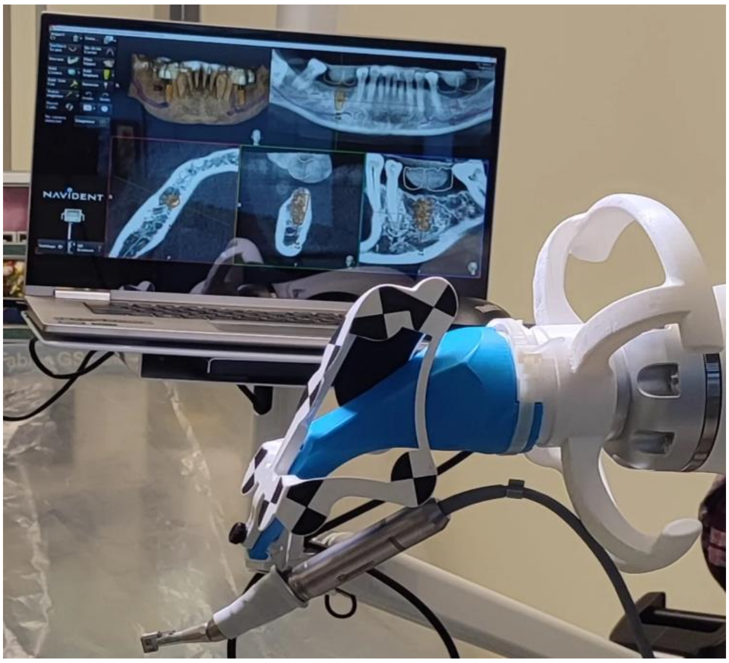

Fig. 4. Experimental configuration of the robotic navigation and control system used in dental implantology [4]

For the transfer of coordinates between the different systems used, homogeneous transformations and rotation matrices have been implemented. These allow the expression of the position and orientation of the points in relation to the robot coordinate system.

The general transformation used for positioning the point of interest is defined by the relationship:

$$^{B}T_{TCP} = {}^{B}T_{R} \cdot {}^{R}T_{C} \cdot {}^{C}T_{M} \cdot {}^{M}T_{P} \tag{1}$$

where each matrix represents the transformation between two successive coordinate systems.

Spatial rotation matrices were used to orient the surgical instrument:

$$R_z(\theta) = \begin{bmatrix} \cos\theta & -\sin\theta & 0 \\ \sin\theta & \cos\theta & 0 \\ 0 & 0 & 1 \end{bmatrix} \tag{2}$$

These mathematical relationships allow the calculation of the final position of the robot and the adaptation of the tool orientation according to the planned trajectory [3].

5. Experimental validation of the system

To validate the operation of the robotic system, experimental tests were performed to evaluate the accuracy and repeatability of the positioning. The tests aimed to verify the correctness of the coordinate transformations and the behavior of the system in different experimental configurations.

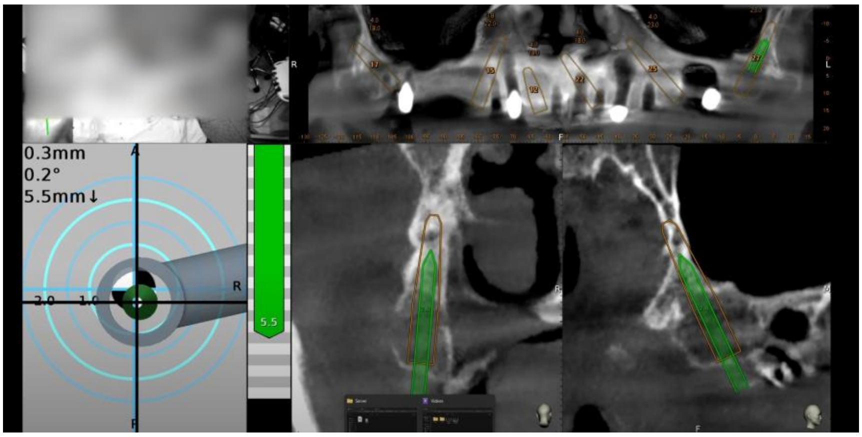

Fig. 5. Medical image processing and coordinating generation for the robotic system [5]

Several measurements of the final position of the robotic effector were performed and compared with the theoretical positions generated by the software system.

6. Personal contributions

Within the development of the robotic application for dental implantology, personal contributions were mainly oriented towards the CAD design and modeling part and the practical integration of the robotic system in the experimental configuration used for validating the medical application.

Fig. 6. Validation of the functionality of the navigation system and robotic integration in the dental implantology application

One of the main contributions consisted in the design and CAD modeling of the mechanical components used in the robotic system. Three-dimensional models were created for the supports and assemblies necessary for the integration of the robot in the experimental application, aiming to obtain a stable, modular structure compatible with the specific requirements of the medical environment. The design process included the development of constructive solutions for fixing the components, checking mechanical interferences and optimizing the geometry of the assemblies for use in the experimental environment. Successive adaptations of the designed components were also made, depending on the experimental needs and the practical integration of the robotic system.

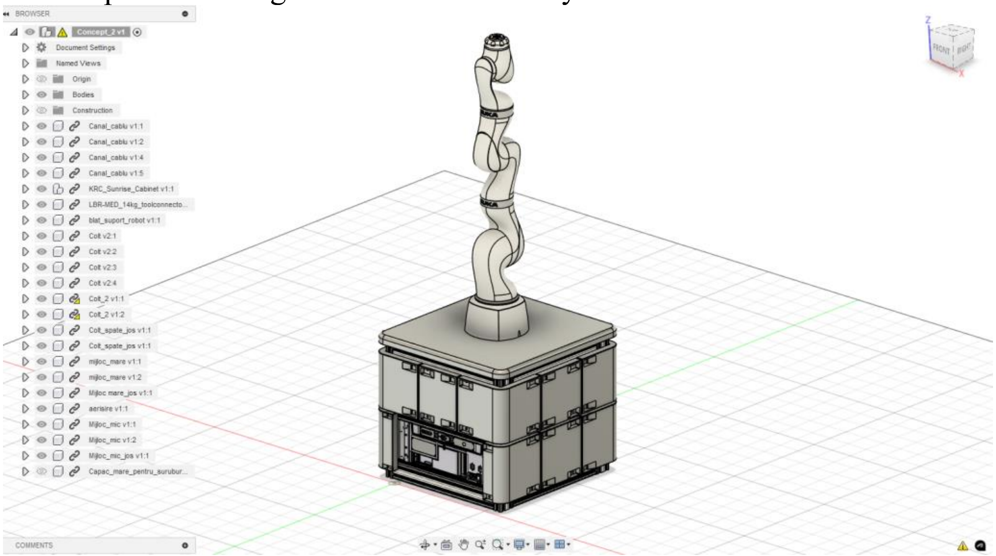

Fig. 7. CAD concept of medical support intended for the integration of the KUKA LBR MED robot

Also, personal contributions included participation in the organization and validation of the experimental setup, aiming at the compatibility between the mechanical, robotic and software components.

A future development direction consists in the design of modular medical support intended for the complete integration of the robotic system in a real clinical environment. The platform aims at the integration of the medical robot, the controller and the electronic components.

7. Conclusions

The paper highlighted the potential of using robotic systems in the field of dental implantology, by developing and integrating a platform capable of combining medical imaging, data processing and robotic control into a unitary system. The experimental results obtained demonstrated the possibility of achieving precise and repeatable positioning, confirming the advantages of using medical robotics compared to conventional methods. The activities carried out included CAD design stages, hardware-software integration and experimental validation, contributing to the development of an experimental platform with potential for extension to real clinical applications.

8. Bibliography

[1]. LBR Med medical robot: Sensitive, precise, safe | KUKA Global
[2]. KUKA KUKA Sunrise.FRI 2.4
[3]. Dobrescu, T., Ivan, M., (2022), Basics of industrial robot kinematics.
[4]. Dental Center Targoviste – Dental Center
[5]. NAVIDENT 3.0 | Dynamic Dental Navigation Surgery

Integrating Parametric Design into Personalized Prosthetics: Analysis of Dimensional Errors and Structural Performance

GOLOGAN Ioana-Elisa and Asst. Prof. Ph.D. Eng. **ISTRIȚEANU Simona-Elena (Scientific Coordinator)**

Faculty of Industrial Engineering and Robotics, Specialization: Mechanical Engineering, Academic Year: II – Master's Program in Modeling and Simulation of Mobile Mechanical Structures, e-mail: ioana_elisa.gologan@stud.aero.upb.ro

ABSTRACT: This paper presents an integrated digital workflow for the development of lower-limb orthoses, utilizing 3D scanning and parametric design. The primary objective is a comparative evaluation of the dimensional accuracy of two additive manufacturing technologies relative to the digital model optimized within the Grasshopper environment. The methodology involved data acquisition via an Einstar scanner, followed by the generation of a parametric structure tailored to the scanned anatomy. The results of the metrological analysis are interpreted through statistical indicators and box plot diagrams generated using Python code, which highlight the variations in geometric fidelity and the influence of printing parameters on structural performance. The study demonstrates the potential of algorithmic design in reducing fitment errors and maximizing user autonomy to provide a high level of comfort.

KEYWORDS: parametric design, 3D printing, dimensional error analysis

1. Introduction

The development of rigid ankle-foot orthoses (AFO) is essential in the context of the high incidence of musculoskeletal injuries, with ankle sprains affecting up to 7 out of 1,000 people annually [1]. The rigid orthosis is critical for protecting ligaments, preventing pathological movements, and facilitating tissue healing.

Currently, the customization of orthoses faces barriers related to high costs and long production times, which is why digital methods have been implemented [2]. The integration of additive manufacturing and computational design offers an efficient solution, allowing for the reduction of the device's weight and the implementation of complex geometries, such as ventilation structures optimized in Grasshopper, which are impossible to achieve through conventional methods.

The motivation of this study lies in the technical validation of the entire digital workflow: from the acquisition of anatomical data with the Einstar scanner to the generation of the parametric geometry. The central element of the research is the comparative accuracy analysis between two 3D printing platforms, using a performance chart generated via Python. By interpreting dimensional errors using Box Plot diagrams, the study quantifies deviations from the reference digital model. This rigorous approach aims to identify the optimal solution that balances low costs with the geometric precision necessary to ensure the user's comfort and autonomy throughout the recovery period.

2. 3D Data Acquisition

The development process of the personalized foot orthosis begins with the digitization of the lower limb's geometry which is a critical stage because any error introduced at this point will propagate throughout the parametric design and directly influence the results of the final precision analysis.

To acquire the point cloud, an Einstar scanner was used. This scanner utilizes structured light technology and is capable of capturing complex geometries and fine textures, featuring a resolution of up to 0.1 mm and a scanning speed of up to 14 fps. The choice of this equipment was dictated by its ability to capture high-resolution details and its scanning speed, which are essential factors in reducing errors caused by involuntary movements of the subject.

The process was carried out according to the following technical steps:

1. **Positioning**: The lower limb was maintained in a neutral position (Figure 1) to ensure the correct geometry of the talocrural joint.

Fig. 6. Scanning in the plantar position

2. **Data Acquisition:** The scanning was performed at an optimal operating distance, ensuring complete coverage of the areas of interest (malleoli, Achilles tendon, and plantar arch). As shown in Figure 2, the EXStar Shining 3D software displays the foot in a point cloud format along with the scanned artifacts around it.

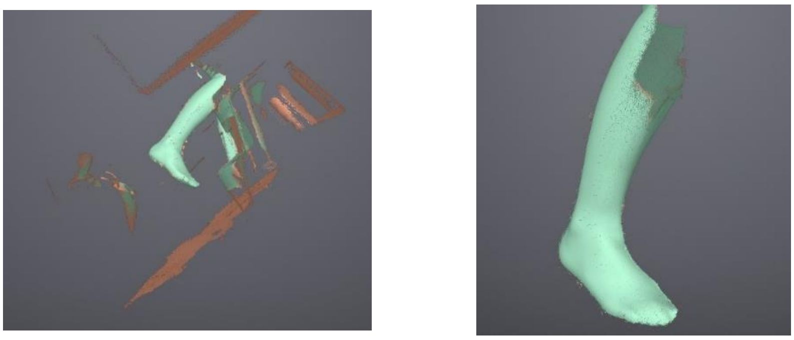

Fig. 7. Point cloud a) with artifacts b) post-processing

3. **Preliminary** Processing: The resulting point cloud was filtered to remove background noise (artifacts), as seen in Figure 3 a), and converted into a polygon mesh in Fig. 3b), in STL format, optimized for the Rhino/Grasshopper environment.

The importance of a rigorous acquisition lies in establishing a "Ground Truth" reference. The precision performance chart generated at the end of the paper compares the physically printed orthoses not only with the parametric model but indirectly with the scanned anatomy.

Thus, a high-fidelity data acquisition allows for:

- **Exact Quantification of Deviations:** Without a precise scan, it would be impossible to determine whether a dimensional error stems from the printing process or a misinterpretation of the anatomical geometry.
- **Validation of the Python Algorithm:** The dataset obtained through the Einstar scan provides the XYZ coordinate baseline against which the analysis script will calculate Euclidean distances and generate the Box Plot diagrams.

Fig. 8. Meshing process a) post-processing point cloud b) foot mesh

In this way, medical reverse engineering enables the transformation of anatomical data obtained via 3D scanning into digital models suitable for designing and manufacturing customized devices, such as prosthetics, orthoses, or implants [2].

3. Parametric Design in Grasshopper

The design phase represents the core of the process of transforming raw scan data into a functional and customized structure for the foot orthosis.

In this study, using the Grasshopper visual programming environment within the Rhino 3D platform enabled the transition from conventional digital modeling to an algorithmic design system. This approach offers the major advantage of a workflow where the orthosis geometry remains dependent on the subject's anatomical parameters, allowing it to automatically adapt to any morphological variation without requiring manual remodeling of the components, thereby ensuring patient comfort [3]. The architecture of the developed algorithm is based on processing the STL mesh model generated by the Einstar scanner.

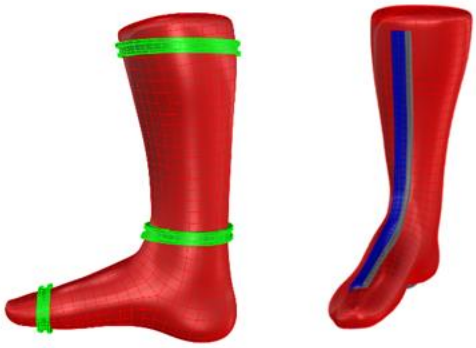

Fig. 9. Generation of the orthosis stability structure through a) rings and b) rails

In the first phase of the workflow, anatomical regions that are unnecessary for generating orthosis, such as the toes and the knee area, are removed, and an offset surface is defined. This offset is essential for establishing a tolerance distance between the skin and the device. This clearance parameter is fundamental not only for ensuring physiological comfort but also for minimizing fitment errors that will later be quantified in the statistical precision analysis.

For the stability structure of the orthosis, a rail consisting of fixing holes and 3 ring areas was generated, which are necessary for the subsequent addition of zip ties, as can be observed in Fig. 4.

Recent studies on additively manufactured custom orthoses highlight the role of ventilated models and lightweight structures in increasing user comfort—aspects that are also important in the design of lower-limb orthoses [4]. Therefore, the generation of the Voronoi-type structure (Figure 5) ensures an ideal ratio between the rigidity required for immobilization and the optimal ventilation of the lower limb. By using mathematical spatial distribution functions, a controlled variation of the wall thickness was achieved, reinforcing areas subjected to high mechanical stress and reducing material density in guiding regions. This topological optimization directly contributes to increasing user autonomy by reducing the total mass of medical devices.

Fig. 5. Longitudinally sectioned Voronoi structure

The integration of parametric design with final data analysis is achieved by inserting digital sampling points inside the algorithm, which serve as mathematical references for metrological validation. This system allows the Python script to compare the theoretical ideal coordinates with those obtained by measuring the physical models from the two FDM printers. Thus, the computational model (Fig. 6) does not merely constitute a finished object, but a precise reference frame for evaluating manufacturing performance, providing the database required to interpret dimensional errors.

Fig. 6. Final model of the foot orthosis prepared for additive manufacturing

4. The Manufacturing Process

One of the critical focal points of the personalized orthosis depends heavily on the interface between the device and the patient, as the skin represents the primary barrier through which mechanical forces are transmitted. From a biomedical perspective, prolonged contact with inappropriate materials can generate secondary skin pathologies, such as irritation, allergic reactions, or edema. Given that the FDA (Food and Drug Administration) classifies certain synthetic polymers as low-risk biocompatible materials due to their history of safe use [5]. BASF Ultrafuse PLA Tough filament was selected for the creation of the orthosis structure. This material, derived from renewable resources such as corn, preserves the biocompatibility benefits of polylactic acid (PLA) while offering superior flexibility and impact resistance, which are essential for the mechanical demands placed on an AFO (Ankle-Foot Orthosis) device.

According to the study conducted by McCrickard and Boyd, the relevance of additive manufacturing in medical applications, as well as the use of FFF/FDM printers within this process, can be determined [6]. Therefore, based on these data, we opted to use a biocompatible material applied to two FDM-type printers (Sovol SV08 and Bambu Lab X1 Carbon).

The production stage involved using two distinct 3D printing technologies to evaluate the variability of dimensional accuracy depending on the equipment. Preparing the digital models required processing them through slicer software applications optimized for each specific hardware architecture, using OrcaSlicer for the Sovol SV08 platform and Bambu Studio for the Bambu Lab X1 Carbon system. This preparation stage is a determining factor for the final geometric fidelity, as the material deposition path generation algorithms directly influence how the complex parametric structure is translated into a physical object.

Fig. 7. 3D printed foot orthosis using the Sovol SV08 printer

A significant variable within the experiment was represented by the volumetric constraints of the equipment, which dictated different spatial orientation strategies. In the case of the Sovol SV08 printer, the generous build volume allowed for positioning the orthosis in an optimal, natural orientation (Figure 7) for the structural integrity of the layers.

In contrast, the smaller print volume of the Bambu Lab X1 Carbon equipment required a strict vertical positioning (Fig. 8) of the orthosis to fit within the limits of the motion axes. This difference in orientation constitutes a major factor in the analysis of precision errors, as the deposition angle of the layers relative to the parametric geometry can generate variations in the distribution of dimensional deviations, aspects that will be detailed and visualized through Python statistical analysis.

5. Comparative Study

Validating the digital workflow required a rigorous metrological evaluation aimed at determining the fidelity of the two additive manufacturing processes relative to the nominal model generated parametrically.

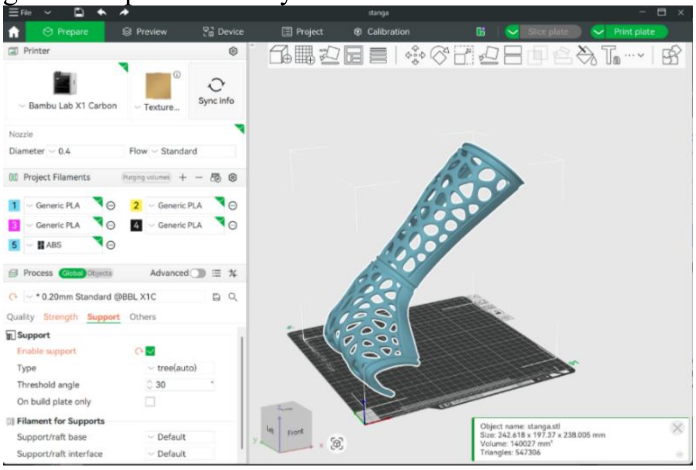

Fig. 8. Bambu Studio Interface

To collect experimental data, a high-precision digital caliper, the Microtech IP67, was used. The physical measurement process targeted the critical dimensions of the orthosis, specifically its total length and height, as well as the internal diameter at three distinct control points corresponding to the fixing rings of the parametric structure. Table 1 displays the measured values of the orthosis printed using the Sovol SV08 printer, the one printed with the Bambu Lab X1 Carbon, and the values according to the 3D model in the Grasshopper environment.

Table 1 Metrological evaluation table

Orthosis Dimension	Sovol SV08	Bambu Lab X1 Carbon	Grasshopper
Length [mm]	291.51	292.42	293.56
Width [mm]	190.23	191.64	192.20
Ring 1[mm]	73.10	76.01	72.30
Ring 2[mm]	63.37	64.33	62.97
Ring 3 [mm]	102.76	105.37	104.48

The raw data obtained through manual measurements were centralized and processed using a statistical analysis algorithm developed in the Python programming language. The use of specialized data analysis libraries allowed for the calculation of absolute errors by comparing each physical measurement with the theoretical value extracted directly from the Grasshopper design environment. This methodology eliminates the subjectivity of visual interpretation, offering a quantitative perspective on the performance of each printing equipment (Sovol SV08 and Bambu Lab X1 Carbon).

The culmination of the statistical analysis is represented by the generation of Box Plot diagrams (Figure 9), which provide a synthetic visualization of the dimensional error distribution. This graphical method was chosen for its ability to simultaneously highlight the central tendency (median), the degree of error dispersion (interquartile range), and the presence of any outliers resulting from the manufacturing process.

The interpretation of these graphs allows for the identification of the correlation between the positioning strategy of the orthosis within the print volume and the resulting dimensional accuracy, providing essential data for optimizing future prosthetic devices in terms of structural performance and anatomical fit.

Evaluating the performance of the two additive manufacturing systems, as visualized by the

Box Plot diagram, highlights distinct kinematic and thermal behaviors relative to the ideal geometry generated in Grasshopper. In the case of the Sovol SV08 equipment, the error distribution is predominantly located in the negative range, with a median deviation of approximately -1.7 mm. This trend indicates a predictable thermal contraction (shrinkage) phenomenon correlated with the global dimensions of the part, where the length of 291.51 mm compared to the reference of 293.56 mm confirms a dimensional reduction along the main axis. Although the values are undersized, the tight dispersion of the data (narrow interquartile range) suggests extrusion process stability, which allows for the correction of these errors in subsequent stages by applying compensatory scaling factors.

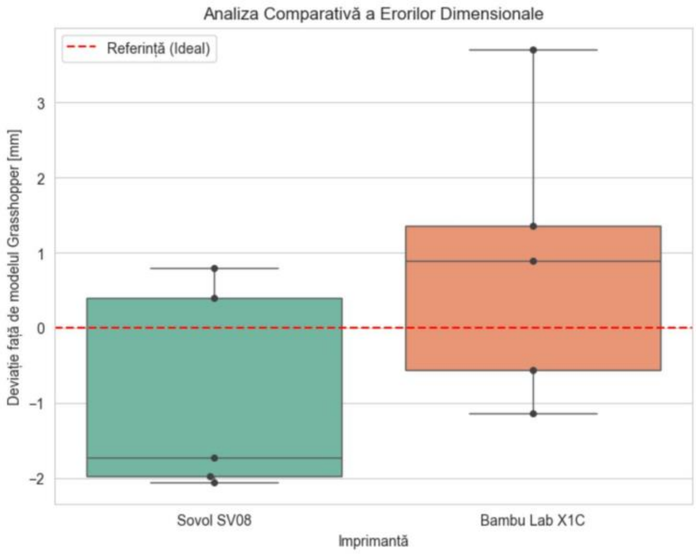

Fig. 9. Comparative analysis of 3D printing dimensional errors

In contrast, the Bambu Lab X1 Carbon system presents an error distribution characterized by an oversizing trend, with the median positioned in the positive zone of the graph at approximately +0.9 mm. A detailed analysis of the sampling points indicates significant variability, particularly in the case of the fixing ring diameters. For example, while Ring 1 shows a major positive error (76.01 mm compared to the theoretical 72.30 mm), the rest of the measurements reflect greater geometric instability compared to the Sovol model. This pronounced dispersion, visible through the extended "whiskers" of the Box Plot diagram, can be attributed to the printer's volume constraints, which forced a strict vertical orientation of the orthosis. This positioning promotes error accumulation along the Z-axis and amplifies vibrations during the deposition of the upper layers, affecting the fidelity of complex circular shapes.

Correlating these data with structural performance and patient comfort indicates that, although both printers produce functional parts, the Sovol SV08 offers superior error predictability. From a clinical perspective, the dimensional instability observed in the Bambu Lab X1 Carbon, despite occasionally being closer to the reference line, introduces risks of non-uniform anatomical mismatch (fitment errors).

The results obtained through Python statistical processing demonstrate that, for large medical devices such as foot orthoses, the print volume and the spatial orientation of the part within the workspace are determining factors that can overshadow the equipment's nominal resolution in ensuring optimal fit accuracy.

6. Conclusions

The present research confirms the viability of integrating parametric design and additive manufacturing into the production of custom orthopedic devices, offering a superior alternative compared to traditional lower-limb immobilization methods.

The use of algorithms within the Grasshopper environment facilitated the generation of an optimized geometry that addresses clinical needs by significantly reducing total weight and integrating ventilation zones. These characteristics not only improve patient comfort but also directly contribute to increasing patient compliance and autonomy during the recovery period.

The comparative analysis demonstrated that the dimensional accuracy of the final product is critically influenced by the technical limitations of the production equipment and spatial orientation strategies.

The data extracted via the Python script and visualized in the Box Plot diagram reveal that the reduced print volume of the Bambu Lab X1 Carbon system, which necessitated vertical positioning of the orthosis, generated greater geometric instability and pronounced positive deviations. In contrast, the Sovol SV08 platform provided a more predictable error and a tighter data distribution, demonstrating that a generous build volume allows for an optimal orientation that minimizes deformations caused by vibrations or gravitational forces during layer deposition.

In conclusion, the success of the proposed digital workflow depends on a rigorous correlation between the accuracy of data acquisition via the Einstar scan and the calibration of printing parameters. The study underscores the necessity of applying compensation factors in the design phase to counteract the contraction of the BASF Ultrafuse PLA Tough material, thereby ensuring maximum anatomical fidelity. The results obtained substantiate the use of computational design as an essential tool for standardizing foot orthoses adapted to the biomechanical requirements of each individual patient.

Future research will focus on structural validation through FEM analysis and mechanical testing, as well as the clinical evaluation of the interaction between parametric geometry and the user through compliance studies.

7. Bibliography

[1]. Martin, R.L., (2021), “Ankle Stability and Movement Coordination Impairments: Lateral Ankle Ligament Sprains Revision”, Journal of Orthopaedic & Sports Physical Therapy.

[2]. Wakjira, Y.K.N. & L.H., (2024), “Reverse engineering in medical application: literature review, proof of concept and future perspectives”, vol. 14, no. 23621, p. Sci. Rep.

[3]. Atallah, H.Q.T.B.H. et al. (2025), “The current state of 3D-printed orthoses clinical outcomes: a systematic review”, BMC Musculoskelet Disord.

[4]. Ambu, R.O.S. & C.M., (2024), “Neck orthosis design for 3D printing with user enhanced comfort features, Int. J. Interact Des Manuf, vol. 18, no. 6055-6068.

[5]. U.F.a.D Administration, “Biological Evaluation of Medical Devices – Part 1: Evaluation and Testing within a Risk Management Process”, FDA Guidance Document. 2023.

[6]. McCrickard, C.B.A.A.E. et al., (2025), “Polyether ether ketone (PEEK) and polyetherimide (PEI) for fused filament fabrication (FFF) in medical applications,” Int. J. Adv. Manuf. Technol., vol. 140, no. 5737-5754.

Thermoplastic Materials in the Era of Additive Manufacturing: Trends and Challenges in FFF/FDM Technology

BARBU Costin-Ciprian and Asst. Prof. Ph.D. Eng. **ISTRIȚEANU Simona-Elena (Scientific Coordinator)**

The Faculty of Industrial Engineering and Robotics, Specialty: Modeling and Simulation of Mobile Mechanic Systems, year: II, e-mail: ciprian.barbu@gmailcom

ABSTRACT: Additive Manufacturing, and especially FDM (Fused Deposition Modeling), popularly known as 3D printing, represents one of the most disruptive technologies of the 21st century, redefining the way products are designed, manufactured, and distributed. Although FDM was initially limited to the creation of visual models and conceptual prototypes, today the technology is capable of producing functional parts for critical sectors such as medicine, aerospace, and the automotive industry. This evolution has been driven by improvements in mechanical components, but above all by advances in materials science. The emergence of the "High-Speed FDM" era has imposed new requirements on thermoplastic raw materials, requiring optimized rheology to ensure rapid melting and controlled crystallization.

KEYWORDS: FDM, FFF, thermoplastic, polymers, high-speed printing

1. Introduction

Additive manufacturing (AM), commonly known as 3D printing, has evolved over the past decade from a tool used exclusively for conceptual prototyping to an industrial production technology capable of producing functional components with complex geometries. Among the various AM processes, Fused Filament Fabrication (FFF/FDM) has established itself as the most versatile and widespread, thanks to the optimal balance between equipment costs and the diversity of usable thermoplastic materials.

In the current context of Industry 4.0, two research directions define the future of FDM technology: material optimization for enhanced structural performance and the transition to ultra-high production speeds. The study by Kundu et al. (2022) [1] provides a critical foundation for understanding how the physicochemical properties of polymers dictate the success of the extrusion process. This fundamental classification is now being challenged by the new era of additive manufacturing, defined by Kantaros et al. (2025) [2] as the "High-Speed FFF" era. While in conventional processes the print speed hovered around 50 mm/s, modern systems aim for thresholds exceeding 500 mm/s, pushing the thermodynamic limits of the raw materials.

The transition to high print speeds is not merely a software or mechanical challenge, but primarily one of materials science. As the print head moves faster, the polymer's residence time in the hot zone decreases, and the cooling dynamics of the deposited layer change radically. Thus, material selection can no longer be based solely on final mechanical strength; shear rheology, crystallization rate, and interlayer molecular diffusion capacity under accelerated thermal conditions must be taken into account.

2. Current state

Additive manufacturing, commonly known as 3D printing, is having a significant impact on the manufacturing sector and the development of Industry 4.0. This phase of the industry is characterized by a higher degree of automation, the use of emerging digital technologies, and extensive automation, building upon previous iterations of the industrial revolution. From this perspective, Industry 4.0 incorporates cutting-edge technologies such as robotics, data analysis (or big data analytics), artificial intelligence (AI), and the Internet of Things (IoT).

As described by Bănică et al. [3], within the context of Industry 4.0, embedded systems integrate hardware and software, and additive manufacturing plays a decisive role in the development of the industry, as it enables more flexible design, rapid prototyping, and the production of complex

components at a competitive price and with greater flexibility compared to traditional manufacturing methods. One of the key features of using 3D printing is the ability to produce components tailored to application needs in a timely manner and at the location where the application is deployed, thanks to the small footprint of additive manufacturing devices compared to traditional production methods, which require large floor space as well as industrial production and operating conditions. For example, a conventional injection molding facility, even for small parts, requires significant floor space, consumes a great deal of energy, and is cost-effective only when producing large volumes of parts.
There are numerous practical applications for additive manufacturing across various industrial sectors, such as the automotive, aerospace, and medical industries, as well as in construction, to name just a few of the most significant ones. Many other specific applications can be found in the production of furniture, handmade jewelry, casings for electronic devices and home appliances, and, of course, as a hobby for enthusiasts and the curious.

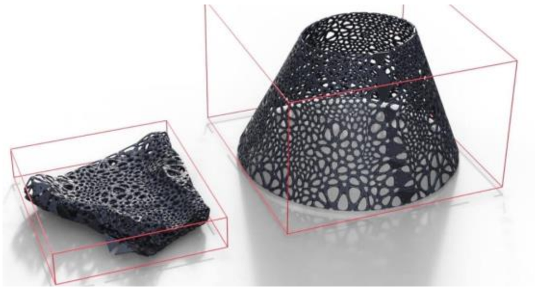

Fig.1. Object with 87% reduced volume with two folds

Another unique aspect of additive manufacturing within Industry 4.0 is that 3D printing has made 4D printing possible [4], by introducing a temporal dimension to materials—for example, by using materials that can alter their shape or properties over time. This method relies on the use of special materials (smart materials) that possess unique properties capable of being altered through physical, chemical, or even biological processes, allowing them to respond to external stimuli such as heat, contact with water, electricity, or light, causing objects to gradually change shape or alter certain properties. There are already numerous applications for 4D printing in sectors such as aerospace, regenerative and dental medicine, as well as the automotive sector, where objects with complex geometries are required or where conventional manufacturing methods do not allow for the creation of products with the necessary parameters.
In the medical field, 4D printing enables the creation of artificial organs, thereby reducing compatibility and ethical issues—a vital consideration for patients with severe conditions where organ transplantation can carry high risks due to rejection of the donated organ. Artificial organs can also be produced without using support structures, utilizing cells from the patient's own body—a more efficient method for creating artificial organs. Furthermore, 4D printing enables the production of smart implants that change shape during surgery, such as artificial valves or joints. Another example is the production of special drug capsules, which, due to their porosity, allow for the delivery of a high dose of medication, used even in the treatment of certain forms of epilepsy.
In other applications, 4D printing allows for the production of objects that would otherwise require a much larger printing space than is currently possible. By using a technique called "computational folding," objects can be designed that expand in volume at the end of the production process, as shown in the image below (Fig. 1), in which an object was reduced by up to 87% to enable printing [5].

3. Thermoplastic materials in FFF and FDM

As for the layer-by-layer FFF (Fused Filament Fabrication) printing method, there has been significant progress over the past decade, but the search for even better solutions continues. However, compared to conventional plastic-based manufacturing methods, additive manufacturing—and FFF in particular—has a more limited range of thermoplastic materials available, due to the limitations of the manufacturing process itself.

Other technologies, such as SLA (Stereolithography), SLS (Selective Laser Sintering), DLP (Digital Light Processing), LCD (Liquid Crystal Display), Powder Bed Fusion, and others offer distinct advantages depending on the application and requirements. However, FFF in particular is one of the most widely used additive manufacturing methods, primarily due to its low cost, efficiency, and versatility. The materials used in 3D printing influence both the performance characteristics of the produced objects and the efficiency, cost, and scalability parameters of the printing process.
Among the multitude of materials used in 3D printing, thermoplastics are more widely used due to their qualities, such as ease of processing, mechanical and chemical resistance, and adaptability to various printing techniques.
As is well known, a typical 3D printer uses thermoplastic material in the form of a filament spool, which is fed into a melting device while the print head moves within a Cartesian coordinate system, depositing the molten material layer by layer, with the first layer being deposited onto a print bed, with subsequent layers placed on top of the previous ones. The thermoplastic materials used in this layer-by-layer deposition process must be rigid within a normal temperature range, yet at the same time must be capable of being melted into thin layers to achieve the final shape.
Obviously, the molten plastic exhibits a certain viscosity. To better understand the challenges associated with this process, it is helpful to examine the rheological properties of the thermoplastic materials used.

3.1 Rheological Properties in the Processing of Thermoplastics

Rheology is the science that deals with the study of the flow and deformation of materials, with an emphasis on the relationships between stress, strain, temperature, and time. Another very important parameter is viscosity, which can be defined as a measure of internal resistance to shear forces within a fluid.
"Consider a pair of large parallel plates, each with area A, separated by a distance Y. One of the plates is set in motion at a velocity V. The space between them is filled with an incompressible Newtonian fluid. The flow is laminar. Under steady-state conditions, a constant force F is required to maintain the plate's motion. The viscosity μ is defined as a proportionality constant (for a given temperature, pressure, and composition) between the tangential force F divided by the area A (i.e., the applied shear stress τyx) and the velocity V divided by the distance between the plates Y, i.e., the velocity gradient $\frac{-dv_x}{dy}$, as shown in the equation below [6]:

$$\frac{F}{A} = \mu\frac{V}{Y} \tag{1}$$

Which can be re-written as follows:

$$\tau_{yx} = -\mu\frac{dV_x}{dY} \tag{2}$$

Equation (2), known as Newton's law of viscosity, states that the shear stress per unit area is proportional to the inverse of the velocity gradient. This is the potential scenario for a rotational rheometer, in which a viscous flow and a constant shear rate can be assumed in the space between the rheometer elements. For a generalized incompressible Newtonian fluid and for the extension of the principle to any arbitrary flow, equation (2) is expressed as follows:[6]

$$\tau = -\eta\dot{\gamma} \tag{3}$$

Where η can be a function of $\dot{\gamma}$, the shear rate [6].
The decrease in viscosity as the shear rate increases is referred to as "shear thinning" behavior, and the fluid is called a "shear-thinning fluid" or "pseudoplastic." When viscosity increases with shear rate, the fluid is called a "shear thickener" or "dilatant."
Water has a viscosity of 10^{-3} $Pa \cdot s$, while the viscosity of most types of polymers melting under

extrusion can vary between 10^2 și 10^5 $Pa \cdot s$. Shear rate dependence, or non-Newtonian viscosity, is an important characteristic of polymeric fluids during polymer processing: an increase in shear rate—that is, faster extrusion through a die—reduces viscosity. This phenomenon has been associated with molecular alignment and polymer chain disentanglements. [6]
Various types of polymer processing often involve different shear rate ranges. Compression molding is an example of a low-shear-rate process, whereas extrusion and injection molding are examples of high-shear-rate techniques. Determining viscosity values within predetermined shear rate ranges is crucial for the design of plastic products, to ensure a smooth process and to prevent clogging and loss of fluidity and productivity [6].
Polymeric fluids are referred to as viscoelastic fluids, exhibiting both viscous and elastic characteristics when deformed under the action of a force. The elastic property refers to a material's ability to return to its original shape after being deformed under the action of a force. The viscous property refers to the process of irreversible deformation of a material, in which the initial shape can no longer be recovered. The viscoelasticity of a material can be determined by applying a force and measuring the material's response. Under linear conditions, stress (τ(t)) and strain (γ(t)) are sinusoidal functions of time (t) according to the following expressions [6]:

$$\tau(t) = \tau_0 sin(\omega t + \delta) \quad (4)$$

$$\gamma(t) = \gamma_0 sin(\omega t) \quad (5)$$

where τ0 and γ0 represent the amplitude of the stress and of the strain respectively; ω is the frequency, and δ is the phase angle. δ = 0° corresponds to a perfect elastic material („Hookeian"); δ = 90 corresponds to a perfect viscous material („Newtonian") [6].

Defining the complex modulus (G*) (equation (6)), it can be divided into two components, the storage modulus – G′ (equation (7)) and loss module – G″ (equation (8)):

$$G \quad = \frac{\tau(t)}{\gamma(t)} \quad (6)$$

$$G' = \frac{\tau_0}{\gamma_0} cos\delta \quad (7)$$

$$G'' = \frac{\tau_0}{\gamma_0} sin\delta \quad (8)$$

G' represents the elastic response of the material and is related to the energy stored and recovered per cycle; G'' represents the viscous response of the material and refers to the loss, or dissipated, energy per cycle. [6].

3.2 The Evolution of 3D Printing Materials: From Prototyping to Industrial Production

The direction of 3D printing—or additive manufacturing—has been shaped less by the mechanical movements of the printers themselves and more by the rapid advancement of the materials they extrude. In its early stages, the industry was limited to a narrow range of basic thermoplastics. Today, however, materials science has expanded that range into a complex array of high-performance polymers and composites, enabling the transition from amateur prototyping to large-scale industrial production.

3.2.1 The founding trio: PLA, ABS and PETG

The early days of 3D printing were dominated by three core materials, each serving a specific niche. Polylactic acid (PLA) was the entry-level material; derived from renewable resources such as cornstarch, it became ubiquitous due to its low printing temperature and minimal warping. Although ideal for education and aesthetic models, its low heat resistance has limited its use in functional environments.[2]

To meet the need for sustainability, acrylonitrile butadiene styrene (ABS) has become an essential material for engineers. As a petroleum-based polymer, ABS offers superior impact resistance and toughness, making it essential for automotive and mechanical components. However, its tendency to warp and emit unpleasant fumes has required specialized equipment, such as heated beds and ventilated enclosures.

Polyethylene Terephthalate Glycol (PETG) subsequently emerged as a well-balanced alternative. It combined the ease of use of PLA with the functional strength of ABS, offering enhanced chemical resistance and superior interlayer adhesion, without the severe warping issues associated with ABS.

3.2.2 High-performance and and industrial applications polymers

As 3D printing hardware has matured, the industry has turned to specialty thermoplastics designed for extreme environments. High-performance polymers, such as polycarbonate (PC), nylon (PA), and PEEK (polyether ether ketone), have expanded the technology's reach into sectors such as aerospace, defense, and medicine. Polycarbonate is valued for its optical clarity and high impact resistance, while nylon's tensile strength and wear resistance make it ideal for functional end-use parts. PEEK represents the pinnacle of this evolution, offering extraordinary thermal stability and chemical inertness, which allows it to be used in medical implants and high-tech aerospace manufacturing.

3.2.3 The Rise of Composite Materials and Functional Additives

A revolutionary leap forward occurred with the introduction of composite materials. By infusing standard thermoplastics with fibers such as carbon or glass, manufacturers have created parts with exceptional rigidity and an optimal strength-to-weight ratio. Metal-reinforced filaments pushed the boundaries even further, offering parts with electrical conductivity and thermal resistance. In addition, the development of flexible materials, such as Thermoplastic Polyurethane (TPU), enabled the production of elastomeric parts, opening doors in the footwear and healthcare sectors.

3.3 A Comparison of Thermoplastic Materials Used in 3D Printing

Table 1 highlights the main characteristics of each type of thermoplastic commonly used in 3D printing processes, in order to highlight the advantages and disadvantages of each based on various parameters.

Table 1. Thermoplastic materials comparison

Material	Properties and advantages	Challenges and limitations	Impact of High-Speed 3D Printing to the material	Applications
PLA (Polylactic Acid)	Biodegradable, derived from renewable resources, easy to print, minimal	Low heat resistance, brittle, slow crystallization rate.	Optimizing rheology and nucleating agents enables high flow rates and	Rapid prototyping, architectural models, consumer

	shrinkage, high rigidity.		rapid crystallization at high speeds.	goods, educational use.
ABS (Acrylonitrile Butadiene Styrene)	High impact resistance, good heat resistance, durable.	Prone to warping and delamination, requires a heated bed and an enclosed space, and emits styrene fumes.	It requires precise temperature control and optimized cooling management to maintain layer adhesion at high speeds.	Automotive components, electronic enclosures, functional prototypes, end-use parts.
PETG (Polyethylene Terephthalate Glycol)	Excellent chemical resistance, durability, easy to print on, and a good balance between strength and flexibility.	Prone to stringing (residual fibers), excessive adhesion to the platform may absorb moisture.	It requires optimized retraction settings and precise nozzle temperature control to minimize defects at high speeds.	Food and beverage containers, mechanical parts, protective housings, medical devices.
PA (Polyamide/Nylon)	Exceptional strength and durability, excellent resistance to wear and chemicals.	Highly hygroscopic, require pre-drying, poor adhesion to the substrate, high shrinkage.	A high material flow rate requires uniform melting; hygroscopic properties can affect print quality at high speeds.	Gears, bearings, functional hinges, heavy-duty industrial components.
(PC) Polycarbonate	Extreme impact resistance, optical clarity, high heat resistance.	Requires very high printing temperatures, prone to significant warping, requires a heated enclosure.	High speeds can cause internal stress; they require strict temperature control to ensure the quality of the part.	Aerospace components, protective visors, automotive parts, lenses, and screens.
TPU (Thermoplastic Polyurethane)	Excellent elasticity and flexibility, high resistance to abrasion and oils.	Difficult to print with Bowden systems; slow print speed due to the filament's flexibility.	Very difficult to adapt to high speeds without high-performance direct extrusion systems (risk of jamming or uneven extrusion).	Footwear, gaskets, flexible hoses, device guards, anti-vibration parts.
PEEK / PEI (High performance polymers)	Extreme mechanical, thermal, and chemical resistance; high	Very high cost; requires specialized industrial equipment (very	High Speed FFF reduces production time for critical parts but requires	Medical implants, aerospace and defense components,

	strength-to-weight ratio.	high temperatures for the nozzle and chamber).	highly advanced thermal management.	and applications in the oil and gas industry.

4. Adapting to the Age of High Speed

The most recent development involves the synergy between hardware and chemistry in the form of high-speed 3D printing. Modern printers operate at significantly higher extrusion rates, requiring materials that flow smoothly and solidify quickly without losing their structural integrity. This has led to the emergence of "high-speed" variants of PLA, ABS, and PETG. These materials are molecularly engineered to handle rapid cooling and maintain a strong bond between layers even at accelerated speeds, ensuring that increased production volume does not come at the expense of part quality or dimensional accuracy.

Ultimately, these advances in materials science have transformed 3D printing from a tool for visual prototyping into a sophisticated manufacturing method capable of producing functional components for the world's most demanding industries.

5. Conclusions: Challenges and Opportunities

The adoption of AM is hindered, first and foremost, by technical and design limitations. The lack of standardization in materials and design procedures leads to inconsistencies in surface quality and part stability. Furthermore, engineers tend to apply traditional design constraints, ignoring the creative freedom offered by AM. From an IT and logistics perspective, processes are still manual, complicating the integration of design software with production software.

Despite the challenges, AM offers unmatched benefits through mass customization. Eliminating the need for tools and molds reduces manufacturing steps, lowers assembly costs, and enables inventory digitization. Another major opportunity is lightweighting; through topological optimization and lattice structures, complex and lightweight components can be created for the aerospace, automotive, and medical industries.

Integration with IoT (Internet of Things) and 5G technologies enables real-time monitoring and the adjustment of production based on user feedback, thereby optimizing the supply chain. Finally, bionic and generative design, supported by machine learning algorithms, allows for the rapid generation of structurally optimized configurations that would be impossible to achieve using traditional methods [3].

However, fully realizing the potential of high-speed printing materials requires a careful analysis of the balance between speed, cost, and performance. Although these materials offer significant advantages, higher production costs and reliance on specialized equipment can pose barriers to their adoption by certain users. Ensuring accessibility will require innovations in both material composition and printer technology to reduce costs while maintaining or improving performance. Furthermore, understanding the trade-offs involved in material selection—such as balancing mechanical strength with printability or optimizing thermal properties for specific applications—will be essential for effectively leveraging the benefits of high-speed materials. Ultimately, high-speed 3D printing materials represent a vital advancement in additive manufacturing, providing a powerful tool for meeting the complex demands of modern industrial and commercial applications.

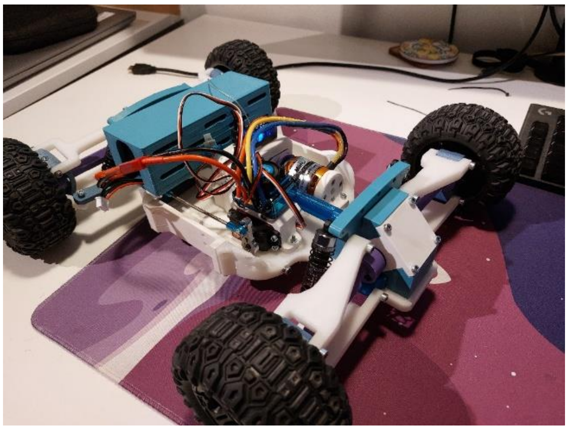

Fig. 2. Details of 3D printed hobby RC buggy

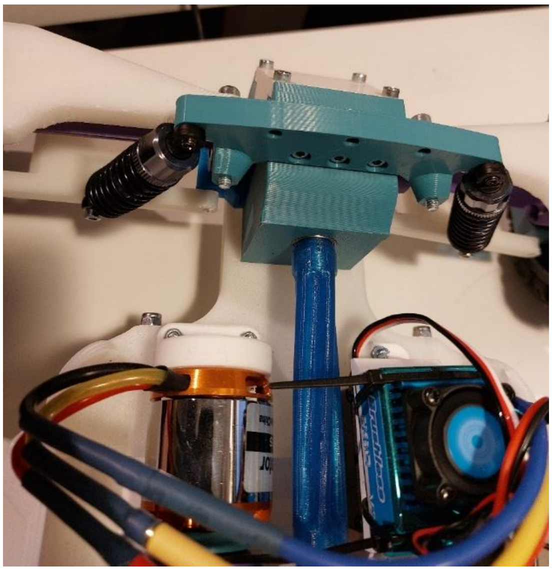

Fig. 3 – TPU flexible driveshaft, twisted under load

As an ending note, here are some pictures showcasing high-speed polymers in action, in a hobby RC buggy which relies heavily on 3D printed parts. The main chase, gears, transmission parts, suspension arms and steering system is made entirely of 3D printed parts. I have combined the use of ABS (white parts), ASA (purple and ash blue parts), PLA (turquoise parts) and even TPU (transparent blue parts) in an effort to optimize the strength and speed of production of critical parts, while keeping non-essential parts on classic PLA. This helped me to get a better practical understanding of the different types of thermoplastics, which include their strengths and challenges, as discussed throughout this article.

8. Bibliography

[1]. R. Ranjan, D. Kumar, M. Kundu et al., A critical review on Classification of materials used in 3D printing process, Materials Today: Proceedings. Elsevier.

[2]. Kantaros, A.; Katsantoni, M.; Ganetsos, T.; Petrescu, N. (2025), The Evolution of Thermoplastic Raw Materials in High-Speed FFF/FDM 3D Printing Era: Challenges and Opportunities. Materials, 18, 1220

[3]. Bănică, C.-F.; Sover, A.; Anghel, D.-C. Printing the Future Layer by Layer: A Comprehensive Exploration of Additive Manufacturing in the Era of Industry 4.0

[4]. Kantaros, A.; Ganetsos, T.; Piromalis, D., (2023) 3D and 4D Printing as Integrated Manufacturing Methods of Industry 4.0. Am. J. Eng. Appl. Sci., 16, 12–22.

[5]. 4D Printing: All you need to know in 2026,

https://www.sculpteo.com/en/3d-learning-hub/best-articles-about-3d-printing/4d-printing-technology

[6]. Acierno, D.; Patti, A., (2023) Fused Deposition Modelling (FDM) of Thermoplastic-Based Filaments: Process and Rheological Properties—An Overview. Materials, 16, 7664.

DEVELOPMENT OF An industrial ROBOT ARM SIMULATOR FOR THE PARAMETRIZATION OF THE ARTIFICIAL POTENTIAL FIELD

TURTUREA Petre-Gabriel and Assoc. Prof. Ph.D. Eng. **UNGUREANU Liviu-Marian (Scientific Coordinator)**

Faculty: Industrial Engineering and Robotics, Specialization: Modeling and Simulation of Mobile Mechanical Structures, Academic Year: I, e-mail: petre.turturea@stud.fiir.upb.ro

ABSTRACT: This paper had as objective the development of a dedicated simulator for a miniature industrial robot arm that allows testing specific automation and modernization options for real-time solutions, mainly live workspace generation and analysis, reach analysis, joint singularity analysis and live obstacle avoidance. The final goal of the solution is maximal automation and reduction of human involvement for a given toolpath.

KEYWORDS: robotics, simulation, automation, potential field.

1. Introduction

In robotics, the avoidance of collisions, singularities, and workspace limits is an intensive process, customized for each robotic cell and very often driven by human experience to find solutions to these constraints. For autonomous resolution, the use of an artificial potential field has been introduced, a mathematical construct that generates a three-dimensional map for the manipulator and represents the effort gradient associated with achieving a particular position and/or orientation by the manipulator. In this context, optimal positioning within this space results in a manufacturing process free from the limitations mentioned above.

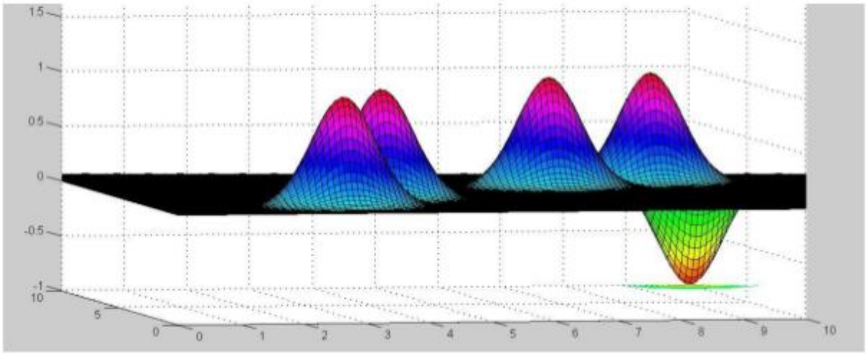

Fig. 4. artificial potential field example [1]

The objective of this work was the design of a dedicated simulator for a robotic arm manipulator and the parameterization of its associated potential field, with the purpose of testing and developing an autonomous system for optimizing the manipulator's operating parameters and the robotic cell.
The serial robotic arm manipulator is a separate design with the intention of being integrated into the simulator and demonstrating the system's real-world behavior. For the purposes of this work, only its 3D STEP model was used.

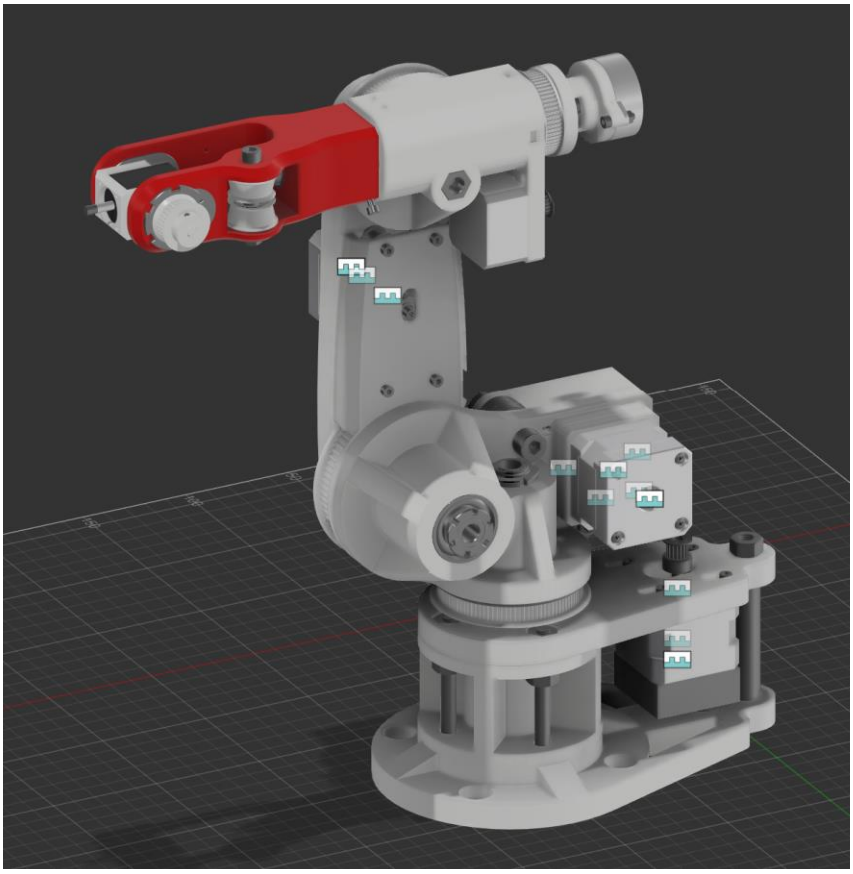

Fig. 5. CAD model of the miniature

2. Current status

The current state of the work is a functional prototype featuring an interactive visual interface developed in the Python programming language using the ImGui [2] and ImGuizmo [3] The interface is continuously updated through an immediate-mode GUI approach *[2]* and includes inverse kinematics solving capabilities for the CAD model, as well as the possibility of future integration with the physical model.

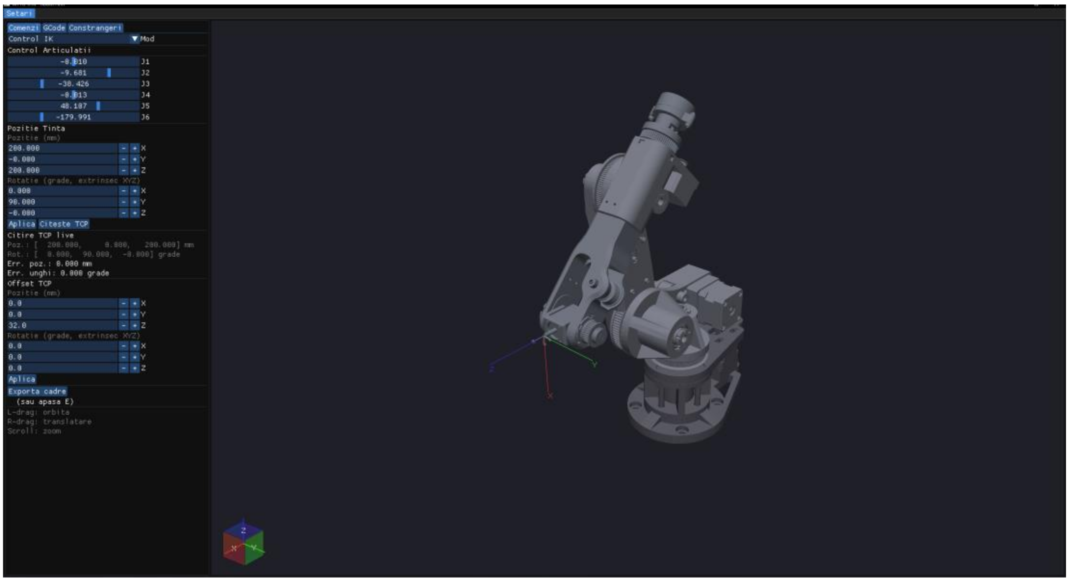

Fig. 6. Main window of the simulator

The inverse kinematics computation is implemented in the C++ programming language using the Eigen library [4], employing a composite iterative calculation method based on the manipulator's Denavit–Hartenberg (DH) parameters, previously computed, exposing three specific types of iterative computation: using the direct inverse of the Jacobian,

$$J^{-1} = inv(J) \quad (1)$$

using the pseudo-inverse (Moore-Penrose) [4, 5]

$$J^{+=V\Sigma^{+U^T}} \quad (2)$$

where Σ^+ is the pseudo-inverse of the diagonal matrix of singular values [4], with:

$$\sigma_i^{+=\begin{cases} \frac{1}{\sigma} if \sigma > \tau \\ 0 otherwise \end{cases} where \tau = rcond \times \sigma_1} \quad (3)$$

and using the damped least squares method (**D**amped-**L**east **S**quares).

$$J^{DLS} = J^T(JJ^T + \lambda^2 I)^{-1} \quad (4)$$

The iterative method for inverse kinematics involves using the Jacobian matrix to create a representation of the relationship between the motion of all the manipulator's joints and the resulting motion at the tool level (end-effector) (forward kinematics computed using Denavit-Hartenberg parameters specific to the manipulator's construction) and inverting it to obtain the inverse relationship, namely the motion required at the joints to achieve a given direction of motion of the tool.

A discrete control step updates the joint configuration **q** using the scaled position error and the chosen method for inverting the Jacobian matrix.

$$q_{k+1} = q_k + J^{-1} * (\alpha e) * \Delta t \quad (5)$$

Due to matrix computation, the most naive method, which uses the direct matrix inverse, presents a problem in robot configurations where the Jacobian is close to rank 1 (the determinant of the matrix being close to 0), which causes the matrix inverse to become invalid and, consequently, the rest of the computation to also become invalid.

The implementation of the computation method is later used in the Python graphical interface through the pybind11 [6] mechanism, which makes it possible to use high-speed C++ code within Python, where flexibility is higher.

The files required for compiling the C++ code and generating the intermediate Python code are handled by the CMake [7] mechanism, an advanced and widely used system for this purpose.

The capabilities of the simulator interface are: real-time control and command in both inverse kinematics and forward kinematics modes, setting a specific tool transformation (**T**ool **C**ontact **P**oint), real-time visualization of positions and joints, exporting coordinate systems associated with all joints, configuring tool constraints, configuring inverse kinematics model parameters, configuring graphical interface parameters, saving configurations, real-time motion analysis of the manipulator, running rudimentary machine code, and configuring the input values of the potential field calculator.

The main control panel where inverse kinematics control and forward kinematics control can be activated, the values of the tool coordinate system (TCP) can be set, angular or positional error values can be visualized in real time, and the values of the tool coordinate system can be configured, which is relative to the coordinate system associated with joint 6.

In addition to these options, there is also the capability to run rudimentary G-code (**GC**ode) specific to machine tools, as well as basic options for constraints (degrees of constraint) applied to the inverse kinematics solution. The mechanisms for avoiding joint limits and real-time collision avoidance are not functional in the current state.

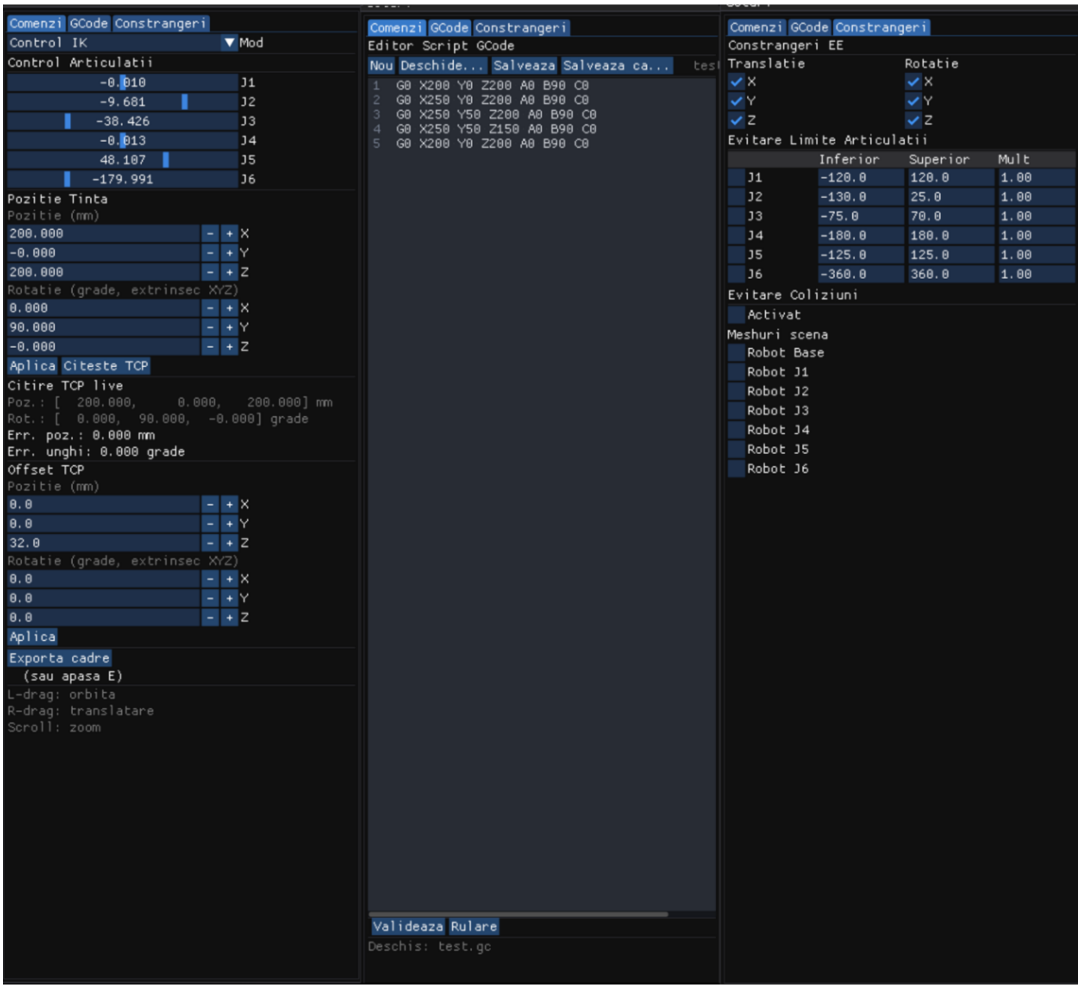

Fig. 7. Collage of the main controls panel and related command tabs

The configuration of the inverse kinematics solving system has the ability to set all relevant system values, namely: the time step (dt), the gain, the Jacobian matrix inversion method, and optionally the lambda parameter for the DLS method.

Fig. 8. Configuration window for the IK (**I**nverse **K**inematics)

The configuration window for the user interface allows setting the overall interface scale, increasing the width of the main control panel, as well as configuring the mouse control mechanism for the tool's end-effector ("gizmo").

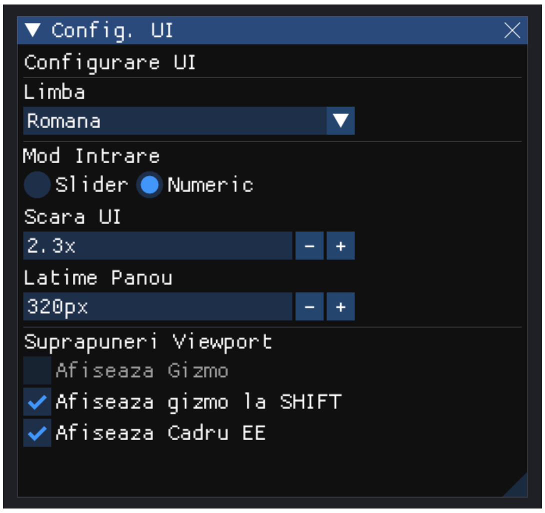

Fig. 9. Graphical UI configuration window (**U**ser **I**nterface)

The last configuration window is the one that actually saves the parameters entered in the other windows, as well as certain parameters from the main control panel, into a file with a name and extension specific to configuration files (config.ini).

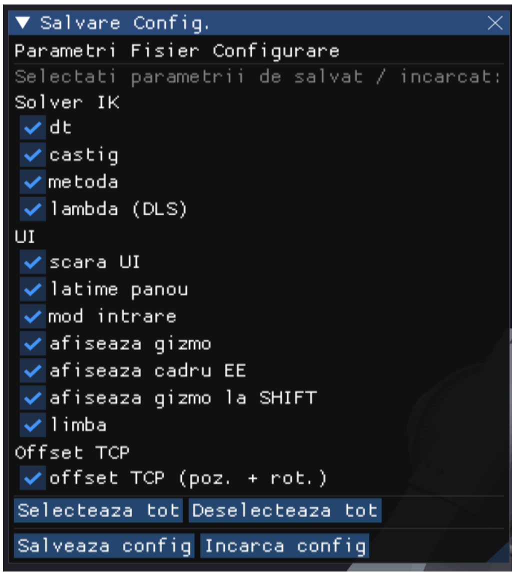

Fig. 10. Window of the save file configuration

In addition to the configuration windows, there are two specific windows dedicated to manipulator motion analysis: the real-time motion analysis window and the launch window for the computational system and export of the potential field.
The motion analysis window generates a dynamic graph, continuously updated in real time with data retrieved from the inverse kinematics computation system, in order to visualize the motion of the manipulator.

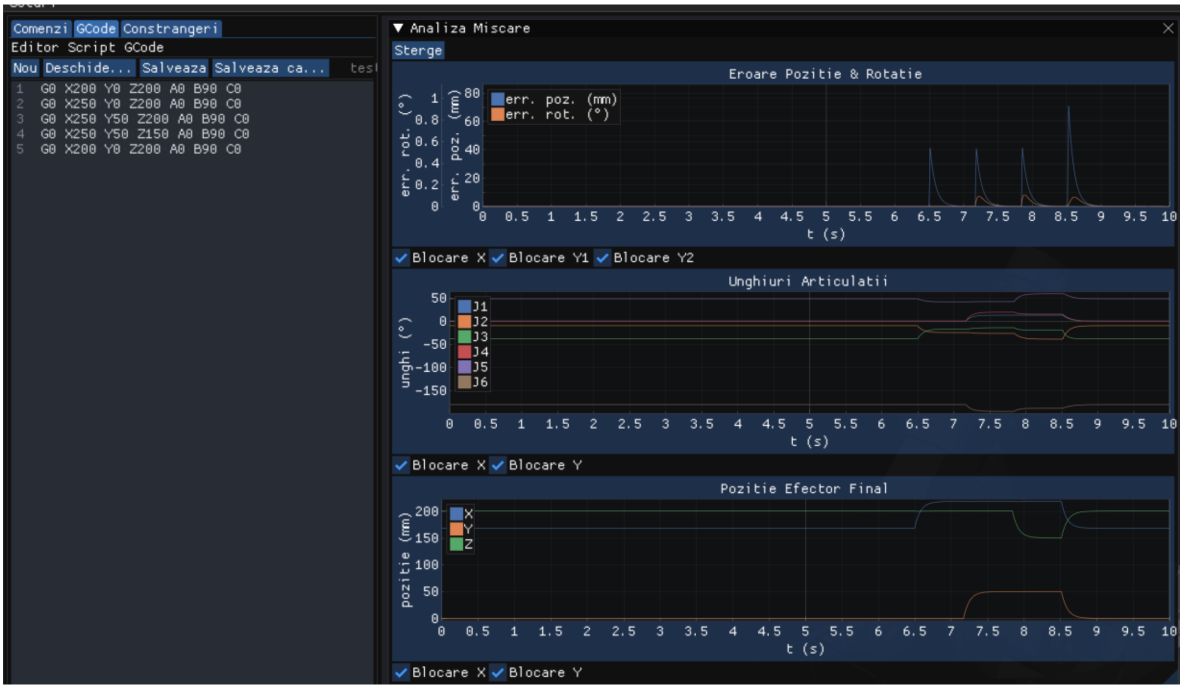

Fig. 11. Movement analysis window open in parallel to GCode control tab

The potential field calculation and configuration window currently performs the computation and generation of a grid of equidistant points in order to test each position, generate a workspace based on a starting position (effective workspace), and visualize potential singularities.

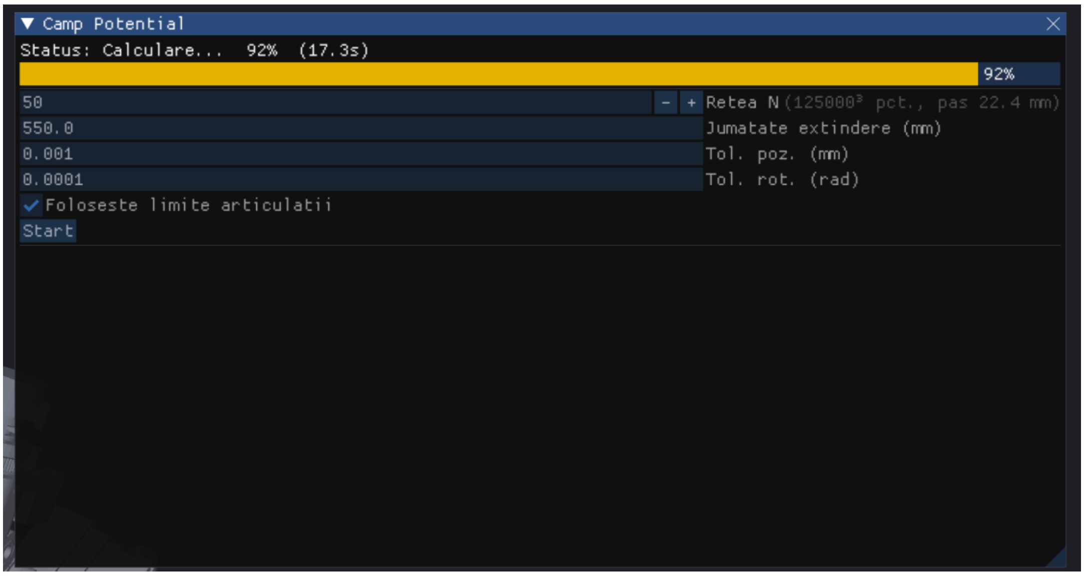

Fig. 12. Window for calculating and configuring the potential field calculator

The mechanism behind the calculator aims to modularize and improve the efficiency of access to a system capable of computing the entire domain of a function. In this case, it performs a mass execution of the inverse kinematics function over a cubic domain who's each side has the size specified in the window, using the current parameters defined in the inverse kinematics configuration window and the parameters specified in the potential field window.

The mechanism works by initially collecting data from the interface, starting a separate supervisory computation thread, and having an orchestrator divide the computation domain into separate worker threads, which then process their assigned subdomains sequentially.

Fig. 13. Calculated effective workspace of the robot

The results of computation for the effective workspace highlight the classic characteristic of a spherical articulated workspace specific to robotic arm manipulators with 6 degrees of freedom. At the same time, on Fig. 12, potential singularities (configuration changes) can be observed, indicated by abrupt color changes, i.e., a deviation from the gradient and from the expected value in such a case.

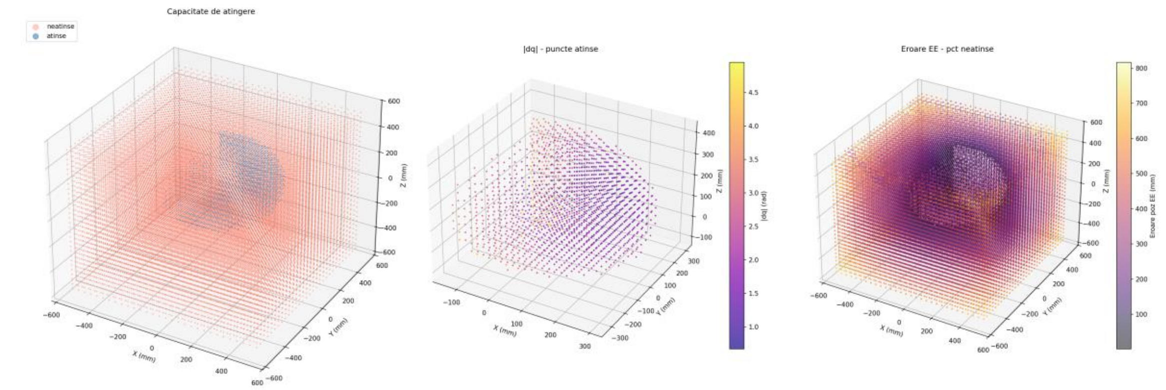

Fig. 14. Results of a calculation of the effective workspace

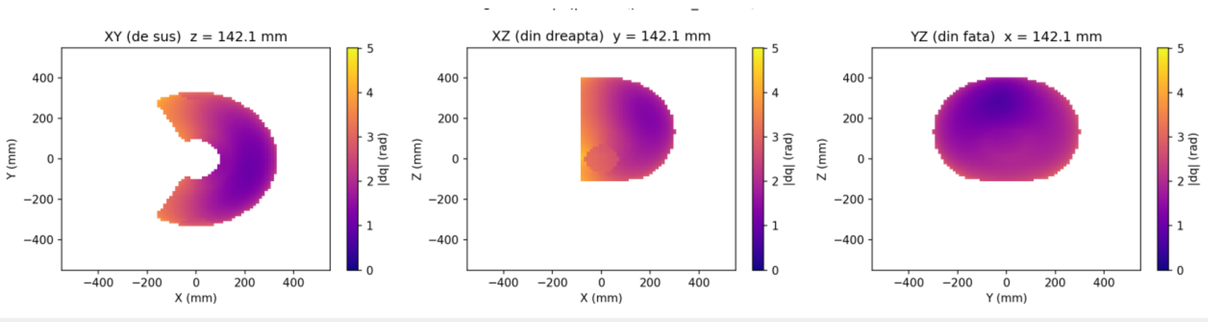

Fig. 15. The magnitude of the differences in joint values relative to the neutral position

3. Conclusions and future research directions

The developed simulation software demonstrates the possibility of integrating existing mechanisms for workspace generation, obstacle avoidance, and singularity avoidance, which are currently used only in offline programming on secondary computers and not integrated into the robot controller, into online programming, meaning directly within the robot controller.

Such integration would enable a higher level of robot functionality, such as active motion obstacle

avoidance, intelligent avoidance and suggestion of solutions for singularities, and the generation of an effective workspace based on a neutral (starting) position, which is currently present in most robot-specific G-code programs, in an effort to compute and optimize the trajectory within the workspace in real time.
A future research direction is the implementation of this system on the miniature robot controller in order to test its performance and capabilities.

4. Bibliography

[1]. Yasim-Ahmad, Y., "MATLAB implementation of Artificial Potential Field," [Online]. Available: https://github.com/Yaaximus/artificial-potential-field-matlab. [Accessed 10 05 2026].
[2]. „Dear ImGui: Bloat-free Graphical User interface for C++ with minimal dependencies," [Interactiv]. Available: https://github.com/ocornut/imgui. [Accesat 09 05 2026].
[3]. "Immediate mode 3D gizmo for scene editing and other controls based on Dear Imgui," [Online]. Available: https://github.com/cedricguillemet/imguizmo. [Accessed 09 05 2026].
[4]. "Eigen: A C++ template library for linear algebra," [Online]. Available: https://libeigen.gitlab.io/. [Accessed 09 05 2026].
[5]. Buss, S. R., "Introduction to Inverse Kinematics with," 7 10 2009. [Online]. Available: https://www.cs.cmu.edu/~15464-s13/lectures/lecture6/iksurvey.pdf. [Accessed 10 01 2026].
[6]. "Seamless operability between C++11 and Python," [Online]. Available: https://github.com/pybind/pybind11. [Accessed 13 05 2026].
[7]. "CMake: A Powerful Software Build System," [Online]. Available: https://cmake.org/. [Accessed 13 05 2026].

5. Notations

The following symbols are used in this work:
J^{-1} = the inverse of the Jacobian (direct, pseudo-inverse, or damped least squares)
q = the vector of manipulator joint values [rad]
α = proportional gain specific to the inverse kinematics function
e = 6D position error vector [mm, rad]
Δt = time step [s]

DEVELOPMENT OF A LOCAL IOT SYSTEM FOR WATER LEVEL MONITORING AND SMART IRRIGATION

RIZEA Nicolae-Cătălin and Asst. Prof. Ph.D. Eng. **MUNTEANU Iulian-Sorin (Scientific Coordinator)**

Faculty of Industrial Engineering and Robotics, Specialization: Engineering and Management of Technological Systems, Year of study: II - Master, e-mail: rizeacatalin2002@gmail.com

ABSTRACT: This paper presents a low-cost, local and scalable IoT prototype for water level monitoring in a small reservoir and for smart micro-irrigation of a household plot. The system integrates a Raspberry Pi 5 Linux server, an ESP32 controller, an ultrasonic distance sensor, soil-moisture sensors and relay-driven actuators for pump or valve control. The proposed architecture uses MQTT communication and visual automation rules in an ioBroker/Blockly environment, allowing local operation, mobile supervision through a secure network connection and future extension with additional sensors. The prototype is suitable for do-it-yourself household automation, educational use and small-scale precision irrigation applications.

KEYWORDS: smart irrigation, water level monitoring, ESP32, Raspberry Pi 5, MQTT

1. Introduction

The digitalization of domestic and household applications supports automation systems that reduce manual intervention, save water and give users real-time control over operating parameters. In small-scale irrigation, many commercial solutions depend on cloud services, closed ecosystems or proprietary mobile applications.

This dependency limits expandability when sensors and actuators from different manufacturers must be integrated into the same installation. For this reason, the present paper proposes a DIY prototype for monitoring the water level in an approximately 20 L tank and for controlling a micro-irrigation system for small plots, from about 1.5 x 3 m to 2 x 4 m.

By combining tank-level information with soil-moisture readings, the solution aims to optimize water use for flowers, vegetables and ornamental plants. The main objective is to design a local, modular and scalable architecture based on Raspberry Pi 5, ESP32, level and moisture sensors, and control relays.

The system can drive a pump that refills the tank when the water level falls below a minimum threshold. It can also control irrigation through a solenoid valve or a secondary pump. Monitoring is available from a laptop or smartphone, either inside the local area network (LAN) or through a VPN connection.

2. State of the art

The technical literature shows that IoT-based smart irrigation systems commonly use soil-moisture sensors, temperature sensors, flow sensors, microcontrollers with wireless connectivity, and web or mobile applications for monitoring and control [1], [2].

The main advantage of controlled irrigation is that water is applied only when the soil condition and the operating context justify it. This reduces losses and improves the reproducibility of the watering process.

For this work, the technical requirements were defined at the level of an educational and household prototype: low cost, local operation, easy configuration, manual intervention capability, electrical safety and extensibility.

Because the system handles both water and electrically powered components, the implementation must clearly separate the low-voltage sensor side from the power side used for the pump or solenoid valve.

Table 1. Main components of the prototype

Component	Role in the system	Interface / signal	Technical observations
Raspberry Pi 5	Local Linux server for automation and interface	Ethernet/Wi-Fi	Runs ioBroker, Blockly and the MQTT broker/adapter.

ESP32	Sensor acquisition and local control	GPIO, Wi-Fi	Suitable for IoT applications due to integrated connectivity.
Ultrasonic sensor	Estimates the distance to the water surface	Trigger/Echo or waterproof version	Calibration is recommended for empty and full tank states.
Soil-moisture sensors	Determine the need for irrigation	Analog/digital	Capacitive sensors are preferable in wet soil.
Relay / Shelly module	Controls the pump or solenoid valve	GPIO/MQTT	Requires insulation and electrical protection.
Pump / solenoid valve	Tank filling and supply of the irrigation line	AC/DC, depending on the solution	Sized according to flow rate and pressure.

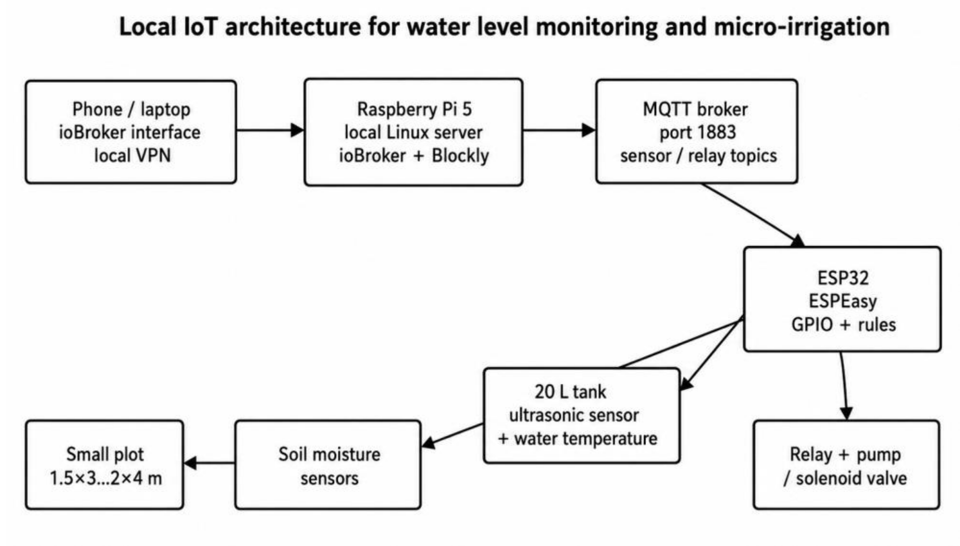

Fig. 1. Local IoT architecture for water-level monitoring and irrigation

3. Measurement principle and control-logic sizing

The water level is measured indirectly by determining the distance between the ultrasonic sensor mounted at the top of the tank and the water surface. The sensor emits an ultrasonic pulse, receives the echo reflected by the water surface and allows the distance to be calculated from the signal time of flight. The relation used is:

$$d = v_s \cdot \Delta t / 2 \tag{1}$$

where d is the distance to the water surface [m], v_s is the speed of sound in air [m/s], and Δt is the measured round-trip time of the ultrasonic pulse [s].

For a simplified volume estimate, the tank is considered to have an approximately constant cross-section. The useful water height is obtained from the difference between the sensor reference position and the measured distance.

$$P_{level} = 100 \cdot h_{water} / H_{useful}, \quad V_{approx} = V_{max} \cdot h_{water} / H_{useful} \tag{2}$$

where h_{water} is the useful height of the water column [m], H_{useful} is the useful tank height [m], and V_{approx} is the estimated volume [L].

For the 20 L tank, the thresholds can be selected experimentally. For example, a lower threshold can trigger filling when the estimated volume drops below 20-30% of capacity, while an upper threshold can stop the pump at 85-95% in order to avoid overflow.

In practice, a hysteresis band is recommended. This prevents the pump from repeatedly starting and stopping around the same level value.

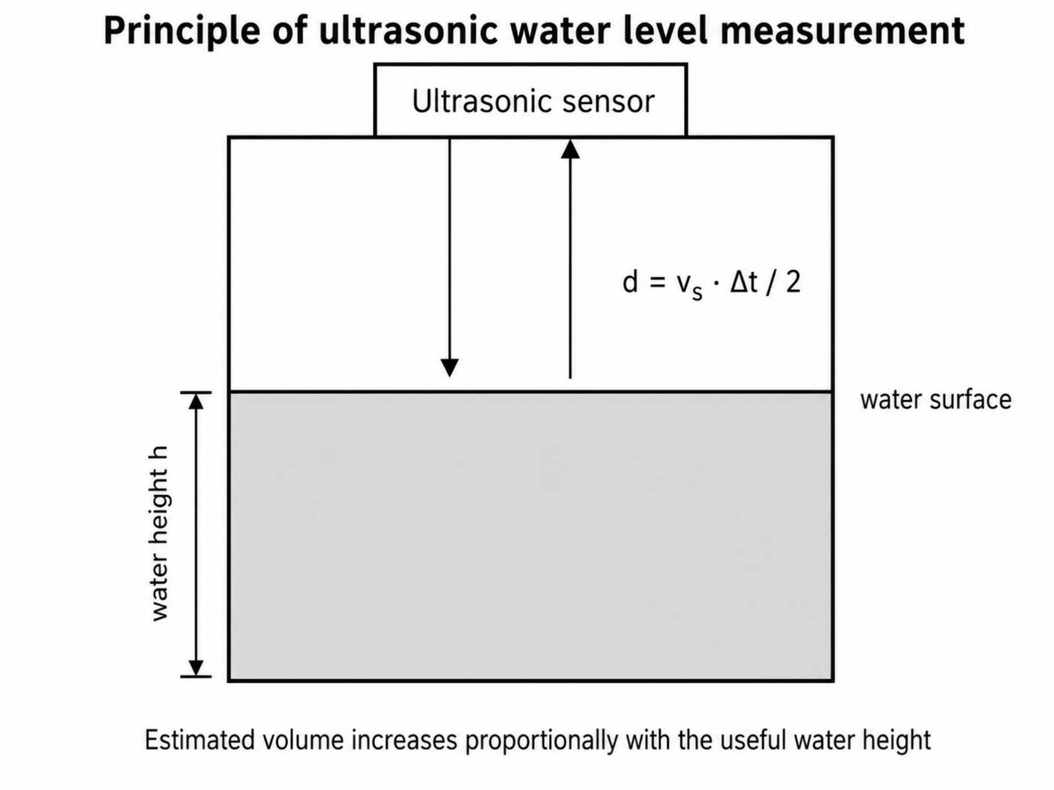

Fig. 2. Ultrasonic measurement principle for the water level inside the tank

4. Hardware and software implementation of the local IoT prototype for water-level monitoring and irrigation control

The prototype was implemented by integrating a local Raspberry Pi 5 server with an ESP32 acquisition and control node. The system also includes sensors for monitoring the water level and soil moisture, as well as relay modules for controlling the pump or the solenoid valve.

Raspberry Pi 5 was selected because it offers dual-band Wi-Fi connectivity, Bluetooth/BLE support, USB ports and sufficient hardware resources for local smart-home applications [3].

The architecture was designed for local operation, low cost, extensibility and manual intervention in the automation process.

Raspberry Pi 5 was used as the central local server. A Linux operating system and the ioBroker platform were installed on it. The server centralizes sensor data, manages MQTT communication, displays parameters and executes the automation rules defined in Blockly.

The ESP32 node was configured as a local acquisition and control unit. It collected data from the ultrasonic level sensor, the soil-moisture sensors and the water-temperature sensor. Based on the configured rules, it controlled the digital outputs associated with the relays. In this way, the measurement layer and the actuation layer were distributed locally. This reduces dependence on the server and increases system flexibility.

Communication between ESP32 and the Raspberry Pi 5 server was implemented through MQTT, which is widely used in IoT applications because of its efficient publish/subscribe model [4]. The ESP32 published measured values to the MQTT broker, including the water level, pump state and soil moisture. The ioBroker platform received these data for display, storage, logical interpretation and automatic command generation.

The automation logic was developed in Blockly [5], integrated in ioBroker. This environment allows clear visual rules that are easy to follow and modify. Level and moisture conditions can be associated with direct actions on the pump or solenoid valve. From this point of view, the software contribution of the work consisted in configuring a local automation architecture, defining the command flows and integrating MQTT communication with the monitoring interface.

4.1. Hardware component implementation and software configuration of the DIY solution

The prototype integrates the following main components: a Raspberry Pi 5 microserver, an ESP32 development board, an ultrasonic sensor for estimating the water level, soil-moisture sensors, a water-temperature sensor, relay modules, LED signaling elements, and the actuator used for pump or solenoid-valve control.

The software solution was built on a local smart-home platform installed on the Linux server. The platform enabled MQTT communication, device definition, parameter visualization and automation-rule creation.

Compared with commercial solutions that are strictly cloud-dependent, the implemented architecture provides direct control over data, local operation and integration of hardware components from different manufacturers.

Blockly was used for visual automation because it defines logic through interconnected graphical blocks. This approach is suitable for an educational and DIY application. It provides an intuitive link between sensor readings, logical conditions and actuator commands.

At the same time, visual rules made it easier to quickly modify level thresholds, start/stop conditions and irrigation timing.

An important original contribution was the configuration of a local software solution without mandatory dependence on an external cloud server.

Remote access was planned through a secure VPN connection. This allows monitoring and parameter intervention without directly exposing the server to the Internet. As a result, the prototype achieves better control, privacy and functional independence.

MQTT was used to integrate the ESP32 devices and control modules into the local server. In ioBroker, the MQTT Broker/Client instance was configured so that messages published by the ESP32 could be received, filtered by topic and used in automation rules.

The ESP32 node was configured with ESPEasy firmware. This firmware was selected because it is compatible with ESP32/ESP8266 boards and allows rapid configuration of sensors, digital outputs and local rules. The firmware was uploaded to the ESP32 through a serial connection, after installing the required drivers on the programming computer.

After the firmware was uploaded, the ESP32 board was connected to the local wireless network. The device was then assigned a name and a fixed IP address in order to support stable network access and reliable integration into the automation platform. GPIO pin configuration associated the inputs and outputs with the sensors and actuators used in the prototype.

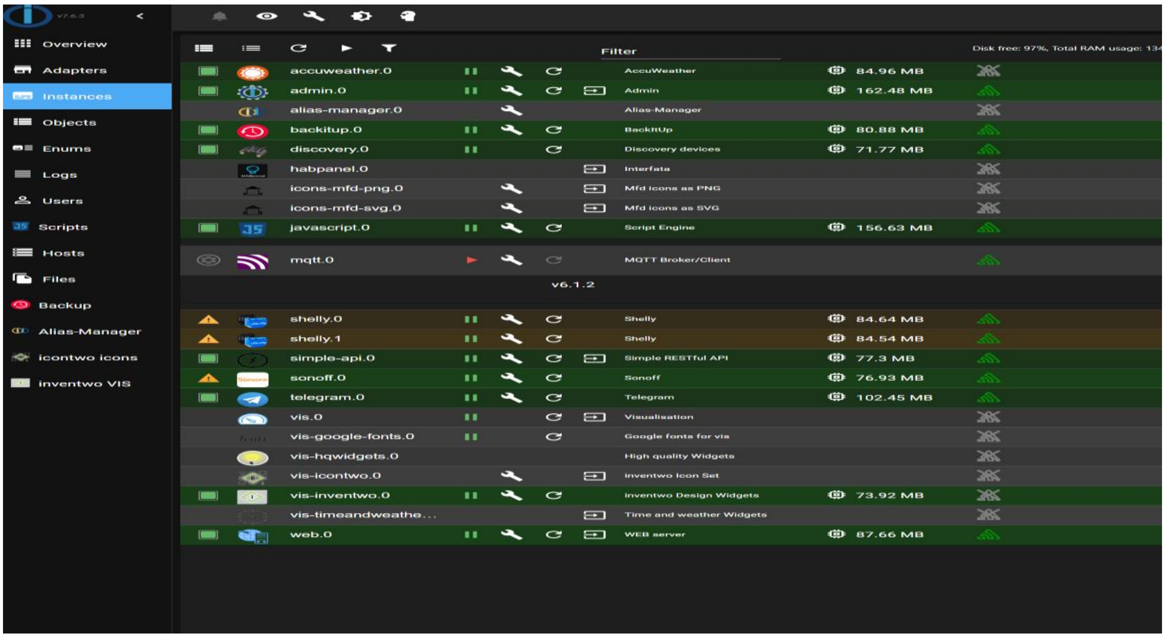

Fig. 3. Configuration of the MQTT Broker/Client instance in the ioBroker platform

Separate GPIO pins were used for the ultrasonic level sensor, the water-temperature sensor, optical LED signaling and the relay command for the pump or solenoid valve. This functional separation on dedicated pins allowed individual testing of the subsystems and easier troubleshooting of the complete assembly.

The local rules defined on the ESP32 aimed to maintain the water level between two preset thresholds. When the distance measured by the ultrasonic sensor indicated that the level had fallen below the minimum threshold, the pump relay was activated. When the upper threshold was reached, the pump was switched off to prevent tank overflowing. This logic can be extended with additional conditions, such as soil-moisture sensor states or manual commands sent from the local interface.

By integrating a relay board with several outputs, the solution was prepared for later extension with other devices, including additional solenoid valves, flow sensors, optical indicators or actuators for different irrigation zones. For this reason, the prototype is not only a single pump-control application. It is also a modular platform for developing smart-household mechatronic applications.

The originality of the software solution results from the correlation of several control levels: local data acquisition on ESP32, parameter transmission through MQTT, processing and visualization on the Raspberry Pi 5 server, and automation-rule definition in Blockly. This structure clearly separates the field level, the communication level and the software decision level. The rules can also be adjusted experimentally, according to the real thresholds of the tank and the behavior of the soil-moisture sensors.

Compared with a preconfigured commercial solution, the specific contribution was not limited to connecting modules. It consisted in building a functional architecture able to integrate sensors, actuators, MQTT communication, a local interface and control logic into a coherent prototype. This approach gives the work both applied and educational value, because it explains the full relation between measurement, decision and actuation.

A functional prototype was therefore obtained, as shown in Fig. 4. It can be used in a household micro-irrigation application, with monitoring of operating parameters through the local IoT interface and through mobile devices connected to the network.

Fig. 4. View of the assembled functional prototype for water-level monitoring and smart irrigation

From the hardware point of view, the originality of the prototype consisted in the physical integration of the components into a functional assembly adapted to a real micro-irrigation application. The design correlated the requirements for measuring water level, reading soil moisture, controlling the pump or solenoid valve, and protecting electronic components against humidity. By using a distributed Raspberry Pi 5 - ESP32 architecture, the prototype separated computing, monitoring and control functions. This made operation safer and further extension easier.

5. Operating logic and experimental validation of the prototype

The prototype operation was structured around two interconnected control loops, as shown in Fig. 5. The first loop managed the water level in the tank by correlating the distance measured by the ultrasonic sensor with the minimum and maximum thresholds established experimentally. When the level fell below the minimum threshold, the filling-pump relay was activated. When the upper threshold was reached, the command was deactivated.

The second loop managed the irrigation process. In this case, the pump or solenoid-valve command depended on the available water level in the tank and on the soil-moisture value. If the soil was identified as dry and the tank contained enough water, the system activated irrigation for a preset duration. After that, the soil state could be checked again in order to avoid excessive watering.

Experimental validation was carried out progressively by testing each subsystem separately and then verifying integrated operation, as summarized in Table 2. The verification focused on reading stability, relay response time, correct display of the state in the interface, pump stop at the upper threshold and transition to a safe state when invalid readings occurred.

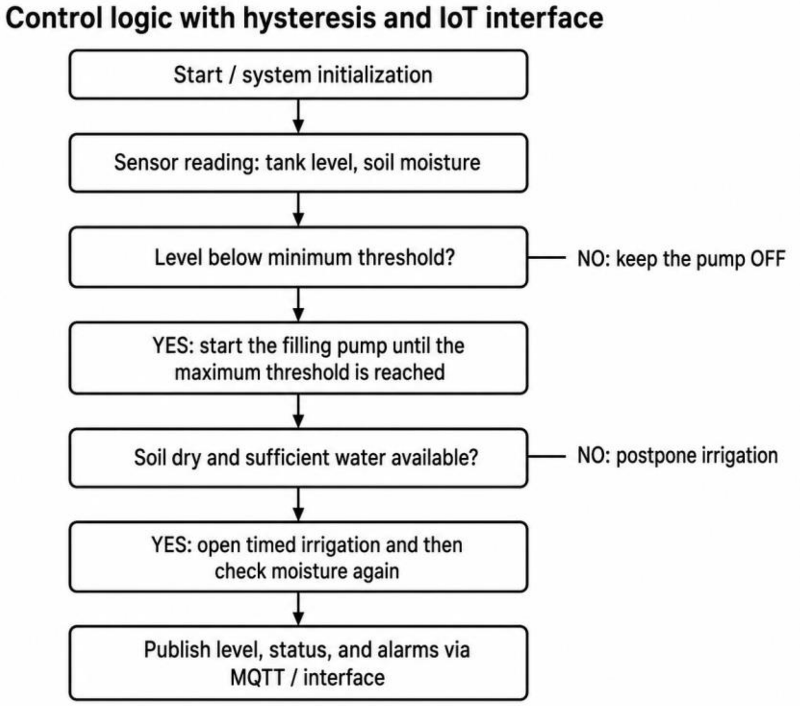

Fig. 5. Logic diagram for automatic tank-filling control and irrigation

Table 2. Experimental validation plan for the prototype

Test	Condition	Expected result	Observation
Tank level	Empty, 50%, almost full	Coherent distance and level percentage	Average over 5-10 readings.
Automatic filling	Level below minimum threshold	Pump/relay starts	The minimum threshold is set experimentally.
Filling stop	Level above maximum threshold	Pump stops	Prevents overflow.
Automatic irrigation	Dry soil and sufficient water level	Timed opening	Duration is adjusted according to flow rate.
Safety	Manual command / sensor error	Transition to safe state	Pump off when data are invalid.

The functional checks showed that the proposed local architecture offers advantages over a strictly cloud-dependent commercial solution. The system provides local control of data, operation independent of an external server and the possibility of extension with sensors or actuators from different manufacturers.

At the same time, the tests highlighted the need for correct sensor calibration, protection of electronic components against humidity, stabilization of Wi-Fi communication and strict compliance with safety rules when controlling pumps supplied from hazardous voltage levels.

6. Conclusions

This paper presented the development of a functional DIY prototype for monitoring the water level in a small tank and for controlling a micro-irrigation system intended for household use. The solution was designed as a local, modular and scalable architecture. It integrates a Raspberry Pi 5 server, an ESP32 node, level and moisture sensors, MQTT communication, control relays and visual automation rules in the ioBroker/Blockly environment.

The main original contribution was the development and integration of a local hardware-software architecture able to acquire data, transmit parameters, interpret logic and command actuators without mandatory dependence on an external cloud service. From the software point of view, the work configured MQTT communication, the local monitoring interface, the automation rules and the command logic for tank filling and conditional irrigation. From the hardware point of view, the measuring, control and actuation components were integrated into a functional prototype adapted to a real smart-household application.

An important element of the work was the functional separation of the system levels: the acquisition and actuation level, implemented through ESP32; the communication level, implemented through MQTT; and the control and monitoring level, implemented on the Raspberry Pi 5 server. This structure allowed individual subsystem testing, parameter modification and later extension of the prototype with additional sensors, actuators or functions.

The developed system enabled automatic tank filling, irrigation conditioned by soil moisture and parameter supervision from a phone or laptop. Through adjustable thresholds, hysteresis and progressive subsystem testing, the prototype demonstrated potential for small-scale applications, such as watering a plot with flowers, vegetables or ornamental plants.

The educational value of the work lies in the fact that the student completed a full mechatronic development cycle: component selection, ESP32 node configuration, MQTT communication integration, command-logic definition, physical prototype assembly and functional validation. Therefore, the work is not limited to presenting electronic modules. It demonstrates the ability to integrate sensors, actuators, local software and IoT communication into a coherent system.

Future developments may include a flow sensor, weather-data integration for predictive irrigation, solar power for external nodes, automatic notifications, historical data storage and a standardized technical enclosure produced by 3D prototyping. In a later stage, the collected data can be used to optimize water consumption and to evaluate system behavior under different seasonal conditions.

7. References

[1]. García, L., Parra, L., Jimenez, J. M., Lloret, J. and Lorenz, P. (2020), "IoT-Based Smart Irrigation Systems: An Overview on the Recent Trends on Sensors and IoT Systems for Irrigation in Precision Agriculture", Sensors, 20(4), 1042, ISSN 1424-8220.

[2]. Pereira, G. P., Chaari, M. Z. and Daruge, G. C. (2023), "IoT-Enabled Smart Drip Irrigation System Using ESP32", IoT, 4(3), 221-243, ISSN 2624-831X.

[3]. Raspberry Pi Ltd., Raspberry Pi 5 Product Brief / Technical Specifications, Raspberry Pi documentation, accessed 2026.

[4]. OASIS / MQTT.org, MQTT: The Standard for IoT Messaging. MQTT Version 5.0 Standard Documentation, 2019–2026, accessed 2026.

[5]. Google for Developers, Blockly Documentation: Visual Programming Editor, accessed 2026.

[6]. ioBroker GmbH/ ioBroker Community, ioBroker Smart Home Automation Platform Documentation, accessed 2026.

[7]. LetsControllt Community, ESPEasy Firmware Documentation and Rules for ESP8266/ESP32 Devices, accessed 2026.

[8]. Hunkeler, U., Truong, H. L. and Stanford-Clark, A. (2008), "MQTT-S – A publish/subscribe protocol for Wireless Sensor Networks", Proceedings of the 3rd International Conference on Communication Systems Software and Middleware, Bangalore, India.

SOLUTION FOR IMPORTING MEASUREMENTS FROM A DIGITAL INSTRUMENT INTO A CAD PROGRAM

POPESCU (TRANDAFIR) Gabriela-Elisabeta, TRANDAFIR Nicolae, and Asst. Prof. Ph.D. Eng. **NICULAE Elisabeta**, Asst. Ph.D. Stud. Eng. **POPESCU Mircea-Daniel (Scientific Coordinators)**

Faculty of Industrial Engineering and Robotics, Master's Degree Program in Modelling and Simulation of Mobile Mechanical Systems, 2nd Year of Study
E-mail: trandafirgabriela07@yahoo.com

ABSTRACT: This paper presents a solution for taking measurement values from a digital measuring instrument and importing them into a CAD program. This facilitates the redesign of spare parts or the statistical processing of data corresponding to dimensional values.
KEYWORDS: caliper, digital measurement, microcontroller, interface, CAD.

1. Introduction

Digital instruments for dimensional measurement in mechanical engineering have become widely accessible and are currently available even in general consumer goods stores. Common digital measuring instruments include:

- digital calipers;
- dial indicators;
- micrometers;
- protractors;
- inclinometers.

From the perspective of data connectivity, these devices can be classified as:

- devices without a data transfer interface;
- devices equipped with a data transfer interface accessible through a dedicated connector;
- devices incorporating a data transfer interface that can only be accessed by disassembling the instrument and establishing direct connections to the printed circuit board;
- devices featuring wireless connectivity via Wi-Fi or Bluetooth protocols.

Data transfer cables typically employ connectors specific to the manufacturer or even to a particular measuring instrument model. Data communication may be implemented through RS-232, RS-485, I^2C, or proprietary protocols.

The objective of the present study was to develop an alternative solution by analyzing the signal provided by a commonly available digital measuring instrument, establishing communication with a computer, and acquiring the measured values. Several potential applications of the proposed system, either in its current form or adapted to specific domains, were identified:

- **Engineering and manufacturing:** verification of component tolerances and statistical processing of measurement data to support corrective actions in manufacturing processes.
- **3D printing and rapid prototyping:** calibration of printing parameters according to filament material properties, measurement of filament diameter, and reverse engineering of replacement parts.
- **Automotive maintenance:** verification of brake disc thickness and measurement of tire tread depth.
- **Mechanism laboratory applications:** measurement and analysis of cam profiles used in cam–follower mechanisms.

2. State of the Art

Manufacturers of digital measuring instruments are generally interested in maintaining exclusive control over accessory supply, including connection cables, and in providing proprietary software solutions for data transfer. Consequently, the cost of a dedicated data transfer cable may be comparable to that of the measuring instrument itself.

3. Practical Implementation

The digital calliper used in this project is a Parkside model that does not provide an external data connector (Fig. 1).

therefore, the following steps were required to enable data acquisition:

- disassembly of the digital measuring instrument;
- identification of a suitable connection point for signal extraction;
- identification of the communication protocol and corresponding connection pins;
- determination of signal voltage levels;
- signal decoding and data transfer to a personal computer.

After removing the main circuit board, four connection pins were identified. The V+ and V− pins were initially located using a digital multimeter. Subsequently, an oscilloscope was used to identify the remaining two pins as the serial communication lines of an I²C interface, namely SCL (Serial Clock Line) and SDA (Serial Data Line).

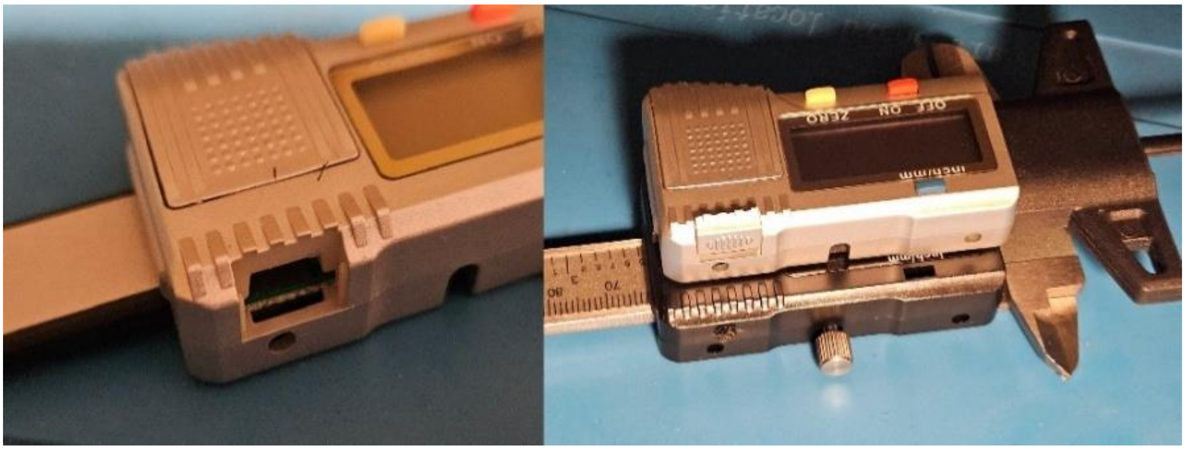

Fig. 1. Digital measuring instrument with and without a data connector

The oscilloscope employed for signal visualization (Fig. 2) was a two-channel digital Rigol DS1102, capable of measuring signals with frequencies up to 100 MHz and providing a sampling rate of 1 GSa/s.

Due to the limited space available inside the instrument housing, a slim CAT6 cable containing eight conductors was selected. Four conductors were allocated to the I²C interface, three conductors were used for the instrument buttons, and one conductor was reserved for future use. A Ø4 mm hole was drilled in the instrument enclosure to allow cable routing. At the opposite end of the cable, a six-pin GX16 female aviation connector was installed, providing a reliable connection to the signal-processing module.

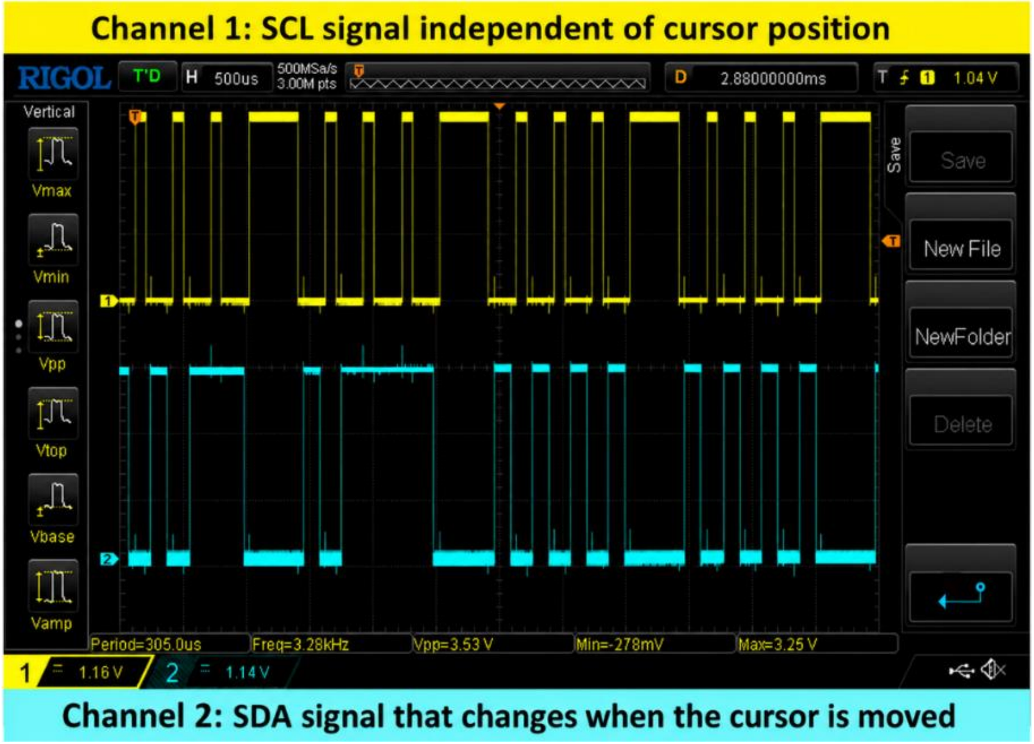

Fig. 2. Signals provided by the measuring instrument circuitry

A Gordak 868D soldering station was used for all soldering operations. This station also supports hot-air soldering for soft solder joints using tin-based alloys (Fig. 3).

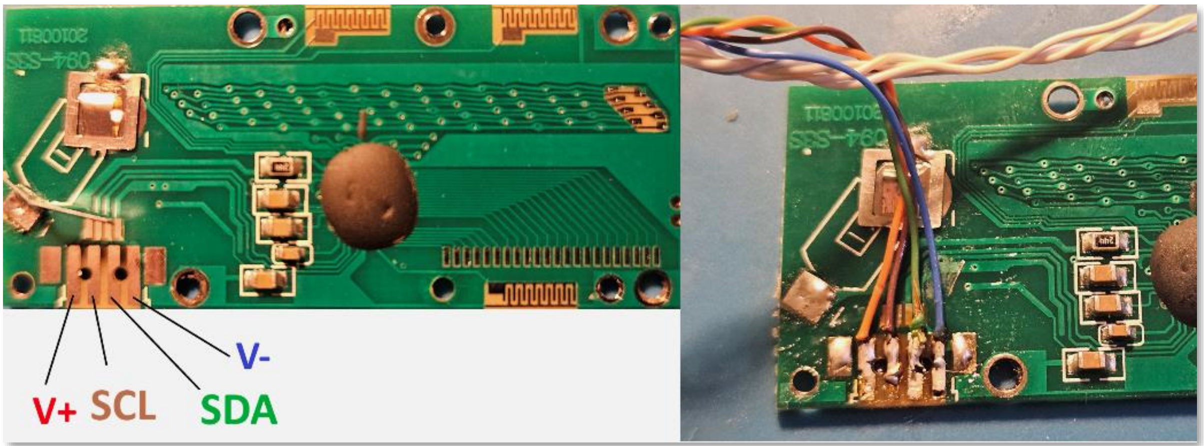

Fig. 3. Soldered cable connection to the circuit board

The signal level indicated by both the oscilloscope and a Fluke 117 digital multimeter corresponded to the 3 V supply voltage provided by the battery. For this reason, a bidirectional level shifter was incorporated to ensure compatibility between the measurement signal and the Arduino Pro Micro development board, which operates at 5 V.

An alternative solution would have been to power the Arduino Pro Micro at 3.3 V. However, the 3.3 V version of the board operates at a clock frequency of 8 MHz rather than 16 MHz and was not available for this project.

Another modification made to the digital caliper consisted of the addition of two momentary push buttons. These buttons were mounted in a custom-designed and 3D-printed component attached to the caliper slider, serving as an extension of the movable jaw assembly.

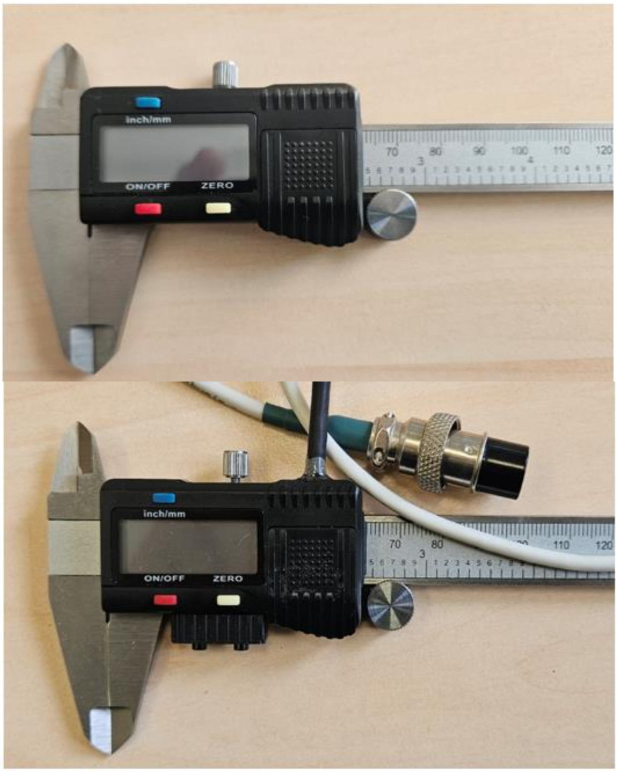

Fig. 4. Modified digital caliper

The measuring instrument before and after the above-mentioned modifications is shown in Fig. 4.

The components used in the project are listed in Table 1.

Tabelul 1. Components

No	Component	Description	Specifications
1	Arduino Pro Micro compatible development board	Development board based on the Atmega32U4 microcontroller with HID capability	
2	Level shifter	Four-channel bidirectional voltage level converter, 3.3 V ↔ 5 V, 4 bitz	
3	Voltage regulator module	Linear 3.3 V regulator based on AMS1117 IC	Vin = 4,5 – 12V Vout = 3,3V I out = 800mA
4	LED module	LED RGB 5 mm	
5, 6, 7	Resistor	Current-limiting resistors for the LEDs	2 x 330Ω; 1 x 470Ω
8, 9, 10	Push Buttons	Momentary push buttons	
11	Digital caliper	Parkside WWS-WMS1 digital caliper	0,01 mm / 0,0005”; 150 mm; baterie CR2032

The electrical schematic integrating the components listed in Table 1 is presented in Fig. 5.

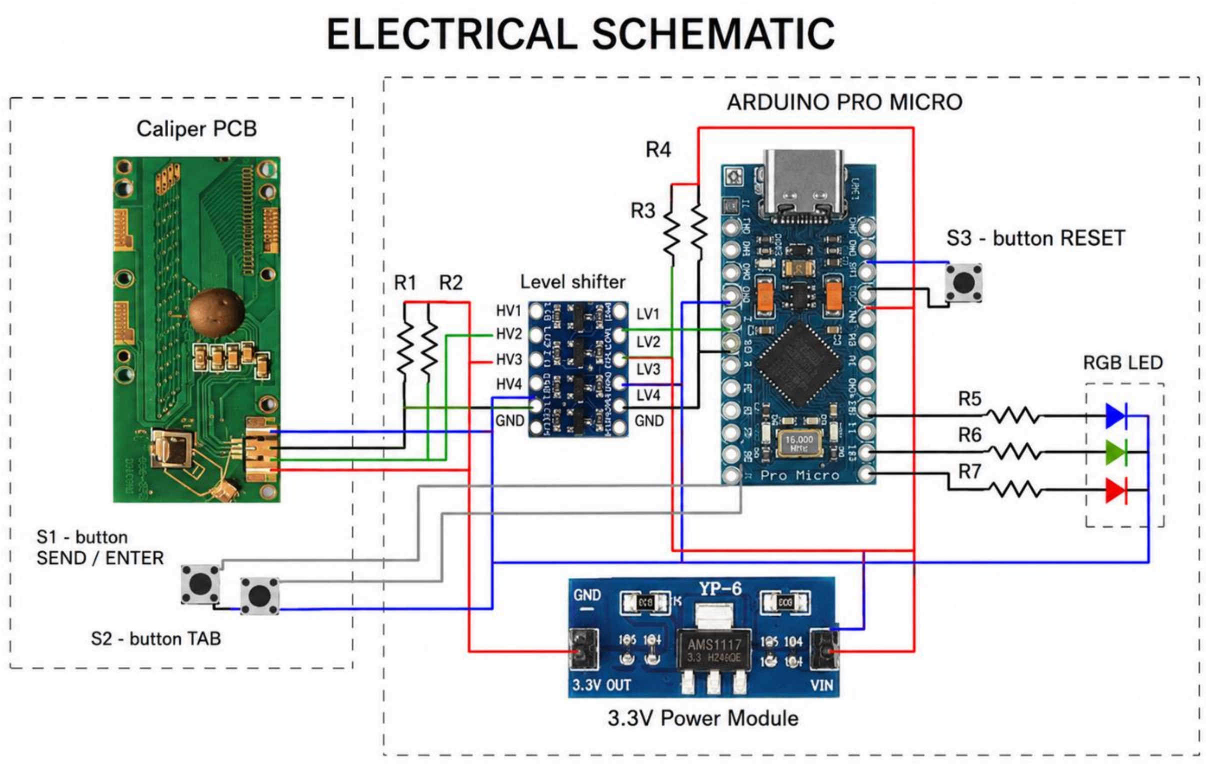

Fig. 5. Electrical schematic of the proposed system

Note: The pull-up resistors R1–R4 shown in the schematic were ultimately omitted because consultation of the level shifter documentation revealed that these resistors are already integrated into the module (Fig. 6).

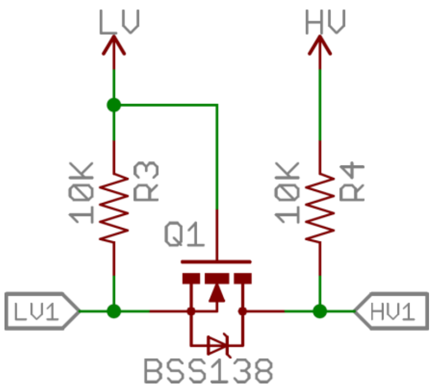

Fig. 6. Level shifter module schematic

4. Data Signal Decoding

Communication is performed according to the following sequence:

- I²C transfers data in messages composed of several packets.
- Start condition: SDA transitions to LOW while SCL remains HIGH.
- Address packet: 7-bit or 10-bit target device address.
- R/W bit: indicates read (1) or write (0) operation.
- ACK/NACK: acknowledgement generated by the receiving device after each byte.
- Data packets: 8-bit data bytes.
- Stop condition: SDA transitions to HIGH while SCL remains HIGH.

The transfer rate ranges from the Standard Mode speed of 100 kbit/s to 3.4 Mbit/s in

High-Speed Mode for bidirectional communication and can reach 5 Mbit/s in unidirectional communication.

Based on the information obtained from the oscilloscope, it was observed that the transmitted data frame contains 25 bits representing the following information:

- Bit 1: start bit, always equal to 1.
- Bits 2–21: stored in the bit_array vector at positions 1–20 and representing the measured value.
- Bit 22: stored in bit_array [21] and indicating the sign of the measured value.
- Bit 25: stored in bit_array [24] and indicating the selected measurement unit (millimetres or inches).

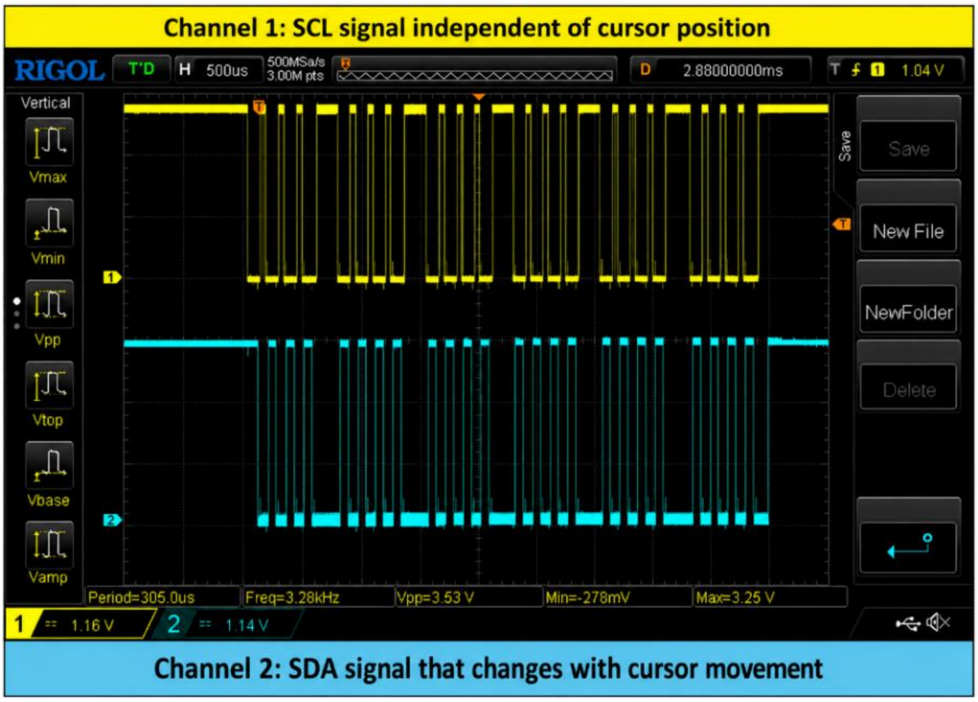

Fig. 7. Structure of an I²C message

The signal can also be monitored using the Serial Monitor window available in the Arduino IDE. Two representative examples are presented below.

a. Measurement value of 1.00 mm

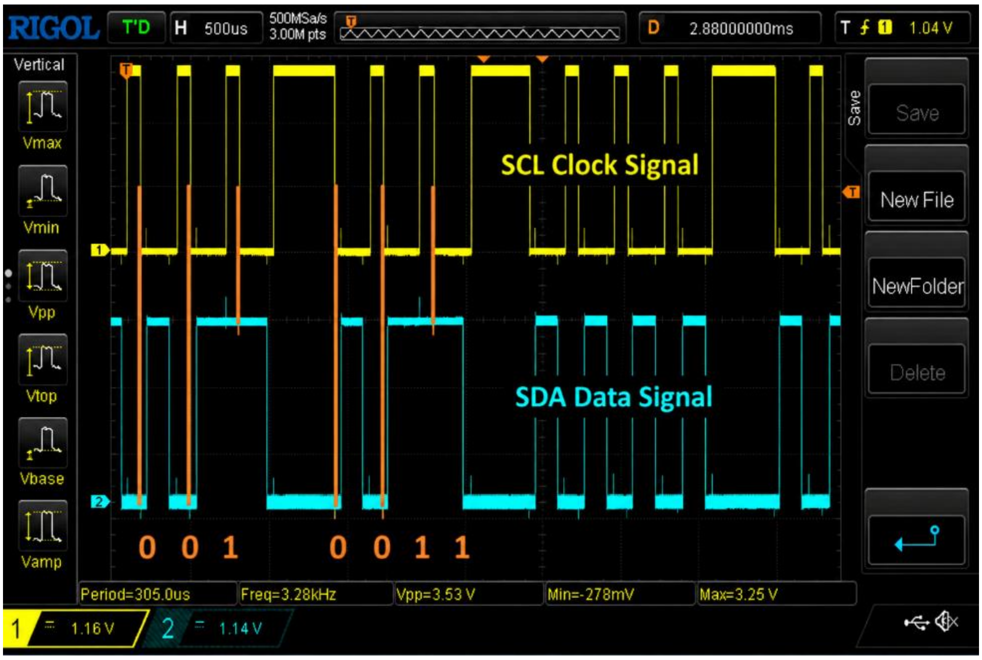

Fig. 8. Message visualization corresponding to a measurement of 1.00 mm

Tabel 2. Decoding of the 1.00 mm measurement

Position	1	2	3	4	5	6	7	8	9	…	20		21	…	24
Bit	**0**	**0**	**1**	**0**	**0**	**1**	**1**	**0**	**0**				**0**		**0**
Multiplication	1	2	4	8	16	32	64	128	256						
Valu	0	0	4	0	0	32	64	0	0		Σ=	100			
Sign													+		
Measurement															100
UM															mm

To determine the actual measured dimension, the decoded numerical value must be divided by:

- 100 when the selected unit is millimetres (mm);
- 2000 when the selected unit is inches (in), rather than 2540, as this is the conversion method implemented by the digital calliper.

The decoded output therefore corresponds to a measured value of 1.00 mm.

b. Measurement value of −2.99 mm

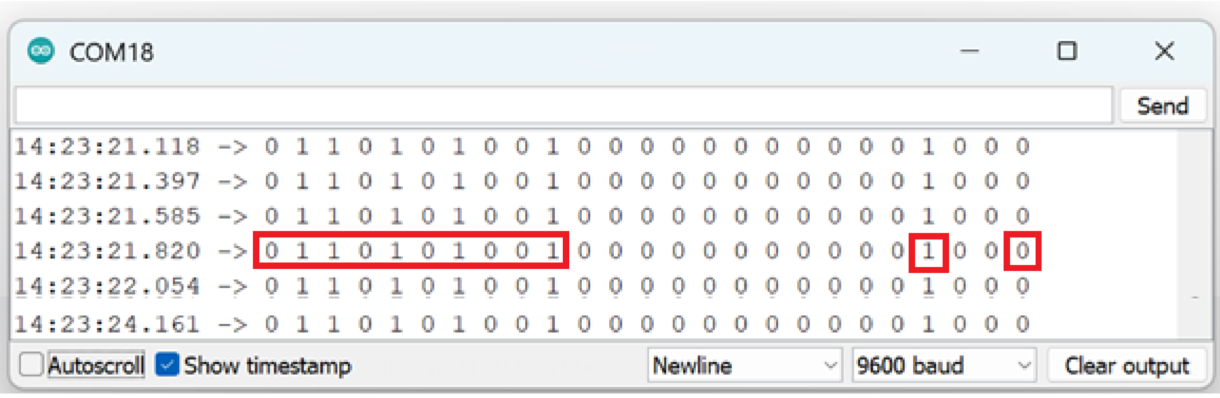

Fig. 9. Signal monitored using the Arduino Serial Monitor

In this case, because bit 24 has a value of 0, the measurement unit is millimeters. The measured value is −2.99 mm because bit 21, which determines the sign of the measurement, has a value of 1.

Tabel 3. Decoding of the −2.99 mm measurement

Position	1	2	3	4	5	6	7	8	9	…	20		21	…	24
Bit	**1**	**1**	**0**	**1**	**0**	**1**	**0**	**0**	**1**				**1**		**0**
Multiplication	1	2	4	8	16	32	64	128	256						
Value	1	2	0	8	0	32	0	0	256		Σ=	299			
Sign													-		
Measurement															-299
UM															mm

5. Microcontroller Programming

The software consists of the following modules:

- Main program loop, void loop (), which contains the logic for reading measurement values.

```
while (digitalRead(pinClock) == LOW) {}
  time_now = micros();
while (digitalRead(pinClock) == HIGH) {}
  if ((micros() - time_now) > 500) {
  decode(); // actualizeaza rezultatul curent
```

Fig. 10. Measurement value acquisition logic

- TAB button event handler: void handleTabButton ()
- Data decoding routine: void decode ()
- SEND/ENTER button press and release event handler: void handleSendButton ()
- Status LED control routine: void settled ()

Keyboard emulation is implemented using the Keyboard.h library:

- Keyboard.begin() – initializes the keyboard emulator;
- Keyboard.write(KEY_TAB) – transmits a TAB keystroke;
- Keyboard.print(...) – emulates the keystrokes corresponding to the character string provided as an argument;
- Keyboard.write(KEY_RETURN) – transmits an ENTER keystroke.

The program also implements software debouncing to eliminate false multiple button activations. An example is provided for the TAB button, including status LED color changes during button actuation.

```
  // logica pentru butonul Tab
void handleTabButton() {
  bool currentTabState = digitalRead(buttonTab);
  if (currentTabState == LOW && lastTabState == HIGH) {
    setLED(HIGH, LOW, LOW); // RED ON
    Keyboard.write(KEY_TAB);
    delay(100);             // Brief flash
    setLED(LOW, LOW, LOW);
  }
  lastTabState = currentTabState;
```

Fig. 11. Debouncing

6. Conclusions

Hardware and software testing demonstrated the feasibility of the proposed solution and its successful integration with both Microsoft Excel and the CATIA CAD environment. The two additional buttons can be reprogrammed to transmit alternative commands, depending on the requirements of the software application receiving the acquired measurement data.

7. Bibliografie

[1]. Arduino SpA, Documentation for Arduino Pro Micro Development Boards.

[2]. Ungureanu, Liviu-Marian, Course Notes.

[3]. Niculae, Elisabeta, Course Notes

[4]. https://wei48221.blogspot.com/2016/01/using-digital-caliper-for-digital-read_21.html?m=1

MECHANISM WITH BAR AND DOUBLE SLIDING WITH SINGLE DEGREE OF FREEDOM

ROB Edward-Andrei, MICU Carmen-Ştefania and Asst. Prof. Ph.D. Eng. **NICULAE Elisabeta**,
Asst. Ph.D. Stud. Eng. **POPESCU Mircea-Daniel (Scientific Coordinators)**
Faculty of Industrial Engineering and Robotics, Specialization Intelligent Industrial Technologies,
Year of study: II
e-mail: edward.andrei.rob@gmail.com

SUMMARY: The project addresses a bar and double-slider mechanism with a single degree of freedom, covering the essential stages of technical development. The work includes a structural analysis to verify the kinematic scheme, followed by the precise sizing of components to ensure the desired operating parameters. Finally, the mechanism was designed in detail, establishing the constructive configuration of both elements and guides. The final result confirms a viable technical solution capable of transmitting motion according to the specified requirements.

CUVINTE CHEIE: mechanisms, elements, sliders, rotation, joints.

1. Introduction

In mechanical engineering, mechanisms are used to transform motions and forces to fulfill specific tasks. Among these, mechanisms with bars and translational kinematic joints (sliders) occupy an important place due to their constructive simplicity and precision in guiding motion.

This project focuses on a bar and double-slider mechanism with a single degree of freedom. By definition, a unitary degree of freedom means that, for a given position of the driving element, all other elements of the mechanism have perfectly determined positions. In this case, the mechanism establishes a connection between two sliders and one or more articulated bars, so that the input motion generates a controlled output motion.

Such a configuration is frequently encountered in practical applications, such as:

- Guiding mechanisms for machine tools (e.g., milling machines, planning machines).
- Actuating mechanisms for pumps or compressors.
- Non-circular gears with an oscillating arm (as a specific synthesis application).
- Mechanisms for transmitting motion between two parallel axes but with a variable stroke.

The purpose of the work is the constructive synthesis of a mechanism with two translational kinematic joints (sliders) to obtain a specific transmission function. The aim is to optimize the dimensions of the bars to ensure jam-free operating conditions and to verify the degree of mobility according to the Chebyshev-Grübler formula.

2. Kinematic scheme and structure (number of joints, elements)

The kinematic scheme of the mechanism is presented in Fig. 1.

- Mechanism Structure:
  - $m = 5$ (number of elements)
  - $C_5 = 7$ (class 5 joints)
  - $C_4 = 0$ (class 4 joints)
- Identifying the elements (m):
  - 0 = fixed element
  - 1 = crank
  - 2 = connecting rod
  - 3 = connecting rod
  - 4 = slider

5 = slider

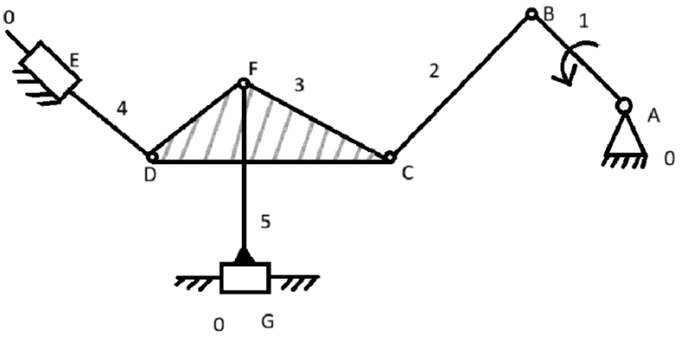

Fig. 1. Kinematic scheme

- Identifying the joints:
  - A (0,1) = rotation
  - B (1,2) = rotation
  - C (2,3) = rotation
  - D (4,3) = rotation
  - E (4,0) = rotation
  - F (3,5) = translation
- Calculation of the Degree of Mobility and the Degree of Indeterminacy

a) Determining mobility is the fundamental stage in structural analysis, having the role of confirming that the mechanism is kinematically determined. For the studied mechanism, located in the category of planar mechanisms, the degree of freedom is calculated using the Chebyshev-Grübler-Kutzbach formula:

$$M = 3m - 2C_5 - C_4 (1)$$

- ~ M = Degree of freedom (mobility) of the mechanism;
- ~ m = Number of mobile elements of the mechanism;
- ~ C_5 = Number of class V kinematic joints;
- ~ C_4: Number of class IV kinematic joints.

$$M = 3(5) - 2(7) - 0$$
$$M = 15 - 14 - 0$$
$$M = 1$$

Conclusion: M = 1 confirms that the mechanism is determined and requires a single driving element.

b) After determining the mobility, it is necessary to verify the degree of indeterminacy of the structure, denoted by N. This calculation has the role of highlighting any passive constraints or redundant degrees of freedom that could influence the actual operation of the mechanism. The calculation is based on the analysis of the configuration of the driven element group and is expressed by the relationship:

$$N = 3m - 2C_5 - C_4 - M (2)$$
$$N = 3(5) - 2(7) - 0 - 1$$
$$N = 15 - 14 - 0 - 1$$
$$N = 0$$

Obtaining the value N = 0 indicates that the mechanism is structurally normal. This means that:

- The mechanism does not contain passive constraints (elements that do not contribute to motion transmission but would introduce additional precision requirements during assembly).
- The system is devoid of redundant degrees of freedom, the entire energy provided by the driving element being usefully transmitted to the driven elements.

- The configuration allows assembly without elastic forcing of the bars, ensuring an optimal lifespan for the kinematic joints.

Separation of the mechanism by structural units is presented in Table 1.

Table 1 Separation of the mechanism by structural units

0	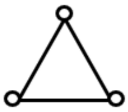	0 (A, G, E)
1	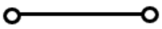	1(A, B)
2	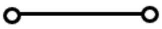	2(B, C)
3	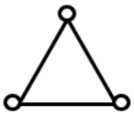	3(C, D, F)
4		4(D, E)
5		5(F, G)

In Fig. 2.a) is presented the scheme of the mechanism formation by structural units and in Fig. 2.b) the scheme of the structural blocks of components is presented in Fig. 3.

Fig. 2. a) Scheme of the mechanism formation by structural units; b) Scheme of the structural blocks of components

3. Constructive configuration and dimensional parameters of the mechanism

The image form Fig. 4 presents the parameterized scheme of the system, defining the lengths of the bars and the positions of the translational joints relative to the fixed reference system.

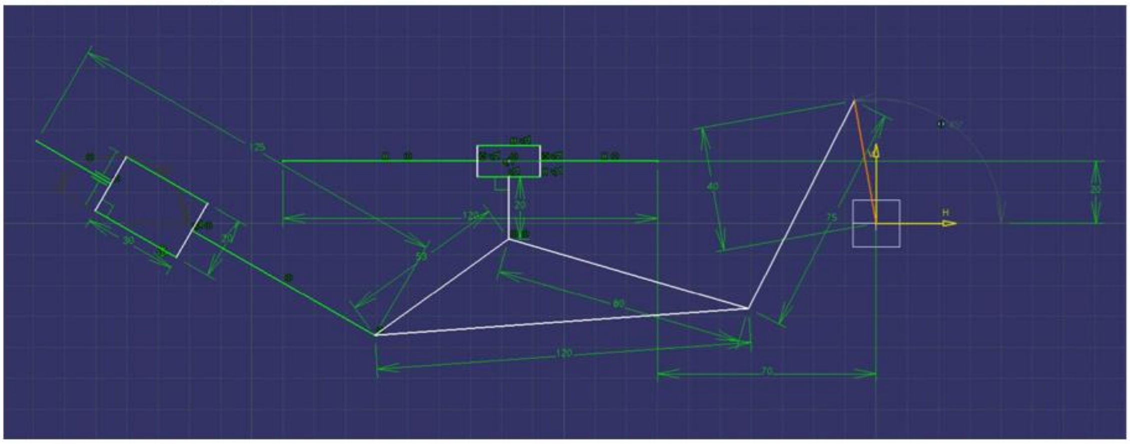

Fig. 4. Geometric and kinematic model of the mechanism

This geometric configuration ensures motion transmission and forms the basis for the analytical calculation of positions and velocities.

4. Conclusions

The project confirmed the viability of the mechanism with bars and double sliding by obtaining unitary mobility. This result demonstrates that the system is kinematically determined and can be rigorously controlled by a single driving element. The structural analysis through the Assur groups method attested that the mechanism is a normal one, being devoid of passive constraints. The established geometric configuration ensures an efficient transformation of rotational motion into translation, eliminating the risk of self-locking in the critical points of the stroke. Finally, the study attests that the chosen dimensional parameters allow a reliable operation, offering a solid theoretical and practical basis for the use of this mechanism in complex industrial applications.

5. Bibliography

[1]. Niculae, E., Course support, National University of Science and Technology, Faculty of Industrial Engineering and Robotics, Bucharest, 2025-2026

[2]. 01_analiza_si_sistematizarea_structurala_a_mecanismelor.pdf

[3]. C12-Structura Mecanismelor-3 - Cinematica P.M. 19.05.2021-Iulian Tabara-Ok | PDF

[4]. 27_01_2020_1998282433.pdf

Analysis of the kinematic behavior of a Jansen mechanism made using additive manufacturing technologies

BALTĂ Anamaria-Gabriela, MÎŢ Maria-Cristina, OLISEVSCHI Ioana, Andrei and Asst. Prof. Ph.D. Eng. **NICULAE Elisabeta**, Asst. Ph.D. Stud. Eng. **POPESCU Mircea-Daniel** **(Scientific Coordinators)**

Faculty of Industrial Engineering and Robotics, Specialization: Industrial Economic Engineering, Year of study: II, e-mail: anamaria.balta@stud.fiir.upb.ro

ABSTRACT The paper analyzes the kinematic behavior of the Jansen stepper mechanism, manufactured using additive manufacturing technologies. The main objective of the paper is to evaluate how different materials, such as PLA, wood, and metal, their stiffness, and surface finish influence the efficiency of the movement of the mechanism. It simulates natural locomotion by transforming rotational motion into a complex stepping trajectory through a single degree of freedom. The research contributes to the optimization of bio-inspired locomotion systems for challenging environments. The correct choice of material is essential for the accuracy and durability of the mobile robot. Finally, the paper provides new insights into the use of additive manufacturing in robotics.

KEY WORDS:
Jansen mechanism, walking leg, additive manufacturing, topological optimization

1. Introduction

The walking mechanism with rods, designed by the renowned Dutch engineer and sculptor Theo Jansen, consists of a gear system intended to simulate natural locomotion, which is characterized by its high efficiency in adverse environments. This is an alternative to mechanisms that use wheels; it operates by converting continuous circular rotational motion into a complex walking trajectory, utilizing a single degree of freedom. The walking assembly is based on a strict set of geometric proportions, referred to in the technical literature as the "Jansen Gene"; in this process, even a fraction of a millimeter can affect the mechanism's continuous motion. This phenomenon is caused by thermal contractions, particularly in additive materials, during 3D printing, which affects the kinematic profile of the sole [1].

In this study, we highlighted the differences between three types of materials: galvanized steel, birch wood, and additive manufacturing. We chose to achieve these objectives by creating three prototypes that are the same length but have different thicknesses and widths. To connect each bar, we used M4 steel screws 30 mm long as the jointing system, and for the fixed points, we used M4 screws 60 mm long and M4 nuts. As a support, we chose to mount each of the three prototypes on a wooden base plate measuring 300 mm × 400 mm × 18 mm to ensure better stability of the mechanisms during movement.

2. Current state

The walking mechanism patented by Dutch sculptor and engineer Theo Jansen in 1991 opened up new avenues of research in the field of bio-inspired robotics and terrestrial locomotion systems. Originally conceived as an autonomous kinematic structure designed to move across sandy surfaces under the action of wind force ("Strandbeest"), the system attracted the attention of the scientific community due to its remarkable ability to generate a quasi-linear trajectory using a single driving element (the crank). In recent literature, research has focused on two major directions: the dimensional optimization of kinematic links and their physical implementation through advanced manufacturing technologies. Giesbrecht (2019) demonstrated that the dynamic performance of the mechanism is extremely sensitive to variations in the position vectors of the fixed and mobile joints. During the lifting phase, modern geometric synthesis often engages numerical and topological optimization algorithms, with the goal of minimizing consuming energy and maximizing ground clearance. With the occurrence of Additive Manufacturing (AM), technologies like Fused Deposition Modeling (FDM/FFF) made the physical enactment of Jansen mechanism widely accessible. However, the transition between idealized computation CAD models and functional 3D printed prototypes hasn't been truly resolved yet.

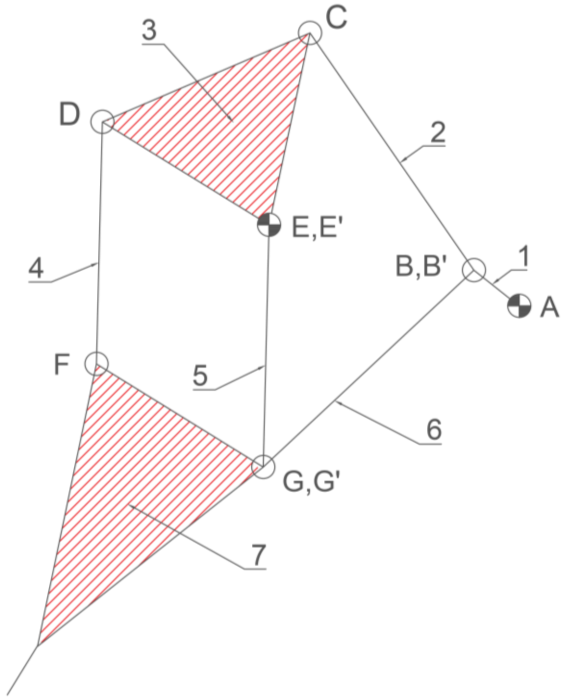

Fig. 1. Kinematic diagram of the mechanism developed by Theo Jansen
1 – Crank; 2, 6 - Connecting rods; 4, 5 - Linkage elements; 3, 7 - Triangular elements

The phenomenon of structural flexibility induced by standard thermoplastic polymers (PLA, ABS, PETG), which have much lower moduli of elasticity than metal alloys. Under the action of dynamic loads and inertial forces, the thin bars undergo transient elastic deformations, causing a significant deviation of the endpoint from the theoretical trajectory [2], [3].

The propagation of errors from kinematic clearance occurs because the Jansen leg is a closed-loop mechanism, with 10 rods per kinematic assembly, and the microscopic radial clearance in Class V kinematic joints—due to the manufacturing tolerances of 3D printers—accumulates exponentially. This phenomenon leads to geometric instability in the critical support phase.

At microscopic scale the tribological behavior is caused by surface roughness of the extruded parts. This will directly affect the coefficient of friction in the joints.

3. Structural analysis of the walking mechanism

The walking mechanism described in this scientific research paper belongs to the category of mechanisms with flat links. Thus, its structure contains kinematic elements connected to one another via kinematic links. To begin with, we chose to develop the kinematic diagram while strictly maintaining its proportions, namely, the distance between the kinematic links—to ensure smooth motion, thereby preventing system jamming during the design and construction of the corresponding prototypes. As can be seen below, the mechanism consists of a crank, two connecting rods, two linkages, and two triangular elements shaded in red.

The mechanism consists of seven moving kinematic elements (m = 7) and two fixed kinematic elements. It contains ten lower kinematic pairs (i = 10) that perform rotational movements: A, B, B’, C, D, E, E’, F, G, G’, and zero upper kinematic pairs (s = 0) [3].

The degree of mobility of the walking mechanism is:

$$M = 3 \times m - 2 \times i - s \quad (1)$$

$$M = 3 \times 7 - 2 \times 10 - 0 = 1$$

$$M = 1$$

The number of links in this walking mechanism is:

$$n = m + 1 \quad (2)$$

$$n = 7 + 1 = 8$$

$$n = 8$$

The number of closed loops in this stepper mechanism is:

$$N = i + s - m \quad (3)$$

$$N = 10 + 0 - 7 = 3$$

$$N = 3$$

In Table 1 are presented the kinematic pairs of the mechanical system, the elements that through their connection form that kinematic pair, class and motion.

Table 1. Kinematic pairs

Kinematic pair	Notation	Clas s	The movement
A	(0, 1)	V	R
B	(1, 2)	V	R
B’	(2, 6)	V	R
C	(2, 3)	V	R
D	(3, 4)	V	R
E	(0, 5)	V	R
E’	(3, 5)	V	R
F	(4, 7)	V	R
G	(5, 6)	V	R
G’	(6, 7)	V	R

In Table 2 are presented the kinematic elements, the connections for each element, type and a representation of for each kinematic element.

Table 2. Kinematic elements

The kinematic element	Pairs belonging to the cinematic element	Type	Representation
0	(A, E)	Binary	
1	(A, B)	Binary	
2	(B, C, B’)	Ternary	
3	(D, C, E’)	Ternary	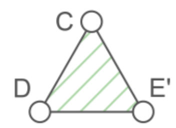
4	(D, F)	Binary	

5	(E’, E, G)	Ternary	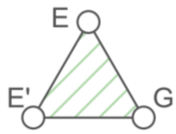
6	(B’, G’, G)	Ternary	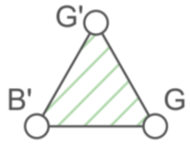
7	(F, G’)	Binary	

Figure 2 presents the structural diagram of the mechanism created by Theo Jansen. Kinematic pair A and kinematic element 1 form an active modular group called Initial Active Modular Group (IAMG). As seen above, the mobility of the mechanical system is 1 so it only needs one engine to put it into motion.

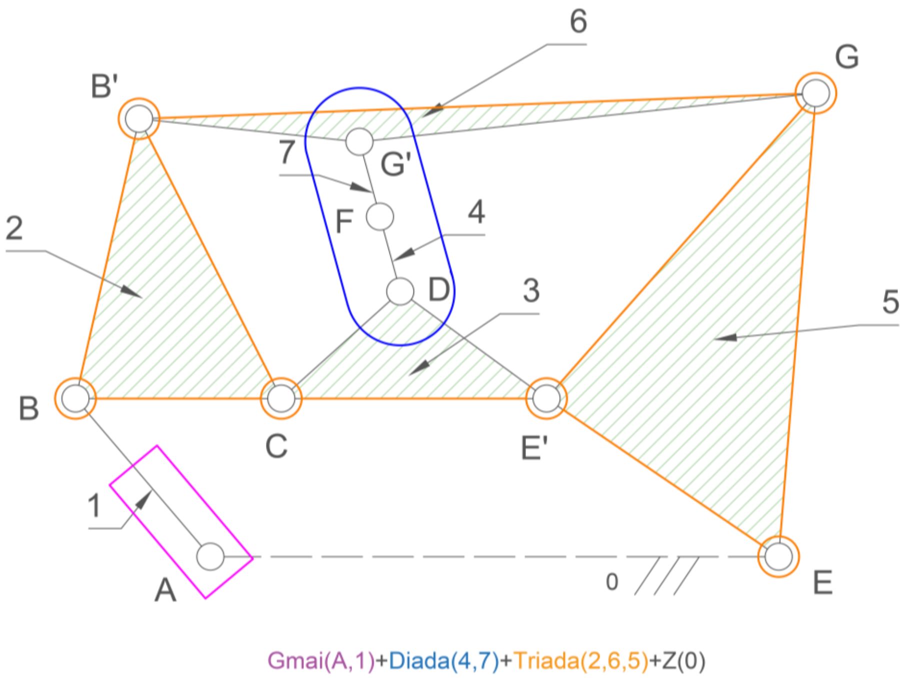

Fig. 2. Structural diagram of the mechanism developed by Theo Jansen

Another two passive groups are found, a dyad and a tetrad. The dyad in Fig. 2 is highlighted through the blue color. is formed by elements 7 and 4 and has kinematic pairs G’, F and D.

The tetrad is formed by elements 2, 3, 4, 5 with B, B’, C, E, E’, G being the kinematic pairs. In Table 3 these structural modular groups are presented in detail.

Table 3. Structural pairs

Modular group	Name	Class	Order	Components	Representation
Active	Initial Active Modular Group	-	-	(A,1)	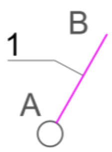

Passive	Dyad	II	2	(4,7)	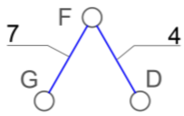
Passive	Tetrad	IV	2	(2,6,5)	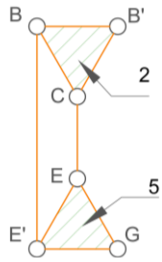

4. Assembling the mechanism from multiple materials

We selected three types of materials: galvanized steel, birch wood, and PLA. All models were assembled using M4 screws (30 mm and 60 mm long) with nuts and washers. Each assembly was mounted on a wooden base plate.

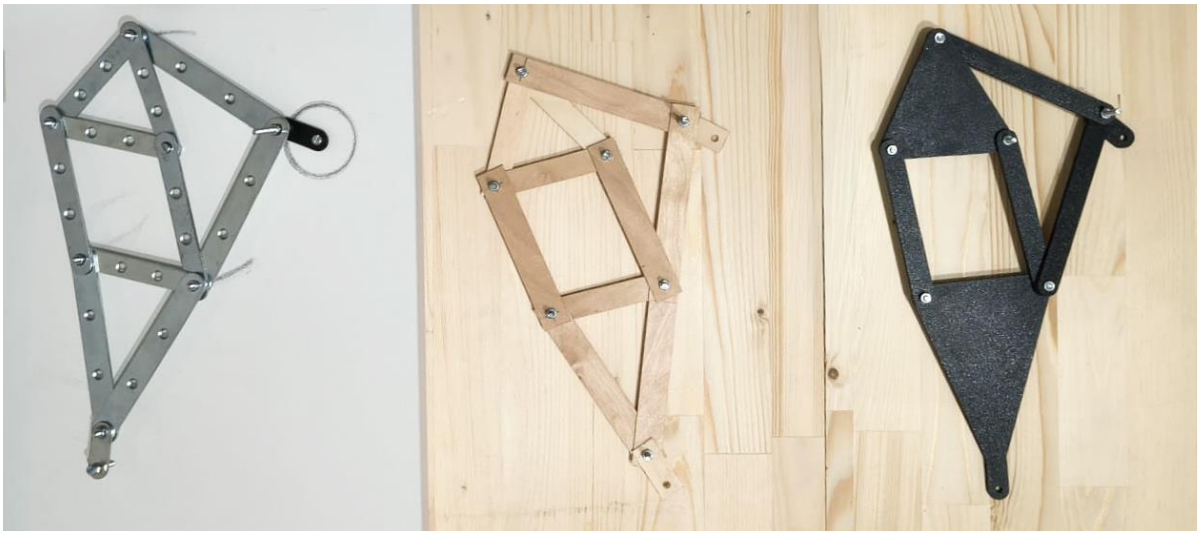

Fig. 3. The three models of the walking mechanism are made from different materials

Figure 3 presents three models of the walking mechanism. They are made from different materials.

4.1 Galvanized steel prototype

To make the galvanized steel model, we needed: steel plates of various standardized sizes that we assembled directly in the shop, thus testing the proportions and smooth movement of the mechanism.

Figure 4 illustrates testing dimensions of the elements and assembling the mechanism. Table 4 gives the dimensions of the galvanized steel prototype.

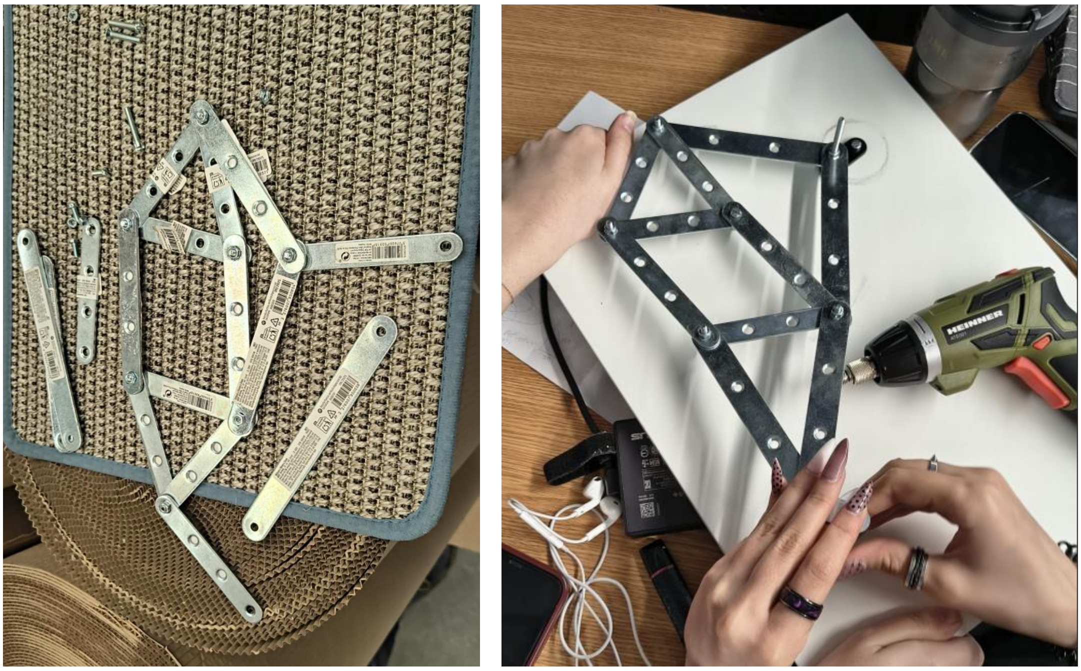

Fig. 4. Testing dimensions directly in the shop and assembling the mechanism

Table 4. Dimensions of the galvanized steel prototype

Dimension:	Length (mm)	Width (mm)	Thickness (mm)	Nr. pieces
1	140	18	2	2
2	120	18	2	2
3	100	15	2	4
4	40	15	2	2

4.2 Birch wood prototype

To build the wooden model, we used: a drill, a utility knife, a precision scalpel, and a metal ruler. Building the mechanism out of this material was more difficult than with the other two because we had to cut the wood ourselves to achieve the correct dimensions.

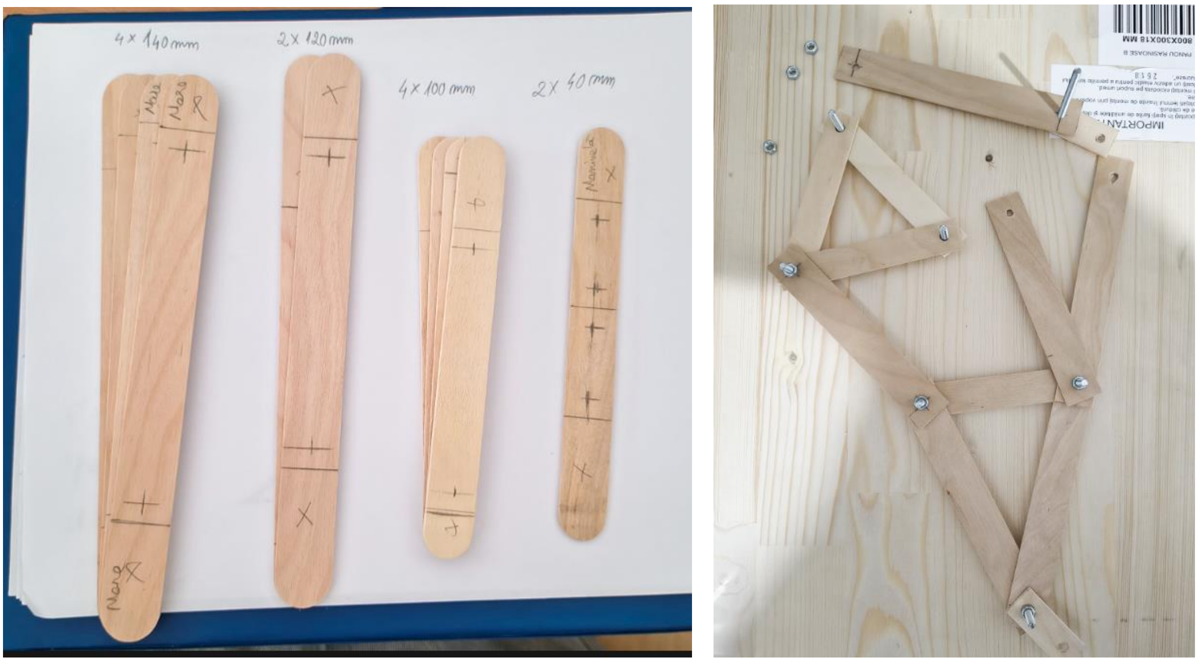

Fig. 5. Sorting the pieces before processing and assembling the mechanism

Table 5. Dimensions of the birch wood prototype

Dimension:	Length (mm)	Width (mm)	Thickness (mm)	Nr. pieces
1	140	20	2	2
2	120	20	2	2
3	100	17	2	4
4	40	17	2	2

4.3 PLA prototype

To create the PLA prototype, we needed: a 3D model designed in Fusion, as shown in Figure 6, and the 3D printer provided by the university. The assembly was completed more quickly because the triangles were printed as a single, self-supporting piece.

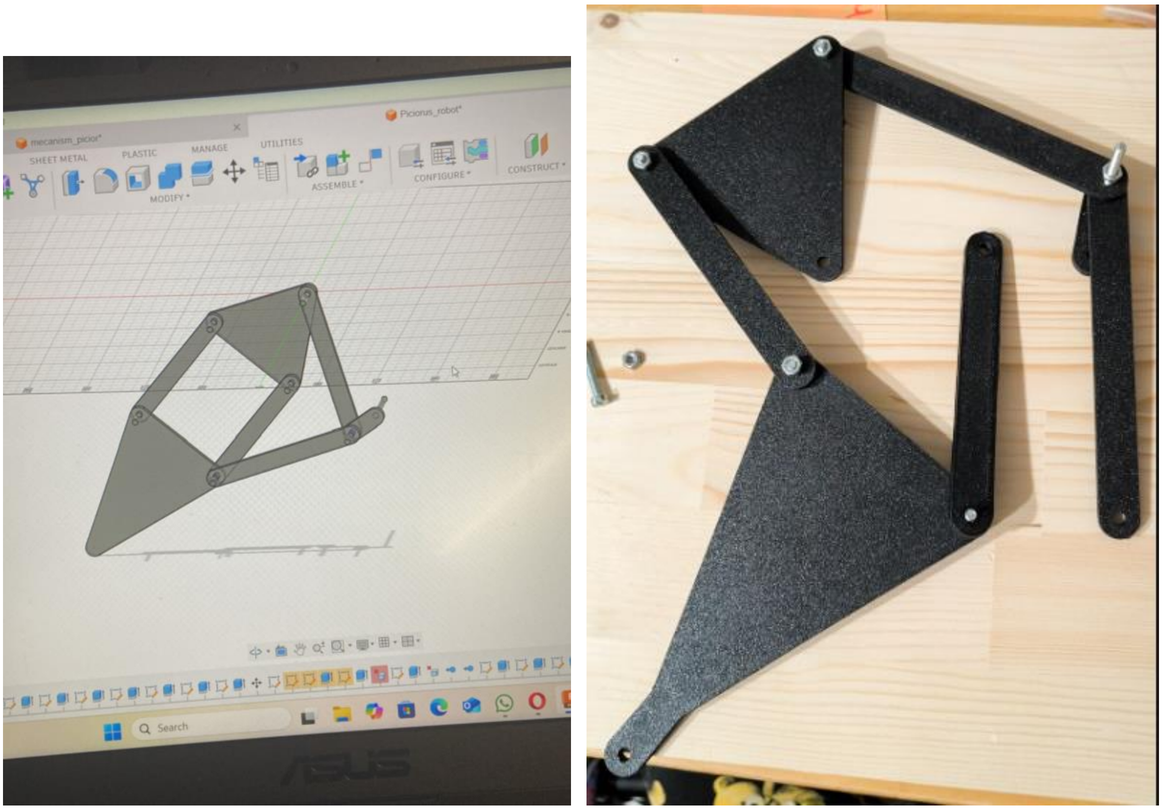

Fig. 6. Design in Fusion and assembly of the mechanism

Table 6 shows the dimensions of the PLA prototype.

Table 6. Dimensions of the PLA prototype

Dimension:	Length (mm)	Width (mm)	Thickness (mm)	Nr. pieces
1	140	15	5	2
2	120	15	5	2
3	100	15	5	4
4	40	15	5	2

5. Conclusions

In conclusion, this paper examined the behavior of the walking mechanism developed by Theo Jansen using various materials, thereby highlighting its importance and applicability in various adverse environments, with an emphasis on the importance of selecting the appropriate material. Analyzing the three mechanisms we ended up with the conclusion that each material value is determined by the context in which it’s used. Therefore, our research focuses on the importance of choosing a material for appropriate situations and its effectiveness across various applications. Furthermore, the paper contributes to the advancement and understanding of new perspectives on additive manufacturing precision, surface finishing, and material stiffness, all of which influence the overall efficiency of the mobile robot's movement.

6. Bibliography

[1]. Moldovan, Florina (2013), "Research regarding the analysis and synthesis of a bar mechanism for the construction of a walking mobile robot", Politehnica Publishing House, Timişoara, pages 27, 28, 31. Depozitul digital / The digital library BUPT: Browsing DSpace

[2]. Carlota, V., (2023), "All you need to know about PLA for3D Printing" PLA for 3D Printing: All You Need to Know - 3Dnatives

[3]. Niculae, Elisabeta, (2026), Course Mechanism, Moodle platform.

[4]. *Autodesk, Fusion 360, official site, https://www.autodesk.com/products/fusion-360/overview

[5]. *Autodesk, AutoCAD, official site, https://www.autodesk.com/products/autocad/overview

[6]. *Adobe, Lightroom, official site, https://lightroom.adobe.com/

[7]. *Adobe, Photoshop, official site, https://adobe-photoshop.en.softonic.com/

7. Notations

n = total number of elements;

m = number of mobile kinematic elements;

M = the degree of mobility of the mechanism;

i = number of lower joints;

s = number of upper joints;

R = rotation;

Z(0) = fixed element;

IAMG= initial active modular group;

* = apps used in the illustrations, photographs, and designs of the models presented in this scientific paper.

LIFT AND TILT DESK FROM A SCISSOR LIFT PLATFORM: SCISSOR LIFT MECHANISM WITH TILTING OF THE TOP SURFACE

OPREA Andrei-Lucian and Asst. Prof. Ph.D. Eng. **NICULAE Elisabeta**, Asst. Ph.D. Stud. Eng. **POPESCU Mircea-Daniel (Scientific Coordinators)**

Faculty of Industrial Engineering and Robotics, Specialization: Intelligent Industrial Technologies, Year of Study: II

e-mail: oprea.andrei.lucian@gmail.com

ABSTRACT: In this project, I started with the idea of a desk that would have the possibility of raising and also tilting its top through a single mechanism, intended for design engineers, architects and artists. Thanks to the guidance of my professors, I structurally analyzed a scissor lift that would be able to tilt its platform by schematizing a scissor lift in its normal operation mode and some actuators that would simultaneously execute the tilting action. Then, by designing it in Inventor, I created a representation model of the mechanism for a better understanding of the proposed idea.

KEYWORDS: mechanism, lifting, tilting, structure, designing

1.Introduction

As a project idea for this Mechanisms course, the proposed was a desk mechanism capable of adjusting not only its height, like standard commercially available desks, but also its angle of inclination relative to the ground. It features a tabletop large enough to accommodate an A0 sheet of paper, aiming to create a comfortable and ergonomic workspace for engineering designers, architects, artists, and others. This mechanism consists of a scissor lift that can rise up to 400 mm, modified to allow its platform to tilt, with a maximum inclination angle of 30°.

The Actuators represent the devices that transform energy (electrical, pneumatic, or hydraulic) into mechanical motion, which, by means of a controller, can execute actions such as pushing, pulling, etc., within a mechanism. In the mechanism of this project, they serve as its motors, being capable of performing both the lifting and the tilting actions, thus describing this mechanism as an automated system [1].

Given the complexity of the mechanism, the objectives set for this project were to conduct a structural analysis to visualize and understand the required movements, as well as a development of a design for the mechanism's conception.

For the structural analysis, the structural analysis methods studied in the Mechanisms course taught by Asst. Prof. Ph.D. Eng. Elisabeta NICULAE, and under the guidance of Asst. Ph.D. Stud. Eng. Mircea Daniel POPESCU were applied, after which the test for the execution model concept of the mechanisms was made using ice cream sticks and cylindrical pins.

For the actual design of the mechanism, Autodesk Inventor was used to create a 3D design of the mechanism.

2. The current status

In terms of the current status, both objectives have been fully achieved. Regarding the structural analysis, after several trials and errors, it ultimately arrived at a simple, clear, and correct result based on the structural analysis methodology. To achieve this, I had to split it into two separate structural analyses: one for the simple scissor lift and the other for the actuators that generate the tilting motion.

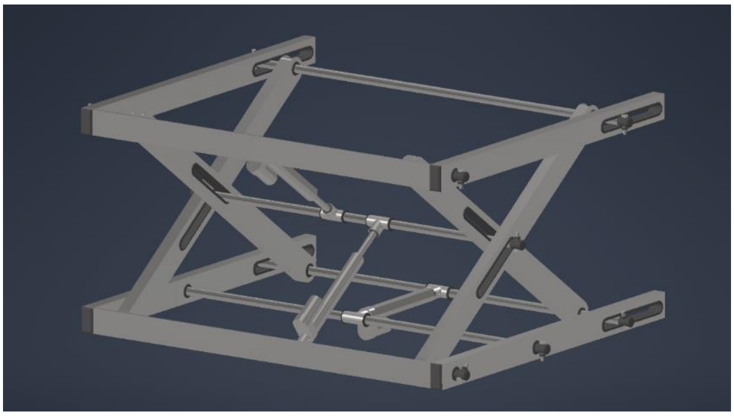

Fig. 1. The assembly design of the scissor lift mechanism model with platform tilting capability

As for the design phase, all the necessary parts for constructing the mechanism were successfully created, as well as a complete assembly model of the mechanism itself as it can be seen in Fig. 1, and some key measurements for the mechanism in Fig. 2.

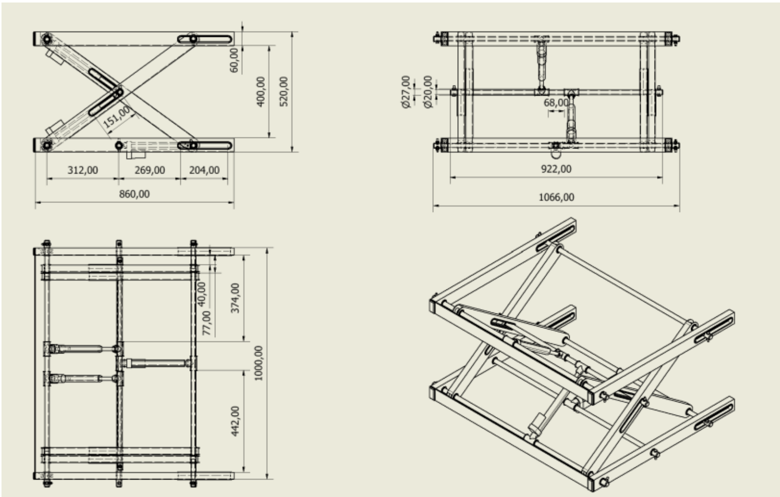

Fig. 2. Key assembly measurements for the mechanism in mm

3. Structural analysis

The first versions of the functional design provided an initial perspective in conceiving the structural analysis, which later helped in designing the final version of the mechanism. However, the completion of this structural analysis proved to be much more complicated due to the increased complexity of the mechanism brought on by the tilting action of the lift platform

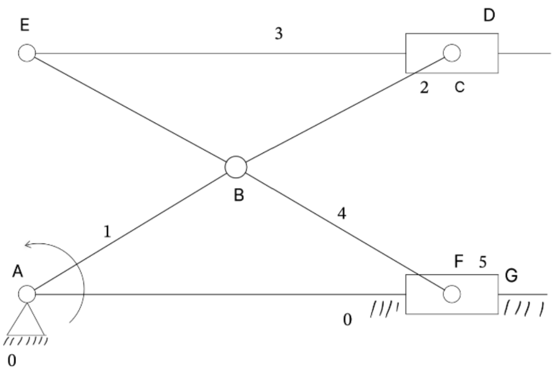

Fig. 3. The analysis for the standard scissor lift mechanism

The most common problems were when calculating the degree of mobility, because across several alternative approaches, the resulting number did not match the number of motors used in the entire mechanism [2].

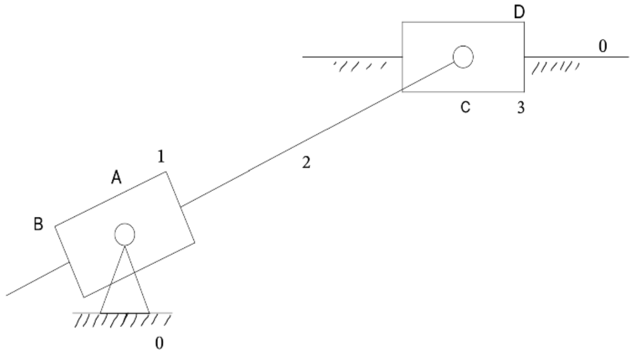

Fig. 4. The analysis for the actuators

After several attempts, a simpler approach to the situation was found, namely creating 2 structural analyses, one for the standard scissor lift mechanism part (Fig. 3), and another for the actuators that carried out the tilting of the platform (Fig. 4).

3.1. The first structural analysis

The analysis for the standard scissor lift mechanism is comprised of 5 elements and 7 inferior kinematic couples (of which 5 rotational and 2 translational). For the degree of mobility, we have used Eq. (1) and have resulted in a number of 1 motor kinematic pairs. After applying Eq. (2) a number of 2 closed loops resulted [3].

Mobility is calculated with the formula:

$$M = 3 \times m - 2 \times ci - cs \quad (1)$$

Number of closed loops is calculated with the formula:

$$N = ci + cs - m \quad (2)$$

In the equation above ci is the lower pairs, cs the number of higher pairs, N the number of closed loops, M the number of motor pairs and m the number of mobile elements.

Table 1 Kinematic elements (first analysis)

Element No.	Kinematic pairs	Type
0	A, G	Fixed link
1	A, B, C	Rocker
2	C, D	Slider
3	D, E	Coupler
4	E, B, F	Rocker
5	F, G	Slider

To create the structural diagram, the type of elements and the couples connected to them were analyzed in Table 1.

The structural diagram (Fig. 5) allowed the identification of two dyads (D1 - RRT (B, C, D), D2 - RRT (E, F, G)), which represent the key mechanisms of the standard scissor lift [4] [5].

Table 2 Dyads (first analysis)

Dyad Number	Type	Pairs
D1	RRT	B, C, D

D2	RRT	E, F, G

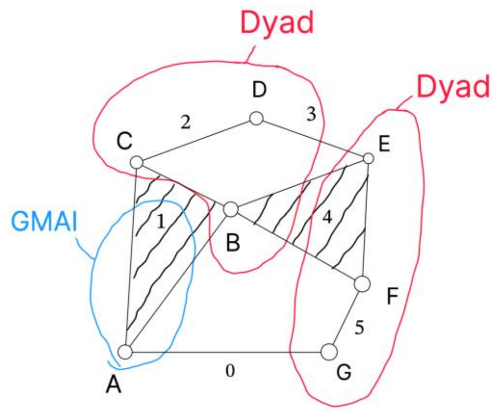

Fig. 5. Structural diagram (first analysis)

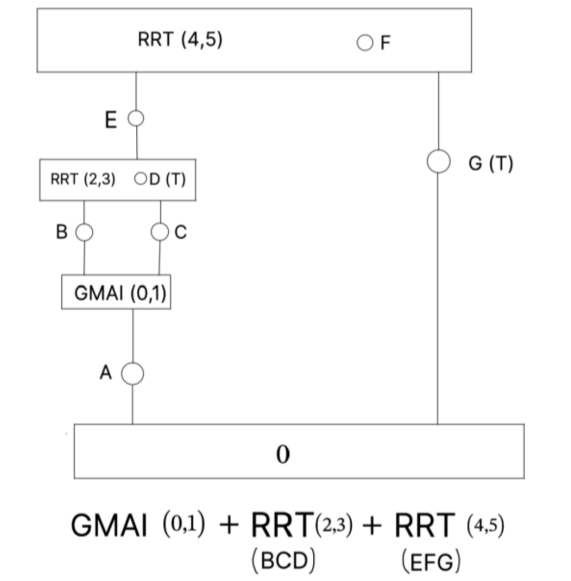

Fig. 6. The connection diagram and the connection relationship (first analysis)

The connection diagram and the connection relationship are presented in Fig. 6.

3.2. The second structural analysis

The analysis for the standard scissor lift mechanism is comprised of 3 elements and 4 inferior kinematic couples (of which 2 rotational and 2 translational). Just like the first analysis, we used the same equations from which resulted in one motor coupling for the degree of freedom, and one loop for the number of closed loops [3].

Table 3 Kinematic elements (second analysis)

Element No.	Kinematic couples	Type
0	A, D	Fixed link
1	A, B	Slider
2	B, C	Coupler
3	C, D	Slider

To create structural diagram, the type of elements and the couples connected to them were analyzed in Table 3.

The structural diagram (Fig. 7) allowed the identification of one dyad (D1 - TRT (B, C, D)), which represents the key mechanisms of the actuators [4] [5].

Table 4 Dyads (second analysis)

Dyad Number	Type	Pairs
D1	TRT	B, C, D

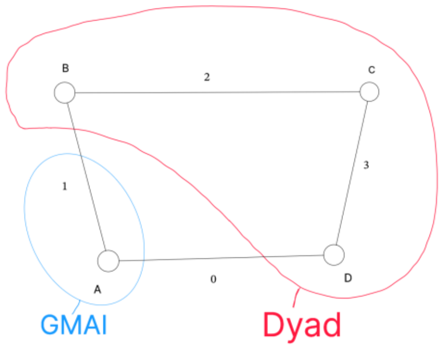

Fig. 7. Structural diagram (second analysis)

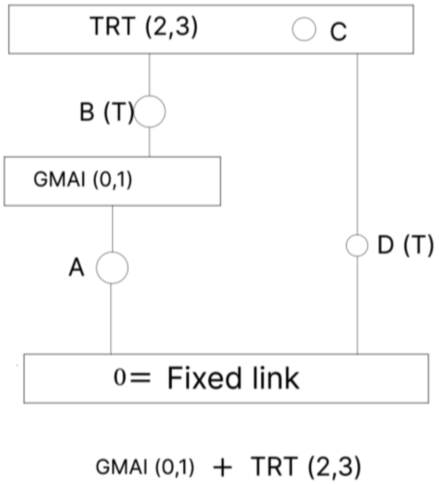

Fig. 8. The connection diagram and the connection relationship (second analysis)

The connection diagram and the connection relationship are presented in Fig. 8.

4. Testing the mechanism

As a testing method, a fairly simple approach was chosen, namely using larger popsicle sticks, some cylindrical sticks, and a utility knife (cutter) to cut out, in a precise manner, the holes and the translation slots, just like it can be seen in Fig. 9.

5. Conclusion

Therefore, in conclusion, this project started as an automated desk concept, which led to the design of this mechanism based on the scissor lift principle, with the additional capability of adjusting its tilt angle relative to the ground. Although the proposed objectives were successfully achieved, this does not mean there are no further aspects to study in order to achieve a highly improved product.


Fig. 9. The testing method chosen

Regarding the future objectives to be achieved, I have proposed the following:

- Studying the kinematic analysis of all joints present in the mechanism.
- Developing a physical mockup for more precise testing of the mechanism, either by creating a more complex stick-model or by 3D printing the parts at a much smaller scale compared to the designed model.
- Stress testing under the loads applied by the mechanism’s own weight.
- Improving the model and the mechanism wherever further modifications possibilities can be made.

- The possibility of presenting a video demonstration of the building and functional mechanism.

Special thanks once again to Asst. Prof. Ph.D. Eng. Elizabeta NICULAE and Asst. Ph.D. Stud. Eng. Mircea-Daniel POPESCU for their guidance and advise in approaching this complex mechanism, which is unique to existing ones, as well as providing the sources that help for applying the knowledge acquired throughout this year.

6. Bibliography

[1]. Grecu B., Adîr G., Bănică (Niculae) E., et al., *Mechanism and machine elements (Laboratory works)*, Bren Publishing House, Bucharest, ISBN 973-648-554-4

[2]. Grecu B., Adîr G., Bănică (Niculae) E., et al., *Mechanism. Laboratory works*, Bren P. H, Bucharest, ISBN 978-973-648-897-9

[3]. Grecu B, Adîr G., Bănică (Niculae) E., et al., *Structural modeling of mobile mechanical systems (Theory and applications)*, Printech P. H., Bucharest, ISBN 978-606-23-0912-1

[4]. Pelecudi, Chr., Comănescu, Adr., et al., *Kinematic analysis of mechanism – problems*, UPB 1985.

[5]. Comănescu, Adr., Grecu, B., Terme, D., (2001), *Mechanisms – structural and kinematic models*, Bren P. H., Bucharest, ISBN 973-8154-36-5

STUDY ON THE CONSTRUCTION AND OPERATION OF A HIGH-RATIO CYCLOIDAL SPEED REDUCER

PĂDUCEL Petre-Mădălin and Asst. Prof. Ph.D. Eng. **NICULAE Elisabeta**, Asst. Ph.D. Stud. Eng. **POPESCU Mircea-Daniel (Scientific Coordinators)**

Faculty: Industrial Engineering and Robotics, Specialization: Intelligent Industrial Technologies, Year of Study: II, e-mail: paducel.madalin123@gmail.com

ABSTRACT This paper investigates the construction and operational principles of a high-precision cycloidal reducer, a unique speed reducer that provides significant reduction ratios within a compact and robust design. The research focuses on the specific geometry of the cycloidal disk and its interaction with housing rollers, achieving a reduction ratio of 18:1 in a single stage. Compared to conventional gear drives, this system offers virtually zero-backlash, higher load capacity, and efficiencies up to 90% [2]. By analyzing the mechanical design and kinematic mapping, the study highlights advantages such as high torque density and exceptional shock resistance. The results provide a technical framework for developing compact reducers that maintain precision and performance, making them ideal for high-accuracy applications in robotics, machine tools, and modern automated systems.

KEYWORDS: cycloidal drive, 18:1 reduction ratio, kinematic analysis, zero-backlash, robotic joints.

1. Introduction

The primary objective of this paper is the rigorous analysis and evaluation of an optimized cycloidal speed reducer, specifically designed for an 18:1 reduction ratio. The selection of this transmission ratio is not arbitrary; rather, it is justified by the technical necessity to balance the kinematic precision of motion with the overall mechanical efficiency of the system, while simultaneously minimizing friction losses. Such a ratio offers the advantage of an extremely compact construction; furthermore, it represents a configuration whose technological characteristics would be impossible to achieve through a single-stage reduction equipped with conventional spur gears of equivalent geometric dimensions.

To counteract the centrifugal forces generated by the eccentric motion and to dynamically balance the vibrations within the system, the proposed configuration integrates two cycloidal discs mounted in phase opposition. By utilizing this unique geometric profile, a uniform load distribution is ensured across multiple lobes simultaneously, thereby eliminating the disadvantages of massive sizing and large angular backlash typical of conventional gearings.

2. The current state

Cycloidal speed reducers represent the optimal solution for applications requiring high precision and a compact footprint, overcoming the limitations of planetary transmissions by eliminating backlash and providing enhanced shock resistance. Currently, research focuses on optimizing the lobe profile through numerical methods and utilizing advanced materials to increase efficiency beyond 90%. In robotics and the CNC industry, the present trend targets miniaturization and the increase of torsional stiffness. This study is highly relevant for rapid positioning systems, ensuring a balance between response speed and load capacity, while simultaneously serving as a starting point for optimizing the contact between the cycloidal disc and the rollers.

3. Cycloidal speed reducer

The operation of the cycloidal speed reducer is determined by the disc geometry and its interaction with the housing elements. The transmission ratio **i** is defined as a function of the number of lobes on the cycloidal disc and the number of pins/rollers in the housing   through the following relationship:

$$i = \frac{z_1}{z_2 - z_1} \qquad (1)$$

For the precise generation of the cycloidal disc profile in the xOy plane, parametric equations defining the position of each point on the disc periphery were utilized. The constructive parameters used have: N (number of rollers), Rr (roller radius), R (roller pitch circle diameter - PCD), and E (eccentricity).

The coordinates of the points on the profile are determined by the following relationships:

(2)

(3)

where **t** represents the angular parameter for generating the curve, within the interval ***[0, 2\π]***. These equations formed the basis for the geometric modeling of the speed reducer with an 18:1 transmission ratio, ensuring smooth motion and optimal contact between the disc lobes and the housing rollers.

4. Geometric parameters

The geometric parameters resulting from the design of the cycloidal speed reducer are summarized in the table below. These parameters were utilized to generate the disc profile within the CAD environment.

Table 1 Geometric parameters

Parameter	Symbol	Value	Unit of measurement
Number of roles	N	19	-
Roller radius	$\boldsymbol{R_r}$	13	mm
Pitch circle radius	R	70	mm
Eccentricity	E	2	mm
Transmission ratio	i	18:1	-

5. Components and assembly method

The visualization of the components and the assembly method is essential for understanding the operation of the speed reducer. Figure 1 presents the cross-sectional view of the assembly, highlighting the raceway and the manner in which power is transmitted from the input shaft to the output shaft through the cycloidal discs.

Figure 2 presents the detailed geometry of the cycloidal profile generated based on the parametric equations introduced previously. The drive pins and the housing, inside of which the bearings supporting the contact pins are mounted, can be clearly observed.

6. Conclusions

The present paper analyzed in detail the design process of the cycloidal speed reducer, aiming to transpose the theorized mathematical model into a demonstrative physical form.

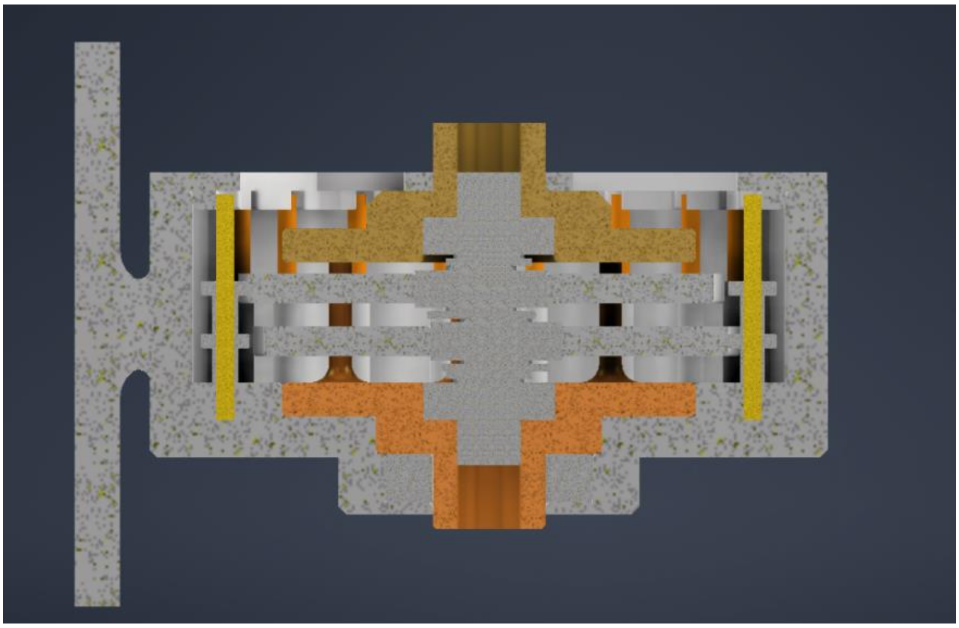

Fig. 1. Cross-sectional view of the cycloidal speed reducer – visualization of the power flow

The utilization of parametric equations to define the lobed profile enabled a rigorous configuration of the gearing within the CAD environment, ensuring precise control over clearances and geometric interfaces between components from the digital design phase.

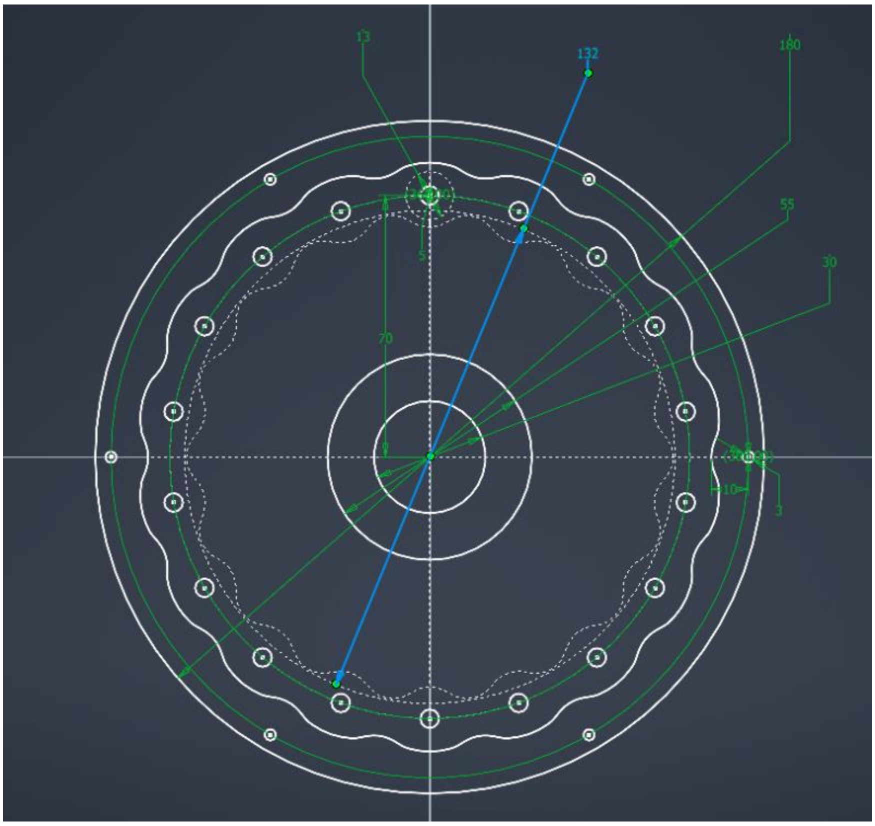

Fig. 2. Geometric design of the cycloidal disc and the arrangement of the housing pins

The realization of the prototype through 3D printing served as an essential validation stage for the design, confirming that the calculated geometry ensures a precise assembly and a coherent kinematic operation of the entire assembly.

This efficient rapid prototyping method facilitated the experimental proof-of-concept without resorting to the considerable technological and financial resources of a complex industrial production. Furthermore, the obtained physical model allowed for direct visual analysis of the kinematic behavior between the pins and discs during rotation.

Future development perspectives aim to optimize the system structurally by replacing the current polymeric material, PLA-CF, with one featuring superior mechanical properties, such as hardened metallic alloys. This technological evolution would enable the transition from a purely didactic and study model to a fully functional prototype, capable of undergoing rigorous load, wear, and efficiency testing for its ultimate integration into real-world technical applications within the fields of robotics or automation.

The text is formatted with single line spacing and justified paragraphs. The bibliography is cited within the text using numbers in square brackets, for example [1] or [2], representing the main sources of inspiration utilized for the completion of this project. The documentation relied on practical CAD design and 3D prototyping guides, which served as a reference point for the construction of the presented model.

7. Bibliography

[1]. Younis, O. (2020), "Building a Cycloidal Drive with SOLIDWORKS", Online Technical Article/Tutorial.

[2]. Dejan (2022), "What is Cycloidal Driver? Designing, 3D Printing and Testing", How to Mechatronics.

8. Notations

The following symbols are utilized in the present paper:

- i = transmission ratio [-];
- = number of lobes on the cycloidal disc [-];
- = number of rollers (pins) in the housing [-];
- N = total number of rollers (equivalent to)[-];
- R = roller pitch circle radius – PCR [mm];
- = roller (pin) radius [mm];
- E = eccentricity of the input shaft [mm];
- x, y = Cartesian coordinates of the cycloidal profile [mm];
- t = angular parameter for curve generation [rad].

EMERGENCY STOP SIGNAL

AVRĂMESCU Elena-Adelina, **CHICIOREANU Ana-Lucia**, IOVA Adriana-Denisa
and Asst. Prof. Ph.D. Eng. **NICULAE Elisabeta**, Asst. Ph.D. Stud. Eng. **POPESCU Mircea-Daniel (Scientific Coordinators)**

Faculty: Industrial Engineering and Robotics; Specialization: Intelligent Industrial Technologies; Academic Year: II; email: ana.chicioreanu@stud.fiir.upb.ro

ABSTRACT: In today's world, road safety is becoming increasingly important, and technology plays a key role in preventing accidents and reducing traffic risks. In this context, the project proposes the development of an emergency stop signal system, designed as an autonomous device that can operate independently of the vehicle's electronic system. The system aims to monitor real-time vehicle motion parameters and generate alerts in critical situations, thereby contributing to improved operational safety and a reduced risk of accidents

KEYWORDS: road safety, sensors, real-time monitoring

1. Introduction

In recent decades, the development of automotive technology has significantly contributed to increasing the level of road safety and to the emergence of intelligent systems capable of preventing accidents or reducing their effects. Modern driver warning systems are increasingly used in motor vehicles, serving to monitor vehicle behavior and react in critical situations.

One such system is the emergency stop signal, used to warn traffic participants in the event of sudden braking or dangerous maneuvers. This type of system helps reduce the risk of collision and improve traffic safety, being factory-integrated into many modern vehicles.

The main purpose of this project is to create an autonomous emergency stop signal system that functions independently of the car's electronics and can be mounted on various vehicles without additional modifications. The system utilizes a GPS sensor to determine speed, and an accelerometer & gyro sensor to monitor the movements and acceleration variations of the vehicle.

The technical requirements are established by Regulation No. 48 of the United Nations Economic Commission for Europe (UNECE). This defines the conditions under which the brake lights are allowed to flash:

- Speed: The system activates only at speeds greater than 50 km/h.
- Deceleration: Flashing is triggered by sudden braking, typically when deceleration exceeds 6 m/s^2 or when the ABS system is fully activated.
- Frequency: The brake lights must flash at a frequency of 4.0 \pm 1.0 Hz (approximately 4 times per second).

2. Current state of the art

Traffic congestion and transit inefficiencies have escalated into some of the most widespread and complex socioeconomic problems in the modern world. Exponential population growth, coupled with rapid urbanization across global metropolitan areas, has systematically led to an unprecedented increase in the absolute volume of vehicles on public roadways. Consequently, this density has caused a severe surge in traffic issues, ranging from prolonged gridlock to elevated rates of rear-end collisions.

Given this critical reality, modern traffic management techniques and advanced driver assistance systems (ADAS) are increasingly being researched and deployed to mitigate these systemic dangers. A highly relevant and profoundly effective example of this technological shift is the Emergency Stop Signal (ESS) system. The ESS is an active safety technology explicitly engineered to instantly communicate imminent danger to trailing drivers positioned behind the decelerating vehicle. Unlike traditional, classic brake lighting architectures, which merely remain constantly and statically illuminated during any standard braking event, the ESS system dynamically utilizes high-intensity, rapidly flashing light signals the precise moment a vehicle undergoes sudden, violent braking or detects a severe deceleration threshold. This distinct operational shift transforms passive illumination into an active visual command, immediately signaling an emergency situation to the surrounding traffic ecosystem.

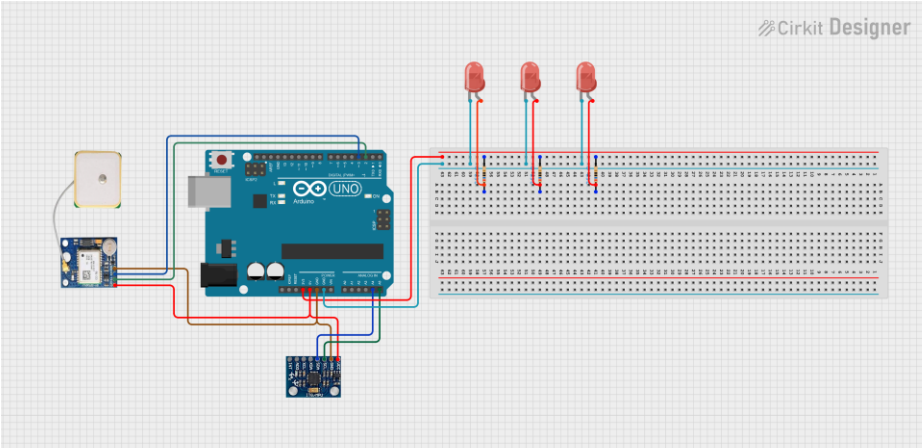

Fig. 1. The emergency stop signal device

Consequently, this system becomes exceptionally useful and lifesaving in low-visibility environmental conditions (such as dense fog, heavy rainfall, or night-time driving), during high-density stop-and-go heavy traffic, or when operating at high speeds on major highways where baseline braking distances are already considerably longer. More than a simple, isolated warning mechanism, the ESS represents a quintessential example of how the integration of electronics, embedded sensors, and automation transforms the modern automobile from a rigid mechanical machine into a highly responsive, active safety system. Furthermore, in advanced vehicular platforms, the ESS does not operate in a vacuum; it often seamlessly collaborates with other modern safety technologies, such as autonomous emergency braking (AEB) systems and electronic stability control (ESC), effectively forming an intelligent, interconnected network designed to sense, evaluate, and prevent accidents before they physically occur.

Therefore, the implementation of the Emergency Stop Signal system not only contributes directly to increasing immediate road safety and reducing collision rates, but also fundamentally reflects the future macro-direction of the global automotive industry. It serves as a foundational building block for the next generation of intelligent transport systems (ITS): a future populated by smart vehicles that are fully capable of autonomously anticipating dangers, communicating hazard states efficiently to their environment, and actively protecting human lives through advanced embedded technology.

3. The Emergency Stop Signal

The Emergency Stop Signal (ESS) is an electronic device that detects sudden brake situations or dangerous movements and automatically activates a visual warning signal. This type of system helps reduce the risk of collision and improve traffic safety, being factory-integrated into many modern vehicles.

3.1 Architecture of ESS

The physical architecture of this device contains several interconnected modules optimized for real-time processing (Fig. 1):

- Arduino UNO: The microcontroller acting as the central processing unit (CPU) of the system, handling I/O operations and executing the threshold logic.
- GPS Module (Neo-6M or equivalent): Dedicated to extracting real-time NMEA sentences to calculate the absolute ground speed of the vehicle via satellite telemetry.
- Accelerometer & Gyroscope Sensor (MPU6050): A 6-axis motion tracking device used for precise detection of the braking force (X-axis deceleration) and vehicle dynamics (Y and Z axes to filter out gravitational distortions caused by sloped roads).
- Red LEDs: High-brightness light-emitting diodes acting as the physical visual warning array.
- Resistors (220\ \Omega): Positioned inline to limit current and protect each individual

LED from burning out.
- Breadboard & Jump Wires: Used for quick, low-resistance, and stable physical interconnection of the prototyping circuit.

4. Technical objectives

The technical objectives of this device are the following:
- Designing and implementing an autonomous system: The main objective of the project is to develop a device capable of operating independently of the vehicle's electronic systems, without modifying the car's original wiring installation or voiding factory warranties. This universal plug-and-play design ensures that the safety module can be seamlessly transferred between different vehicular platforms regardless of their make or manufacturing year.
- Real-time monitoring of vehicle travel parameters: The system must accurately utilize a GPS sensor to determine absolute speed and an accelerometer & gyro sensor to detect dynamic accelerations and sudden braking forces.
- Data processing and analysis using an Arduino board: The data collected by the sensors must be parsed instantly, filtered mathematically, and compared against preset algorithmic values to identify dangerous anomalies. By maintaining a highly optimized loop cycle, the microcontroller eliminates computational lag to guarantee that threat detection happens concurrently with the physical braking event.
- Automatic activation of the visual warning signal: Upon meeting specific conditional thresholds (Speed > 50 km/h and Deceleration > 6 m/s^2), the system must trigger a precise pulsing strobe sequence to alert following drivers.

5. Operation of ESS

Regarding the operation of the device, the execution flow is strictly split into three continuous phases: data collection, central processing and output reaction.

5.1 Data collection

Every second, the GPS measures the car's speed (in km/h), while the accelerometer measures how abruptly the car is slowing down (G-force). The gyroscope checks whether the road is straight or sloped to correct data errors.

5.2 Processing (Arduino)

The Arduino Uno board receives this data and checks if two conditions are met simultaneously:
- The car's speed is greater than 50 km/h (verified by GPS).
- The braking is violent, indicating an emergency (deceleration greater than 6 m/s^2, verified by the accelerometer).

5.3 Reaction (Output):

If both conditions are true, the Arduino board sends current through the 5 resistors of 220 Ω (which serve to protect the circuit) and turns on the 5 red LEDs in a strobe pattern (flashing rapidly, 5 times/second) to instantly alert the driver behind.

6. Advantages of the system

The proposed prototype yields several distinct operational benefits over integrated factory solutions:
- Universal Independence: Because it relies entirely on its own sensor array, it does not require access to the vehicle's Controller Area Network (CAN-bus) system.
- Zero-Invasive Installation: It can be powered via a simple 12V auxiliary outlet (cigarette lighter) or an internal battery pack, making it plug-and-play for older vehicle models lacking advanced driver-assistance systems (ADAS).
- Cost Efficiency: Built from readily available off-the-shelf micro-electronics, making life-saving active safety components affordable for everyday consumers.

- High Sensitivity and Adaptability: Threshold parameters (50 km/h and 6 m/s^2) can be calibrated via software updates to match unique vehicle profiles, such as commercial trucks or motorcycles.

7. Conclusions

The implementation of the emergency stop signal system represents an essential advancement in increasing road safety, offering an active solution for collision prevention by reducing drivers' reaction times.

The system leverages the human brain's capacity to process flashing light signals much faster than static ones, transforming sudden braking into an immediate visual warning for other traffic participants.

The project stands out through the development of a completely autonomous device capable of operating independently of the vehicle's complex electronic systems, which facilitates its installation on a wide range of motor vehicles without requiring structural modifications. Future iterations of this prototype could integrate Bluetooth low energy (BLE) modules to send local wireless warnings directly to adjacent cars, moving toward a Vehicle-to-Vehicle (V2V) safety ecosystem.

8. Bibliography

[1]. What Is Emergency Stop Signal in a Car? | Stop Signal Basics

[2]. Emergency Stop 101 - Electrical Engineering Center

COMPARATIVE STUDY ON THE KINEMATICS OF QUICK-RETURN MECHANISMS: THE INFLUENCE OF GEOMETRIC PARAMETERS AND GEAR TRANSMISSION

VASILE Andreea-Patricia and Asst. Prof. Ph.D. Eng. **NICULAE Elisabeta**, Asst. Ph.D. Stud. Eng. **POPESCU Mircea-Daniel (Scientific Coordinators)**

Faculty of Industrial Engineering and Robotics, Specialization of Economic Engineering, Year 2, e-mail: patriciavasile24@gmail.com

ABSTRACT: This study presents a comprehensive three-dimensional model and motion analysis of a quick-return mechanism incorporating an oscillating lever. The system was virtually assembled and simulated in Autodesk Fusion 360, enabling extraction of positional and velocity data for the cutting ram. Mathematical and graphical validation of the quick-return phenomenon confirms the temporal efficiency of the asymmetric stroke in industrial machining applications. The extracted data distinctly differentiates between the slow forward working stroke and the rapid return stroke.

Keywords: quick return mechanism, kinematic analysis, oscillating slide, 3D simulation, machine tools.

1. Introduction

The manufacturing industry has always been the main engine of technological and economic development. Over time, optimizing manufacturing processes has been a constant challenge for engineers, with the central goal of maximizing productivity and minimizing downtime [1]. Within machine tools, the mechanisms for transmitting and transforming motion are of particular importance, as they must ensure both the parameters necessary for the technological cutting process and maximum time efficiency.

The work cycle in machining operations with rectilinear main reciprocating motion, like shaping or slotting, is split into two separate phases: the idle (return) stroke, when the tool returns to its starting position, and the active (working) stroke, when the tool removes material and needs regulated speeds to protect the cutter [2]. Since the return stroke does not produce useful mechanical work, it represents dead time from a production standpoint. Therefore, reducing the duration of this stroke is essential to increasing the machine's overall efficiency.

This technical problem is successfully solved by using quick return mechanisms. The main subject of this paper is the study, 3D modeling, and kinematic analysis of a quick return mechanism with an oscillating slide, a classic but extremely efficient kinematic system used to transform continuous rotational motion into asymmetric alternating translational motion. [3].

The main purpose of this work is to demonstrate the operating principle of the mechanism through modern means of computer-aided design (CAD) and digital simulation. [4]. The specific objectives pursued during the development of the project included:

- Design and 3D modeling of mechanism components (gear transmission, crank, swing arm, connecting rod and linear slide) using Autodesk Fusion 360 software.
- Virtual assembly and correct definition of kinematic couplings (rotational, translational joints and sliding contacts) to ensure fluid and realistic movement.
- Performing a detailed kinematic analysis on the final execution element (the machine ram), by extracting positional data and deriving them to obtain working speeds.
- Mathematical and graphical validation of the “fast return” phenomenon by demonstrating a clear asymmetry between the time allocated to the forward and return strokes.

To achieve these objectives, the paper was logically structured. The project phases began with a theoretical study of the kinematics of the swing-arm mechanism, continued with the practical stages of 3D modeling of the subassemblies, and concluded with the extraction and processing of motion data. The position and velocity graphs obtained from the simulation confirm the theoretical hypotheses and attest to the viability of the model designed for integration into a modern machine tool.

2. Current Status

Quick-return mechanisms have been a central focus of interest in mechanical engineering since the 19th century, introduced by Joseph Whitworth in the 1800s to optimize machining processes requiring reciprocating rectilinear motion [5]. This innovation significantly improved the efficiency of classic machine tools, such as planing and mortising machines, by allowing the cutting tool to quickly return to its original position after completing the active cutting stroke, thereby considerably reducing the machine's downtime. [6].

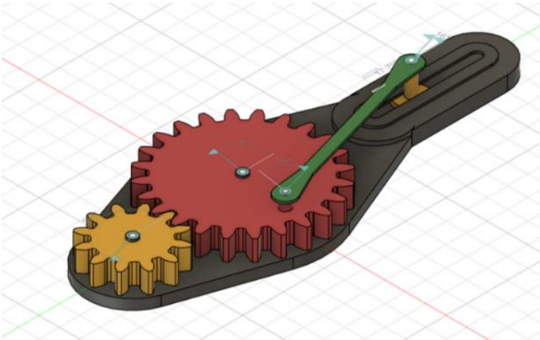

Fig. 1. 3D model of the slider-crank mechanism

Today, although manufacturing processes have evolved through the integration of CNC technologies and digital drive systems, the quick-return mechanism with an oscillating slide continues to play an essential role in the industry. This mechanism is used in both traditional machines and automatic cutting systems, mechanical presses, and packaging equipment, where productivity depends on reducing non-productive operating time [2]. Current research aims to integrate adaptive control algorithms to adjust the return rate depending on the characteristics of the processed material and tool wear. [7].

The current state of design for these systems reflects a transition from traditional analytical and graphical methods to the use of advanced CAD/CAE (Computer-Aided Design/Engineering) software solutions. Platforms such as Autodesk Fusion 360 allow engineers to both perform precise three-dimensional geometric modeling and perform complex kinematic and dynamic analyses in a virtual environment [8]. This iterative approach facilitates the optimization of kinematic parameters, such as the rapid return coefficient, and the refinement of the theoretical model, eliminating the need for expensive physical prototypes in the initial testing phases [8].

3. Design and 3D modeling of the studied mechanisms

To conduct this comparative study, the Autodesk Fusion 360 CAD software was used, which offers precise parametric modeling and rigorous definition of kinematic pairs through its “Joints” feature. The models were developed to highlight the transition from symmetric to asymmetric kinematics, a characteristic of systems with rapid return.

3.1. Slider-crank mechanism

The first model made serves as a reference (control) and represents a standard slider-crank mechanism [9]. A distinctive feature of this model is that the sliding axis is aligned with the crank’s center of rotation. This geometric configuration ensures a perfectly symmetrical stroke, in which the angle allocated to the leading movement equals that of the turning movement (180° each), resulting in a quick return coefficient K=1.

3.2. Quick-return mechanism with oscillating slotted arm

The second version introduces the swing arm as an intermediate element. In this model, the motor wheel drives a pin that slides along the channel of the green arm, causing it to undergo an asymmetric pendulum motion. This model was used to analyze the angular variation of the arm and how the distance between the pivots influences the rotation speed.

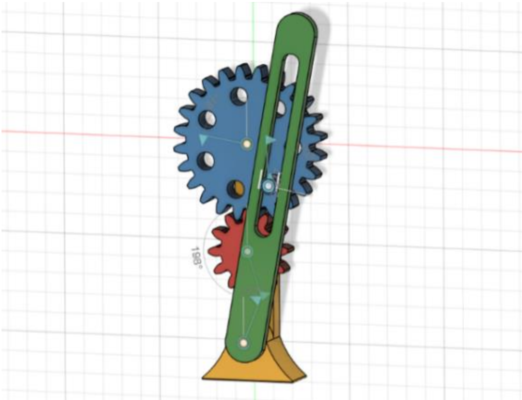

Fig. 2. 3D model of the quick-return mechanism with oscillating slotted arm

3.3. Linear ram shaping quick-return mechanism

This is a complete model of an industrial cutting machine. The oscillating arm is connected by a slide to a sliding block (ram), which performs the main horizontal translational motion. This configuration converts the arm's oscillation into a reciprocating linear motion, optimized to maintain constant speed and enable rapid tool retraction.

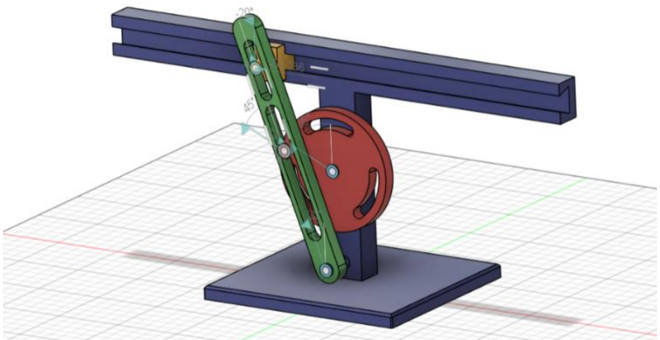

Fig. 3. 3D model inspired by the linear ram shaping quick-return mechanism

3.4. Gear-driven quick-return mechanism with oscillating lever

The last model studied integrates a gear transmission (pinion and driven wheel), adding an additional layer of complexity by introducing the transmission ratio into the kinematic analysis. This variant is the closest to the technical reality of heavy machine tools, where the cutting force requires a reduction in the electric motor's speed while simultaneously applying the rapid return principle.

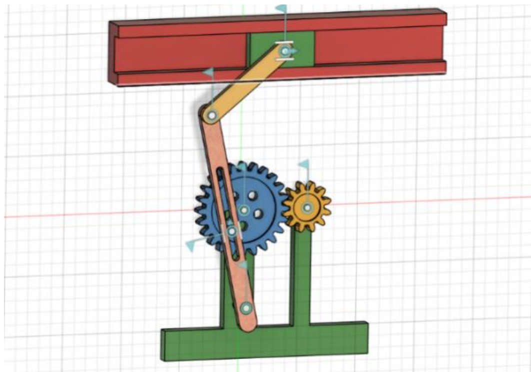

Fig. 4. 3D model of a gear-driven quick-return mechanism with oscillating lever

4. Kinematics Analysis and Experimental Results

This chapter presents the methodology for the mathematical calculation of kinematic parameters, followed by the results obtained from simulations for each of the four mechanisms studied.

4.1. Methodology and Calculation Formulas

To validate the behavior of the mechanisms, two fundamental parameters were used:

A. Quick return coefficient (K) represents the ratio between the time allocated to the active stroke and that of the empty stroke. It is calculated by relating the crank rotation angle for the two phases [1], [4]:

$$K = \frac{\alpha}{\beta} \quad (1)$$

B. Instantaneous linear velocity (v): Since the data extracted from Fusion 360 is discrete (position relative to time), the velocity was calculated in Excel using the finite difference method [2]:

$$v_i = \frac{s_{i+1} - s_i}{t_{i+1} - t_i} [mm/s] \quad (2)$$

K = quick return coefficient [-]; α = working stroke angle [°]; β= return stroke angle [°]; v= linear speed [mm/s]; s = displacement [mm]; t = time [s]

4.2. Results: Slider-crank mechanism

This mechanism serves as a reference for verifying the symmetry of the motion.

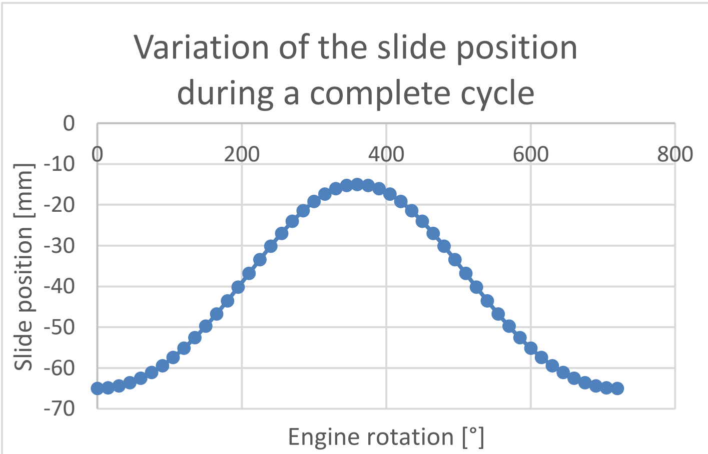

Fig. 5. Variation of the slide position during a complete cycle

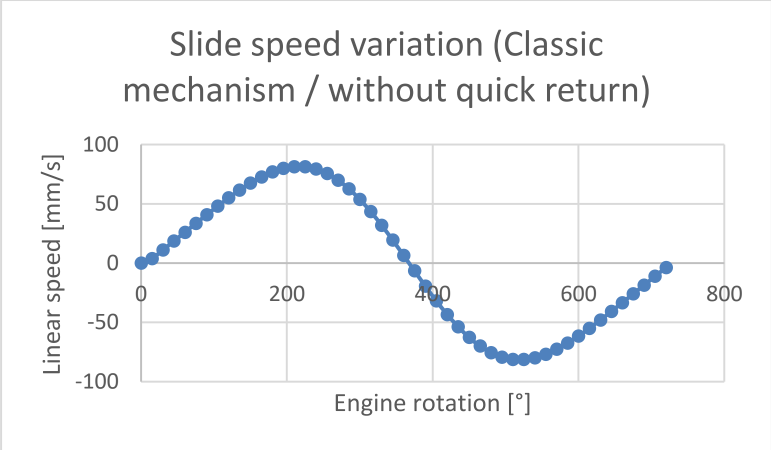

Fig. 6. Slide speed variation – classic mechanism

The speed curve is a perfect sinusoid, indicating an equal distribution of time between the two runs. In conclusion, there is no quick return effect.

$$\alpha = 180° \; ; \; \beta=180° \tag{3}$$

$$K=180/180=1 \tag{4}$$

4.3. Results: Quick-return mechanism with oscillating slotted arm

This model introduces a swing arm to generate movement asymmetry [3], [5].

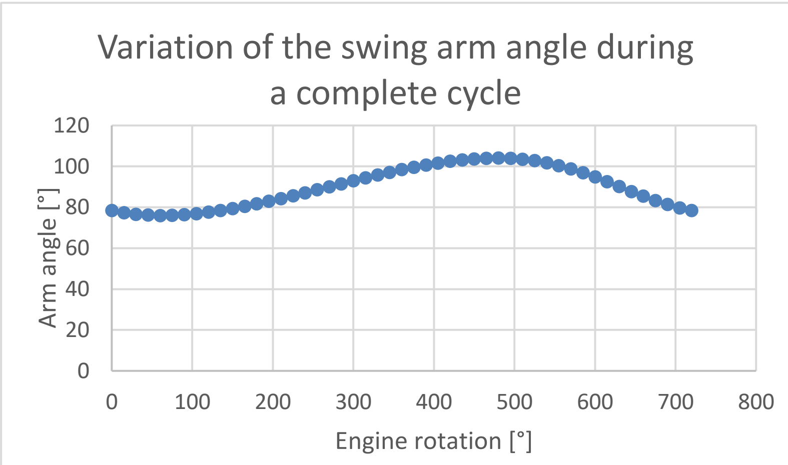

Fig. 7. Variation of the swing arm angle during a complete cycle

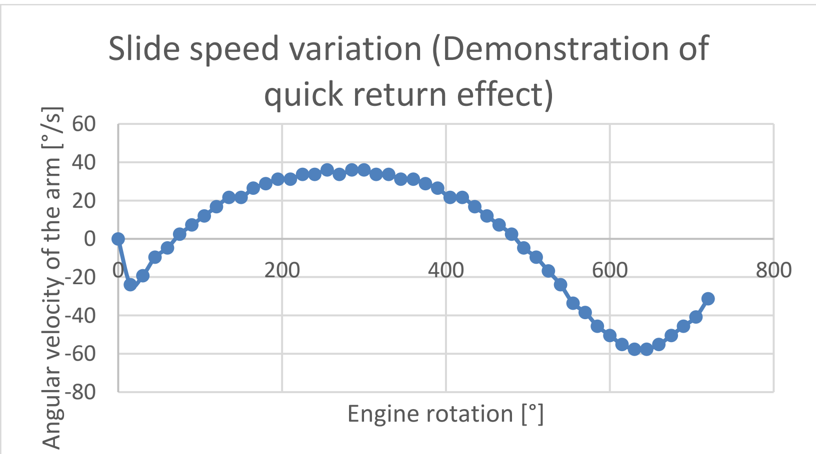

Fig. 8. Slide speed variation

A much steeper slope is observed in the return area, indicating a greater negative speed than positive speed. The results demonstrate the mechanism's clear efficiency, with the return stroke 43% faster than the working stroke.

$$\alpha = 292° - 80° = 212° \text{ (working stroke angle)} \quad (5)$$

$$\beta = 360° - 212° = 148° \text{ (return stroke angle)} \quad (6)$$

$$K = \frac{212}{148} = 1.43 \quad (7)$$

4.4. Results: Linear ram shaping quick-return mechanism

This is the model that most accurately reproduces the actual shaping machine presented earlier.

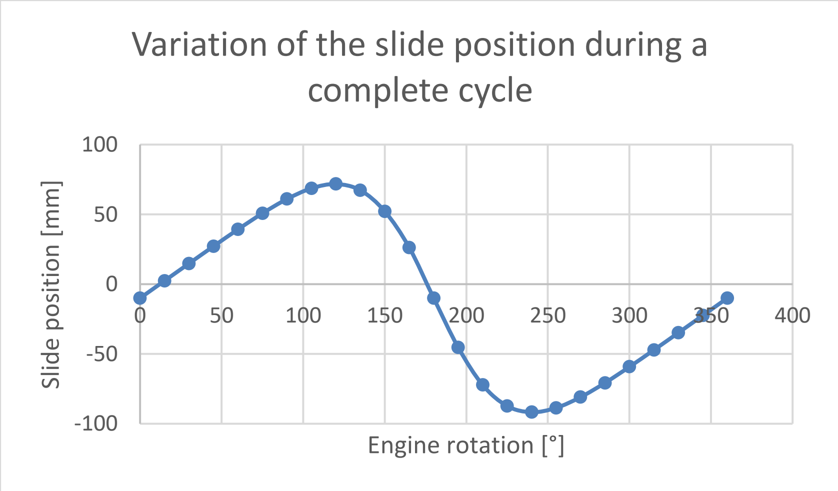

Fig. 9. Variation of the slide position arm during a complete cycle

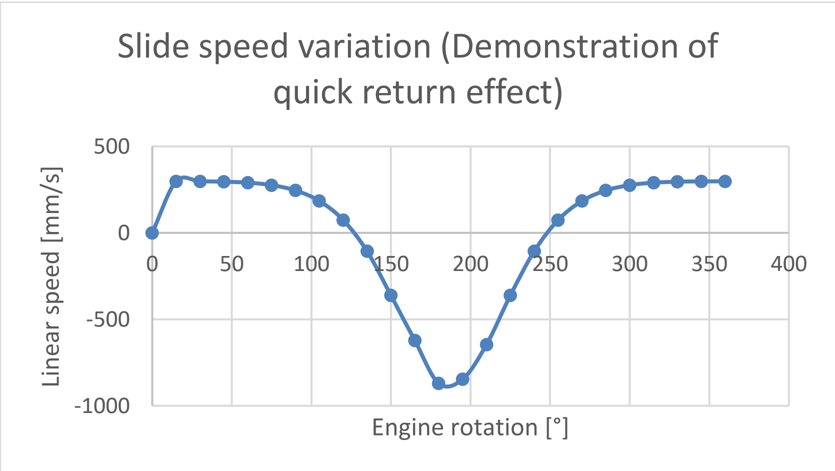

Fig. 10. Slide speed variation

$$\alpha = 360° - 120° = 240° \text{ (working stroke angle)} \quad (8)$$

$$\beta = 245° - 125° = 120° \text{ (return stroke angle)} \quad (9)$$

$$K = \frac{240}{120} = 2 \quad (10)$$

This mechanism demonstrates excellent performance, with a return coefficient of K=2. This means that the cutting time is exactly twice the return idle time, and the maximum retraction speed is nearly 3 times the working speed, representing the ideal kinematic profile for a shaping machine.

4.5. Results: Gear-driven quick-return mechanism with oscillating lever

This model studies the influence of the transmission ratio on the final kinematics. Since the cycle is completed at 720° (due to the pinion), the curve is more "stretched," visually indicating a transmission ratio of 2:1.

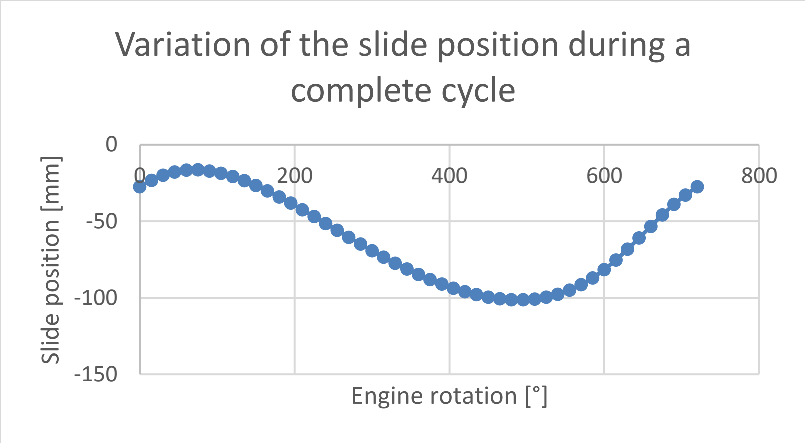

Fig. 11. Variation of the slide position during a complete cycle

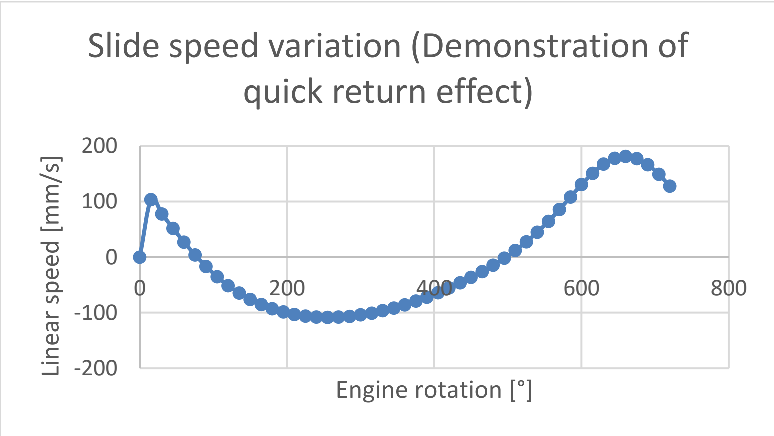

Fig. 12. Slide speed variation

$$\alpha = 500° - 80° = 420° \text{ (working stroke angle)} \tag{11}$$

$$\beta = 720° - 420° = 300° \text{ (return stroke angle)} \tag{12}$$

$$K = \frac{420}{300} = 1.4 \tag{13}$$

The gear drive reduces the absolute linear displacement velocities, which, in theory, translate to higher cutting force/torque at the tool tip, while maintaining a clear kinematic advantage. The time required for retraction is effectively reduced, resulting in a rapid retraction coefficient of 1.4, perfectly suited for roughing operations where cutting force takes precedence over speed.

5. Conclusions

This paper has achieved its primary objective of modeling, simulating, and kinematically validating the operating principle of rapid return mechanisms. The use of the Autodesk Fusion 360 virtual environment enabled detailed comparative analysis, progressing from fully symmetrical kinematics to complex industrial systems.

- **The standard slider-crank mechanism** demonstrated a perfectly equal distribution of times (K=1), being inefficient for processes that involve an idle stroke.
- **The quick-return mechanism with oscillating slotted arm** introduced the required asymmetry, resulting in a 43% faster return stroke (K=1.43).

- **The linear ram shaping quick-return mechanism** proved to be the most efficient kinematic profile for machining applications, effectively doubling the speed during the idle stroke (K=2).
- **The integration of a gear transmission** demonstrated the feasibility of speed reduction and cutting force enhancement, while simultaneously preserving return stroke efficiency (K=1.4).

Although virtual simulations confirm the theoretical hypothesis, our study reveals certain limitations of rigid-body modeling. The kinematic models did not account for mass inertia, joint friction, or the large dynamic forces that occur during real metal cutting. These shortcomings provide directions for future research, in which the 3D models can be subjected to complex finite element analysis (FEA) to determine the stress distribution and to structurally optimize the swing arm.

6. Bibliography

[1]. Antishi CNC (2025), "Understanding the Shaper Machine: Working Principle and Types", Technical article, [Online] Available: https://antishilathe.com/blog/shaper-machine/
[2]. Testbook (2023), "Shaping Machine - Parts, Working Principle, Diagram, PDF, Types & Applications", Educational resource, [Online]: https://testbook.com/mechanical-engineering/shaping-machine-diagram-and-process
[3]. Al-Sabaawi, A. W. S. (2012), "Theoretical Study and Computer Simulation of a Modified Quick Return Mechanism", Al-Rafidain Engineering Journal, [Online]: https://rsci.uomosul.edu.iq/index.php/rengj/article/download/30770/30607/30909
[4]. Monková, K., Monka, P. et al. (2014), "Kinematic analysis of quick-return mechanism in three various approaches", ResearchGate, [Online]: https://www.researchgate.net/publication/232729807
[5]. Testbook (2023), "Quick Return Mechanism - Whitworth, Crank and Slotted Link", Scribd (Digital archive).
[6]. Ali, S. (2018), "Quick return mechanism applications and working principles", SlideShare, Technical presentation.
[7]. (2020), "Whitworth Quick Return Mechanism Study - Efficiency and performance in modern machine tools", Scribd, online case study.
[8]. Costanzo, C., et al. (2017), "Autodesk FUSION 360: static stress analysis of a mechanical support", ResearchGate (Scientific Publications), Scientific article, pg. 1-6
[9]. RELUvance (2019), Fusion 360 Tutorial: Gear and Slider Modeling, [Online]: https://youtu.be/EmxC22lEbXY?si=0IWNbb6Bziz3EN

THE MECHANISM OF A ROBOT END-EFFECTOR

PASERE Sebastian, ŞERBAN Andrei and Asst. Prof. Ph.D. Eng. **NICULAE Elisabeta**, Asst. Ph.D. Stud. Eng. **POPESCU Mircea-Daniel (Scientific Coordinators)**
Faculty of Industrial Engineering and Robotics, Specialization: Computer-Aided Structural Engineering, Year of study: II
e-mail: paseresebastian0504@gmail.com

ABSTRACT: This paper presents the design and verification workflow for a 3D-printed robotic gripper mechanism actuated by a 12 kg · cm servomotor controlled using an ESP32 board. The mechanism was designed in CATIA V5, kinematically verified using the DMU Kinematics module, and structurally evaluated in ANSYS Static Structural. In the first stage, a more massive geometry was analysed in order to identify the critical stress areas, especially in the region of the toothed transmission. Subsequently, material was removed from the areas with lower stresses in order to reduce the volume and improve the structural distribution. The final geometry was selected after performing a second FEA simulation, which indicated a more uniform stress field and an acceptable structural behaviour for manufacturing from PLA.

KEYWORDS: robotic gripper; planar mechanism; structural analysis; PLA; 3D printing

1. Introduction

The paper focuses on the development of a gripper-type mechanism intended for use on a robot or on an experimental stand. The mechanism transforms the rotational motion of a servomotor into a coordinated motion of the jaws, in order to grip an object. The proposed solution aims to obtain a compact, rigid assembly that is easy to manufacture through 3D printing.

The topic is relevant because robotic grippers are frequently used in handling, sorting, and testing applications. In the case of a 3D-printed prototype, the design must include both the verification of the mechanism's motion and the analysis of its behaviour under loading.

The objectives of the paper are to define the kinematic structure, establish the degree of mobility, create the 3D model in CATIA V5, verify the motion in DMU Kinematics, and perform the structural analysis in ANSYS for both the initial version and the optimized version.

2. Current state

Robot gripping mechanisms can be designed in several variants, such as parallel grippers, grippers with articulated jaws, or electrically actuated systems. For educational prototypes, servomotors are frequently used because they allow angular position control and torque transmission to the mechanism. In this paper, the actuation is considered to be achieved by means of a servomotor controlled with an ESP32.

The analysed gripper is a planar mechanism consisting of rigid elements connected by revolute joints. The motion of the jaws is correlated through a toothed area, which allows the simultaneous opening and closing of the mechanism. For this reason, the kinematic analysis aims to identify the elements, joints, loops, and degree of mobility.

In the case of 3D-printed PLA parts, the most sensitive areas are the teeth and the joints, where stress concentrations or functional clearances may occur. Therefore, FEA analysis is used to verify the stresses and to optimize the geometry of the mechanism.

Tabel 1. The main stages of the mechanism' implementation

Phase	Working environment	Desired result
Geometric Modeling	CATIA V5	3D assembly and printable components
Kinematic Analysis	CATIA V5 - DMU Kinematics	Verification of the correct motion of the jaws
Structural Analysis	AutoCAD / structural	Identification of elements, joints, and

	schemes	loops
Initial FEA analysis	ANSYS Static Structural	Location of areas with high stresses
Geometric optimization	CATIA V5	Reduction of volume in lightly loaded areas
Final FEA analysis	ANSYS Static Structural	Validation of the final version for 3D printing

The stages were carried out iteratively, because the results obtained in the structural analysis were used to modify the shape of the parts. Thus, the design was not treated as a linear sequence, but as a development process in which the model is improved after each verification.

3. Structural and kinematic analysis of the mechanism

In order to describe the mechanism, the elements were numbered, while the kinematic joints were marked with letters. Element 0 represents the fixed base, and the other elements represent the arms, jaws, and intermediate elements. Through this notation, the structural scheme can be constructed, the kinematic chains can be identified, and the degree of mobility can be calculated. In the paper, the main objective was to confirm that the mechanism has a single independent motion, controlled by the servomotor.

For a planar mechanism consisting of rigid elements and lower revolute joints, the degree of mobility can be calculated using the Grübler-Kutzbach structural relation. In the form used in the paper, the relation is:

$$M = 3 \cdot (n - 1) - 2 \cdot c_5 - c_4 \tag{1}$$

where M is the degree of mobility, n is the total number of elements, including the fixed base, c5 is the number of lower joints with one relative mobility, and c4 is the number of higher joints.

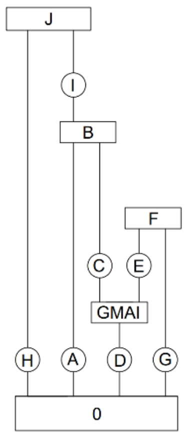

Fig. 1. Structural scheme of the mechanism

For the analyzed scheme, n = 8 elements, c5 = 10 revolute joints, and c4 = 0 idealized higher joints were considered.

$$M = 3 \cdot (8 - 1) - 2 \cdot 10 - 0 = 1 \tag{2}$$

The result M = 1 shows that the mechanism has a single independent motion. This conclusion is consistent with the selected actuation solution, because a single servomotor must be sufficient for the simultaneous closing and opening of the jaws.

Tabel 2. Elements and joints used in the structural scheme

Element	Connected joints	Role in the mechanism
0	A, D, G, H	Fixed base / mechanism support
1	J, H	Upper kinematic link
2	J, I	Intermediate element
3	I, B, A	Transmission arm

4	B, C	Articulated element
5	C, E, D	Actuated element / driving area
6	E, F	Intermediate element for the jaw
7	F, G	Jaw / final element

The number of independent loops of the mechanism can be verified using the relation between the number of joints and the number of elements. This verification is useful because it allows the structural scheme to be compared with the loop scheme and helps identify any notation errors.

$$N_c = c - n + 1\ 10 - 8 + 1 = 3 \tag{3}$$

Three independent kinematic loops result. These are marked in the loop scheme by areas I, II, and III. The loops allow the way in which the motion introduced into the driving joint is distributed to the jaws to be followed. In the case of the gripper, the functional symmetry of the motion is important because the jaws must move in a coordinated manner in order to center the gripped object.

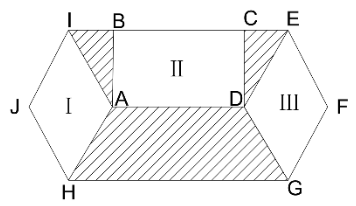

Fig. 2. Scheme of the independent loops of the mechanism

From the point of view of group analysis, the mechanism can be interpreted as a kinematic chain consisting of the driving element and structural groups attached to it. Dyad-type groups are characterized by two elements and three joints, having zero internal mobility when they are connected to the rest of the mechanism. A planar dyad can be verified using the relation:

$$M_d = 3 \cdot 2 - 2 \cdot 3 = 0 \tag{4}$$

Therefore, the addition of such a group does not modify the total degree of mobility of the mechanism but only transmits and transforms the motion. In the gripper, this interpretation is useful for separating the actuation area from the jaw guidance area and for analyzing more clearly the role of each joint.

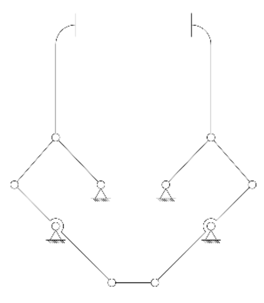

Fig. 3. Simplified kinematic scheme of the mechanism

4. 3D modeling and kinematic verification in CATIA V5

The 3D model of the mechanism was created in CATIA V5, with each main element modeled as a separate part in order to allow correct assembly and definition of the joints. In this stage, the minimum wall thickness, the space required for the rotation of the elements, the constructive clearances between components, and the possibility of printing without unnecessary fragile details were considered.

The initial version was designed with a more robust structure, meaning with more material in the arms and support areas. This choice was useful for the first FEA analysis, because it allowed the identification of the areas where high stresses occur without the result being influenced by premature optimization. After this stage, the shape was modified by reducing the volume in the areas with low stresses.

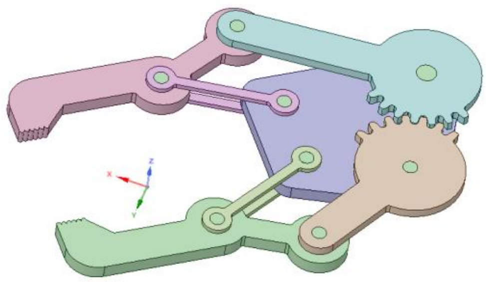

Fig. 4. Initial 3D model of the mechanism

The kinematic verification was performed in the DMU Kinematics module. In this module, the revolute joints were defined, the motion of the driving element was imposed, and it was verified whether the jaws move correctly, without geometric blockages. This stage is important before the structural simulation, because a part may have acceptable strength but may be unusable if the mechanism does not close or if interferences occur between components.

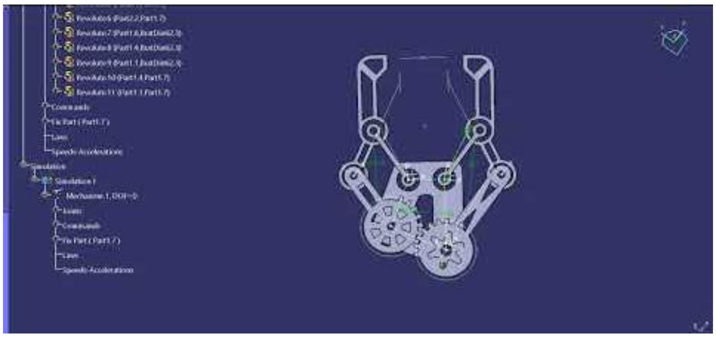

Fig. 5. Motion verification in the DMU Kinematics module

Following the verification, it was confirmed that the motion introduced by the servomotor is transmitted to the jaws according to the desired function. The kinematic simulation does not calculate stresses or deformations, but it provides an important validation of the assembly and of the geometric relationships between the elements.

5. Definition of the material and initial FEA analysis in ANSYS

For the structural analysis, ANSYS Static Structural was used. Before running the simulation, a custom material corresponding to the PLA used for 3D printing was defined in Engineering Data. Since the actual properties of 3D-printed PLA may vary depending on the manufacturing parameters, the entered values were considered indicative values for comparing the geometric variants.

Tabel 3. Properties used for the PLA material in ANSYS

Property	**Entered value**	**Unit of measurement**
Density	625	kg/m³
Young's modulus	1.4	GPa
Poisson's ratio	0,33	-

These values were used to estimate the stress state and to compare the initial version with the final version. For the complete validation of the real part, experimental tests on specimens printed with the same manufacturing parameters would be necessary.

The servomotor used has a specification of 12 kg · cm. This does not represent the mass of the servomotor, but the approximate maximum torque commonly expressed as the product between an equivalent force and a 1 cm lever arm. The conversion to SI units is performed using the relation:

$$M_s = 12\text{kgf}\cdot\text{cm}$$

$$12 \cdot 9{,}81\text{N} \cdot 10\text{mm} \approx 1177\text{N}\cdot\text{mm} \quad (5)$$

In the FEA model, this value was rounded and introduced as a concentrated moment of approximately 1200 N · mm, applied in the driving area of the mechanism. The jaws were fixed in order to simulate the severe case in which the gripper clamps an ideally rigid object and the mechanism can no longer continue closing. This assumption generates a more severe loading condition than gripping a deformable object.

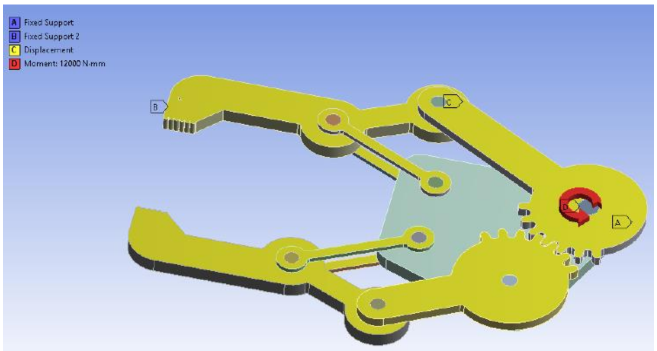

Fig. 6. Boundary conditions used in the initial FEA analysis

The results of the first simulation showed that the highest stresses occur in the tooth area and near the fillets. This distribution was expected, because torque transmission produces high local loads on the teeth, while sudden section variations promote stress concentrations.

6. Geometric optimization and final FEA analysis

After the analysis of the initial version, the part was modified in CATIA V5 by removing material from the areas where the stresses were low.

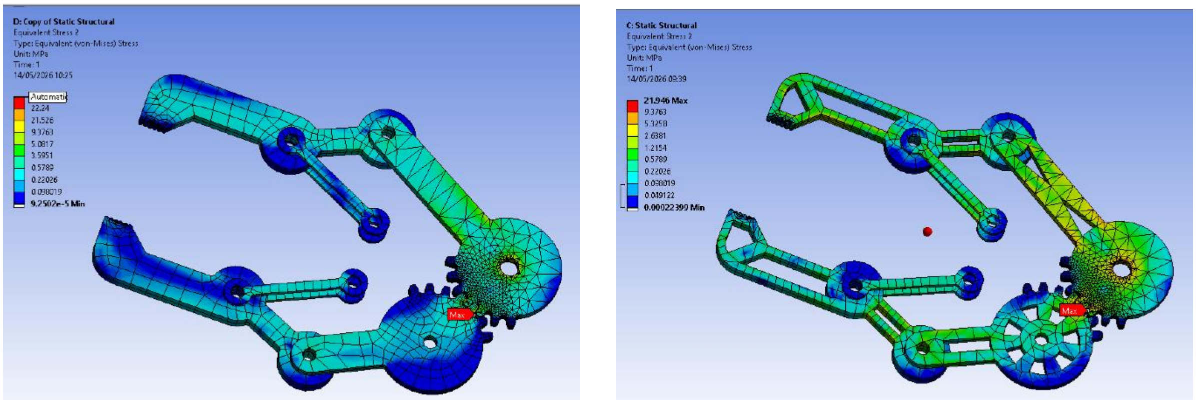

Fig. 7. Comparison between the initial version and the optimized version

The purpose was not only to reduce mass, but also to obtain a more efficient material distribution. In a 3D-printed mechanism, volume reduction has several advantages: lower filament consumption, reduced printing time, lower inertia of the moving elements, and reduced load on the servomotor.

To evaluate the efficiency of the modifications, the same set of boundary conditions was maintained: PLA material, a concentrated moment of 1200 N · mm, and fixed jaws. Thus, the differences between the results can be mainly attributed to the geometry modifications, not to changes in the simulation assumptions.

Tabel 4. Qualitative comparison between the analyzed versions

Criteria	Initial version	Optimized version
Material volume	Higher [mm³]	Lower [mm³]
Estimated printing time	Higher [min]	Lower [min]
Stress distribution	Concentrated in the tooth area	More uniform across the elements
Local stiffness	High in unloaded areas	Material preserved in the

		important areas
Recommended use	Preliminary analysis version	Final version for printing

The second simulation indicated a more uniform stress distribution compared to the initial version. The tooth area remained critical, because the actuation torque is transmitted directly there, but the rest of the part was used more efficiently. Based on these results, the optimized version was considered the final version for 3D printing from PLA.

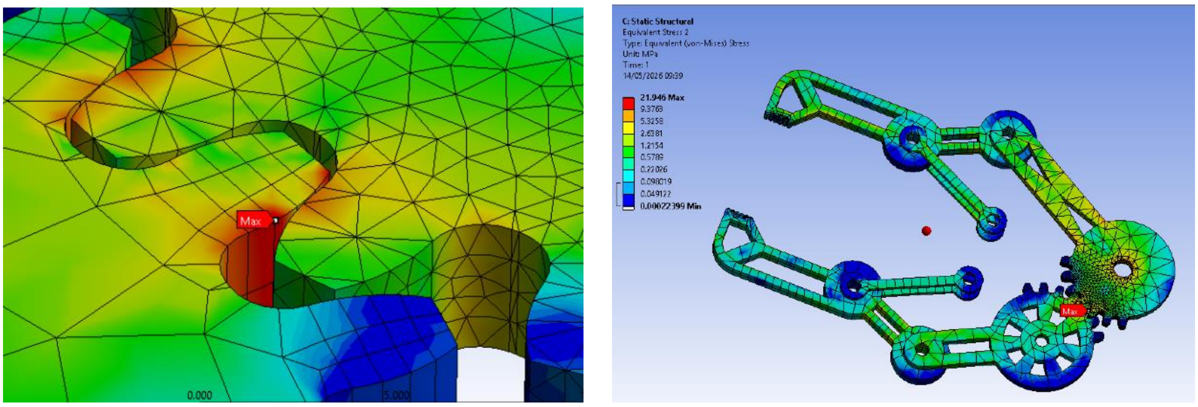

Fig. 8. Equivalent stress distribution for the final version

For the interpretation of the results, the von Mises equivalent stress was analyzed, because it allows a complex stress state to be compared with an allowable limit of the material. In its general form, the equivalent stress can be expressed by the relation:

$$\sigma_{VM} = \sqrt{\frac{(\sigma_1-\sigma_2)^2+(\sigma_2-\sigma_3)^2+(\sigma_3-\sigma_1)^2}{2}} \quad (6)$$

7. Conclusions

The paper presented the design and verification of a robotic gripper-type mechanism that can be manufactured through 3D printing. Through the structural analysis of the mechanism, it was determined that it has a degree of mobility M = 1, which confirms that a single servomotor can control the motion of the assembly. Three independent kinematic loops were also identified, which is useful for understanding the transmission of motion to the jaws.

Modeling in CATIA V5 allowed the geometry of the components to be defined, while the verification in DMU Kinematics confirmed the kinematic operation of the mechanism. The FEA analysis in ANSYS was used to compare two constructive versions. The initial, more massive version highlighted the concentration of stress in the tooth area, while the optimized version allowed volume reduction and more efficient use of the material.

The main contribution of the paper consists in completing a full design workflow: structural schematization, kinematic verification, material definition, FEA simulation, geometric optimization, and preparation for 3D printing. Future research may include experimental testing of the printed part, measurement of the real gripping force, comparison of several printing orientations, and replacement of PLA with more resistant materials, such as PETG, ABS, or reinforced nylon.

8. References

[1]. Norton, R. L. (2012), *Design of Machinery*, McGraw-Hill, New York, ISBN 978-0073529356.

[2]. Uicker, J. J., Pennock, G. R. și Shigley, J. E. (2017), *Theory of Machines and Mechanisms*, Oxford University Press, New York, ISBN 978-0190264482.

[3]. Budynas, R. G. and Nisbett, J. K. (2015), *Shigley's Mechanical Engineering Design*, McGraw-Hill, New York, ISBN 978-0073398204.

9. Notations

M = degree of mobility of the mechanism [-];
n = total number of elements, including the fixed base [-];
c_5 = number of lower joints with 1 degree of freedom [-];
c_4 = number of higher joints [-];
N_c = number of independent loops [-];

M_s = servomotor torque [N·mm];
σ_{VM} = equivalent Von Misses stress [MPa].

Modeling of an Adaptive Gripper with Force SENSOR

TRĂISTARU Mihai-Claudiu, BĂNICĂ Bianca-Teodora and Assoc. Prof. Ph.D. Eng. **UNGUREANU Liviu-Marian**, Asst. Prof. Ph.D. Eng. **BĂJENARU Valentina-Daniela (Scientific Coordinators)**

Faculty of Industrial Engineering and Robotics, Specialization: Applied Computer Science in Industrial Engineering, Year of Study: II, e-mail: mihai.traistaru@stud.fiir.upb.ro

ABSTRACT: Robotic manipulation of fragile objects with irregular shapes or variable stiffness remains a significant challenge in industrial automation. ***.*** *Traditional grippers, constructed from rigid materials, often apply non-uniform or excessive force, risking damage to the handled object. This paper proposes the design of an adaptive gripper equipped with phalanges made of thermoplastic elastomer, a material capable of conforming to the geometry of the grasped object. To ensure a secure grip that does not pose a destructive risk, the system integrates an Elektroweb FLEX pressure sensor, managed via a feedback loop implemented on a programmable logic control unit (embedded development platform). The study details the system architecture, the selection of the elastomer material, sensory integration, and control logic, demonstrating the mechanism's ability to adjust gripping pressure in real-time. Furthermore, the paper analyzes existing adaptive grippers—such as magnetic, thermo-responsive, and fluid-based systems—to conclude the efficiency of the modeled gripper.*

KEYWORDS: adaptive gripper, Arduino, pressure sensor, soft robotics, conformal grasping.

1. Introduction

In the field of industrial and collaborative robotics, object manipulation has always been a fundamental task. Nevertheless, although robotic arms have reached a high level of precision in terms of movement, the actual grasping of parts (through end-effectors or grippers) still poses considerable challenges. Most traditional grippers are built from rigid materials, such as aluminum or hard plastics; for this reason, when they must handle fragile objects with irregular shapes or asymmetric structures, conventional systems risk applying excessive force and damaging them.

To address this rigidity problem, an increasingly studied direction in the field is "soft robotics". The core idea is the use of flexible materials capable of deforming upon contactF with a payload. Starting from this concept, the present paper aims to model an adaptive gripper whose phalanges are made of a thermoplastic elastomer (TPE). The choice of this material is based on its hyperplastic properties, allowing the fingers to naturally conform to the shape of the grasped object. As a result, the mechanical stress is distributed over a much larger surface area, considerably reducing local pressure.

However, a purely mechanical approach based solely on material flexibility is not always sufficient to guarantee the safety of extremely sensitive objects. For a higher level of control, the mechanism must possess a "sense of touch". Therefore, this project proposes a hybrid and intelligent system through the integration of a pressure sensor Elektroweb FLEX on the contact surface of the phalanges.

This sensor reads the applied force in real time and transmits the data to a logic control unit (an Arduino development board). Through a feedback loop written in software, the control unit commands the actuation system: when the measured pressure reaches an optimal threshold for the respective object, the gripping action is automatically stopped, thus preventing structural damage.

This paper will detail the technical steps taken in developing this prototype: from structural modelling using the 3D-FUSION design software and material selection, to the electronic integration of sensors and the definition of the control algorithm. Furthermore, in order to highlight the advantages of the proposed solution, an analysis of other types of adaptive grippers currently under study will be conducted, such as pneumatic, magnetic, and thermo-responsive ones.

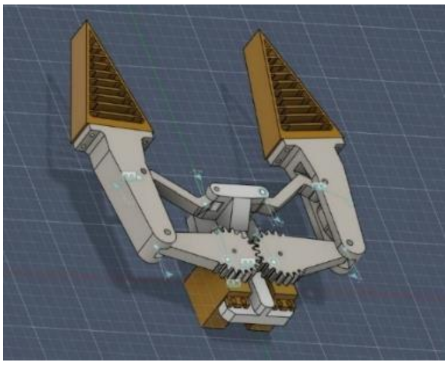

Fig. 1. 3D Gripper Model (with 2 motors)

2. Current State of the Art

The challenge of conformal grasping has generated a multitude of technological innovations over the last decade, as researchers have sought to replicate the dexterity and adaptability of the human hand. In order to properly evaluate the performance of the gripper modelled in this paper, a critical analysis of the adaptive technologies already existing in industry and academia is necessary. These can be classified according to the physical principle underlying their adaptability:

3. Soft grippers with fluid actuation (Pneumatic and Hydraulic)

Soft grippers operate by converting fluid energy into mechanical work, using pressure variations to deform elastic structures capable of grasping or releasing objects with high flexibility. In the specialized literature, these systems are classified according to the actuation medium: pneumatic systems (such as the PneuNet model, (Fig. 2) are preferred for the optimal balance between speed and force, while hydraulic systems (Fig. 3) are used in industrial applications requiring higher forces and torques.

Fig. 2. Soft gripper with pneumatic actuation [2]

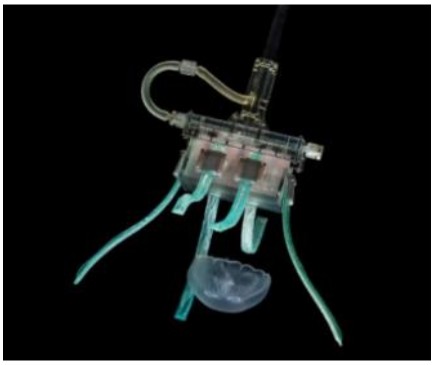

Fig. 3. Ultra-soft underwater gripper (hydraulic actuation) [2]

Both technical solutions are distinguished by their ability to absorb positioning errors, offering a versatile and precise alternative to conventional rigid mechanisms [1].

4. Soft grippers with magnetic actuation

Soft magnetic grippers (fig.4) are produced by integrating metallic particles (neodymium or iron oxide) into an elastomeric matrix, enabling precise manipulation of objects at the microscale or through sealed barriers. Owing to their non-invasive nature and reduced dimensions, they are ideal for the semiconductor industry and for the collection of fragile biological samples in underwater exploration. However, the limited gripping force restricts the use of this type of actuation to objects of very small dimensions and weights [3].

Fig. 4. Soft gripper with magnetic actuation

5. Grippers with Thermo-Responsive Actuation

Thermo-responsive grippers (fig.5) make use of smart materials — shape memory polymers (SMP), shape memory alloys (SMA), and liquid crystal elastomers (LCE) — which alter their geometry or stiffness upon crossing a critical transition temperature. Although the actuation process is slow due to the time required for heating and cooling, these systems offer major advantages such as high lifting force and the ability to self-lock without constant energy consumption. Thanks to these properties, they are employed in medical applications, complex mechanical assemblies, and the aerospace industry for deployable structures [4].

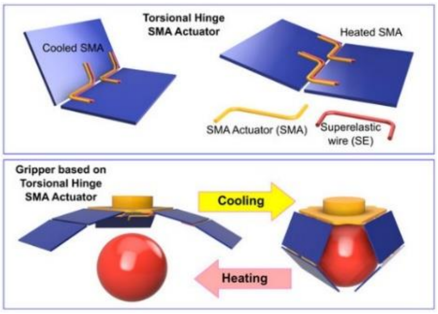

Fig. 5. Operating principle of a thermally actuated gripper

6. Structural Analysis

The mechanism of the studied gripper, as shown in figure 6, consists of 8 lower revolute kinematic pairs, one upper kinematic pair, and 6 mobile kinematic elements.

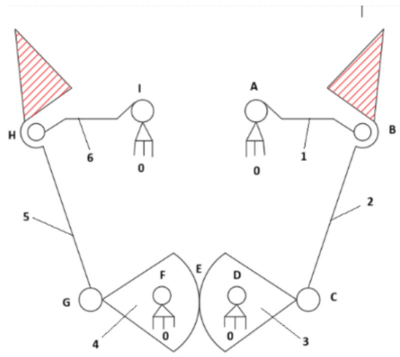

Fig. 6. Structural representation using international symbols

The degree of mobility is calculated with the formula:

$$M = 3 \cdot 6 - 2 \cdot 8 - 1 \quad (1)$$

M = 1

The number of closed contours is calculated with the formula:

(2)

$$N = 9 - 6$$
$$N = 3$$

where:
m = number of mobile elements
c_i = number of lower kinematic pairs
c_s = number of upper kinematic pairs

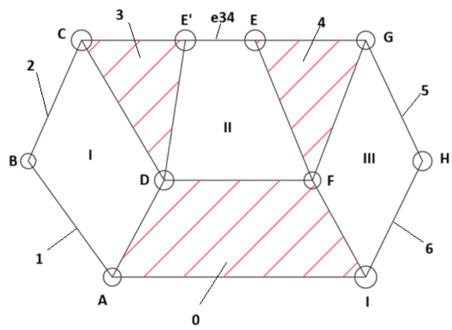

Fig. 7. Structural diagram

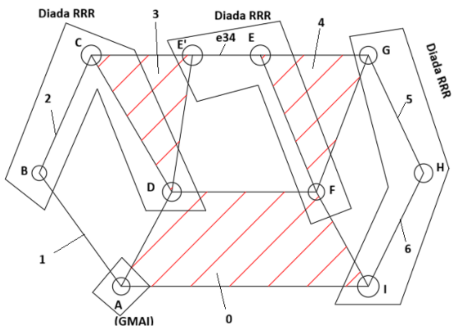

Fig. 8. Decomposition into structural groups

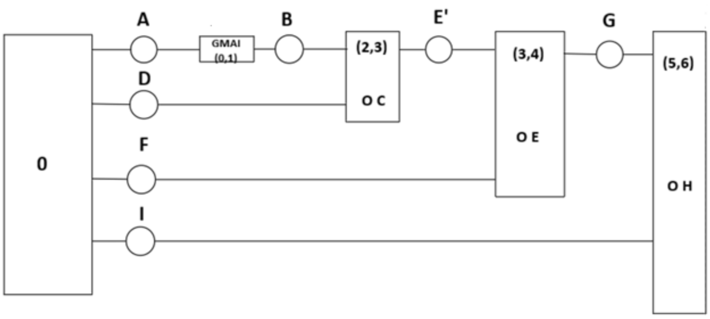

Fig. 9. Connection diagram

7. Material and Component Selection

7.1 PETG HF (High Flow) – Gripper Body

PETG is the most widely used material for 3D printing, and the HF variant is optimized for speed and improved layer bonding.

Technical Properties [5]:

– Young's Modulus (E): approx. 2.0 - 2.2GPa
– Tensile Strength: approx. 50 Mpa
– Heat Deflection Temperature (HDT): 70 **°C**
– Elongation at Break: 10-20%

This material was chosen for its **high Young's Modulus**, which ensures the structural rigidity required for movement precision under load, and the **HF (High Flow)** technology that facilitates rapid printing; the resulting part benefits from superior inter-layer adhesion and optimal **isotropic** strength.

7.2 TPU 95A – Phalanges (Contact Pads)

TPU (Thermoplastic Polyurethane) is an elastomer that combines the properties of rubber with those of plastic.

Technical Properties [5]:

- Shore Hardness: 95A (similar to the hardness of a shoe sole).
- Young's Modulus (E): 0.026 GPa– much lower than PETG, allowing elastic deformation.
- Elongation at Break: > 450%.

The use of TPU fingers ensures superior grip through elastic deformation on the surface of objects, increasing the contact area and preventing slippage without causing damage. At the same time, the material's shock-absorbing properties protect the rigid structure and servomotors in the event of accidental impacts, efficiently absorbing mechanical energy.

7.3 MG996R Motor

MG996R Motor is chosen for its optimal power-to-price ratio; it delivers a torque of 11–12 kg/cm (at 6V), sufficient to compress the TPU fingers and ensure a firm grip. Thanks to its metal gears, it withstands the mechanical stress transmitted through the rigid PETG HF structure, absorbing shocks and opposing forces without the risk of stripped gears, unlike variants with plastic components.

7.4 FSR Sensor - Force Sensitive Resistor

It is considered the "sense of touch" of the assembly, as this analogue sensor transforms the gripper into an intelligent system. With an ultra-thin thickness of 0.4 mm, it is discreetly integrated beneath the TPU layer or on the inner face of the fingers, providing real-time feedback without altering the designed geometry of the device.

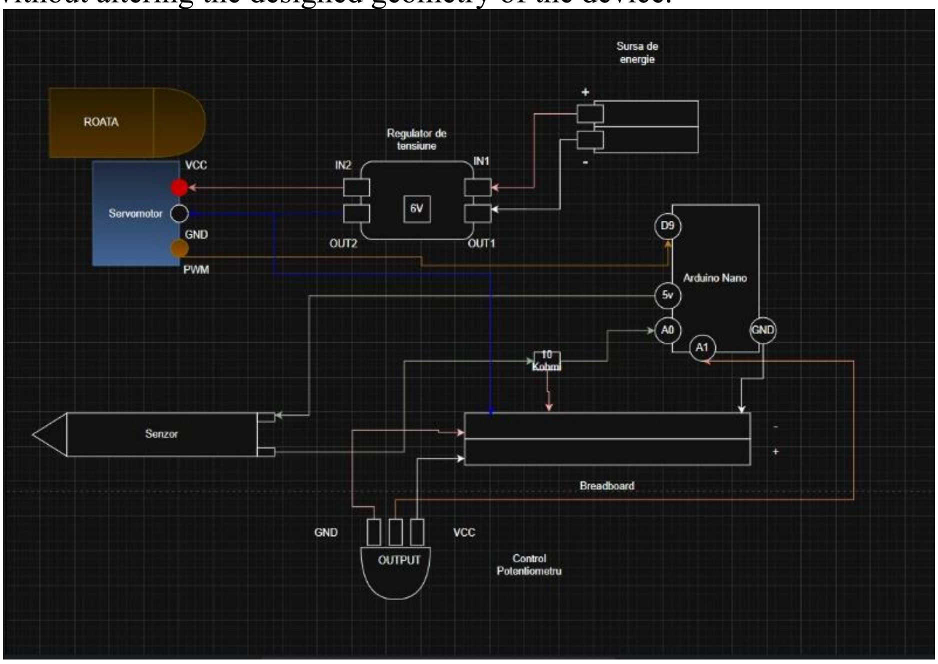

Fig. 10. Gripper actuation circuit diagram

The pressure sensor is essential for the mechanical protection and versatility of the gripper. It enables the implementation of a safety protocol that stops the 12 kg/cm motor when a force threshold is exceeded, thus preventing component breakage in the event of a jam. At the same time, tactile feedback allows the delicate handling of fragile objects, such as eggs or thin packaging, by limiting the gripping force as soon as contact is confirmed.

8. Connecting the Sensor to the Electronic Platform

The electronic architecture uses a programmable Arduino Nano development platform. An essential design feature is the separation of the power plane from the data plane, using an external 6V voltage regulator for the servomotor, thereby ensuring the stability of the logic signal and the current required for maximum loads.

Manual control is provided by an analogue potentiometer, allowing precise calibration of the operating limits.

9. Conclusions

The modelling of the adaptive gripper presented in this paper marks a transition from purely mechanical, rigid grasping mechanisms towards intelligent systems capable of sensory interaction and geometric adaptability.

Following the research and testing of the prototype, the following fundamental conclusions were drawn:

- The combination of **PETG HF** (structural rigidity) and **TPU 95A** (hyperplastic conformity) provides the optimal balance between precision and the ability to grasp irregular objects without complex algorithms.
- The integration of the **FSR** sensor and the control loop on **Arduino** gives the gripper an essential “sense of touch”. This enables the handling of fragile objects and protects the **MG996R** motor from overloading.
- Compared to pneumatic or magnetic solutions, the proposed prototype is simpler, more robust, and more energy-efficient, offering a superior force-to-weight ratio thanks to its metal gears and optimized design.
- The use of 3D printing and accessible sensors opens the path towards modernizing *soft robotics* technologies. Future extensions will target the implementation of *machine learning* for texture recognition and the scaling of the system for large industrial loads.

10. Bibliography

[]. Youyou Zhang, Jianhao Man, Xiaoang Liu, Shuai Li, Bo Cao, Liang Yu, Xiaojun Tan (2025), “Soft robotic grippers: a review”, Hebei University of Technology, Tianjin, China

[2]. Meenakshipriya, B., Suhas, R.M., Shivashankaran, D., Dhinesh Kumar, M., Raswim, K.T., Manoj, V., Dharanish, P.K (2024), “Design and Analysis of Soft Robotic Gripper with Different Materials for Object Handling”, 15th International Conference on Computing Communication and Networking Technologies (ICCCNT)

[3]. Denys Gutenko, Janusz Goldasz, Bogdan Sapinski, Pawel Orkisz (2025), „Soft MRE Gripper: Preliminary Study”, AGH University of Krakow, al. Adama Mickiewicza, Krakow;

[4]. Dennis Shonfeld, Dilip Chalissery, Franziska Wenz, Marius Specht, Chris Eberl, Thorsten Pretsch (2021), “Actuating Shape Memory Polymer for Thermoresponsive Soft Robotic Gripper and Programmable Materials

[5]. Taylor & Francis Ltd (2023), *3D Printing, Fundamental to Emerging Applications,* publisher Crc Press, Boca Raton, ISBN 9781032283999

IMPROVING ORGANIZATIONAL COMMUNICATION IN THE CONTEXT OF THE TRANSITION TO INDUSTRY 4.0

NICULESCU Miruna-Andreea, CARAMAN Marina-Izabela
Supervisor: Assistant Professor PhD Eng. Bogdan DUMITRU
Faculty: Faculty of Industrial Engineering and Robotics, Specialization: Intelligent Industrial Technologies, Year of study: IV, e-mail: niculescu_miruna@yahoo.com

ABSTRACT:
This research analyzes the optimization of organizational communication in the context of the transition to Industry 4.0, highlighting the strategic role of emerging technologies (AI, IoT, Big Data) in streamlining managerial processes. The paper emphasizes the need to develop employees' digital skills and adopt collaborative platforms, such as Slack or Microsoft Teams, to support hybrid work and decision-making transparency. Strategies based on digital planning, ethics, and cybersecurity are proposed to prevent information overload. The case studies demonstrate concrete benefits, such as a 50% increase in active participation within the educational environment and a 30% reduction in approval times for technical documentation in engineering. Ultimately, the authors conclude that digitalization transforms the manager into an "architecture of communication," which is essential for the adaptability and performance of the modern organization.

1. Introduction

1.1 General context of the research

In an economic and social context marked by accelerated changes, organizational communication becomes an essential element for the success and adaptability of any organization. In the digital era, characterized by rapid technological advancement and the emergence of the Industry 4.0 concept, the way organizations communicate—both internally and externally—is undergoing a profound transformation. Industry 4.0 represents both a technological revolution and a challenge for managerial thinking, organizational structure, and employee work behaviors. The transition to Industry 4.0 involves integrating advanced digital technologies, such as artificial intelligence, the Internet of Things (IoT), data analytics (Big Data), automation, and intelligent robotics, into all production and management processes. In this context, communication is no longer just a process of transmitting information, but a strategic mechanism that facilitates collaboration between people and technologies.

1.2 Objectives and methodology of the paper

This paper aims to analyze how organizational communication can be improved in the context of the transition to Industry 4.0, focusing on the adaptation of processes, channels, and organizational culture to new digital realities. The main objective is to identify effective communication management strategies that support performance, innovation, and technological integration in the contemporary organizational environment.

2. Theoretical foundations of organizational communication

2.1 The concept of organizational communication

Organizational communication represents the process through which information is transmitted, received, and interpreted within an organization to achieve common objectives. This involves both formal flows (reports, meetings, emails) and informal flows (spontaneous conversations, unofficial feedback).

Effective communication contributes to team cohesion, increases decision-making transparency, and reduces uncertainty. In the digital era, organizational communication is no longer just an internal process, but a complex system of technologically mediated interactions.

2.2 Types and models of communication in organizations

Several types of communication are recognized in the specialized literature: Vertical communication between hierarchical levels (manager-employee); Horizontal communication between colleagues or departments; Diagonal communication between individuals at different levels but in distinct functional areas; External communication between the organization and partners, clients, or the public.

2.3 The role of communication in organizational management

Communication represents the foundation of all managerial processes. Without a clear, coherent, and bidirectional communication system, no plan, objective, or strategy can be implemented effectively. Managers do not just transmit information; they also create meaning, direction, and motivation among employees.

In modern management, communication fulfills several essential functions: The informational function, which ensures the transmission of data necessary for decision-making; The motivational function, which encourages and actively involves employees in achieving goals; The control function, which allows verifying the conformity of actions with established plans; The integration function, which consolidates team cohesion and promotes organizational values.

In the context of the transition to Industry 4.0, the role of communication expands. The manager becomes a digital leader, capable of managing hybrid teams (physical + virtual), utilizing online collaboration platforms, and promoting transparency through digital channels. Tools like Slack, Microsoft Teams, Zoom, or Trello are no longer just communication channels, but true collaborative management ecosystems that centralize information, documents, and processes.

3. Industry 4.0 – The digital transformation of the organizational environment

3.1. Defining the Concept of Industry 4.0

Industry 4.0 refers to the integration of advanced digital technologies into industrial and organizational processes. The concept emerged in Germany as part of a government strategy launched in 2011 and represents the fourth industrial revolution, succeeding traditional automation.

The main characteristics are: Interconnectivity of cyber-physical systems; Intelligent process automation; Real-time data analysis; Human-machine collaboration.

3.2. Emerging technologies: Automation, Artificial Intelligence, IoT, Big Data

Emerging technologies facilitate a new form of organizational communication based on data, algorithms, and digital assistants.

- Artificial Intelligence (AI) allows for employee sentiment analysis, message personalization, and the automation of repetitive communication..
- IoT connects equipment and sensors, generating continuous streams of relevant data for rapid decision-making.
- Big Data provides a vast informational foundation for evaluating performance and identifying trends.
- Automation reduces temporal and spatial barriers, enabling global collaboration in real time.

3.3. Employees' digital skills in the 4.0 era

The transition to Industry 4.0 has profoundly redefined the profile of the modern employee. While in the past technical skills were sufficient, today the labor market demands a combination of technological, cognitive, and interpersonal abilities. Digital skills no longer represent a competitive advantage, but a strategic necessity for the survival and development of organizations.

A. Definition of Digital Skills

According to the European Commission (2020), digital skills represent the "safe, critical, and creative use of information and communication technologies for work, learning, and participation in society". In an organizational context, these involve the ability to use digital tools for communication, analysis, collaboration, and innovation.

B. Categories of Digital Skills

1. Technical skills: using collaborative platforms (Teams, Slack, Asana), analysis tools (Excel, Power BI), and ERP systems..
2. Cognitive skills: critical analysis of information, filtering relevant data, and the ability to make decisions based on digital insights.
3. Virtual collaboration skills: working effectively in geographically distributed teams using digital channels.
4. Digital security and ethics skills: complying with GDPR regulations, protecting personal data, and responsible online behavior.

C. Impact on Organizational Performance

Developing digital skills increases productivity, stimulates innovation, and improves internal communication. Employees become more autonomous, and decision-making processes become faster and more transparent.

Organizations that invest in digital training (workshops, e-learning, technological mentoring) succeed in creating a culture of continuous learning, prepared for the future.

3.4. Digitalization of communication processes. Digital platforms and collaborative tools (Slack, Teams, etc.)

The digitalization of organizational communication has become an essential pillar of digital transformation. In a context where hybrid work and distributed teams are increasingly widespread, collaborative platforms ensure efficient coordination, transparency, and speed in transmitting information.

A. The Concept of Communication Digitalization

Digitalizing communication involves using technologies and digital tools to manage internal and external information flows. This does not mean simply replacing traditional channels (physical meetings, paper reports) with online alternatives, but a profound reconfiguration of how the organization communicates, collaborates, and makes decisions.

B. Platforms and Collaborative Tools

1. Slack: allows the creation of thematic channels, the integration of applications (Google Drive, Trello, Asana), and instant communication. It is ideal for dynamic teams and agile projects.
2. Microsoft Teams: offers integrated features for chat, video calls, file sharing, and document collaboration. It is widely used in the corporate environment.

3. Zoom and Google Meet: provide remote video communication, with options for recording and automatic transcription.
4. Trello / Asana / Monday.com: project management platforms that offer transparency regarding the status of tasks and responsibilities.
5. Miro / Notion / ClickUp: creative tools for brainstorming, documentation, and visual coordination of teams.

C. Advantages of Communication Digitalization: Increases the speed of information transmission; facilitates real-time collaboration between remote teams; reduces logistical and travel costs; offers traceability and automatic archiving of conversations; contributes to the development of a digital organizational culture.

D. Challenges and Limitations: Information overload; loss of human contact and empathy in virtual communication; risks related to data security; difficulties in maintaining employee attention and engagement.

To avoid these problems, organizations must adopt balanced digital communication strategies that combine online channels with direct interactions, thereby promoting a culture of authentic connection.

3.5. Ethics and information security in digital communication

With the digitalization of communication, aspects of ethics and information security acquire major importance. In an environment dominated by data, algorithms, and artificial intelligence, organizations must ensure that information flows responsibly, securely, and transparently.

A. Ethics in Digital Communication

Digital ethics refers to the moral behaviors and principles that govern online interactions. In an organizational context, this implies:

- Respecting the confidentiality of employee and partner data;
- Using digital platforms responsibly (without online discrimination, abuse, or harassment);
- Transparency in communicating decisions and internal changes;
- Avoiding information manipulation and disinformation.

Managers have an obligation to create clear digital ethics policies, and employees must be trained to realize the impact of their online actions on the organization's image.

B. Information Security

The security of digital communication involves protecting data and information transmitted through electronic means. The main risks include:

- Cyberattacks (phishing, malware, ransomware);
- Unauthorized access to files and conversations;
- Loss of sensitive data due to human negligence.

To prevent these risks, organizations must implement:

- Cybersecurity policies (complex passwords, multi-factor authentication, data encryption);
- Periodic training for employees on recognizing digital threats;
- Incident response plans in case of security breaches;
- Compliance with GDPR and ISO/IEC 27001 regulations regarding data protection.

C. The Balance Between Ethics and Efficiency

In a hyperconnected digital environment, the major challenge is balancing communication efficiency with the protection of sensitive information. An organizational culture based on trust, respect, and digital responsibility becomes a key factor for the sustainability and reputation of the organization.

4. Strategies and best practices for improving organizational communication

4.1. Strategic planning of communication in the digital environment

Strategic planning in the digital environment involves establishing clear objectives, choosing the right channels, and structuring an efficient communication flow adapted to the organization's needs and the specifics of the employees.

A well-built strategy includes:

Analysis of communication needs:

- Identifying existing problems: information bottlenecks, delays, lack of transparency.
- Evaluating current channels (email, intranet, digital platforms) and their efficiency.
- Consulting employees through questionnaires or interviews.

Establishing strategic objectives:

- Improving internal vertical and horizontal communication.
- Increasing the speed of information transmission.
- Reducing operational errors caused by a lack of communication.
- Increasing the level of employee engagement through digital interactions.

Choosing the right digital channels:

- Collaborative platforms (MS Teams, Slack) for synchronous and asynchronous communication.
- Intranet and document management systems for centralizing information.
- Project management tools (Asana, Trello, Jira) for tracking tasks.
- Internal newsletter for important communications or official announcements.

Defining responsibilities:

- Clarifying roles: who communicates, who approves, who forwards.
- Establishing standard procedures: templates, communication guides, tone of messages.

Continuous monitoring and optimization:

- Using key performance indicators (KPIs): response time, platform utilization level, employee feedback.
- Adapting the strategy according to technological evolution and organizational changes.

4.2. Training and development programs for communication skills

Developing employees' communication skills is vital in a digitalized work environment because technology changes how people interact, present information, and collaborate.

Training for effective digital communication:

- Professional use of platforms like Teams, Slack, Zoom.
- Asynchronous communication techniques (clear, concise, structured messages).
- Written communication: wording of messages, digital etiquette, appropriate tone.

Developing presentation skills in the online environment:

- How to structure a digital presentation.
- Using visual tools (Canva, advanced PowerPoint).
- Managing emotions and maintaining attention in video calls.

Training for collaboration and remote teamwork:
- Conflict management in the virtual environment.
- Working on shared documents and version control systems.
- Online brainstorming techniques.

Specialized programs for middle and top management:
- Digital leadership.
- Strategic communication in crisis situations.
- Coordinating geographically distributed teams.

Skills assessment and follow-up:
- Periodic testing to check progress.
- Correcting weaknesses through micro-learning or personalized sessions.

4.3. Promoting a collaborative culture and trust in the digital environment

A strong collaborative culture is essential for organizational performance, especially in the context of digitalization and remote or hybrid work.

Creating a climate of trust:
- Transparency in communicating decisions and objectives.
- Leadership's availability to answer questions and provide clarifications.
- Promoting an environment where employees can express ideas without fear of consequences.

Stimulating collaboration:
- Using shared platforms for documents, projects, and communication.
- Sharing responsibilities fairly among members.
- Promoting interdepartmental projects.

Rewarding collaborative initiatives:
- Recognizing employees who actively contribute to communication and collaboration.
- Implementing "Employee of the Month" programs or non-financial bonuses.

Ethics and professional behavior in the digital environment:
- Internal regulations regarding the use of digital platforms.
- Clear norms regarding respect, confidentiality, and data protection.
- Internal awareness campaigns regarding cybersecurity (phishing, passwords, data access).

Activities that consolidate the organizational community:
- Online events (digital team building, coffee talks).
- Internal discussion groups on various topics (wellbeing, hobbies).
- Social projects and digital volunteering to increase the sense of belonging.

5. Case study (within the internship companies)

5.1. Case Study 1: Trainer within the Young Engineers Robotics Workshops

Organizational Context: Robotics workshops for children represent a modern educational environment oriented toward using advanced technologies—educational robots, sensors, microcontrollers, software platforms—which directly reflects the principles of Industry 4.0. The trainer's activity involves coordinating groups of children, facilitating learning through exploration, and effectively communicating with parents and the organization's team.

Identified Problem: Within the workshops, communication between trainers, coordinators, and parents was carried out predominantly through traditional methods (phone messages, short discussions before/after classes). This generated:

- Incomplete transmission of technical information about the children's progress;
- Lack of a centralized digital support system for organizing lessons;
- Difficulties in team coordination when schedule changes occurred;
- Impossibility of tracking educational objectives in real time.

Implementation of Industry 4.0 Specific Communication:

To modernize the process, digital tools were introduced that changed the communication flow:

1. Collaborative platform (Google Classroom / Teams): Materials for children, worksheets, exercise results, and tutorials were uploaded online; parents could track their children's progress in real time.
2. Applications for robotics design and simulation (e.g., Tinkercad, Blockly): Allowed students to test programs before working on the physical robot; facilitated the visual communication of technical concepts.
3. Internal communication channel between trainers (Slack / Discord): Rapid exchange of educational resources, lesson plans, and solutions for technical problems; increased coherence among team members.

Results:

- A 40-50% increase in children's active participation due to interactive materials;
- informarea părinților a devenit completă și predictibilă;
- Informing parents became complete and predictable;
- Decrease in organizational errors related to the schedule;
- A higher level of uniformity among trainers in teaching robotics modules;
- Development of digital skills for both trainers and students, in the spirit of Industry 4.0.

Conclusion: The digitalization of communication led to the efficiency of the educational act and the improvement of organizational coordination. The study shows that the principles of Industry 4.0 are applicable not only in the industrial environment but also in education, where digital communication becomes essential for coherence and performance.

5.2. Case study 2: Design engineer within austing insurance company

Organizational Context: Austing Insurance is a company that integrates modern technologies for risk assessment, design of technical systems related to insurance policies, and automation of workflows. The design engineer's role is to elaborate technical documentation for assessments, digital models, and technical solutions used in the insurance industry.

Identified Problem: Internal communication between the technical department, the underwriting department, and the claims assessment department was carried out through:

- Multiple emails without a clear tracking system;
- Technical documents in different formats, hard to integrate;
- Delays in approvals due to the lack of a digitalized flow;
- Difficulties in updating technical documentation in real time.

This affected design efficiency and the synchronization of information between departments.

Implementation of Industry 4.0 Specific Communication:

To solve the problems, modern digital tools were integrated:

1. PLM (Product Lifecycle Management) Platform / Document Management System: All technical documents were uploaded into a unified system; controlled versions and differentiated access for each department.

2. Use of 3D Digital Models (Digital Twin) for technical assessments: The design engineer can quickly transmit digital models to colleagues in underwriting; communication becomes visual, clear, and complete.
3. Automated Approval Workflow (e.g., Jira / Monday): Each stage of the design is tracked digitally; response times are shortened; document loss is avoided.
4. Hybrid meetings integrated with live model-sharing systems: Allow simultaneous discussion of technical solutions with all colleagues involved.

Results:

- Reduction of technical documentation approval time by up to 30%;
- Elimination of errors caused by using wrong versions of documents;
- Increased transparency between departments;
- Optimization of collaboration between engineers, assessors, and analysts;
- Modernization of the operational flow towards Industry 4.0.

Conclusion: The implementation of advanced digital tools significantly improved internal communication, reducing working times and increasing the accuracy of technical processes. The transition to Industry 4.0 brought about an organizational culture based on digital collaboration, transparency, and efficiency.

6. Conclusions

The digitalization of communication in the era of Industry 4.0 represents not just a change of tools, but a profound reconfiguration of organizational culture. The research demonstrates that the success of the transition depends on the balance between advanced technologies and the development of human skills, transforming information flows into interactive and transparent systems. Implementing these digital strategies ensures not only operational efficiency but also increased adaptability, essential for sustainable performance in the contemporary economic environment.

7. Bibliography

[1]. Argenti, P. (2021), Organizational Communication: A Managerial Perspective, McGraw-Hill Education.

[2]. Robbins, S. și Judge, T. (2020), Organizational Behavior, Pearson Education.

[3]. Daft, R. (2018), Management: Communication and Collaboration in a Digital World, Cengage Learning.

[4]. Heath, R. L. și O'Hair, H. (2020), Handbook of Strategic Communication, Routledge.

[5]. Lind, P. (2022), Digital Communication in the Workplace: Tools, Trends, and Strategies, Springer.

[6]. Men, L. R. și Qin, Y. (2021), Public Relations and Strategic Communication in the Digital Age, Wiley.

[7]. Leonardi, P. (2020), Technology Choices: Why Occupations Differ in Their Embrace of Digital Tools, MIT Press.

[8]. Bălăceanu, A. și Ionescu, M. (2021), Comunicare organizațională în era digitală, Editura ASE.

DESIGN OF AN EXPERIMENTAL INTELLIGENT MECHATRONICS SYSTEM FOR AUTOMATED DRUG DISPENSING

RADOVENEANU Vlad-Alexandru and **GHEORGHIȚĂ Vlad**
Faculty: Industrial Engineering and Robotics, Specialization: Applied Informatics in Industrial Engineering, Study year: 4, e-mail: vlad.radoveneanu@stud.fiir.upb.ro

REZUMAT: The PharmaBot is an automated pharmacy assistant integrating a Python/Flask web interface with an ESP32-controlled gantry robot. When a user selects a product, the backend retrieves precise raft coordinates and medicine dimensions from a database. The ESP32 coordinates high-speed stepper motors for X-Z alignment, while a linear actuator and vacuum pump handle the physical extraction. Safety is prioritized through a robust safeMove protocol that monitors limit switches in real-time to prevent collisions. After retrieval, the robot navigates to a designated drop-off zone, releases the medicine by venting the vacuum, and returns to a calibrated position. The system ensures a fully autonomous, precise, and safe delivery cycle for pharmaceutical products.

Key Words: Automation, Pharma Industry, Gantry Robot, Numeric Control, Industry 4.0

1. Introduction

Unrestricted access to healthcare and pharmaceutical products is a fundamental pillar of a modern healthcare system. [2] In the current context of Industry 4.0, process automation has become an essential component in optimizing production and logistics workflows. However, the pharmaceutical field often faces logistics and staffing limitations. Minor medical issues do not depend on pharmacy operating hours, creating a need for autonomous distribution systems capable of bridging the gap between patient needs and the availability of over-the-counter pharmaceutical products. [1,2]

In many countries, the number and location of pharmacies are regulated by authorities, with specific requirements for management and operation. Even under these conditions, it is very common to have multiple pharmacies in a limited area, usually on the ground floor of residential buildings, which is convenient for quickly procuring medication. [1,2]

2. Current status

In the current context of automation, robots are defined as electro-mechanical machines controlled by a computer or microcontroller, being divided into two major categories: industrial robots and service robots. According to ISO standards, an industrial robot is defined as an automatically controlled, programmable manipulator that can have multiple axes and is designed to handle tools, parts, and materials. In contrast, service robots operate autonomously or semi-autonomously to perform services useful to human well-being. [3]

For the pharmaceutical industry, the literature shows a clear trend in shifting from conventional gravity-based vending machine systems to intelligent product handling systems, which reduce product damage. [4]

A relevant example is the system proposed by Satheesh Kumar, which describes the design and development of an experimental medicine vending machine model. This model is based on an elevator system combined with lead screws from conventional vending machines, which simultaneously prevents medication from getting damaged. [4]

The system taken from the literature uses simplified gantry architecture, featuring two axes (X and Z) controlled by an Arduino Mega 2560 microcontroller. [4] Its operating principle is like the one proposed in this bachelor's thesis.

Regarding positioning, a carriage is moved along the horizontal and vertical axes using NEMA17 stepper motors driven by a timing belt until it reaches the front of the selected product, utilizing a 2D matrix to locate the medications. [4]

For product delivery, once positioned in front of the chosen medicine, a servomotor rotates a spiral (also called a lead screw) to advance the medications until they fall into the carriage. After the servomotor's advance command is given, the carriage waits for a few moments, then gently retracts to the delivery slot, where the buyer retrieves the medicine. [4]

As for the user interface and payment processing, the system integrates a GSM module (SIM900A) to manage digital payments made via QR codes, and uses an LCD display for user interaction, showing the relevant order information. [4]

This study validates the feasibility of using intelligent medicine handling systems through Cartesian positioning built into the vending machine to eliminate shock from dropping. It retains the advance mechanism of classic vending machines (the lead screw) but adds the horizontal and vertical movement of the medicine carriage. [4]

A few limitations of that paper include:

- Geometric incompatibility: medicine boxes come in various sizes and can get jammed in the standard spirals.
- Lack of precision during product retrieval: the spiral can only push the medicine as much as needed but does not actually secure it.

The system presented below aims to overcome these limitations by implementing a vacuum-based gripper along with a linear actuator, eliminating the classic lead screw for advancing medications. This architecture allows products to be retrieved safely and precisely, regardless of their shape or size.

In developing this thesis, we use a flowchart to ensure a rigorous methodological structure that helps align human needs with product development. To guarantee logical flow and demonstrate that product design is a direct consequence of human demand and needs, a methodological flowchart was developed. This chart, shown in Figure 2.1, represents the conceptual map of the entire project, structured into three key phases: defining the context, validating the need, and technical execution.

- Validating the need: conducting a survey to confirm or refute the need for such a system.
- Technical execution: breaking down the hypothesis into subassemblies and assembling them to achieve the final product.

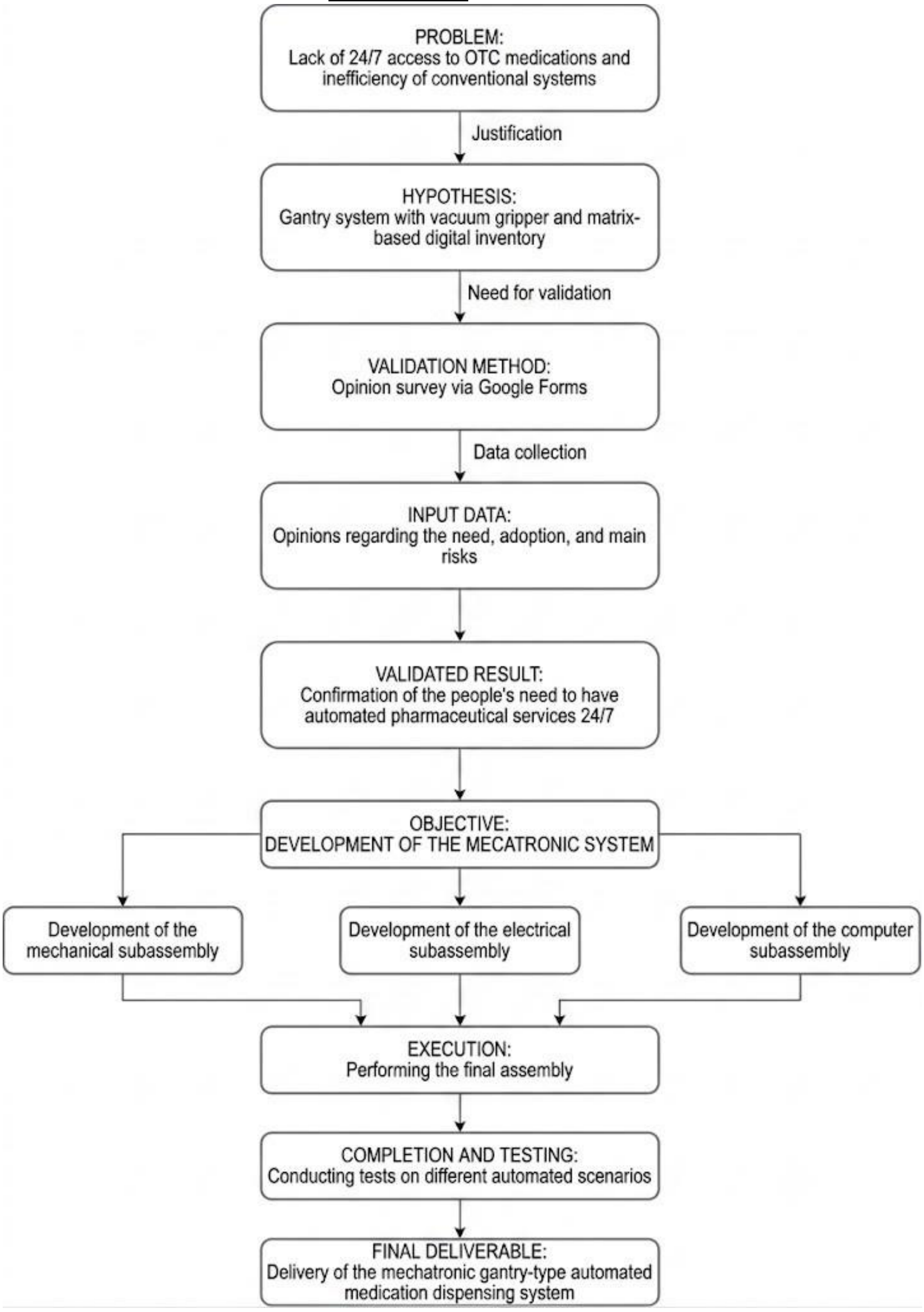

Figure 2.1 Methodology of the system

Next, each stage will be analyzed individually, detailing the specific methods and tools used to move from the problem to the final product, validated from both a technical and social perspective.

The Problem: As presented in the previous chapter, "Problem Description", we focus on the lack of 24/7 access to OTC (over the counter) medications which can be bought from a pharmacy without a prescription and the inefficiency of conventional systems.

The Hypothesis: This helps us better understand what we propose to achieve in this thesis: a vending machine system that provides access to OTC medications. The proposed method to accomplish this is a 3-axis Gantry system with a vacuum-based gripper and a matrix-based digital medication storage system.

The Validation Method: A highly secure and 100% anonymous way to validate this proposal is through a survey. We chose Google Forms to create this survey, given that it offers many built-in tools for data collection, making it very easy to design. Distributing the survey is straightforward as it is linked to a URL like https://forms.gle/xXxXxXxXx; users only need to access the link, answer the questions, and then close the browser.

The Validated Result: Following the distribution of the survey, we received highly important information regarding the development direction of the medicine vending machine, confirming demand and usability potential, possible locations for the system, and potential risks of the vending machine.

3. General Structure and Operating Principles of the Mechatronic Automated Medication Dispensing System

This section presents the objectives and components of the bachelor's thesis project. The project aims to optimize the logistics workflow and the dispensing process within modern pharmacies. The PharmaBot mechatronic system represents an overall automated ASRS (Automated Storage and Retrieval System) solution. Specifically, the project proposes a 3-axis Cartesian robot architecture capable of navigating autonomously within a predefined storage matrix to retrieve and deliver medicine boxes to a fixed drop-off point. The brain of the robot is a microcontroller, which enables full control of the system via an IoT (Internet of Things) web interface. By mapping the medicine shelves into a predefined matrix through a coordinate system, PharmaBot ensures instant tracking of the medications, reducing the risk of identification errors caused by human fatigue or oversight.

From a structural perspective, the system is based on a series of fixed and mobile elements that allow us to manipulate the robot along 3 axes. The horizontal axis, responsible for left-right movement along the storage columns, is driven by a stepper motor coupled to a timing belt transmission, providing high speed and smooth travel over long distances. In contrast, the vertical axis utilizes a lead screw transmission mechanism, offering superior torque for lifting the load and a mechanical self-locking feature that prevents the robotic arm from falling in the event of a power failure. The electric linear actuator, the end effector, is the main element allowing extension and retraction in depth. Together with a pneumatic gripping system based on a vacuum pump controlled via an electromechanical relay, it ensures an extremely gentle grip on the medicine boxes without risking deformation. Structural integrity and spatial referencing are achieved through a network of limit switches read via the internal pull-up resistors of the microcontroller, which allow a calibration sequence to run at each system initialization to establish the absolute origin of movement.

Regarding software architecture and control, PharmaBot runs a complex code that synchronizes asynchronous network request processing with the real-time generation of the pulses required to drive the motors. To overcome the limitations of single-threaded main loop execution and interference caused by the wireless communication module, the programming architecture logically separates the machine's operating modes. Thus, for manual operation or calibration mode, the system uses simple functions that prioritize motion fluidity. Meanwhile, for the automated pick-and-place mode, the specialized AccelStepper library is implemented, providing the essential mathematical functions that dynamically calculate smooth acceleration and deceleration ramps.

This integration precisely manages the velocity profile of the motors, allowing smooth starts and stops that eliminate inertial mechanical shocks and prevent missed steps during transport tasks. Furthermore, the system memory maps the physical shelf into a digital matrix with predefined coordinates for each row and column, while also offering the flexibility of a teaching module through which the operator can save new spatial points of interest. Micro stepping pulse modulation, implemented directly on the power drivers, ensures not only sub-millimetric positioning accuracy of the effector but also highly silent operation.

In conclusion, the PharmaBot project represents a vending-machine-type automatic dispenser that successfully combines mechanics, electronics, and programming to modernize the medicine dispensing process. This thesis practically demonstrates how a robotic system can bring accuracy and speed into a commercial space, serving the end user directly and efficiently. By automatically selecting and delivering products to the collection point, the machine eliminates waiting times and completely prevents human errors that can occur during treatment handovers. Thus, the developed solution is fully functional, easy to query through a digital interface, and confirms that automated dispensers represent a modern, safe, and highly practical method for the future of the pharmaceutical retail.

The IDEF0 diagram of the system includes all the subassemblies and components of the automated medication dispensing system.

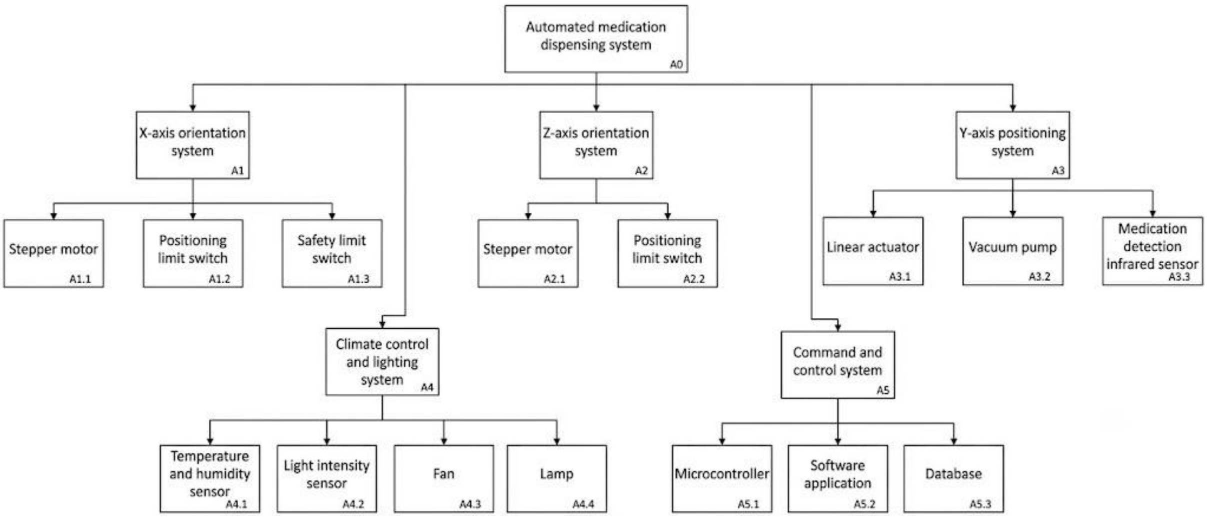

Figure 3.1 IDEF0 diagram

System Operating Principle: The automated medication dispensing system operates in stages, as follows:

- Standby: the mode in which the machine is idle and waiting for commands; nothing happens in this mode, and power consumption is reduced.
- The customer approaches the machine and touches the screen to "wake up" the system.
- The customer selects the medication using the interactive screen.
- The system receives the command to check the availability of the selected medication.
- If the medication is available, the payment sequence begins.
- After payment, if successful, the orientation sequence along the X and Z axes begins.
- Once it reaches the position of the selected medication, the positioning sequence along the Y axis begins.
- Upon completion of the medication retrieval sequence via the Y axis, the orientation system on the X and Z axes returns to the medication drop-off point.
- The customer collects the medication from the drop-off point.
- A recalibration sequence begins to prevent orientation and positioning errors.

All these stages of the medication dispensing process are detailed in the system process diagram shown in Figure 3.2.

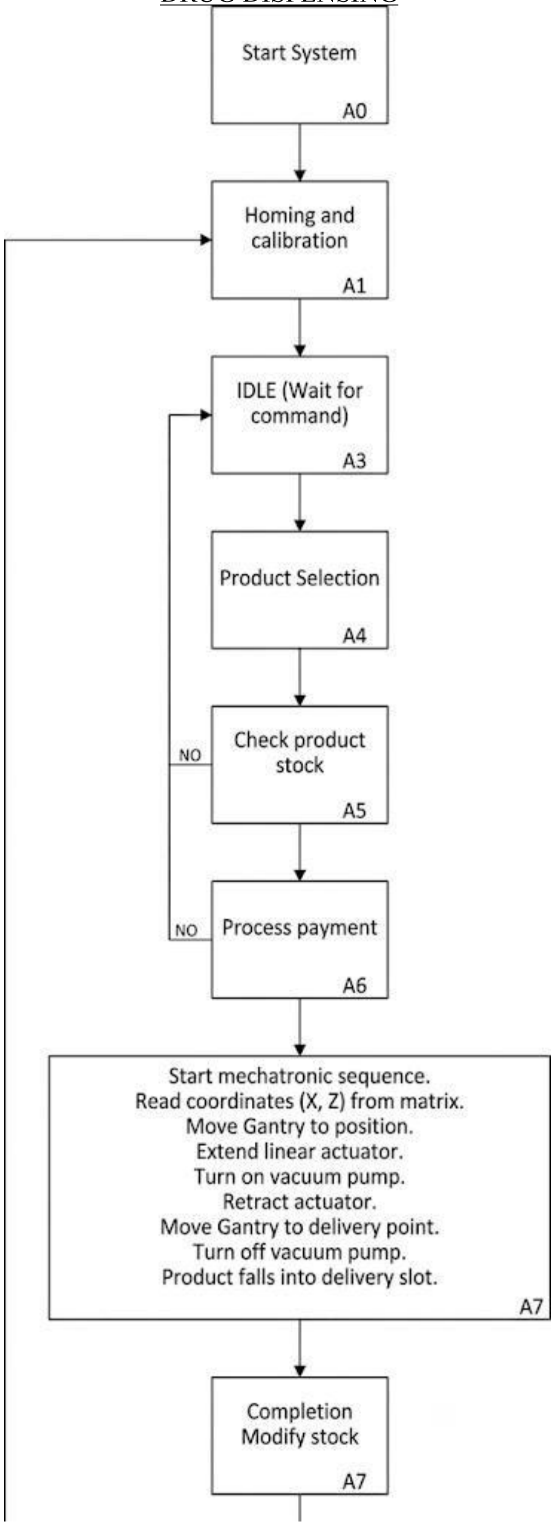

Figure 3.2 Process diagram

The mechanical subassembly represents the backbone of the automated medication dispenser. It serves as the mandatory physical infrastructure upon which all electrical command and control elements are mounted and aligned. Without this solid frame, the practical implementation of the entire assembly and the execution of movements would be impossible. To guarantee rigidity and absorb vibrations, the core structure is made of aluminum profiles and metallic components. At the same time, to anchor components with atypical geometries, the project integrates parts made through additive manufacturing. This subassembly will be designed downstream to support the weight of all components as well as the weight of the retrieved medications.

The electronic subassembly functions as the processing center of the medication dispenser. It takes the logic from the code and converts it into physical actions, using a microcontroller as its core. The development board manages Wi-Fi communication, interprets data received from sensors, and generates the necessary signals to coordinate movements. Without this digital network, the mechanical components could not synchronize to execute an automated cycle. Motor drivers and relays distribute energy in a controlled manner to the kinematic elements and the pneumatic vacuum system. Simultaneously, sensors provide real-time feedback to validate the machine's position and the presence of boxes.

The computer subassembly represents the decision-making center of the automated dispenser, responsible for receiving, processing, and executing user commands. The operational workflow for dispensing a product follows a precise logical sequence. The process begins on the web interface, where the user chooses the desired treatment. Immediately, the command triggers a query to the MySQL database, which checks stock availability and extracts the physical address of the product, defined by row and column spatial coordinates. The extracted coordinates are then transmitted via HTTP protocol to the microcontroller. In the final stage, the system converts the received data into electrical pulses using the AccelStepper library, which dynamically calculates the required speed and acceleration ramps, initiating the mechanical retrieval and delivery sequence. To prevent data collisions and positioning errors, the system integrates a safety procedure using a logical lock. The moment coordinates are received, and the movement cycle begins, the internal server restricts access to the selection menu and automatically ignores any new request coming from the network. This software barrier ensures the correct completion of the current command, protecting the machine's mechanics from accidental or simultaneous instructions that could corrupt task execution.

4. Mechanical and electrical component testing

The testing process began by verifying the mechanical integrity of the Cartesian system. The focus was on calibrating the step-to-millimeter ratio for the X and Z axes, a stage during which positioning and repeatability tests were conducted. The results indicated a margin of error of 0.1–0.2 mm for positioning and 0.2 mm for repeatability, providing the necessary precision for the correct alignment of the suction cup with the center of the packaging. The tension of the transmission belts and the parallelism of the axes were verified to eliminate mechanical backlash that could have caused the robot to hit the shelves during rapid maneuvers. Additionally, the airtightness of the pneumatic circuit was evaluated, measuring the time required for the suction cup to reach optimal negative pressure and its gripping capacity on matte, glossy, or plastic-coated cardboard packaging.

On the electronics side, the tests focused on the stability of the control signals sent from the ESP32 to the TB6600 drivers and on managing electromagnetic interference. For the limit sensors, a false triggering phenomenon was initially observed due to electrical noise on the cables. This issue was resolved by implementing a software filter that validates the sensor's state only after several consecutive readings. In the final stage, the serial communication protocol between the Python script and the microcontroller was tested, guaranteeing that the JSON data packets are received and interpreted without information loss, even under heavy CPU utilization.

5. Final assembly

The final stage of the PharmaBot development consisted of integrating the mechanical, electronic, and pneumatic subassemblies into a single structural unit. The chassis, built from aluminum profiles, was reinforced to minimize vibrations during X-axis accelerations. Attention was paid to cable management; given that the limit sensors and motors are in continuous motion, plastic cable ties were used to prevent tension or conductor breakage. The electronic components were centralized on a wooden board, ensuring adequate ventilation to prevent driver overheating during prolonged operation. The final system can be observed in Figure 5.1.

Following the completion of assembly and manual calibration, the system underwent automated testing sessions under real operating conditions. The primary objective was to verify the reliability of the delivery algorithm, from product selection in the web interface to its release into the drop-off bin.

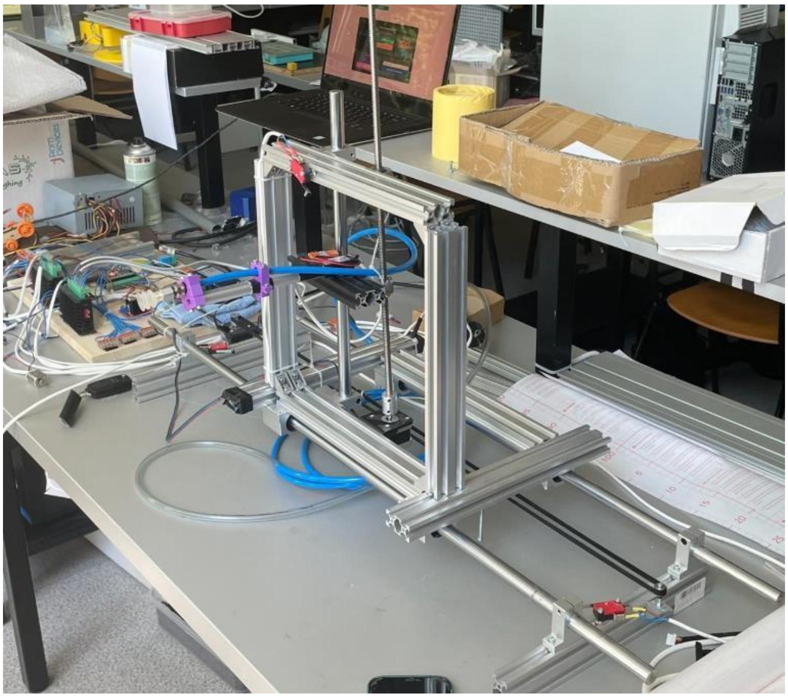

Figure 5.1 Final assembly

6. Conclusions and future developments

The project validated the efficiency of the hybrid Python-ESP32 control system in pharmaceutical automation, demonstrating high precision in product handling and delivery through the coordination of the Cartesian axes and the pneumatic system. The implemented architecture ensures stable workflow, protected by anti-collision safety algorithms, turning the prototype into a solid foundation for optimizing pharmacy operations. Future developments of the system aim to integrate computer vision for automated barcode scanning and to implement route optimization algorithms, thereby expanding the capacity for intelligent, real-time inventory management.

7. Bibliography

[1] Jairoun, A. A., Al-Hemyari, S. S., Shahwan, M. et al., Examining the evolution and impact of OTC vending machines in Global Healthcare Systems, Exploratory Research in Clinical and Social Pharmacy, Vol. 16, 100540, 2024.

[2] Demchenko, I. S., Pletenetska, A. O., Dispensing of medicines via vending machines, Wiadomości Lekarskie Medical Advances, Vol. LXXVIII, Issue 6, pp. 1102-1107, 2025.
[3] Covaciu, F., Designing and Manufacturing a Delta Robot for Pick and Place Applications, Acta Technica Napocensis, Series: Applied Mathematics, Mechanics, and Engineering, Vol. 63, Issue I, pp. 67-72, 2020.
[4] Satheesh Kumar, K. G., Sooraj, P. S., Binu, M., Food Vending Machine, 2024 International Conference on Futuristic Technologies in Control Systems & Renewable Energy (ICFCR), pp. 1-6, 2024.

RESEARCH ON THE DEVELOPMENT OF A MINI-FORKLIFT ROBOT FOR WEIGHT-BASED GOODS SORTING

BRĂTUIANU Radu-Mihai, GHIONEA Ionuț-Gabriel

Facultatea: Inginerie Industrială și Robotică, Specializarea: Informatică Aplicată în Inginerie Industrială, Anul de studii: IV, e-mail: radubrm12@gmail.com

Conducător științific: Conf. Dr. Ing. **Ionuț-Gabriel GHIONEA**

ABSTRACT: The paper entitled "Research on the Development of a mini-Forklift Robot for Weight-Based Goods Sorting" aims to reduce human workload in warehouse goods sorting by designing and developing a robotic experimental model whose main purpose is to assist human operators from an organizational perspective, thus contributing to the overall efficiency and productivity of a company. The operating process is structured into several stages: lifting the box from the stand where it was placed by the user, scanning the QR code attached to it in order to identify the storage area assigned to the package — an area predetermined by the worker according to the package contents — and, in the same time, weighing the package to determine the appropriate storage level. Ultimately, the process results in the correct placement of the parcel within the warehouse.

KEY WORDS: forklift, reduce human workloud, weight.

1. Introduction to Automated Sorting Systems and Their Evolution

The sorting of goods in a warehouse is an essential factor in the success and efficiency of a company, regardless of its field of activity.

The development of this experimental robotic model aims to reduce the organizational workload of human operators and improve the operational flow of an enterprise through the design and implementation of a miniature forklift robot.

To reduce manufacturing and maintenance costs, it was decided to produce as many components as possible using additive manufacturing techniques [1]. Fundamental principles of mechanical design [2] were applied to develop a simple and efficient model using the CATIA CAD software [3], ensuring a compact and ergonomic design.

The first robots designed for automated sorting appeared as early as the 1950s, initially in the postal sector, where mechanical systems and early computer technologies were used to classify mail. During the 1960s and 1970s, the introduction of barcodes and Optical Character Recognition (OCR) systems enabled the partial automation of sorting processes in postal and logistics centers [4] (Fig. 1).

Fig. 1 Prim model de sortare

At the same time, in 1966, the first **Automated Storage and Retrieval System (AS/RS)** was developed. It is regarded as a precursor to modern logistics automation systems, enabling the automated storage and retrieval of goods within warehouses and distribution centers [5](Fig. 2)

Fig. 2 Rackbuil and Rack Master System

Odată cu dezvoltarea microprocesoarelor și a controlului programabil (PLC), sistemele de sortare au devenit mai rapide și mai precise. Au fost introduse sisteme precum:

- Sortere cu bandă transportoare,
- Sisteme cu brațe mecanice,
- Sisteme cu tăvi basculante (tilt-tray),
- Sortere cu valuri (cross-belt).

Aceste tehnologii au permis trecerea de la sortarea manuală la fluxuri continue automatizate, sisteme care asistă umanitatea chiar si în prezent.

2. State of the Art

With the development of microprocessors and programmable logic controllers (PLCs), sorting systems became faster, more reliable, and more accurate. During this period, several automated sorting technologies were introduced, including:

- Conveyor belt sorting systems,
- Mechanical robotic arm systems,
- Tilt-tray sorting systems,
- Cross-belt sorting systems.

These technologies enabled the transition from manual sorting to continuous automated workflows, forming the foundation of the modern logistics systems that continue to support industrial operations today.

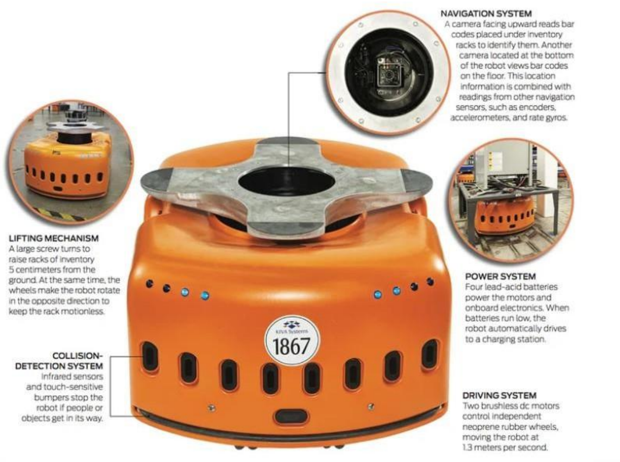

Fig. 3 Kiva System - Amazon

These systems can be classified into several categories, including:

- Conveyor-based sorting systems,
- Mobile robot sorting systems (AMR/AGV),
- Intelligent sorting systems, which integrate Artificial Intelligence (AI) to make autonomous decisions based on parameters such as weight, destination, dimensions, and priority.

Studies have shown that the implementation of automated sorting systems makes a significant contribution to improving industrial productivity and operational efficiency, offering several important advantages, including:

- Reduced human intervention, leading to fewer human errors,
- Increased processing speed,
- Optimized warehouse space utilization,
- Lower operating costs,
- Continuous 24/7 operation without interruptions.

3. Design and Development of the System

The development of this robotic system aims to create a simple and ergonomic design that minimizes manufacturing and maintenance costs while providing effective organizational support in warehouse operations. Accordingly, the development of the prototype began with the 3D modeling of the complete assembly, shown in Fig. 4, using specialized CAD software such as CATIA.

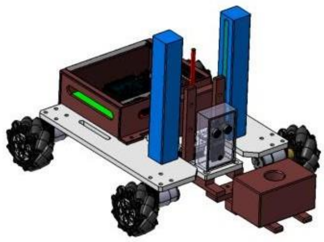

Fig. 4 Miniature Forklift Robot

The proposed system consists of two main parts. The first is the forklift robot itself, while the second comprises both the package pickup station (Fig. 5) and the storage rack where the packages are placed after sorting (Fig. 6).

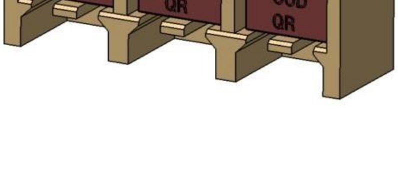

Fig. 5 Package Pickup Station

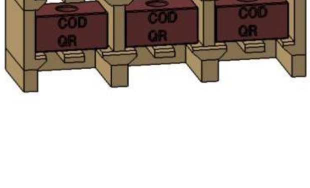

Fig. 6 Storage Rack

The two components illustrated in Fig. 5 and Fig. 6 were designed with a simple geometry, taking into account their manufacturing method, namely additive manufacturing. A 3D printer was used to produce these components, while the design was intentionally optimized to eliminate the need for bulky auxiliary elements such as pallets, including both modified pallets and standard Euro pallets. Although pallets have played a significant role in logistics, their main drawback is the considerable amount of storage space they occupy, which may reduce warehouse efficiency.

4. Electrical Assembly and Component Testing

To enable the movement of the robotic assembly, the electronic components were selected following an analysis of the system requirements, taking into account cost, ergonomics, and functional performance.

List of electronic components:

1. 1 × Arduino Mega,
2. 4 × DC motors (for the Mecanum wheels),
3. 2 × L298 motor drivers,
4. 1 × NEMA 17 stepper motor (for the lifting mechanism),
5. 1 × A4988 stepper motor driver,
6. 1 × LiPo battery (to power the system),
7. 1 × ESP32-CAM module (for scanning QR codes on the packages),
8. 1 × Load cell (for measuring package weight),
9. 1 × HX711 amplifier (for interfacing the load cell with the Arduino),
10. 1 × HC-SR04 ultrasonic sensor (for unexpected obstacle detection and avoidance).

Based on the components listed above, an electrical wiring diagram was created using Microsoft Visio to facilitate the integration and testing of the electronic system. The resulting connection diagram is presented in Fig. 7.

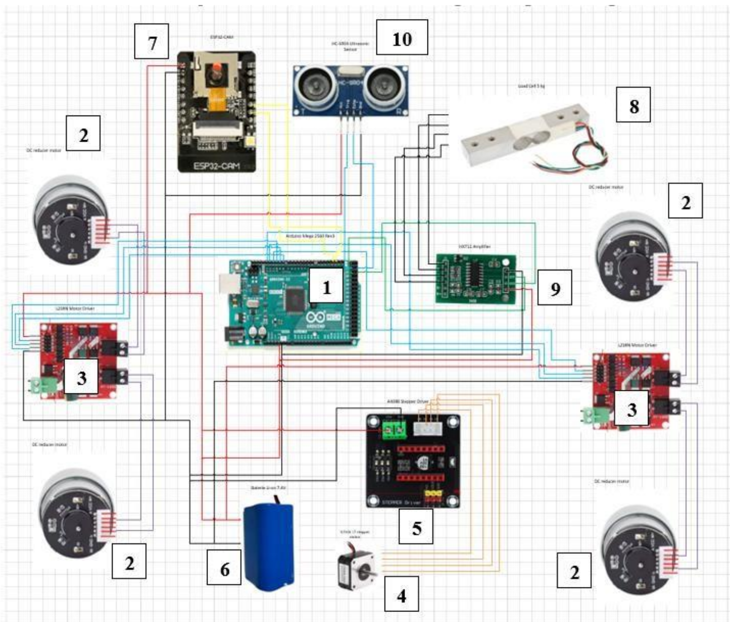

Fig. 7 Electrical Wiring Diagram

Based on the wiring diagram presented in Fig. 7, the electronic components were interconnected and the circuit was powered using a 12 V power supply to test several of the system's functions. It should be noted that, at the time this study was conducted, not all of the mechanical and electronic components required for the complete assembly of the experimental model were available. Consequently, only a partial assembly and functional testing of the available components could be carried out (Fig. 8, Fig. 9, and Fig. 10).

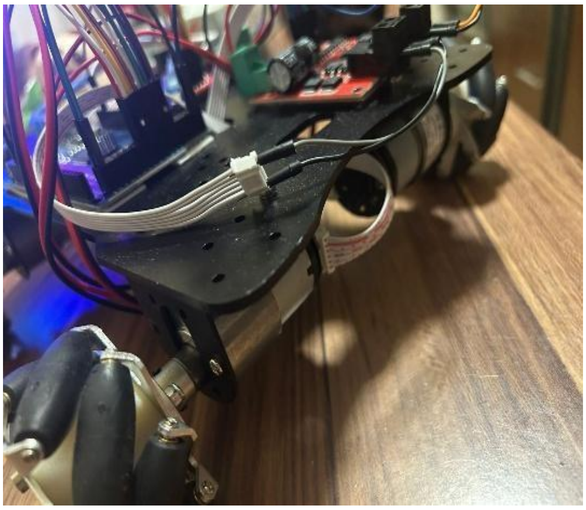

Fig 8 Connection Between the DC Motors and the Motor Drivers

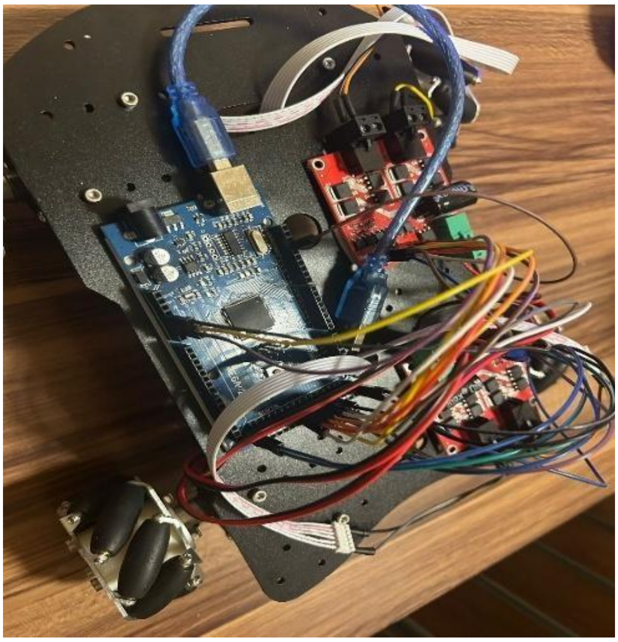

Fig. 9 Connection Between Driver #1 and the Arduino

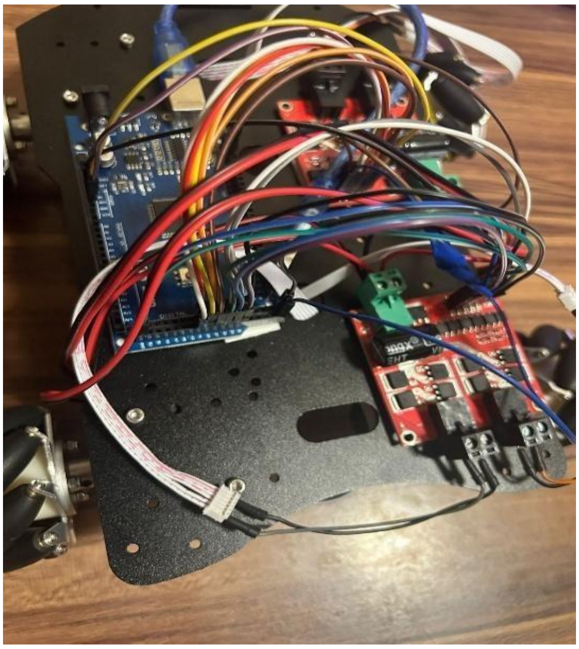

Fig. 10 Connection Between L298 Driver #2 and the Arduino

For the preliminary assembly used to test these components, a prefabricated chassis was employed, as the custom chassis designed during the 3D modeling stage was not yet available.

After completing the electrical connections, the Arduino IDE Legacy (version 1.8.4) development environment was used to create a simple test program. The purpose of this program was to verify the functionality of the electronic components and to demonstrate the robot's ability to move in all four primary directions: forward, backward, left, and right (Fig. 11).

test §

```
const int enable1 = 32;
const int in1 = 34;
const int in2 = 30;
const int enable2 = 35;
const int in3 = 33;
const int in4 = 31;
const int enable3 = 39;
const int in1_2 = 40;
const int in2_2 = 37;
const int enable4 = 41;
const int in3_2 = 38;
const int in4_2 = 36;
void setup() {
  pinMode(enable1, OUTPUT);
  pinMode(enable2, OUTPUT);
  pinMode(enable3, OUTPUT);
  pinMode(enable4, OUTPUT);
  pinMode(in1, OUTPUT);
  pinMode(in2, OUTPUT);
  pinMode(in3, OUTPUT);
  pinMode(in4, OUTPUT);
  pinMode(in1_2, OUTPUT);
  pinMode(in2_2, OUTPUT);
  pinMode(in3_2, OUTPUT);
  pinMode(in4_2, OUTPUT);
  digitalWrite(enable1, HIGH);
  digitalWrite(enable2, HIGH);
  digitalWrite(enable3, HIGH);
  digitalWrite(enable4, HIGH);
}
void loop() {
  digitalWrite(in1, HIGH); digitalWrite(in2, LOW);
  digitalWrite(in3, HIGH); digitalWrite(in4, LOW);
  digitalWrite(in1_2, HIGH); digitalWrite(in2_2, LOW);
  digitalWrite(in3_2, HIGH); digitalWrite(in4_2, LOW);
  delay(5000);
  digitalWrite(in1, LOW); digitalWrite(in2, HIGH);
  digitalWrite(in3, LOW); digitalWrite(in4, HIGH);
  digitalWrite(in1_2, LOW); digitalWrite(in2_2, HIGH);
  digitalWrite(in3_2, LOW); digitalWrite(in4_2, HIGH);
  delay(5000);
  digitalWrite(in1, HIGH); digitalWrite(in2, LOW);
  digitalWrite(in3, HIGH); digitalWrite(in4, LOW);
  digitalWrite(in1_2, LOW); digitalWrite(in2_2, HIGH);
  digitalWrite(in3_2, LOW); digitalWrite(in4_2, HIGH);
  delay(5000);
  digitalWrite(in1, LOW); digitalWrite(in2, HIGH);
  digitalWrite(in3, LOW); digitalWrite(in4, HIGH);
  digitalWrite(in1_2, HIGH); digitalWrite(in2_2, LOW);
  digitalWrite(in3_2, HIGH); digitalWrite(in4_2, LOW);
  delay(5000);
}
```

Fig. 11 Code for Component Testing

5. Conclusions

In conclusion, automated goods sorting systems have evolved from simple postal classification mechanisms into complex solutions based on advanced Artificial Intelligence. This evolution has been driven by the growing demand for efficiency, the rapid expansion of e-commerce, and continuous advances in information technologies.

The primary objective of the proposed system is to combine the simplicity, affordability, and ease of maintenance characteristic of earlier solutions with the efficiency, speed, and functionality required by modern logistics environments.

8. Bibliography

[1]. Cristian-Vasile DOICIN, .. 06-FIIR-L-A4-S1: Tehnologii şi echipamente pentru fabricare aditivă;
[2]. Mihaela-Elena ULMEANU, .. 06-FIIR-L-A2-S2: Bazele proiectarii tehnologice asistate de calculator;
[3]. Ionuţ-Gabriel GHIONEA, .. 06-FIIR-L-A3-S1: Proiectare asistată de calculator;
[4]. Smart LogitecX, accesat la 13.05.2026;
[5]. Daifuku, accesat la 13.05.2026;
[6]. Kiva Systems, accesat la 13.05.2026.

EDGE AI-BASED GESTURE AND VOICE INTERACTION BETWEEN ROBOTIC HANDS AND AN AUTONOMOUS MOBILE PLATFORM

ACIOBĂNIȚEI Radu-Ioan, **DOICIN Cristian-Vasile, ABAZA Bogdan-Felician**
Faculty: Industrial Engineering and Robotics, Specialization: Industrial Informatics, Year of study: IV, e-mail: r.aciobanitei03@gmail.com

ABSTRACT: This paper presents an edge AI architecture for gesture-based and voice-assisted communication between dexterous robotic hands and an autonomous mobile platform. Two recognition pipelines are combined: MediaPipe-based detection for human hands and a visual-marker-based method for robotic hands. A fully offline vocal channel integrates local speech recognition, language-model response generation and text-to-speech synthesis. All processing runs on a Raspberry Pi 5 without cloud dependency. Validation shows 89.2% gesture classification accuracy, 93.7% macro F1-score, stable operation at 21.8 FPS and no thermal throttling, confirming the feasibility of transparent robot-to-robot communication through physical gestures and local multimodal processing.

Keywords: natural communication, gesture recognition, mobile platform, edge AI, dexterous hands

1. Introduction

The transition towards Industry 5.0 [1] and the emergence of Physical AI [2] drive the need for autonomous robotic subsystems that communicate naturally and transparently. In current multi-robot architectures, inter-robot communication relies on opaque digital protocols invisible to human observers. This work establishes a human-readable robot-to-robot communication channel where one robotic subsystem (dexterous hands) encodes commands as physical gestures while another (mobile platform) decodes them through onboard perception. Unlike digital protocols, this channel remains interpretable by any human observer.

The original contributions are: (C1) a modular software architecture for edge-based robot-to-robot communication on embedded hardware; (C2) a multimodal gestural and vocal communication channel operating entirely offline; (C3) edge AI algorithms for gesture detection, including a novel visual-marker-based method extending human-hand recognition to non-anthropomorphic robotic manipulators; and (C4) experimental validation on the target embedded platform, confirming real-time, thermal and accuracy constraints.

2. Related work

Autonomous companion robots evolved from task-specific platforms such as HelpMate [3] to socially interactive systems such as Robovie [4], yet their communication remained strictly human-to-robot. Gesture-based human–robot interaction (HRI) is now a mature field [16], but most published systems address uni-directional human-to-robot command, not inter-robot signalling. In multi-robot communication, Gielis et al. [17] show that coordination still relies on opaque digital protocols invisible to human observers. The absence of a transparent, physically observable robot-to-robot channel motivates contributions C1 and C2.

Contemporary platforms such as Furhat Robotics [5], Unitree G1 [6] and Figure AI F.03 [7] converge towards edge processing and natural communication, yet none implements gesture-based inter-robot control. From an algorithmic perspective, MediaPipe [8] and OpenCV [14] enable real-time hand detection, Whisper [9] provides multilingual transcription, BitNet-style 1-bit Transformer architecture [10] enables on-device reasoning, and Piper TTS [11]offers neural speech synthesis. Recent work demonstrates that visual gesture recognition can run on resource-constrained edge devices [18], but these pipelines target human hands exclusively. Marker-based robotic perception, widely used for localization through fiducial systems such as AprilTag [19], has not been applied to reconstruct hand-like landmarks on non-anthropomorphic robotic manipulators, directly motivating contribution C3.

The proposed architecture combines computer vision, serial communication [15], NLP and mechatronic integration [13] into a fully offline edge system. Most existing works present either algorithmic contributions without embedded deployment, or deployed systems without rigorous validation. Contribution C4 bridges this gap.

3. System architecture

The proposed system, reflecting the modular architecture introduced as contribution C1, comprises two principal subsystems: the dexterous robotic hands RH56DFTP acting as the command emitter, and the autonomous mobile platform acting as the receiver and executor. Gestural communication flows unidirectionally from the hands to the platform, while the vocal channel (C2) enables bidirectional interaction between the platform and the user. All computational processing is performed locally on the Raspberry Pi 5, ensuring complete independence from external network resources. The system's architecture is summarised in Fig. 1.

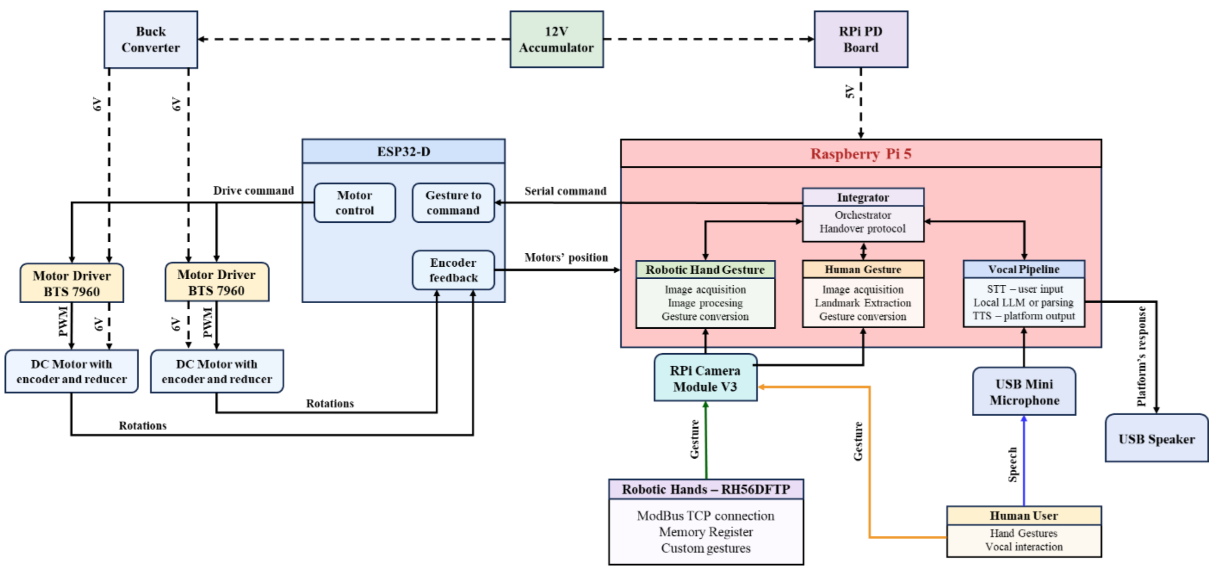

Fig 1: Complete system block diagram

3.1. Hardware architecture

Table 1: Main hardware components of the system

No.	Component	Role	Key Specification
1	Raspberry Pi 5	Central processing unit	16 GB RAM
2	ESP 32 D	Motor control via UART	PWM, encoder feedback
3	Rpi Camera Module V3	Visual perception (CSI)	12 MP, 120° FOV
4	2 x DC motor with encoder and reducer	Platform actuation	6V

5	2 x BTS 7960 motor driver	PWM power stage	43 A peak, H bridge
6	RH56DFTP dexterous hands	Gesture emission	6 active DOF, MODBUS-TCP
7	USB microphone	Vocal input channel	
8	USB speaker	Vocal output channel	
9	Accumulators	Power supply	12V, 15000 mAh

The Raspberry Pi 5 runs all AI inference without a dedicated GPU. The ESP32-D is dedicated to motor control via UART at 115200 baud, ensuring real-time response independently of the perception load. The serial communication protocol follows a text-based command structure over USB UART: ASCII strings (STOP, FWD, BWD, LEFT, RIGHT) terminated by a newline character. A rate-limiting mechanism transmits a command only when it differs from the previous one or after 200 ms. A fail-safe design ensures that upon initialization, mode transition, vocal interaction, exceptions or shutdown, an explicit STOP command is issued to the ESP32.

The RH56DFTP hands represent the other end of the robot to robot communication. The six active DOF of the hands can successfully mimic a large portion of the human gestures and each DOF is independently actuated by a DC motor, further actuating six passive DOF. Four active DOF govern the flexion of the little, ring, middle and index fingers, while the other two articulate the thumb's rotation relative to the metacarpal plane and the flexion. The hands communicate over MODBUS-TCP on port 6000 through a structured register map: each DOF exposes dedicated registers for command and actual angle, force limit, signed contact force, motor current, temperature and feedback from 17 tactile zones. For this paper, the firmware's capability of using 23 data registers for storing custom action sequences were used to define movements that translate into commands after image processing. Furthermore, this capability ensured a steady batch of data for validating the software architecture by being able to read the values stored in the indexed registers and feeding the information back to the hand via a read-write Python pipeline that connects to the hands.[12]

3.2 Software architecture

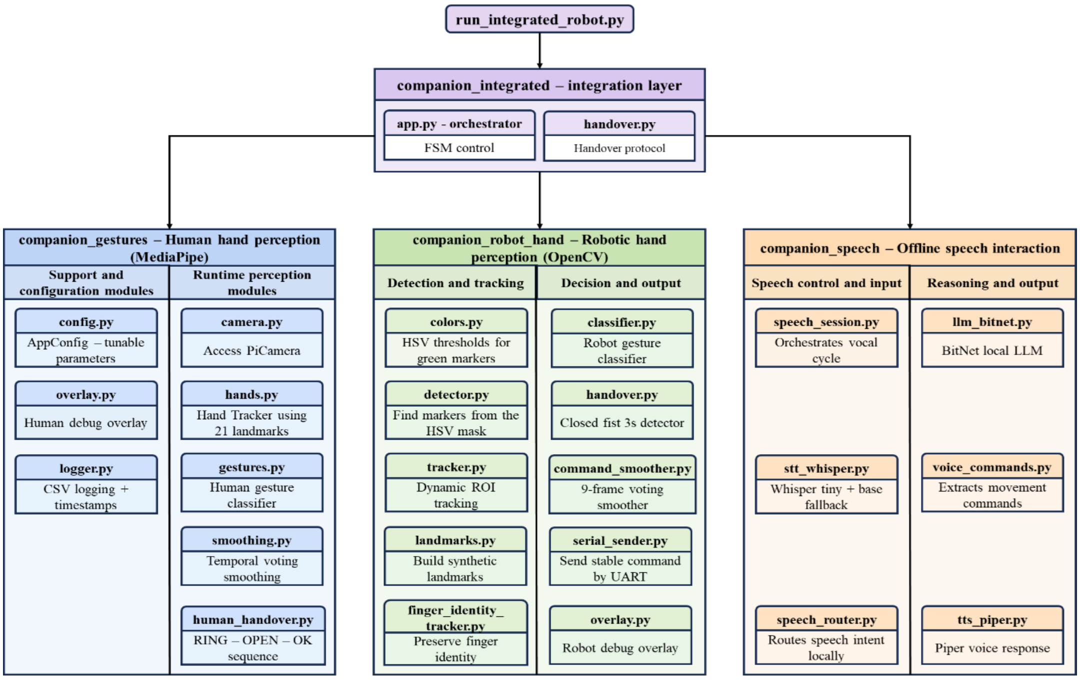

Fig. 2. Software architecture of the autonomous mobile platform

The software system is organized into four Python packages, totaling 26 modules, coordinated by a central orchestrator as illustrated in Fig. 3. The companion_gestures package (8 modules) handles human hand perception: frame capture, MediaPipe landmark extraction, gesture classification and temporal smoothing. The companion_robot_hand package (8 modules) implements a parallel path for the RH56DFTP hands: HSV marker detection, synthetic landmark reconstruction and a deeper command smoother (9 frames, 6 votes). The companion_speech package (4 modules) encapsulates the complete vocal pipeline as a blocking session triggered by the SPEAK gesture. The companion_integrated package contains the orchestrator: a finite state machine (FSM) whose principal states are HUMAN_MEDIAPIPE, ROBOT_HAND, SPEECH_SESSION, STOP/SAFE and HANDOVER. The FSM manages cross-package data flow, handover protocols and fail-safe motor dispatch, following the pipeline: camera → detection → classification → smoothing → command dispatch → ESP32 → motors.

Table 2: Specialized software modules

No.	Module	Function	Platform
1	OpenCV	Frame capture, preprocessing marker detection	Python/RPi5
2	MediaPipe Hands	Human hand detection, 21 landmark extraction	Python/RPi5
3	Whisper Tiny with fallback on Base (C++)	Speech to text transcription	whisper.cpp/RPi5
4	BitNet-based local LLM	Lightweight local conversational response generation	bitnet.cpp / RPi5
5	Piper TTS	Neural text to speech synthesis	Python/RPi5
6	PySerial	UART serial communication with ESP32	Python/RPi5

The personal contribution is reflected mainly in the optimization and adaptation of the software pipeline for real-time embedded execution. The implemented solution does not rely only on the direct use of the existing libraries shown in *Table 2*, but introduces additional control layers for stability, safety and synchronization between subsystems, as shown in *Fig 2*. Gesture outputs are filtered through temporal smoothing and stable-state validation, reducing the probability of false activations caused by transient landmark errors or marker noise. The command dispatch logic was designed conservatively, so that ambiguous detections are converted into safe STOP states instead of being transmitted as active motion commands. For the robotic hand, a custom marker-based interpretation method was implemented to approximate landmark behavior and enable gesture recognition in the absence of a standard robotic-hand tracking model. The integration layer was further optimized by isolating computationally blocking routines and maintaining a clear separation between perception, control and interaction tasks. These decisions improved the robustness, maintainability and testability of the system while preserving real-time performance on the Raspberry Pi 5.

4. Implementation

4.1. Autonomous mobile platform

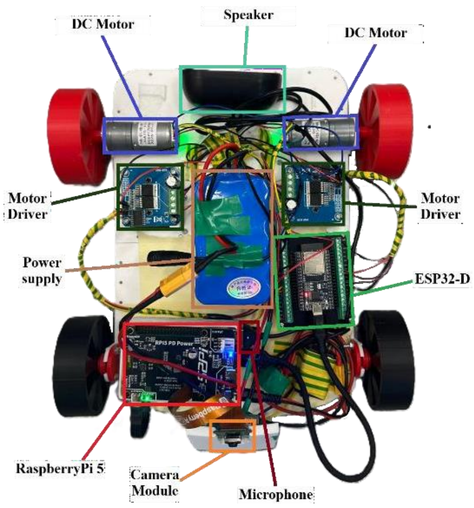

Fig. 3 a: The assembled autonomous mobile platform with annotated components

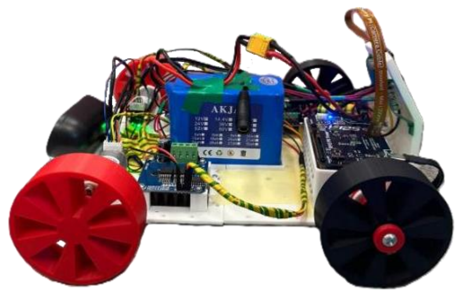

Fig. 3 b: Side view of the assembled autonomous mobile platform

The chassis was designed in SolidWorks and fabricated via FDM with PLA filament (Fig. 3). A central 12 V battery powers both motors and the Raspberry Pi 5. The camera is mounted at the front, optimized for gesture capture at 0.3–1.5 m.

4.2. Gestural Classification

The pipeline captures frames at 1280 x 720 px, 30 fps, detects hands via MediaPipe (complexity 0), extracts 21 landmarks, classifies gestures, applies temporal smoothing and dispatches commands via UART.

Six gesture classes are defined from finger extension states: index finger direction relative to the metacarpophalangeal joint determines FWD, BWD, LEFT, RIGHT; open palm triggers STOP; index and middle extended with ring and pinky retracted triggers SPEAK after 3s of holding the gesture. A directional threshold of 0.12 in normalized coordinates and two consecutive consistent frames are required before issuing a command.

The smoothing module uses a five-frame sliding window requiring three concordant votes. No hand detected for over 0.35 s defaults to STOP, ensuring fail-safe behavior.

4.3. Adaptation for Robotic Hand

A critical challenge was the inability of MediaPipe Hands to recognize the RH56DFTP robotic hands, as shown in Fig. 4. The proposed solution (C3) involves applying green physical markers on key reference points: a large marker on the wrist, a secondary marker on the palm, and smaller markers on each fingertip.

Fig. 4: a) OpenCV marker-based detection on the RH56DFTP robotic hand (left); b) MediaPipe detection on a human hand (right)

Detection uses pure OpenCV: HSV color conversion, morphological filtering and contour extraction with geometric validation. The landmark builder reconstructs a synthetic hand model by identifying wrist, palm, and fingertip markers based on area and spatial ordering. The gesture classifier operates on these synthetic landmarks using vector projections along the wrist-to-palm axis to determine finger extension states. This method demonstrates that standard gesture pipelines can be extended to non-anthropomorphic hands through physical marker augmentation without retraining the detection models. The marker-based synthetic landmark reconstruction method constitutes the main technical novelty of this paper, allowing a non-anthropomorphic robotic hand to be interpreted through gesture-recognition logic inspired by human-hand landmark pipelines.

4.4. Handover protocol

Control transfer between human and robotic hands uses handover protocols: a three-step gestural sequence (0.35 s hold per phase, 4.0 s timeout) for human-to-robot, and a 3.0 s closed fist for robot-to-human. STOP is issued and smoothers reset upon handover.

4.5. Vocal Interaction Pipeline

The vocal pipeline (C2) is activated by the SPEAK gesture. Audio is captured at 16 kHz mono for 4 s and transcribed by Whisper Tiny with fallback on Base (whisper.cpp for ARM). The transcription is passed to BitNet 1.58 – 2B then synthesized by Piper TTS (en_EN-lesaac-medium). Latency is ~10 s for pre-trained responses and ~30 s under full LLM inference, all without network dependency. The pipeline is complementary to the low-latency gesture-based control and is intended for user interaction, explanation and confirmation.

5. Testing and results

The validation (C4) used logged runtime data from controlled sessions recording expected and detected gestures, FPS, CPU load, temperature and throttling. Human and robotic modes were evaluated independently with 300 manually labeled frames per gesture. Results are reported at two levels: frame-level accuracy (per-frame correctness) and segment-level accuracy (command stability after smoothing), alongside macro F1-score and runtime metrics.

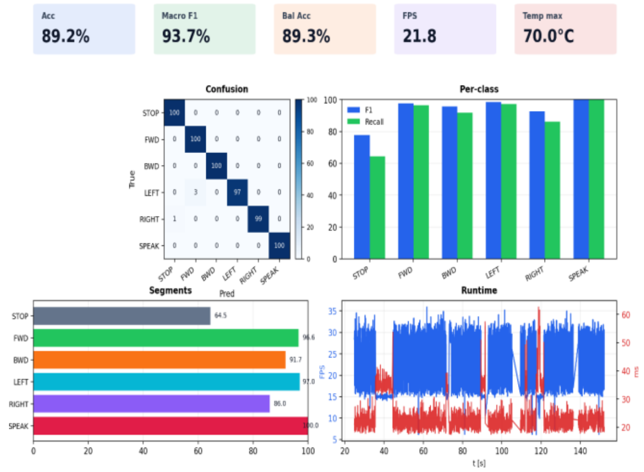

Fig. 5. Human hand gesture classification dashboard: confusion matrix, per-class F1/Recall, segment accuracy, and runtime performance

The human hand results are presented in Fig. 5. Overall accuracy reached 89.2% with a macro F1-score of 93.7%. Per-frame classification was near-perfect: STOP, FWD, BWD, SPEAK at 100%, RIGHT at 99%, LEFT at 97%. Segment accuracy shows lower values (STOP: 84.5%, FWD: 96.5%, BWD: 91.7%, LEFT: 92.0%, RIGHT: 86.0%, SPEAK: 80.0%) due to smoother convergence periods. The system sustained 21.8 FPS with 70.0 °C peak and no throttling.

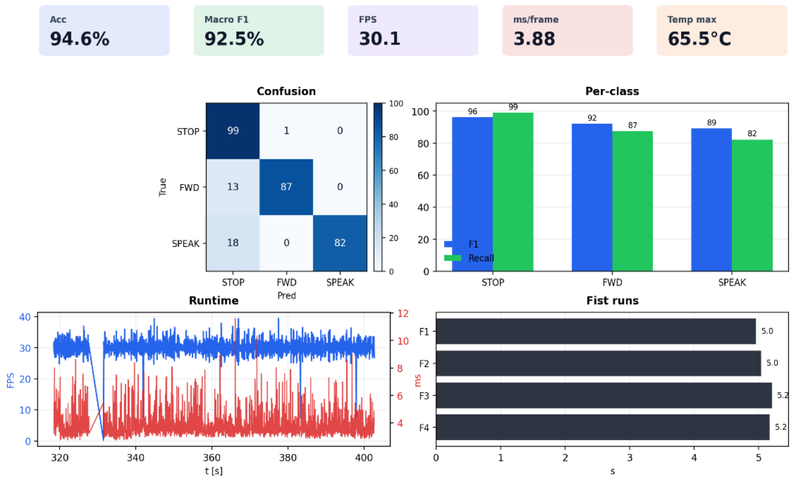

Fig 6: Robotic hand gesture classification dashboard: confusion matrix, per-class F1/Recall, segment accuracy, and runtime performance

The robotic hand results (Fig. 6) validate the marker-based method (C3). The pipeline operates within the same real-time envelope as MediaPipe despite additional OpenCV stages. Together, both result sets validate all four contributions: C1, C2, C3 and C4.

6. Conclusions

This paper presented four contributions: a modular edge architecture (C1), an offline multimodal channel (C2), a novel marker-based method for non-anthropomorphic hands (C3), and systematic validation (C4). Results confirm 89.2% accuracy, 93.7% macro F1, 21.8 FPS and no thermal throttling. Every command is expressed through observable physical gestures or speech.

Current limitations include controlled visual conditions, limited gesture vocabulary, sensitivity of marker-based detection to illumination and camera positioning, and high vocal latency unsuitable for real-time control. These define the next development stage.

Future work includes PID-based motor control for smoother actuation, compound gesture vocabulary, LLM inference optimization to reduce vocal latency, and full integration on the Unitree G1 [6] humanoid platform. The modular design and reliance on standard protocols (UART [15], MODBUS-TCP) position the architecture for portability to alternative ARM and RISC-V boards and industrial edge gateways.

7. References

[1]. van Erp, T., McMillan, A., et al. (2024), "Industry 5.0: A Strategy Framework for a Human-Centric, Sustainable, and Resilient European Industry", European Commission, Brussels.
[2]. Bousetouane, F. (2025), "Physical AI Agents: Bridging Digital Intelligence and Physical Interaction", arXiv preprint arXiv:2501.02345.
[3]. Krishnamurthy, B. and Evans, J. (1992), "HelpMate: A Robotic Courier for Hospital Use", Proceedings of IEEE/RSJ IROS, Raleigh, NC.
[4]. Ishiguro, H., Ono, T., Imai, M., Maeda, T., Kanda, T. and Nakatsu, R. (2001), "Robovie: An Interactive Humanoid Robot", Industrial Robot, 28(6), pp. 498–504.
[5]. Furhat Robotics AB (2024), "Furhat Robot: Technical Documentation and SDK Reference", Stockholm, Sweden.
[6]. Unitree Robotics (2024), "G1 Humanoid Robot: Technical Specifications and Educational Package", Hangzhou, China.
[7]. Figure AI (2025), "F.03: Autonomous Humanoid Companion with Helix AI Architecture", Sunnyvale, CA.
[8]. Lugaresi, C. et al. (2019), "MediaPipe: A Framework for Building Perception Pipelines", arXiv:1906.08172.
[9]. Radford, A., Kim, J.W. et al. (2023), "Robust Speech Recognition via Large-Scale Weak Supervision", Proceedings of ICML, PMLR 202.
[10] Wang, H., Ma, S., Dong, L., Huang, S., Wang, H., Ma, L., Yang, F., Wang, R., Wu, Y. and Wei, F. (2023), "BitNet: Scaling 1-bit Transformers for Large Language Models", arXiv:2310.11453.
[11]. Rhasspy Project (2024), "Piper: A Fast, Local Neural Text-to-Speech System", GitHub Repository. [12]. Inspire Robots (2024), "RH56DFTP Dexterous Hand Series: User Manual", Shenzhen, China. [13]. Zambare, M., Joshi, B. and Thosar, A. (2016), "Evolution and Current State of Mechatronic Systems", Int. J. Advanced Research, 4(2), pp. 223–230.
[14]. Bradski, G. (2000), "The OpenCV Library", Dr. Dobb's Journal of Software Tools, 25(11), pp. 120–125.
[15]. Axelson, J. (2007), Serial Port Complete: COM Ports, USB Virtual COM Ports, and Ports for Embedded Systems, 2nd ed., Lakeview Research, Madison, WI.
[16]. Wang, X., Liang, X. and Zhu, B. (2022), "Hand and Arm Gesture-based Human-Robot Interaction: A Review", Proceedings of ICACS, ACM, pp. 1–8.
[17]. Gielis, J., Shankar, A. and Prorok, A. (2022), "A Critical Review of Communications in Multi-Robot Systems", Current Robotics Reports, 3, pp. 213–225.
[18]. Singh, G., Gautam, S., Puri, Y., Parikh, J. and Mishra, G. (2024), "Novel System Based on Amalgamation of Embedded Systems and Edge AI for Hand Gesture Recognition", IC3 2024, ACM, Noida, India.
[19]. Olson, E. (2011), "AprilTag: A Robust and Flexible Visual Fiducial System", Proceedings of IEEE ICRA, Shanghai, pp. 3400–3407.

EDGE AI ARCHITECTURE FOR AUTONOMOUS ROBOTIC NAVIGATION AND COGNITIVE INTERACTION IN A VIRTUAL ENVIRONMENT

CIUCĂ Virgiliu-Gabriel și Prof. dr. ing. DOICIN Cristian-Vasile (Scientific Advisor), Conf.dr.ing. ABAZA Bogdan Felician (Scientific Advisor)

Facultatea de Inginerie Industrială și Robotică, Specializarea: Informatică Industrială, Anul de studii: III,
e-mail: virgiliu.ciuca@stud.fiir.upb.ro.

ABSTRACT: This paper presents PoliNAV, an integrated Edge AI architecture for autonomous navigation and cognitive interaction in a high-fidelity virtual environment (CoppeliaSim). The system combines a locally deployed Qwen 2.5 model for intent extraction, achieving up to 92% accuracy on semantic commands, a fine-tuned YOLOv8 Nano model for real-time object detection, A* path planning on an occupancy grid, and a PD controller for motion execution. Semantic information extracted from vision and language is stored in a persistent JSON-based map, enabling the robot to navigate toward objects even when they are no longer visible. Experimental results demonstrate the feasibility of local AI-based perception and decision-making for robotic assistance in virtual academic environments, with the PD controller successfully reducing positioning error below the 0.30 m tolerance threshold within 11.5 seconds, providing a solid foundation for future Sim-to-Real deployment.

CUVINTE CHEIE: Edge AI, LLM*, Computer vision, Autonomous navigation, Data synthesis.

1. Introduction

The development of autonomous assistant robots requires a complex integration between sensory perception, logical reasoning, and natural user interaction [1]. The objective of the PoliNAV project is to implement a cognitive navigation system validated within a high-fidelity virtual environment. PoliNAV is a prototype of an academic navigation robotic assistant capable of interpreting natural language commands, identifying relevant objects in the environment, and autonomously planning paths toward semantic destinations.

The proposed architecture adopts an Edge AI strategy: vision processing via YOLOv8 Nano and linguistic reasoning through the Qwen 2.5 model are executed locally to ensure minimal latency and computational autonomy. In addition to these, the system utilizes the ElevenLabs** API for voice synthesis, delegating the quality of verbal interaction to a high-performance Cloud solution. The validation of the entire ecosystem is carried out in the CoppeliaSim simulator, where A* path planning algorithms [2] [3] and motion control are tested using a virtual prototype within a faithful replica of the academic space.

2. Stadiul actual

Currently, assistive robotics is undergoing a transition phase from rigid, script-based systems to solutions endowed with cognitive intelligence. The dominant trend in research is

the migration from Cloud processing to Edge AI architectures, motivated by the need to reduce latency and protect data. The integration of Large Language Models (LLMs) into the robot control loop has opened new perspectives in the semantic interpretation of complex commands. At the same time, the use of vision models from the YOLO family remains the industrial standard for real-time object detection, providing the necessary speed for navigating dynamic environments. The present project aligns with this trend, exploring the use of quantized models to bring the computational power of artificial intelligence directly onto the robotic platform [4].

3. Simulation Environment: CoppeliaSim for Virtual Prototype Validation

The CoppeliaSim* platform [5] constitutes the technical foundation of the project, operating as a high-fidelity simulation environment for Sim-to-Real validation. As illustrated in Figure 1, the developed virtual scene reproduces a representative section of the faculty, being configured as a multifunctional space that includes a small presentation room, an office, and a relaxation area.
To optimize RAM consumption and computational resources during the simulation, a controlled environment geometry was chosen, integrating approximately 24 static and dynamic objects. Among the relevant object classes defined as semantic targets are: tables, chairs, armchairs, coffee vending machines, decorative plants, and video projectors. This framework provides a safe testing environment for verifying physical and sensory interactions without the risk of damaging real equipment.

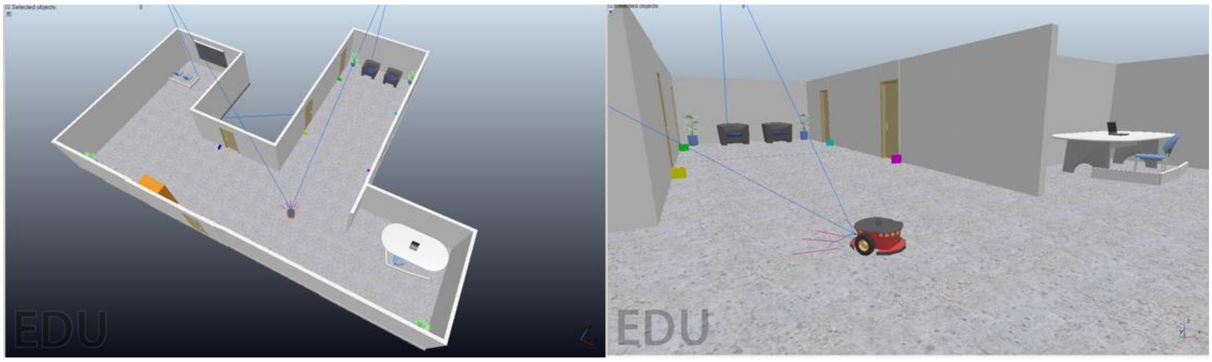

Fig. 1. Representation of the academic environment in the CoppeliaSim simulator

The perception of the assistant robot is supported by an array of simulated sensors, essential for local processing: a monocular camera (Vision Sensor) configured to generate the RGB video stream required for YOLOv8 Nano inference, proximity sensors (based on ray-casting) used for distance extraction, and an internal odometry** system for continuous monitoring of the relative position in the plane. The software implementation relies on decoupling the control logic from the virtual environment via the ZeroMQ Remote API, ensuring the direct portability of the Python scripts to a physical hardware platform. The use of the Bullet Engine allows for the simulation of gravity, collisions, structural inertia, and ground friction forces, providing a dynamic behavior extremely close to that of a real physical platform.

---

*CoppeliaSim – Robotics simulation platform (formerly V-REP) that allows modeling complex systems and validating algorithms in a virtual environment equipped with physics engines (Bullet, ODE).
**Odometry – Method of estimating the position and orientation of a mobile robot based on data provided by wheel rotation sensors (encoders).

The decision-making core of the PoliNAV system is powered by the Qwen 2.5* large language model [6] (the 1.5B parameter variant), implemented within an Edge AI architecture. Utilizing local inference via the llama-cpp-python library guarantees total autonomy of the system and a minimal response time, eliminating network latency and security risks inherent to Cloud services. To optimize hardware resource consumption on the computing platform, the model was enhanced through 4-bit GGUF quantization (Q4_K_M), a process that reduces the memory footprint to approximately 1.2 GB of RAM while maintaining a high logical reasoning capability.

From a functional standpoint, this module performs the critical step of Intent Extraction. The process converts user commands from natural language into structured data using a semantic mapping dictionary. The experimental validation of this module was conducted by testing a dataset of approximately 50 distinct commands, yielding an average response time (inference latency) of 3.5 seconds per command. The results regarding the success rate of correct intent extraction are presented in detail in Figure 2.

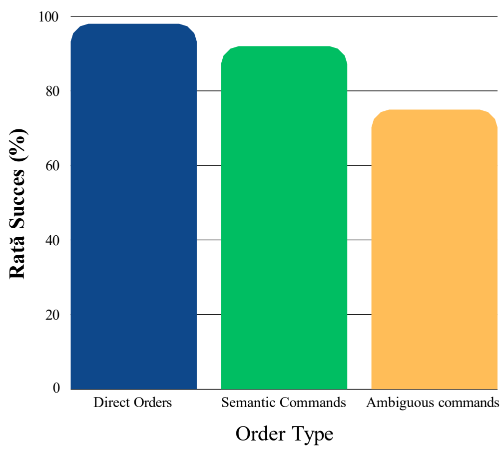

Fig. 2. Performance evaluation of the Intent Extraction process for the local Qwen*2.5 model, reported at different degrees of command complexity.

To eliminate the risk of the model generating erroneous destinations or invalid commands, the system includes a strict software data validation filter. The LLM output is not transmitted directly to the navigation module. Instead, it is filtered and validated through the semantic mapping dictionary, which only accepts identifiers that exist in the CoppeliaSim scene and coordinates already registered in the persistent semantic map. Completely ambiguous commands or destinations that cause hallucinations** from the model are automatically rejected, and the robot requests verbal clarifications through the speech synthesis module. Finally, the behavior is calibrated via System Prompting, a procedure through which the robot acquires the faculty-specific context and strict safety rules during navigation.

---

*Qwen 2.5 – State-of-the-art family of language models, developed to offer an optimal balance between logical reasoning capability and efficiency on resource-constrained systems.

**Hallucination (LLM) – A phenomenon specific to large language models whereby the algorithm generates a syntactically correct response that is completely false or fabricated relative to the provided factual data.

5. Visual Perception: Object Detection and Mapping with YOLOv8

The perception system of the PoliNAV robot relies on the YOLOv8 Nano* computer vision model [7] [8], selected for its optimal balance between processing speed (high FPS) and detection accuracy on Edge-type hardware. To ensure faithful recognition within the virtual environment, a fine-tuning process was performed on the pre-trained yolov8n.pt model. Training was conducted locally on a CPU architecture, utilizing a synthetic dataset generated directly from the CoppeliaSim simulator. Since no pre-trained open-source models were available for this specific virtual scene, the entire dataset was structured, annotated, and managed through the RoboFlow platform, applying a data split ratio of 60% for training (train), 25% for validation (val), and 15% for testing (test). Figure 3 displays an annotated validation batch from the synthetic dataset managed via the RoboFlow** platform. It illustrates how bounding boxes and labels corresponding to the defined classes are applied

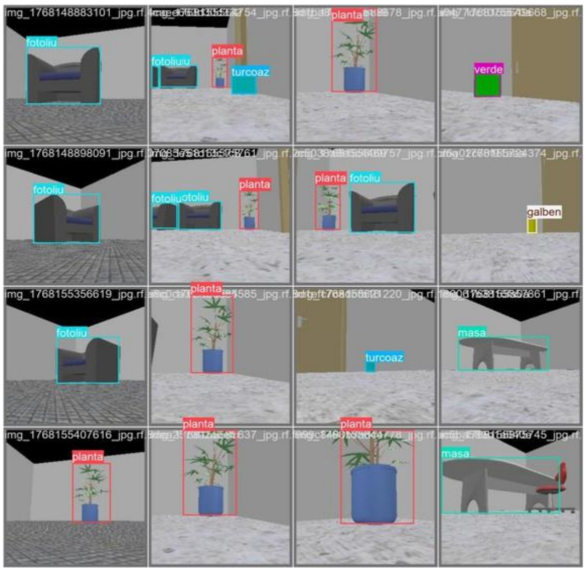

Fig. 3. Batch of images from the validation set annotated in RoboFlow, illustrating the application of bounding boxes for object classes in the virtual environment.

From a technical perspective, the training process was configured for 100 epochs at a resolution of 640x640 pixels, ensuring a stable convergence of the model. The performance of this process and the accuracy of the model under test conditions are validated through the analysis of the confusion matrices presented in Figure 4. These demonstrate an excellent classification capability for objects essential to navigation, such as tables, chairs, vending machines, or video projectors.

---

*YOLOv8 Nano – The most compact variant of the "You Only Look Once" architecture, optimized for real-time object detection with minimal video memory consumption and processing power.
**RoboFlow – Web platform used in computer vision for dataset management, image annotation, labeling format conversion, and the application of augmentation techniques.

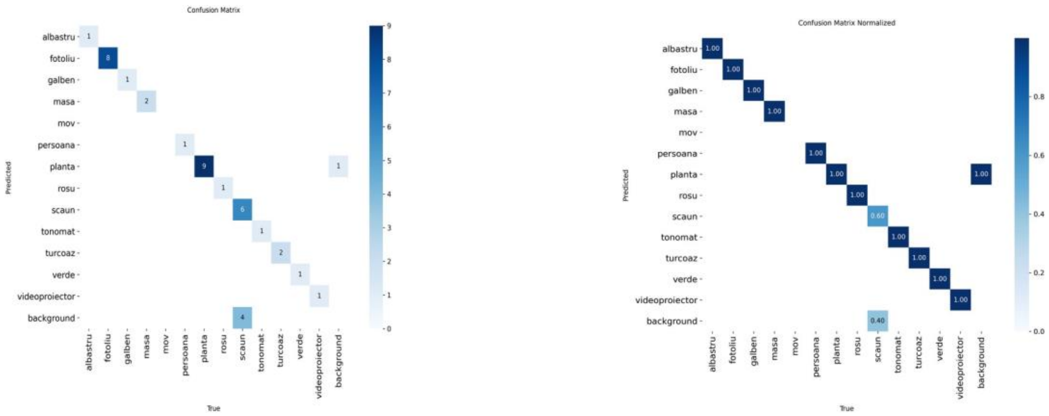

Fig. 4. Confusion matrix: absolute values (left) and normalized values (right) of the YOLOv8 Nano validation process

6. Navigation System: Path Planning via the A* Algorithm and Occupancy Grid

The navigation system of the PoliNAV platform represents the final stage of the processing pipeline, transforming semantic and visual data into precise motor actions. The process begins by discretizing the workspace from CoppeliaSim into an Occupancy Grid. This matrix represents the operating environment in a digital format, being specifically constructed to map the geometry of the academic space. The visualization of the simulated scene and its digital counterpart are presented in Figure 5 and Figure 6, respectively.

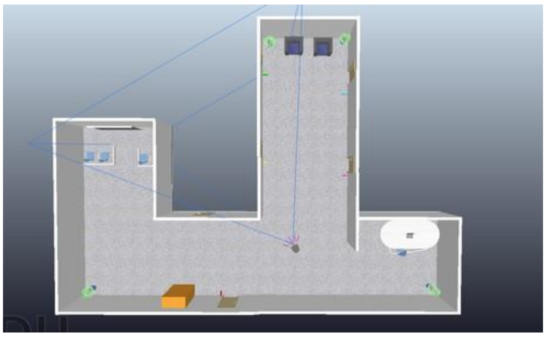

Fig. 5. Visualization of the working environment in the CoppeliaSim simulator

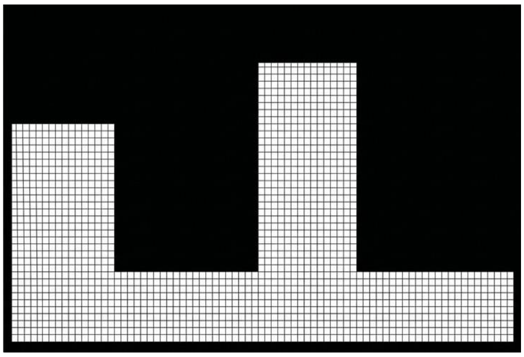

Fig. 6. Representation of the digital map of the Grid type (Occupancy Grid)

For efficient processing, a map resolution (MAP_RESOLUTION) of 0.5 meters was selected, allowing a balance between movement accuracy and the computational speed of the pathfinding algorithm. The origin of the coordinate system is established at X = -12.20 and Y = -12.30, ensuring the correct translation of points from the virtual world into matrix indices.

Trajectory planning is achieved via the A* algorithm [2] [3], which utilizes the information stored in harta_robot.json to identify target coordinates. The algorithm determines the optimal path by minimizing the cost function:

$$f(n) = g(n) + h(n)$$

where the mathematical elements are defined as follows:
$f(n)$ = the total estimated cost of the path through the current node;
$g(n)$ = the cost of the path from the starting point to the current node n ;
$h(n)$ = the heuristic to the destination, calculated within the system via the Manhattan distance.

Traiectoria generată sub formă de puncte de "follow up" este ulterior executată prin intermediul unui controler PD*. Validarea experimentală a acestui modul de control, efectuată pe o traiectorie nominală de 12 metri, confirmă corelația directă cu parametrii de configurare (BASE_SPEED = 1.3). Așa cum se observă în Figura 7, sistemul atinge pragul de toleranță de 0,30 metri în aproximativ 11,5 secunde, asigurând o oprire stabilă și fluidă, fără oscilații critice sau depășiri de traiectorie.

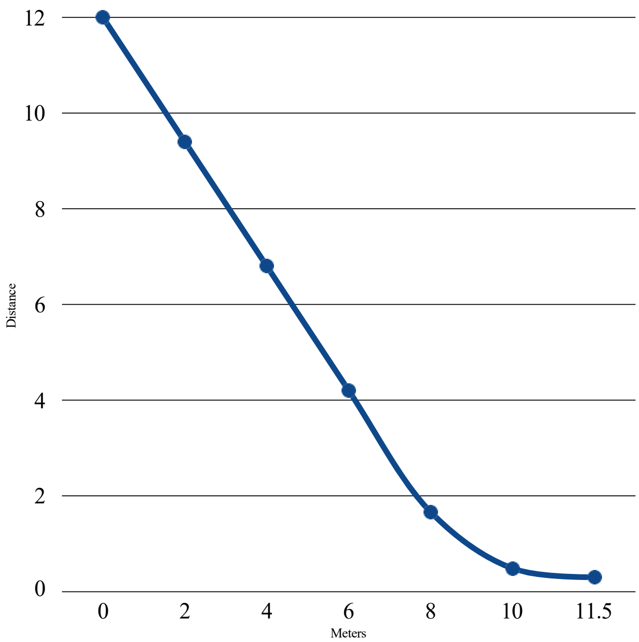

Fig. 7. PD controller performance graph: Evolution of positioning error (meters) versus execution time (seconds).

*PD Controller (Proportional-Derivative) – Closed-loop automatic control algorithm that continuously calculates the linear and angular velocity commands of the robot.

7. Conclusions and Future Work

The present paper has demonstrated the feasibility of an integrated architecture for cognitive navigation within a virtual environment, combining natural language command interpretation via a local LLM, visual detection through YOLOv8 Nano, semantic object memorization, and path planning using the A* algorithm. Through the development of the PoliNAV system, a functional bridge has been established between natural language processing (NLP), computer vision, and classical robotics algorithms, with the results obtained in the CoppeliaSim simulator proving that the system can transform high-level commands into executable navigation actions.

7.1. Synthesis of Obtained Results

The performance of the modules composing the PoliNAV architecture was evaluated based on clear quantitative indicators, eliminating purely qualitative assessments:

- Cognition Module (LLM): The evaluation of the Qwen 2.5 (1.5B) model on a test set of approximately 50 distinct commands indicated a 92% success rate in the Intent Extraction* process for semantic commands, recording an average local inference latency of 3.5 seconds.
- Visual Perception Module (YOLOv8): Training on approximately 140 synthetic images, structured in RoboFlow with a controlled split ratio (60% train, 25% val, 15% test), ensured a 91.2% accuracy in correct object identification. During the execution phase, video stream processing stabilized at a frequency of 50 FPS* on the local CPU architecture.
- Navigation System (A* and PD): Experimental tests validated the capacity for smooth movement. Over a 12-meter nominal trajectory, the PD controller guided the mobile platform to the destination in 11.5 seconds, ensuring a stable stop and reducing the final positioning error below the 0.30 m tolerance threshold.

7.2. Original Contributions

- The primary contribution of this project consists in the design and implementation of an Edge AI architecture completely independent of external server connections for perception and decision-making processes. Prioritizing local processing eliminates network latencies and protects data integrity, while the use of Cloud services (ElevenLabs) is strictly limited to optimizing voice interaction. Furthermore, defining a software filter based on a semantic dictionary to block LLM hallucinations, along with the custom training of the YOLOv8 model on a controlled synthetic data distribution (60% train, 25% val, 15% test), represents engineering solutions tailored specifically to the requirements of the academic application.

7.3. Future Research Directions

Although the initial objectives have been successfully achieved, the project offers multiple avenues for development. A priority for the upcoming stages is the Sim-to-Real transition, which involves implementing the algorithms on a physical hardware platform (e.g., Jetson Nano). From an algorithmic perspective, future work aims to integrate a dynamic replanning system capable of handling moving obstacles (people in motion) in real time. Furthermore, extending the LLM's capabilities to manage multi-robot tasks and integrating additional sensors (such as LiDAR) could increase positioning accuracy in low-visibility environments, transforming PoliNAV into a fully autonomous and robust academic assistant.

Fig. 8. Visual identity of the PoliNAV project

8. Bibliography

[1] ScienceDirect, „Human-Robot Interaction - an overview," ScienceDirect Topics, Elsevier, 2026. [Online]. Available: https://www.sciencedirect.com/topics/computer-science/human-robot-interaction

[2] Foead, D., A. Ghifari, M. B. Kusuma, N. Hanafiah, and E. Gunawan, „A Systematic Literature Review of A* Pathfinding," Procedia Computer Science, vol. 179, pp. 507-514, 2021.

[3] Yan, Y., „Research on the A Star Algorithm for Finding Shortest Path," Highlights in Science, Engineering and Technology, vol. 46, pp. 154-161, 2023.

[4] Abaza, B. F. (2026), Rețele Neuronale, Suport de curs, Facultatea de Inginerie Industrială și Robotică, Universitatea Națională de Știință și Tehnologie Politehnica București.

[5] Rohmer, E., S. P. N. Singh, and M. Freese, „CoppeliaSim (formerly V-REP): A versatile and scalable robot simulation framework," in Proceedings of the IEEE/RSJ International Conference on Intelligent Robots and Systems (IROS), 2013, pp. 1321-1326.

[6] Alibaba Qwen Team, „Core Concepts," Qwen Documentation, 2024. [Online]. Available: https://qwen.readthedocs.io/en/latest/getting_started/concepts.html

[7] Redmon, J., S. Divvala, R. Girshick, and A. Farhadi, „You Only Look Once: Unified, Real-Time Object Detection," arXiv preprint arXiv:1506.02640, 2016.

[8] Ultralytics, „YOLOv8 Models Documentation," Ultralytics Docs, 2023. [Online]. Available: https://docs.ultralytics.com/models/yolov8